Towards fabrication of novel photocatalysts: investigation of morphology control of metal oxide nanoparticles

A thesis
submitted in partial fulfilment
of the requirements for the Degree
of
Doctor of Philosophy
by

Campbell McNicoll

Supervisor: Dr. Tim Kemmitt

Co-Supervisor: Dr. Vladimir Golovko

School of Physical and Chemical Sciences

University of Canterbury

2018

To Vladimir, Tim, Callaghan Innovation, Fisher & Paykel Healthcare, Avertana, The MacDiarmid Institute and the University of Canterbury for teaching me everything I know and keeping faith over the past five years.

To my parents for support and relentless nagging!

“The inability to predict outliers implies the inability to predict the course of history”

“Consider a turkey that is fed every day. Every single feeding will firm up the bird’s belief that it is the general rule of life to be fed every day by friendly members of the human race “looking out for its best interests,” as a politician would say. On the afternoon of the Wednesday before Thanksgiving, something unexpected will happen to the turkey. It will incur a revision of belief.”

By: Nicholas Taleb (The Black Swan: The Impact of the Highly Improbable)

Abstract

In this work titanium dioxide (TiO_2) was synthesised using hydrothermal methods. Initial studies were based on TiO_2 oxalic acid passivated sols previously synthesised by Dr Tim Kemmitt. These sols were hydrothermally treated in the presence of ammonium fluoride (NH_4F) as a morphology directing agent. The hydrothermally treated titanium dioxide was characterised using powder X-ray diffraction (PXRD), scanning electron microscopy (SEM), transmission electron microscopy (TEM) and dynamic light scattering (DLS). It was found the phase, size and shape of the TiO_2 nanoparticles produced could be controlled by tuning the NH_4F concentration, temperature profile and time of the hydrothermal treatment.

The high-temperature hydrothermal treatment caused the decomposition of organic species present in the reaction mixture, which resulted in a partial reduction of the TiO_2 observed as a blue colouration

Characterising the blue colour-causing defect and identify the mechanisms behind the formation of this defect quickly became the focus of the forthcoming studies. The hydrothermal synthesis was tuned to produce a phase-pure blue anatase TiO_2, which was a better candidate for an in-depth study of the electronic features of the blue TiO_2. The conditions need to generate the blue colour were studied and the blue TiO_2 was characterised by the following techniques: synchrotron powder X-ray diffraction (PXRD), scanning electron microscopy (SEM), transmission electron microscopy (TEM), X-ray photoelectric spectroscopy (XPS), valence band spectroscopy (VBS), near edge absorption fine structure spectroscopy (NEXAFS), electron paramagnetic resonance (EPR), superconducting quantum interference device (SQUID), Raman spectroscopy, ultraviolet-visible light spectroscopy diffuse reflectance (UV-VIS DRS), infrared spectroscopy (IR), thermal gravitational analysis (TGA), particle induce gamma emission spectroscopy (PIGE), nitrogen adsorption isotherms and gas mass spectrometry (GC-MS).

Evidence from the various characterisation techniques showed that bulk phase self-doping with Ti^{3+} occurred during synthesis of the blue TiO_2. The Ti^{3+} was stabilised by fluorine ions (F^-) substituted for oxygen in the lattice. The reduction of Ti^{4+} to Ti^{3+} was a consequence of *in-situ* H_2 formation due to the thermal decomposition of the isopropanol liberated from the hydrolysis of titanium isopropoxide (the titanium precursor). The reduced Ti^{3+} ions were incorporated into the growing nanocrystals where F^- would substitute for O^{2-} forming a stable defect. The Ti^{3+} defect produced an intermediate band below the conduction band which allowed the absorption of red light to produce the blue colour observed.

Although the Ti^{3+} was causing the blue colouration, the synthesis conditions and F^- doping had other effects. First, it was found the anatase crystals grew preferentially along the *c* axis, this was found to be as a result of ammonium titanate formation. The ammonium titanate also encouraged the growth of very large crystals in a narrow concentration range. Secondly, the Ti^{3+} defects where found to be mostly located close to the surface. Finally, the TiO_2 was very deficient in Ti as a result of Ti vacancies possibly due to hydroxyl inclusions.

Having determined the synthetic methodology to produce the blue colouration, the synthesis was reworked to produce even more novel blue brookite and blue rutile phase TiO_2 which was characterised using many of the same methods as above.

It was found that the brookite was formed *via* the conversion of anatase *via* a sodium titanate mechanism. The temperature of hydrothermal treatment and NaF ratio could be used to control the aspect ratio of the brookite formed. Finally, it was found that Ti^{3+} was present as both a bulk and surface dopant causing the blue colour.

Blue rutile was formed by adding oxalic acid to the synthesis. The NH_4F was found to change the shape of the rutile crystallites so there was a greater exposure of the {001} facet. The blue rutile was found to have the highest concentration of Ti^{3+} defects and was hence very blue.

Lastly, studies were carried out on the TiO_2 to assess the effects the synthesis conditions and blue colour on the photocatalytic activity of the TiO_2. In particular, there was an interest as to whether the absorption of red light could drive photocatalytic activity into the visible-light range (>400 nm). Reactive blue (RB-19) and methylene blue (MB) was used as a model dyes to examine the photocatalytic activity of the TiO_2. The blue TiO_2 was found to be more active than commercial photocatalyst under broad-spectrum light. The TiO_2 was also capable of harnessing the energy of visible-light to degrade the dye, making it visible light active. Furthermore, the blue brookite and rutile were found to be effective photocatalysts.

.

Table of Contents

Abstract i

Table of Contents iii

Supervisor Team viii

Fellow Students viii

Fellow Colleagues viii

Funding and Enablers ix

Chapter 1 : Introduction 1

1.0 Overview 1

1.1 Aims of This Work 4

1.3 Publications 4

Chapter 2 : Literature Review 6

2.0 Catalyst 6

2.0.1 The Size Effect 6

2.0.2 Photocatalysis 7

2.1 Titanium Dioxide 10

2.1.1 Structure and Phases of Titanium Dioxide 10

2.1.2 Synthesis of Titanium Dioxide Nanoparticles 11

2.1.3 Morphology Control of Titanium Dioxide 12

2.2 Improving the Photocatalytic Performance of Titanium Dioxide 14

2.2.1 Physical Changes to Improve Photocatalytic Performance of Titanium Dioxide 14

2.2.1 Electronic Changes to Improve Photocatalytic Performance of Titanium Dioxide 17

2.3 Blue Anatase Titanium Dioxide 21

2.4 Blue Rutile and Brookite Phase Titanium Dioxide 23

2.4.1 Blue Rutile 24

2.4.2 Blue Brookite 24

2.5 Conclusion 25

Chapter 3 : Experimental 26

3.0 Reagents 26

3.1 Synthesis 26

3.1.1 Oxalic Acid Passivated Sol Synthesis 26

3.1.2 Hydrothermal Treatment of Oxalic Acid Sols 26

3.1.3 Direct Hydrothermal Synthesis of Anatase Phase TiO_2 27

3.1.4 Direct Hydrothermal Synthesis of Rutile Phase TiO_2 29

3.1.5 Direct Hydrothermal Synthesis of Brookite Phase TiO_2 30

3.1.6 Direct Hydrothermal Synthesis of Organic Free Anatase Phase TiO_2 31

3.2 Photocatalysis Experiment 32

3.2.1 Photocatalytic degradation of RB-19 under Xe broad spectrum light 32

3.2.1 Photocatalytic degradation of MB under Xe broad spectrum light 33

3.3 Characterisation 34

3.3.1 Synchrotron Powder X-ray Diffraction 34

3.3.2 Lab Powder X-ray Diffraction 34

3.3.3 Nitrogen Adsorption Isotherms 35

3.3.4 Scanning electron microscopy 35

3.3.5 Transmission electron microscopy 35

3.3.6 Ultra-Violet Diffuse Reflectance Spectroscopy 36

3.3.7 Synchrotron Soft X-ray Spectroscopy 36

3.3.8 Mass Spectrometry of Gas 37

3.3.9 Electron Paramagnetic Resonance 37

3.3.10 Ion Beam Analysis 37

3.3.11 Raman Spectroscopy 37

3.3.12 Dynamic Light Scattering 38

Chapter 4 : Oxalic Acid Passivated Sols and Hydrothermal treatment 39

4.0 Introduction: 39

4.0.1 Oxalic acid passivated TiO_2 Sols 39

4.0.2 Hydrothermal Treatment of Oxalic Sols Modified with NH_4F 39

4.1.0 Results and Discussion: 41

4.1.1Characterisation of Oxalic Acid Stabilised TiO_2 Sols 41

4.1.2 The Hydrothermal Treatment of Oxalic Sols and the Effects of Temperature and Oxalic Acid Concentration 42

4.1.3 Hydrothermal Treatment of Oxalic Sols Modified with NH_4F 47

4.1.4 Hydrothermal Treatment of Oxalic Sols Modified with Mineral Acids and NH_4F 55

4.1.5 The Blue Coloured TiO_2 Produced 61

4.1.6 The Development of the Sol-Less Hydrothermal Synthesis of Phase Pure TiO_2 64

4.3 Conclusions: 68

Chapter 5 : Defect Characterisation in Blue Anatase 70

5.0 Introduction: 70

5.1.1 Ultraviolet-visible light diffuse reflectance spectroscopy 70

5.1.2 Electron Paramagnetic Properties of the Blue TiO_2 70

5.1.3 Raman Spectroscopy Study of Blue TiO_2 73

5.1.4 Synchrotron Powder X-ray Diffraction study of Blue TiO_2 77

5.1.5 Synchrotron Soft X-ray Study of Blue TiO_2 78

5.1.6 Electron Microscopy Study of Blue TiO_2 81

5.1 Results and Discussion: 85

5.1.1 Synthetic Clues 85

5.1.2 Ultraviolet-Visible Light Diffuse Reflectance Spectroscopy 90

5.1.3 Identifying the Reducing Agent 99

5.1.4 Electron Paramagnetic Properties of the Blue TiO_2 103

5.1.5 Raman Spectroscopy Study of Blue TiO_2 108

5.1.6 Synchrotron Powder X-ray Diffraction study of Blue TiO_2 116

5.1.7 Synchrotron Soft X-ray Study of Blue TiO_2 130

5.1.8 Electron Microscopy Study of Blue TiO_2 143
5.1.9 Ion Beam Analysis 168
5.1.10 Nitrogen Adsorption Analysis 169
5.3 Conclusions: 171
Chapter 6 : Blue Rutile and Brookite Phase TiO_2 174
6.1 Introduction: 174
6.1.1 Blue Rutile 174
6.1.2 Ultra-Violet Diffuse Reflectance Spectroscopy studies of Blue Rutile 174
6.1.3 Raman spectroscopy studies of Blue Rutile 174
6.1.4 Soft X-ray Characterisation of Blue Rutile 174
6.1.5 Powder X-ray Diffraction Characterisation of Blue Rutile 175
6.1.5 Electron Microscopy Characterisation of Blue Rutile 175
6.1.6 Characterisation of Blue Brookite 176
6.1.7 Ultra-Violet Diffuse Reflectance Spectroscopy Studies of Blue Brookite 177
6.1.8 Raman Spectroscopy Studies of Blue Brookite 177
6.1.9 Soft X-ray Characterisation of Blue Brookite 177
6.1.10 Powder X-ray diffraction Studies of Blue Brookite 177
6.2 Results and Discussion: 178
6.2.1 UV-VIS DRS Blue Brookite and Rutile Phase TiO_2 178
6.2.2 Raman Spectroscopy on Rutile and Brookite Phase TiO_2 186
6.2.3 PXRD study of Rutile and Brookite Phase TiO_2 190
6.2.3 Electron Microscopy Study of Rutile and Brookite Phase TiO_2 194
6.2.4 Nitrogen adsorption study of Rutile and Brookite Phase TiO_2 202
6.2.5 Soft X-ray study of Rutile and Brookite Phase TiO_2 203
6.3 Conclusions: 210
Chapter 7 : Photocatalysis 212
7.0 Introduction: 212
7.1 Results and Discussion: 214

7.1.1 Photocatalytic activity of oxalic acid sols tested with RB-19 214

7.1.2 Photocatalytic activity of Blue Anatase tested with RB-19 215

7.1.3 Photocatalytic activity of Blue Anatase tested with MB 216

7.1.4 Photocatalytic activity of Blue Brookite tested with MB 223

7.2 Conclusion: 224

Chapter 8 : Conclusions and Future Work 226

8.0 Final Conclusions 226

8.1 Future Work 228

8.1.0 The Hydrothermal Treatment of Oxalic Acid Sols 228

8.1.1 Defect Characterisation in Blue Anatase 229

8.1.2 Blue Rutile and Brookite phase TiO_2 229

8.1.3 Photocatalysis 230

Appendix 231

References 233

Acknowledgements

Supervisor Team

A special thank you must go out to my supervisors Dr Tim Kemmitt and Prof Vladimir Golovko. Who provided guidance, assistance, endless proofreading and patents throughout the 5-year saga. Thank you for not giving up on me!

Fellow Students

Jan-Yves Ruzicka, who help with the analysis of data and on countless occasions proofread papers provide scientific feedback.

Faridah Abu Bakar, who developed the robust RB-19 photocatalytic testing procedures, ran some of my samples and helped with various other photocatalysis experiments.

Fellow Colleagues

Ryan Martin, who helped train me in the art of PXRD, phase identification and assisted in the interpretation of the synchrotron PXRD data.

Dr Bridget Ingham who help collect and process the synchrotron data. The experiments could not have been done without her input. The data would still be unprocessed without her help.

Prof Gunther Anderson, who analysed my samples using XPS and UPS, helped to write the synchrotron proposal and helped process the synchrotron data.

Raaz Kler who stayed up all night with me for 5 nights in a row while collecting synchrotron data.

Prof Richard Tilly, who allowed me to use the TEM at Victoria University.

Prof Eric Le Ru who allowed me to use the Raman spectroscopy at Victoria University.

Dr Shen V Chong who collected and analysed the SQUID data.

Dr John Kennedy who helped me to use GNS's equipment.

Dr Ruth Knibbe for training and allowing me to use Robinson Institute's SEMS.

Funding and Enablers

The MacDiarmid Institute who funded my scholarship, provide research funding, hosted conferences and provided educational training courses which were extremely valuable. Also, who arranged my internship a Fisher and Paykel Healthcare which led to my current job.

Callaghan Innovation who hosted me for 3 years, provide equipment and facilities.

The Australian Synchrotron who allowed me to use their beamline on two occasions for a total of 7 days.

The University of Canterbury who provided research funding and facilities.

The University of Victoria who provided the use of their equipment.

The University of Auckland who provided the use of their equipment.

Chapter 1 : Introduction

1.0 Overview

In the following thesis, the synthesis and morphology control of titanium dioxide (TiO_2) was extensively researched. The main research was done in the following areas:

- TiO_2 oxalic acid (OX) passivated sols were synthesised at different ratios of oxalic acid to TiO_2. These sols were characterised by DLS and PXRD. It was found that the oxalic acid ratio influenced the relative ratios of phases in the sols, along with the average crystallite and agglomerate sizes.
- The TiO_2 oxalic acid sols were hydrothermally treated to produce larger anatase and rutile crystals which were characterised by PXRD and SEM. It was found that the oxalic acid ratio influenced the size and phase of the crystallites produced. At low oxalic to Ti ratios (0.25 OX:Ti), rod-like rutile crystallites were produced. At greater oxalic acid ratio (>0.5 OX:Ti), isometric anatase phase crystallites were formed. Of particular interest, there was some evidence that at greater oxalic acid ratios (>0.5 OX:Ti), a reverse phase transformation of rutile to anatase was taking place.
- The TiO_2 oxalic acid sols were modified with NH_4F and hydrothermally treated to produce larger crystallites. The crystallites were characterised by SEM, PXRD and UV-VIS DRS. It was found that the phase and morphology of the crystallites were highly dependent on the NH_4F to Ti ratio. At lower NH_4F to Ti ratios (<0.3 Ti:NH_4F), rutile phase TiO_2 was formed. Compared to the unmodified rutile crystallites produced by treating unmodified oxalic acid sols, the NH_4F modified rutile crystallites were much larger and expressed a bi-pyramidal shape with a much greater exposure of the {111} facet. At greater ratios of NH_4F to Ti (>0.25 Ti:NH_4F) a mixture of anatase and rutile was produced. The anatase phase crystallites remained small and isotropic in shape.
- To examine the impact of pH in the hydrothermal treatment of NH_4F modified oxalic acid sols, mineral acids were added to the synthesis. The crystallites were characterised by SEM and PXRD. It was found that the acids had little impact on the morphology at temperatures less than 270 °C. Nonetheless, at 270 °C, the sulphuric acid modified (H_2SO_4) synthesis produced large lozenge-shaped anatase crystallites with increased {001} facet exposure. The pH manipulating experiments showed the phase composition was related to the initial composition of the oxalic acid sol unless the pH was low enough to dissolve the rutile nuclei (already present in the sol).

- All the TiO_2 hydrothermal synthesised by the modifying oxalic acid sols with NH_4F produced was blue! It was found that this was related to the formation of Ti^{3+} defects produced by the thermal decomposition of the oxalic acid.
- In order to study the blue TiO_2, a sol-less synthesis that developed that produced phase pure blue TiO_2.
- To understand and precisely characterise the defect responsible for the blue colour. Blue phase pure anatase was synthesised and characterised by PXRD, Raman spectroscopy, UV-VIS DRS, EPR, SQUID, XPS, VBS, NEXAFS, PIGE, SEM, TEM and N_2 adsorption. The following was found through experimental work:
    - The blue colour was due to the absorption of red light possible extending far into the infrared region. Increasing the temperature of hydrothermal treatment deepened the blue colour. Organics (oxalic acid or isopropanol) were necessary to form the blue colour. However, the ratio of NH_4F to Ti was the most influential variable. The bluest TiO_2 was produced at 0.25 equivalent NH4F. As more NH_4F was added, the colour lightens until it was almost white again at 4 equivalents.
    - SQUID and EPR confirmed Ti^{3+} was present in the blue TiO_2 crystallites. Experiments showed it was most likely bulk phase Ti^{3+} due to its chemical stability and g value.
    - IR spectroscopy and mass spectroscopy showed the organics (isopropanol present in the hydrothermal mother liquor) decomposed under the hydrothermal conditions producing H_2 gas which reduced Ti^{4+} to Ti^{3+}. The Ti^{3+} was incorporated into the growing crystallites.
    - Synchrotron: XPS, VBS and NEXAFS, showed the Ti^{3+} was located on the surface as well as in the bulk of both white and blue TiO_2. There was a direct correlation between the NH_4F:Ti ratio and Ti^{3+}/Ti^{4+} ratio. However, there was no correlation between detected Ti^{3+} and colour as most of the Ti^{3+} detected was located on the surface of the particles. Quantification of bulk Ti^{3+} was elusive. On the other hand, surface plus bulk Ti^{3+} equated to approximately 6 -9 %.
    - Synchrotron PXRD showed the NH_4F manipulated the crystallite's size and shape. More importantly, it found that the as-synthesised TiO_2 was Ti deficient in most cases. Increasing the ratio of NH_4F to Ti increased the number of Ti vacancies. It is believed the increased number of Ti vacancies whitened the blue TiO_2 at greater NH_4F to Ti ratios. This was because it became more energy efficient to maintain charge neutrality by substituting four Ti^{3+} defects for one

    Ti vacancy. Also, the crystal defect (most likely Ti vacancies) was found to lie along the (*c*) axis of the crystals; causing expansion of the lattice.
    - TEM, SEM and N_2 absorption isotherms agreed with the PXRD findings, showing the crystallite size and shape to be influenced by the NH_4F concentration.
    - Experiments using NaF and NH_4OH showed the phase, shape and size of TiO_2 crystallite were controlled *via* the formation of either ammonium titanate or sodium titanate. Also, it became clear the F^- was responsible for stabilising the Ti^{3+} and creating the blue colour, but had little impact on the shape of crystallites.
- It was found that by manipulating the NaF to Ti ratio, phase pure brookite could be synthesised. The synthesised brookite could be made blue or white by changing the conditions as with the anatase. The following was also found:
    - Raman spectroscopy showed the brookite formed by the NaF dissolving and re-precipitating anatase as brookite.
    - The brookite crystallites were elongated along the [001] axis exposing a greater ratio of the {210} facet.
    - The aspect ratio of the brookite could be altered using the NaF to Ti ratio.
    - The blue brookite contained the same defects as the blue anatase.
- By adding oxalic acid to the sol-less synthesis blue rutile could be formed. The following was found:
    - The blue rutile crystals were very large and had increased exposure of the {111} facet.
    - The blue rutile contained the same defects as the blue anatase and blue brookite.
- The photocatalytic activity of the as-synthesised blue anatase, rutile and brookite was evaluated. It was found that:
    - The blue anatase showed increased visible light photocatalytic activity for RB-19 degradation compared to P-25.
    - Blue and white anatase modified with NH_4F was more active than P-25 for MB degradation.
    - Blue rutile phase TiO_2 was surprisingly active for a given surface area. Much more active than anatase phase TiO_2 on an m^2/g basis.
    - The blue brookite was photocatalytic activity. However, excessive NaF lowered the photocatalytic activity.

1.1 Aims of This Work

The aims of this work were to:

1. Develop methods of growing TiO_2 crystallites hydrothermally from TiO_2 oxalic acid passivated sols while controlling the phase, shape and size of the crystallites.
2. Synthesis phase pure morphologically controlled crystallites hydrothermally without the need of oxalic acid sols as the starting material.
3. Use synthetic methods and advance analytical methods to:
    a. Understand the formation of blue coloured TiO_2.
    b. Understand the conditions necessary to produce the blue TiO_2.
    c. Understand the nature of the crystallite defect that produces the blue colour.
4. Use knowledge gained to synthesise blue TiO_2 as other phases *i.e*. rutile and brookite phase.
5. Evaluate the photocatalytic activity performance of the blue coloured TiO_2 under broad-spectrum and visible-light.

1.3 Publications

- McNicoll C., Abu Bakar F., Golovko V. and Kemmitt T. (2017) *Hydrothermal synthesis of mixed phase blue titanium dioxide from oxalate stabilised sols.* In International Journal of Nanotechnology 14(1-6): 265-275. http://dx.doi.org/10.1504/IJNT.2017.082476.(Conference Contributions - Published)
- Ruzicka JY., Abu Bakar F., Hoeck C., Adnan R., Mcnicoll C., Kemmitt T., Cowie BC., Metha GF., Andersson GG. and Golovko VB. (2015) *Toward Control of Gold Cluster Aggregation on TiO2 via Surface Treatments.* Journal of Physical Chemistry C 119(43): 24465-24474. http://dx.doi.org/10.1021/acs.jpcc.5b07732. (Journal Article)
- Bakar FA., Ruzicka JY., Williamson BE., McNicoll C., Ingham B., Kemmitt T. and Golovko VB. (2014) *Enhanced photocatalytic activity in F-TiO2: effect of solvent and fluorine modifier towards the morphology of TiO2.* Auckland, New Zealand: 38th Annual Condensed Matter and Materials Meeting, 4-7 Feb 2014 (Conference Contributions - Other)
- Ruzicka JY., Bakar FA., Thomsen L., Cowie BC., McNicoll C., Kemmitt T., Brand HEA., Ingham B., Andersson GG. and Golovko VB. (2014) *XPS and NEXAFS study of fluorine modified TiO2 nano-ovoids reveals dependence of Ti3+ surface population on the modifying agent.* RSC Advances 4(40): 20649-20658. http://dx.doi.org/10.1039/c3ra47652a. (Journal Article)

- McNicoll CS., Kemmitt T. and Golovko VB. (2014) *Electronic Defect Characterisation in Blue Titanium Dioxide and Implications for Visible Light Photocatalysis.* Moscow, Russia: XII International Conference on Nanostructured Materials (NANO 2014), 14-14 Jul 2014(Conference Contributions - Other)
- McNicoll C., Kemmitt T. and Golovko V. (2013) *Hydrothermal rutile to anatase reverse phase transformation.* Auckland, New Zealand: AMN-6, 11-11 Feb 2013. In International Journal of Nanotechnology 11(5-8): 493-501. http://dx.doi.org/10.1504/ijnt.2014.060570.(Conference Contributions - Published)
- McNicoll C., Ruzicka JY., Kemmitt T. and Golovko VB. (2013) *Rietveld Refinement of Synchrotron PXRD of Fluorine Modified Titanium Dioxide Nanoparticles.* Wellington, New Zealand: New Zealand Institute of Chemistry (NZIC) Conference, 1-5 Dec 2013 (Conference Contributions - Other)
- Ruzicka JY., Bakar FA., McNicoll C., Cowie B., Thomsen L., Andersson G., Kemmitt T. and Golovko VB. (2013) *Modification of titanium dioxide by fluorine-containing surface modifying agents.* Auckland, New Zealand: Sixth International Conference on Advanced Materials and Nanotechnology (AMN-6), 11-15 Feb 2013 (Conference Contributions - Other)

Chapter 2 : Literature Review

2.0 Catalyst

Catalysts have been one of the greatest improvements in the chemical industrial revolution. Dating back to the Haber process where N_2 and H_2 were reacted over a Fe-based catalyst to form NH_3. Although, initially invented by Fritz Haber and Carl Bosch to produce NH_4NO_3 based explosives to support the Germans in World War 1. Post World War 1, this process significantly removed our dependence on nitrogen-fixing bacteria and prevented Europe from starving. In modern day life, we use products that are a direct result of the inventions of catalyst daily.

Catalysts come in two forms: homogeneous and heterogeneous. Homogeneous catalysts are in the same phase as the reactants *e.g.* acid in the catalysation of condensation reaction forming polyester bonds. Whereas heterogeneous catalysts are in a different phase to the reactants, *e.g.* particulate vanadium pentoxide beads are used in the oxidation of SO_2 to SO_3 to produce H_2SO_4.

Heterogeneous catalysts tend to be less active than homogeneous catalysts as the reaction only takes place on the boundary where the heterogeneous catalyst is in contact with the reactant phase. Yet, heterogeneous catalysts are preferred by industry because they are generally much easier to separate from the product stream. The solution to this boundary issue can be significantly reduced by increasing the surface area of the heterogeneous catalyst. Industry has achieved this by reducing the particle size of the catalyst to the nano ($1x10^{-9}$ m) range.

The move towards smaller, nano-sized, particles not only changed the available surface area for the catalysed reaction to take place but also began to change the fundamental properties of the catalysts. This was due to the “size effect” explained in more detail below. The move towards nanoparticulate catalysts opened a whole new field of research into both the properties of these nano-sized particles and how to manipulate their properties.[1]

2.0.1 The Size Effect

In attempts to maximise the surface area of heterogeneous catalysts, the particle sizes have been reduced to only 10 – 100s of atoms. Once less than 100 nm, the properties of materials begin to change *i.e.* melting points, bond lengths, magnetic and optical properties. This is referred to as the quantum size effect or simply just the size effect. This effect is in part due to the size of the electron's wavefunction relative to the particle’s size. As a particle’s size nears the size of its own electrons’ wavefunctions, quantum confinement begins to alter and restrict the places where those elections can exist. To compensate for the confinement the properties of the materials change.[2,3] This change in properties can be both good and bad. In the case of gold, a normally catalytically inert material, it becomes active for benzyl alcohol oxidation once the particle size is sub 10 nm.[4] On the other hand, sub 10 nm TiO_2 particles begin to lose their photocatalytic activity as the poor crystallinity hinders electron/hole migration.[4-6]

Precise control over the size of particles due to the development of new synthetic approaches has allowed scientist to study the changes in properties with respect to size. This has intern led to the development of new catalysts whose catalytic activity relies on the size effect. An example of this is the movement from platinum to gold nanoparticles in catalytic converters used in the automotive industry. As stated before, gold is normally catalytically inert, however, sub 10 nm particles show high activity towards CO oxidation; gold is more catalytically active for CO oxidation than platinum at lower temperatures. Thus CO emissions on a cold start can be significantly reduced.[4]

2.0.2 Photocatalysis

Photocatalysis is a process where light energy is used to catalyse a reaction. The light can either catalyse the reaction directly such as the bromination of toluene or work through an intermediate material referred to as a photocatalyst. Photocatalysts can both be homogenous or heterogeneous. An example of a heterogeneous photocatalytic reaction can be seen below in Equation 2.1. The general procedure that occurs is photoexcitation by the absorption of a photon with energy equal to or greater than the band gap (1.1). This results in the generation of a positive hole (h^+_{vb}) and excited electron (e^-_{cb}). The excited electron and hole can catalyse the reduction and oxidation of target molecules (1.2-1.4). Alternatively, photocatalysis can occur by an indirect mechanism. In the indirect mechanism, photoexcitation still occurs as aforementioned, however, the excited electron-hole pair generates *in-situ* radical species from the solvent (*e.g.* $O_2{\cdot}^-$) that react with the target molecule (1.5).[7]

$$TiO_2 + h\nu\ (UV) \rightarrow TiO_2\ (e^-_{cb} + h^+_{vb}) \quad (1)$$

$$TiO_2\ (h^+_{vb}) + H_2O \rightarrow TiO_2 + H^+ + OH\cdot \quad (2)$$

$$TiO_2\ (h^+_{vb}) + OH^- \rightarrow TiO_2 + OH\cdot \quad (3)$$

$$TiO_2\ (e_{cb}^-) + O_2 \rightarrow TiO_2 + O_2{\cdot}^- \quad (4)$$

$$O_2{\cdot}^- + H^+ \rightarrow HOO\ \cdot \quad (5)$$

Equation 2.1 an example of a photocatalytic reaction.

Photocatalysts are a type of material that can accelerate many reactions. The most common reactions are photolysis (photolysis is a chemical reaction in which a chemical compound is broken down by photons) or accelerate reduction reactions using photons as the reducing agent. The heterogeneous photocatalytic materials are often semiconducting metal oxides (*e.g.* TiO_2, Fe_2O_3, ZnO *etc.*) as well as many other materials such as GaP and CdSe *etc.*[6]

Semiconducting materials are generally used as heterogeneous photocatalysts as they can capture electromagnetic radiation (light) and use the captured energy to oxidise or reduce molecules at the surface. Semiconductor materials are materials that have a non-continuous band structure, see *Figure 2.1*.

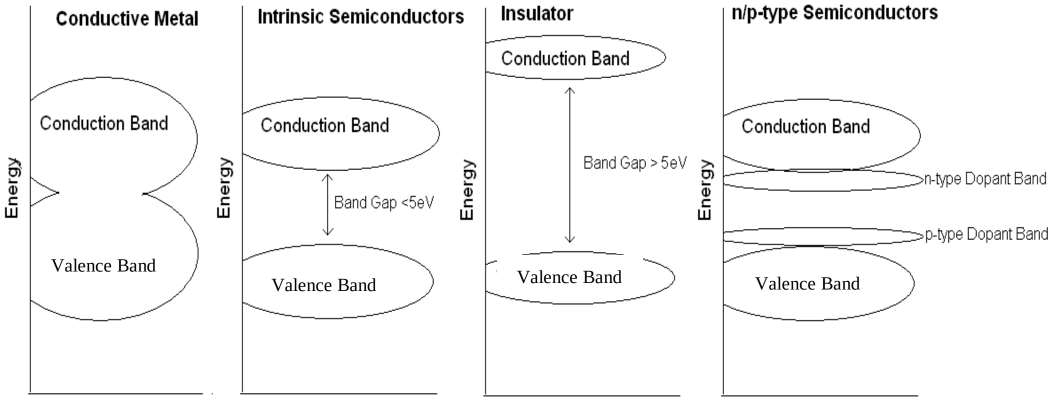

Figure 2.1. Graphical representation of the band structures of conductors, semiconductors and insulators.

The non-continuous band structure results in an energy gap between the top of the filled valence band and the bottom of the empty conduction band. This energy gap is referred to as the band gap. The size of the band gap separates semiconductors (less than 5 eV) from insulators (more than 5 eV), see *Figure 2.1*. There are three main types of semiconductors: intrinsic, n-type and p-type. Intrinsic semiconductors are made of pure materials such as Si or Ge where the charge carriers (e^-_{cb} + h^+_{vb}) are balanced. In p-type semiconductors, the positive charges (h^+_{vb}) are the dominant charge carriers. The excess of positive holes comes from dopants *e.g.* Si doped with Al. Alternatively, in n-type semiconductors, the negative charges (e^-_{cb}) are the dominant charge carriers, again the excess of negative charges comes from dopants *e.g.* Si doped with P. N-type semiconductors are a popular choice for photocatalysts. Metal oxides such as TiO_2, Fe_2O_3, ZnO *etc.*[6] as well as many other species, GaP and CdSe *etc.*[6] are well-known n-type semiconductors. Pure metal oxides would be intrinsic semiconductors, although in reality, surface defects *e.g.* Ti^{3+} on TiO_2 due to surface-bound O_2, causes them to behave as n-type semiconductors.[8]

During photoexcitation, the precursor to photocatalysis, an electron in the filled valence bands absorbs a photon of energy equal to or greater than the bandgap. As a result, the electron is promoted to the conduction band, see *Figure 2.2*.[6] This results in the formation of an excited electron and a positive hole pair (e^-_{cb} + h^+_{vb}). The fate of the excited electron and hole can take many paths. Inherently, the probability of each event following excitation plays a very important role in determining the effectiveness of the semiconductor as a photocatalyst. The first two paths involve the recombination of the hole and electron: either internally or after migration to the surface of the semiconductor as is illustrated in *Figure 2.2* (paths A and B). In a recombination event, the energy of the excited state is radiated as heat and no net reaction takes place. The third and fourth pathways define the activity of the semiconductor as a photocatalyst, *Figure 2.2* (paths C and D). If the excited electron migrates to the surface it can be transferred to an electron acceptor adsorbed onto the surface of the semiconductor. This results in the reduction of the electron acceptor, see *Figure 2.2* (path C). If the hole migrates to the surface it can accept an electron from a donor species pre-adsorbed on the surface of the semiconductor. This results in the oxidation of the electron donor, see *Figure 2.2* (path D). If the energy levels of the electron acceptor or donor species are reasonably matched with the semiconductor's conduction and valence bands, the charge transfer is faster.[6]

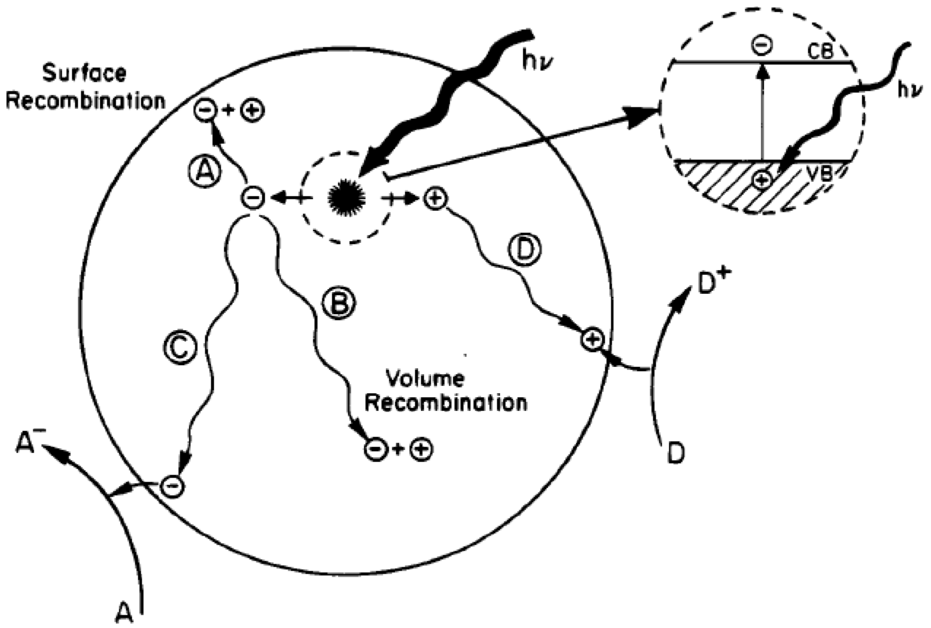

Figure 2.2 Scheme illustrating the formation of the electron-hole pair due to the photoexcitation process in a metal oxide semiconductor material and several de-excitation mechanisms (A-D). Taken from Linsebigler et al.[6]

There are many potential uses of these photocatalysts in the modern world. Some of these are (but not limited to) cleaning up the environment by breaking down organic industrial waste, capturing heavy metals, offsetting NO_x footprints, energy capture and self-cleaning materials.[7,9-12]

2.1 Titanium Dioxide

Titanium is the 9th most abundant element in the earth's crust. It is commonly found bound in minerals such as ilmenite, geikielite, perovskite or as natural rutile.[13] Titanium is a transition metal with fantastic mechanical properties. Yet, the main use of titanium is not as metal but as the oxide, titanium dioxide (TiO_2). Every year around 6,000,000 tonnes of the oxide is produced. Of which 90 % is used as a pigment due to its high refractive index. The remaining 10 % is used as fillers in medicines, photocatalysts, solar panels, welding rods and as UV-blockers. TiO_2 as a photocatalyst currently has limited industrial uses. However, it has the potential to be used in many of the aforementioned applications.[13]

2.1.1 Structure and Phases of Titanium Dioxide

TiO_2 can exist in three main phases: anatase, rutile and brookite. The crystal structures of anatase, rutile and brookite appear as chains of octahedral TiO_6 units linked together, see *Figure 2.3*. The different phases come about due to different distortions of the octahedral units. This results in different symmetry elements. In the anatase phase, the TiO_6 octahedral shows significant distortion resulting in the low overall symmetry of the structure (I41/amd). On the other hand, the rutile phase shows only a slight distortion of the TiO_6 octahedral. This leads to an orthorhombic structure with high levels of symmetry (P42/mnm), see *Figure 2.3*.[14-16] Such structural variations cause differences in the spacing between atoms: anatase shows shorter Ti-Ti distances but longer Ti-O distances compared with rutile (Ti-Ti distance 3.79/3.04 Å anatase and 3.57/2.69Å rutile; Ti-O 1.934/1.980 Å anatase and 1.949/1.980 Å rutile).[14-16] These structural differences led to different thermodynamic and electronic properties. As a consequence, anatase is formed as the kinetically stabilised phase while rutile is the thermodynamically stable phase.[17] In most cases, anatase is formed first but converts to the thermodynamically more stable rutile phase upon heating.[18,19] Brookite phase is an intermediate between anatase and rutile.[6] It has an orthorhombic layered structure that lies between anatase and rutile and shows little symmetry (Pbca).[20] There has been far less research into brookite as it is difficult to synthesize as a phase-pure material.[21]

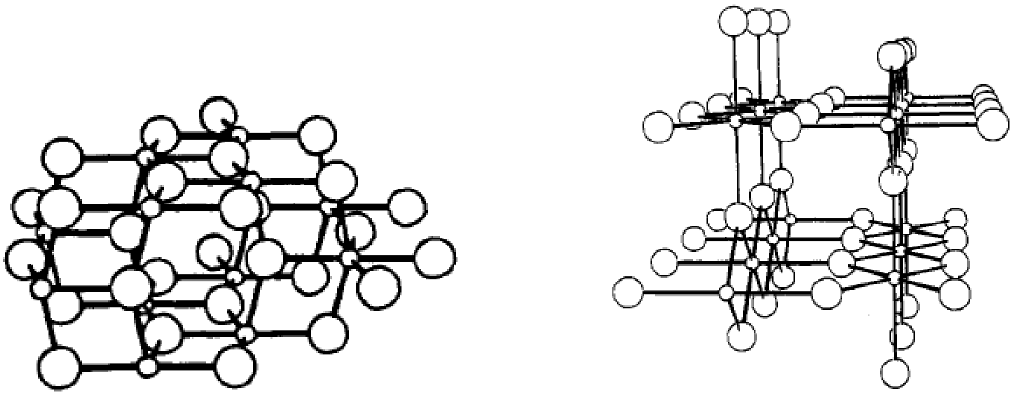

Figure 2.3 Structural diagrams of anatase phase TiO_2 (left) and rutile phase TiO_2 (right). The small balls are Ti^{4+} and large balls are O^{2-}. Taken from Burdett et al.[14,15]

2.1.2 Synthesis of Titanium Dioxide Nanoparticles

There are many reported methods for synthesising nano-TiO_2 some of which are: sol, sol-gel, micelle methods, hydrothermal, solvothermal, direct oxidation, chemical vapour deposition, physical vapour deposition, electrodeposition, sonochemical, arc discharge, calcination and microwave methods.[22] Throughout the literature, the most prevalent methods used are sol-gel, hydrothermal and calcination. Industrially, the bulk of TiO_2 is synthesised by either direct oxidation of $TiCl_4$ or through the hydrolysis of $TiOSO_4$ and calcination of the resulting metatitanic acid to TiO_2.[13] Lastly, vapour deposition is most commonly used in the coatings industry *e.g.* self-cleaning windows.[23]

The general principles of the wet chemistry synthesis of TiO_2 nanostructured materials involve the hydrolysis of a Ti-containing precursor ($TiCl_4$, $Ti(OAlk)_4$ *etc.*) in the presence of capping agents.[22] This produces a very amorphous TiO_2 but the morphology is controllable. Often the amorphous TiO_2 is further treated by hydrothermal methods or calcined to induce crystallinity. The original morphology of the amorphous TiO_2 influences the crystal growth during calcination or hydrothermal treatment.[22]

In the case of the sol method, a Ti precursor such as $Ti(O(CH_2)_xCH_3)_4$ is hydrolyzed into $TiOH_xOR_y$ by water. This can be done in either pure water or a mixture of water and solvents. Then in a second step, the condensation of $TiOH_xOR_y$ occurs forming TiO_2 chains. The condensation reaction is generally acid or base catalysed, or as a result of heating the solution.[22,24] The acid/base and heat (typically less than 80 °C) continues to catalyse the condensation reaction, gradually increasing the crystallinity of the TiO_2 particles. The resulting colloidal suspension of TiO_2 nanoparticles is called a sol. The acid, base, solvent and Ti precursor chose can be used to control the phase of TiO_2 produced, the size of the colloids, the degree of crystallinity and the stability of the colloids.[25,26]

The hydrothermal treatment of amorphous TiO_2, TiO_2 sols or even TiO_2 particles results in particle growth and crystallisation. The hydrothermal treatment of a sol or TiO_2 precursor involves heating the precursor in water to elevated temperatures in an enclosed vessel, generating elevated pressures. The high temperatures and pressures dissolve and redeposit the TiO_2 building blocks resulting in the growth of well-defined TiO_2 particles.

Calcination of a sol or other TiO_2 precursors also results in particle growth and crystallisation. However, the growth mechanisms, when compared to the hydrothermal mechanisms, are quite different. During calcination, TiO_2 particles are heated to high temperature (600 °C +). At these temperatures, small particles on the surface of larger particles melt and sinter together. If the temperature is high enough or a flux is present, the particles will coalesce into one another forming a bigger and more crystalline particle.

In the sol, hydrothermal and calciner methods aforementioned above, the addition of modifying agents influences the morphology of the product produced.[22]

2.1.3 Morphology Control of Titanium Dioxide

Morphology control can be defined as design and precise fabrication of materials with well-defined size, shape, composition and other specific details of its structure (crystallinity, facets exposure, the presence of pores *etc.*). The ability to control shape, size, composition and structure/phase of photocatalysts is very important as it affects the surface area, band gap, recombination rates and other properties of these materials.[6] Controlling one particular property from the aforementioned list above has been achieved for many photocatalysts. For example, phase-pure anatase TiO_2 has been synthesized in many different ways.[22] However, controlling all the key elements of morphology at once is more difficult. One of the first examples of morphology control was done by Yang *et al.*[27] where anatase phase nanoparticles were produced with increased {001} facet exposure.[27] This was achieved through the use of HF to modify the surface of the growing TiO_2 nanoparticles. Research into anatase shape-control using F^- ions continues even today. The reason this method works is the F^- ions bind to the higher energy {001} facet blocking growth along the [001] direction.[28] As *Figure 2.4* illustrates, the TiO_2 crystallites have changed from a pyramid shape (B) to a lozenge shape (A) due to F^- ions binding to the {001} facet thus preventing growth along the [001] direction. The higher coverage of {001} facets has been shown to increase photocatalytic activity.[28]

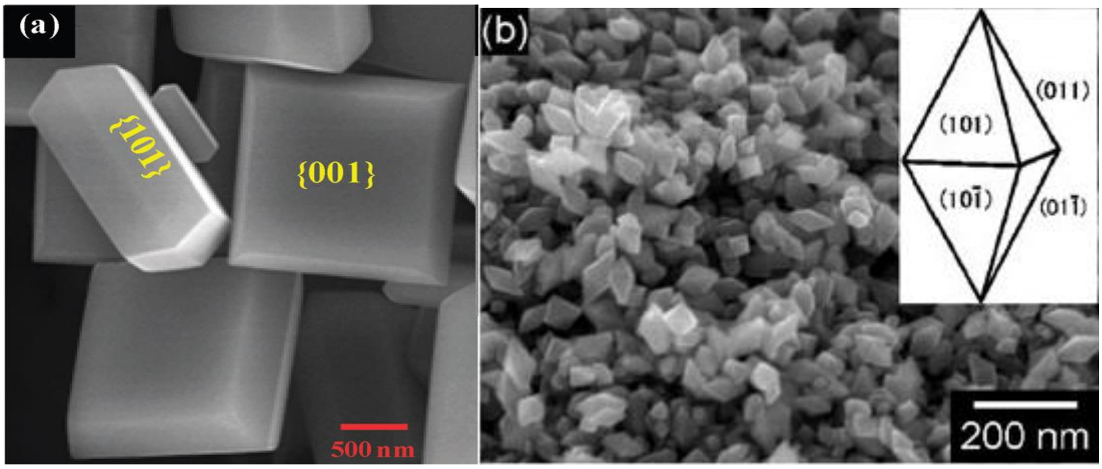

Figure 2.4 Left: SEM image of F^- *modified anatase taken from Wang et al.*[29] *Right: SEM image of an unmodified anatase. Taken from Amano et al.*[30]

The morphology and shape control is not just limited to anatase. The morphology control of rutile phase TiO_2 has also been achieved. Snonawane *et al.*[31] showed the morphology of rutile can also be controlled with the use of trifluoroacetic acid. *Figure 2.5* shows the rice-like grains of rutile synthesised by Snonawane *et al.*[31]

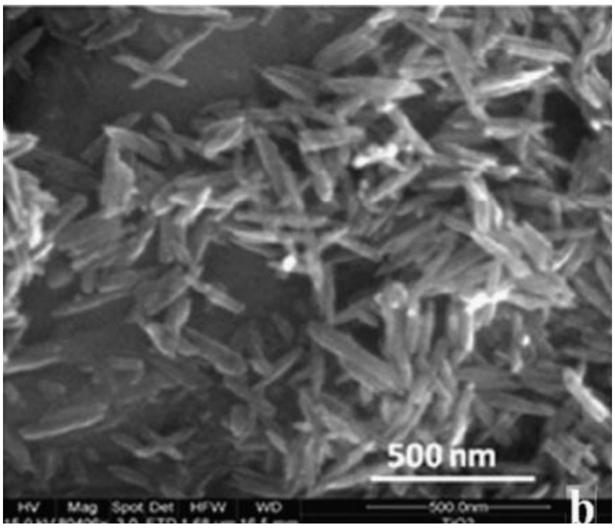

Figure 2.5 SEM of rod-like rutile synthesised by Snonawane et al.[31]

Hierarchical structures can also be formed. TiO_2 will often self-assemble into larger structure under the right conditions. An example can be seen in *Figure 2.6* where Yu *et al.*[32] synthesized TiO_2 in the presence of NH_4F. Yu *et al.*[32] found that the particles had self-assembled into either packed or hollow spheres depending on the amount of NH_4F added to the hydrothermal synthesis.[32]

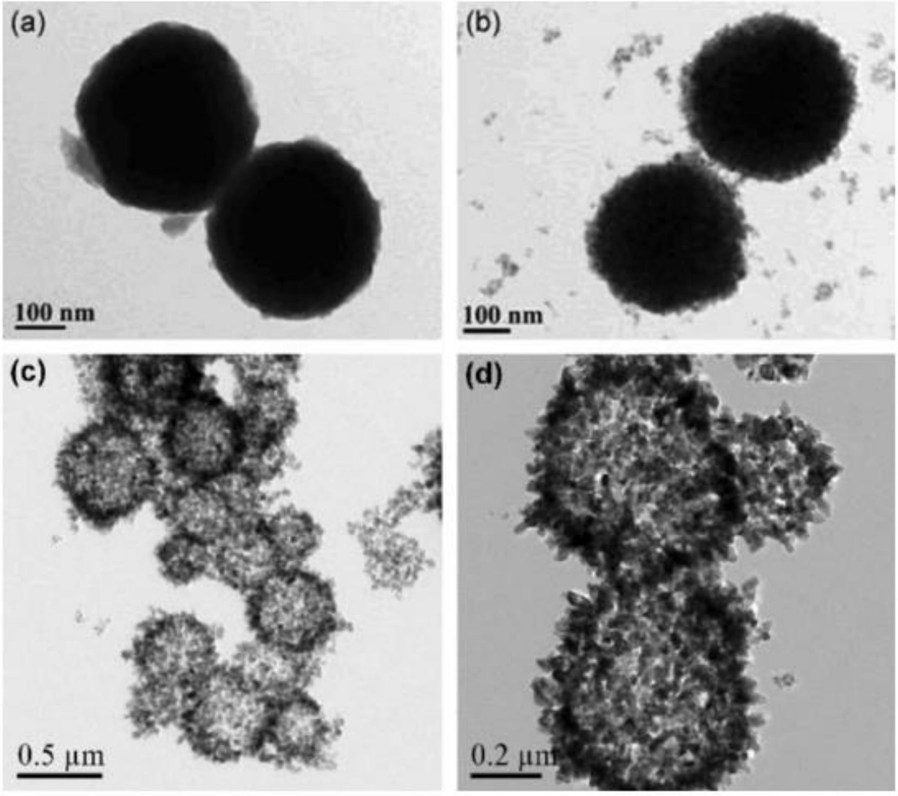

Figure 2.6 TEM images of hollow anatase spheres synthesised by Yu et al.[32]

The science of controlling the morphology of TiO_2 is a massive field which is still growing. Countless articles have been published demonstrating TiO_2 can be grown into anything from cubes to flat sheets to flowers.[33-35] However, controlling all aspects of morphology is still difficult with room for improvement.

2.2 Improving the Photocatalytic Performance of Titanium Dioxide

Improving the photocatalytic performance of TiO_2 has been the prime objective of countless research teams. TiO_2 has many positive properties as a photocatalyst: photostability, chemically stable, relatively long-lived excited states and a high absorption coefficient.[6] The main drawback of TiO_2 is its rather large band gap (*ca* 3.2, anatase, 3.0 eV rutile).[6] Improving the photocatalytic performance of a photocatalyst can be split into two groups. First are physical changes *i.e.* shape, size, phase. Second are electronic changes *i.e.* doping, coupling *etc*.

2.2.1 Physical Changes to Improve Photocatalytic Performance of Titanium Dioxide

The phase of TiO_2 dramatically impacts photocatalytic activity. As aforementioned TiO_2 has 3 common phases anatase, rutile and brookite. Each phase has its own photocatalytic properties. Generally, anatase is believed to be the most photocatalytic activity.[6,36-38] Work on single crystals of anatase and rutile have shown that anatase has an electron/hole diffusion length double that of rutile (5 *vs* 2.5 nm respectively).[39] This results in more electron/hole migrating to the surface of the particle and hence a higher quantum yield. The exact reason for this is still a much-debated topic. One potential reason for higher charge mobility is that anatase is an indirect semiconductor whereas rutile is a direct semiconductor. The indirect nature of anatase results in a lower probability of the excited electron and hole recombining.[39] However, this is still unconfirmed. It should be noted very little is known about the photocatalytic activity of brookite as it is so difficult to synthesise phase pure.[21]

Crystallite size is one of the most important variables defining the photocatalytic performance of $TiO_{2.}$ The size of the crystallites effects three features of the TiO_2. First, if the crystallites are large, there is little surface area for reactants to adsorb to, therefore limiting the probability of electrons transfer between the excited photocatalyst and reactants. Secondly, if the crystallites are very small *i.e.* sub 10 nm then the quantum size effect increases the band gap reducing the excitation for a given wavelength. Lastly, small crystallites with poorly crystalline bulks, suffer reduce charge carrier mobility. As a consequence, the number of charge carriers that make it to the surface to perform reactions is reduced. Overall when all these factors are considered there is an optimal size range for TiO_2 photocatalysts. In general, this has been reported to be between 20 and 40 nm.[6]

The shape of crystallites alters the photocatalytic properties of the TiO_2. Manipulation of the crystallite shape changes the ratios of exposed facets and indeed, in some cases, the exposed facets themselves. The exposed facets play an important role in photocatalytic activity as the majority of photo-induced reactions occur at the surface.[28] The specific type of exposed facets can alter the photocatalytic activity due to different affinities for target species *i.e.* by influencing the effectiveness of pre-adsorption. Also, different facets have different local electronic properties that affect electron and hole migration/recombination.[38] For example, Ohno *et al.*[38] demonstrated that reduction and oxidation can preferentially take place on specific facets. As *Figure 2.7* below illustrates, selective oxidisation of Pb^{2+} to PbO_2 occurred preferentially on the {011} facets while selective reduction of Pt^{2+} to Pt^0 occurred on the {110} facets of rutile.[38]

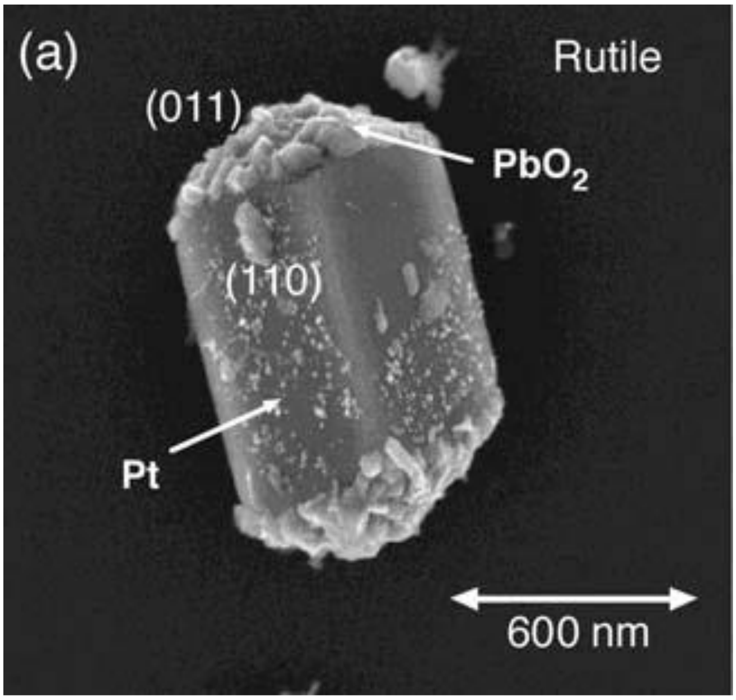

Figure 2.7 SEM image of rutile crystallite showing facet-selective deposition of PbO_2 and Pt after irradiation in baths containing Pt and Pb salts. Taken from Ohno et al.[38]

The reason for the differences in pre-adsorption, electron-hole migration, *etc*. associated with different facets is due to the specific chemical structure of the exposed surface. Facets (*e.g. {101}, {001} etc.)* expose different uncoordinated bonds (dangling bonds) at different angles, this can be seen on the various anatase facets, see *Figure 2.8*. These dangling bonds *e.g.* the uncoordinated bond of Ti_{c5} (Ti_{c5} are Ti atoms with only 5 bonds as opposed to the usual 6) atoms exposed on the {001} facet, act as binding sites for reactants and hence can increase the reactivity of the surface.[28] The dangling bonds also affect the electronic properties such as electron migration. Unsaturated surface atoms such as Ti_{c5} on the TiO_2 crystallites surface can act as energy wells trapping and prolonging the life of photoexcited electrons. The Ti_{c5} sites can also be O_2 terminated resulting in a fast electron transfer to the O_2 forming an $O_2^{\cdot -}$ radicle, as described above in Equation 2.1.[6,40] It can be seen in *Figure 2.8*, the different facets expose different quantities of dangling bonds *e.g.* the {001} facet with 100 % Ti_{c5} coverage *vs* the {101} facet with only 50 % Ti_{c5} coverage.[40] The above is just one of many reasons for variations in photocatalytic activity associated with different facets; there are more to be uncovered.

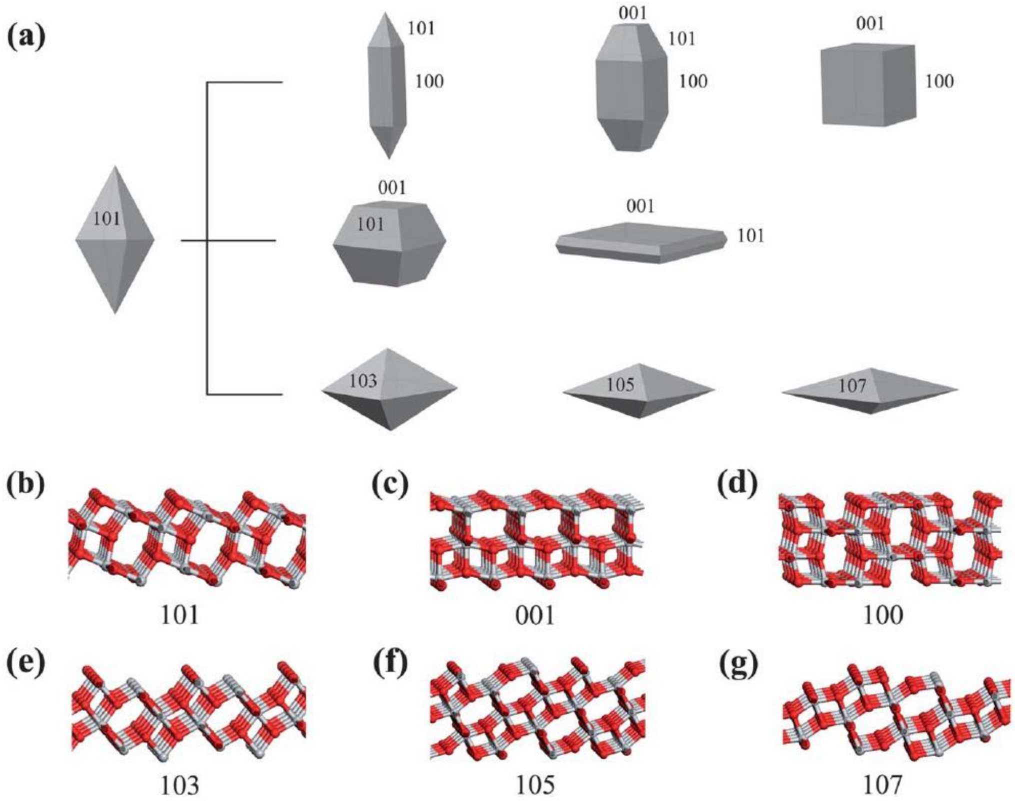

Figure 2.8 Diagram illustrating the facets and surface structure of anatase phase TiO_2. Diagram taken from Wen et al.[28]

Another impact of shape can be in the absorption of light and electron-hole migration. Due to the absorption length of light through TiO_2 a minimum size is needed to ensure the light is absorbed. However, making the particles larger to be more efficient at absorbing light reduces the surface area. Electron-hole migration has been found to be more efficient in specific crystalline directions.[39] Therefore, a crystal can be elongated in a specific direction increasing light absorption but not greatly impairing electron-hole migration to the surface.

2.2.1 Electronic Changes to Improve Photocatalytic Performance of Titanium Dioxide

Tuning the electronic structure of TiO_2 can have a profound effect on its performance as a photocatalyst. Two main categories of electronic tuning exist. The first involves extending the lifetime of the excited state. The other involves tweaking the band gap of TiO_2 to utilise visible light.

Extending the lifetime of the excited state can enhance photocatalysis. There are 2 competing reactions: one is the electron and hole recombining and radiating heat, the other being photocatalysis, see *Figure 2.2*. By reducing the rate of recombination the photocatalytic performance can be enhanced. The excited state is normally in the order of nanoseconds. Several methods of reducing the recombination rate exists, these are: coupling semiconductors, depositing metal nanoparticles on the surface and inducing trap sites.[6,41]

Coupling semiconductors can result in electron-hole separation due to the movement of electrons and holes between the semiconductors. When two or more semiconductors are coupled with different band gaps, electron transfer between the semiconductors from the higher energy band to a lower energy band can occur. Once this occurs the electron and hole cannot recombine as they are separated by an energy barrier. The separated holes and excited electrons can only react with adsorbed reactants, therefore recombination is not possible. Although coupling has advantages it also has many disadvantages. One of the main disadvantages is that holes or electrons can build up in one semiconductor, resulting in photo-corrosion.[6,41]

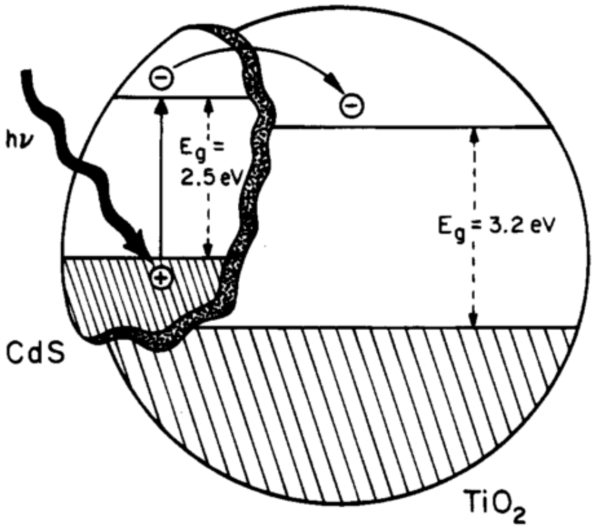

Figure 2.9 Example of coupled semiconductors. Taken from Linsebigler et al.[6]

Depositing metal nanoparticles on the surface of TiO_2 is an effective way of altering its photocatalytic performance. Metals such as gold, palladium, platinum and ruthenium are commonly deposited as nanoparticles on the surface of the TiO_2.[6,42] This can be beneficial in 2 ways: first, the metal nanoparticles can adsorb target species which would not normally adsorb to the surface of TiO_2. The metal nanoparticles may catalyse specific reactions that TiO_2 would not normal catalyse.[6] An example of this can be seen in *Figure 2.10*. Secondly and probably more importantly, the metal nanoparticle can allow charge transfer between itself and the semiconductor. This, like coupling semiconductors, results in separation of the excited electrons and positive holes. However, it occurs in a different fashion when compared to coupled semiconductors. Electrons flow into the conduction bands of the metal where the electrons lower the Fermi level of the metal towards that of the semiconductor's conduction band. This results in the band bending at the junction between the metal and the semiconductor's conduction band.

As the band bends upwards electrons cannot flow back into the semiconductor, this effect is known as a Schottky barrier. Much like coupling, this increases the electron yield by reducing recombination and hence enhances photocatalytic performance.[6,42]

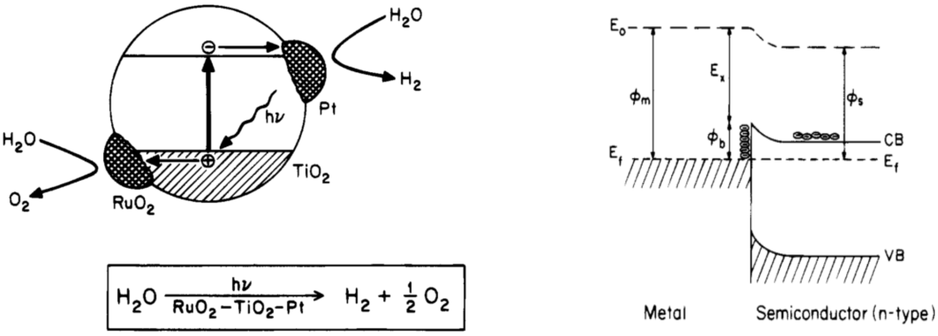

Figure 2.10 Left: Schematic of metal nanoparticles on the surface of a semiconductor. Right: A diagram showing electron transfer between the semiconductor, conductive metal and Schottky barrier. Taken from Linsebigler et al.[6]

Electrons and hole trap sites can be formed on the surface or in the bulk of the TiO_2. Often these traps are a consequence of the synthesis conditions. Synthesis conditions where crystallinity is slightly impaired can often result in stacking faults and point defects. Surface modification can also result in rearrangements generating traps. The crystalline imperfections can act as energy wells resulting in the trapping of electrons. Traps act in a very similar way to the aforementioned coupling of semiconductors and metal nanoparticle deposits. They reduce the rate of recombination. Of course, trapping the states for too long can equally result in poor photocatalytic activity.[43]

One of the most common modifications to TiO_2 and other photocatalysts is dye sensitization. Dye sensitization is the process of adsorbing dyes on to the surface of the particles by weak Van der Waals forces.[41] In the event of photoexcitation of the adsorbed dye molecule, an excited electron is ejected from the dye's highest occupied molecule orbital (HOMO) into the conduction band of the semiconductor. The excited electron in the conduction band of the semiconductor can react with adsorbed species on the surface of the host semiconductor, see *Figure 2.11*. Since the dye is the light absorber, the choice of dye changes the wavelengths of light absorbed. Some examples of the dyes used are methylene blue or 8-hydroxyquinone, although there are many more.[41] The major drawback of this process is that the positive holes can oxidise the dye molecules, thereby breaking the conjugation that gives the dye its light absorbing properties. In some cases, an electron created by photoexcitation of the host semiconductor will reduce the dye back to its original state, although this is rare. Generally, the oxidation of the dye destroys the chromophore and makes the dye inactive for light absorption.[41]

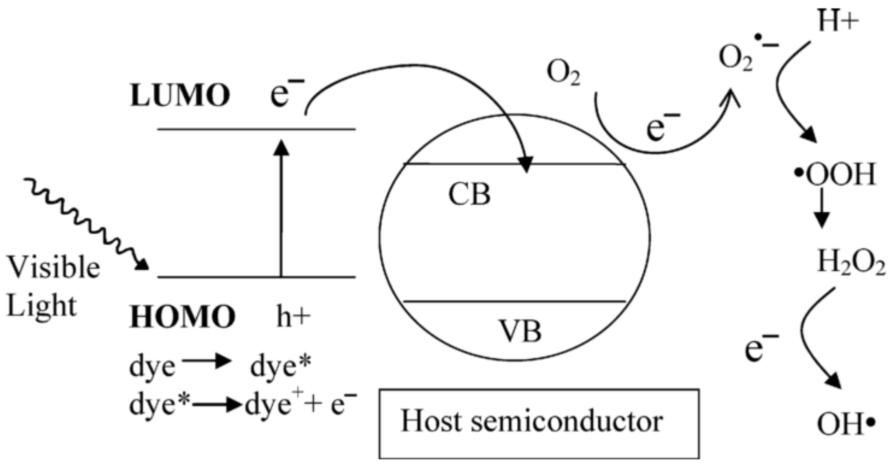

Figure 2.11 Schematic showing dye sensitised semiconductor. Taken from Rehman et al.[41]

TiO_2 in all phases has a bandgap greater than 3.0 eV.[6] This leads to an inherent inefficiency when considering the use of solar radiation to excite the photocatalyst. The solar spectrum seen below in *Figure 2.12,* shows the natural solar spectrum and in blue the 10 % of the solar radiation utilised by anatase TiO_2.[22] Morphology control has been building momentum in the art of tuning the electronic structure so that wide bandgap semiconductors can capture and utilise visible light. Utilisation of visible light for photocatalysis is referred to as visible light photocatalysis.[41] The tuning of TiO_2 to utilise visible light is currently a major field of photocatalysis research.

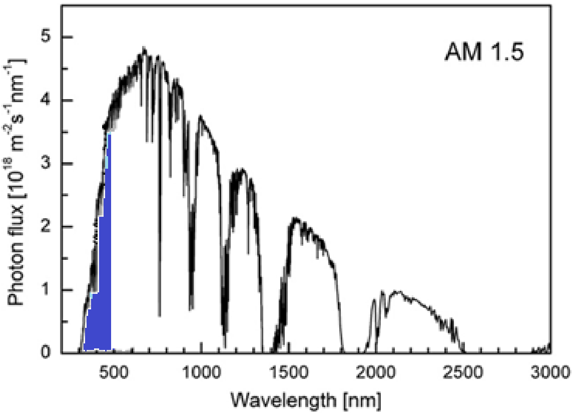

Figure 2.12 Solar spectrum AM 1.5. Note: Blue indicates the absorption band of anatase TiO_2.

The addition of dopants has been explored to narrow the band gap, thereby increasing the minimum wavelength required for photoexcitation. The addition of dopants introduces another valence band between the valence band and conduction band of the TiO_2. An example of this can be seen in the case of nitrogen doping, see *Figure 2.13*. Nitrogen, boron and other non-metals have been used as dopants along with metals such as Fe, Cr, V *etc*.[41] The problem with doping is the defect sites generated by the addition of the dopant can act as recombination centres, decreasing the number of photo-generated holes and electrons that migrate to the surface to perform photocatalysis. This increased rate of recombination lowers the ultraviolet light photocatalytic activity, thus producing a photocatalyst that although visible light photoactive, is actually less active than non-doped TiO_2 under solar irradiation.[44,45]

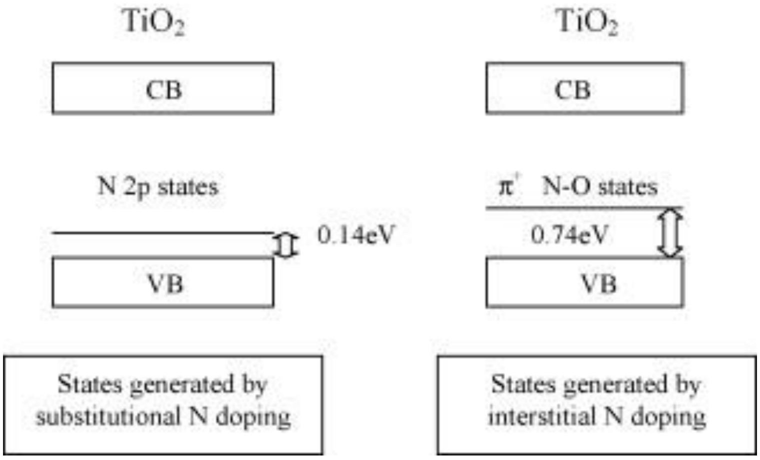

Figure 2.13 Diagram of the effects of dopant's valence bands within the electronic structure of TiO_2*. Taken from Rehman et al.*[41]

The final method of increasing visible light photocatalytic activity is the addition of metal nanoparticles to the surface of the TiO_2 particles. The surface plasmon of the metallic nanoparticle can inject excited electrons into the conduction band of TiO_2. Using metal nanoparticles to inject electrons into the conduction band of TiO_2 works much the same as dye sensitisation and coupled semiconductors. However, unlike dyes, the metal nanoparticles are more resilient to photocorrosion and photodegradation. Although metal nanoparticles offer many advantages, the main disadvantage is the cost and difficulty of selectively depositing the metal nanoparticles onto the nano TiO_2 particles.[41]

So far all of these methods reviewed have drawbacks. Doping introduces defect sites often encouraging recombination. Coupled semiconductors suffer from photocorrosion if exposed to both UV and visible light at the same time. Depositing metal nanoparticles on the surface of TiO_2 is expensive and hard to control. Dye sensitisation is only useful in solar cells as the dye itself gets oxidised if the positive holes are not removed.[41] Morphology control has shown promise in increasing the photocatalytic activity of TiO_2 but it is not currently without its drawbacks.

2.3 Blue Anatase Titanium Dioxide

Blue TiO_2 is a general term given to TiO_2 that is blue in its appearance. The blue colour or in some cases a black colour is due to defect sites changing the electronic structure of the TiO_2 allowing it to absorb red light or in the case of black TiO_2 all visible light. Often blue TiO_2 is referred to as self-doped or self-activated TiO_2 as there are no foreign species doping the TiO_2, just Ti^{3+} sites caused by oxygen deficiencies or interstitial Ti. In the introduction to Chapter 5, the characterisation and theoretical nature of the Ti^{3+} is explained in much more detail.

Throughout the literature, there is much interest in blue TiO_2 as a visible light photocatalyst.[46] Although, the reported visible light activity often varies from researcher to researcher. The differences in reported photocatalytic activity are due to different synthesis methods used to produce blue coloured TiO_2. The different synthetic methods produce a similar looking material but the crystals contain different defects. There is much debate in the literature as to the exact nature of the defect sites, both in blue TiO_2 made the same way as well as different ways. The following briefly explains three different TiO_2 synthesises producing three different self-proclaimed Ti^{3+} activated photocatalysts.

First of all, white TiO_2 that is Ti^{3+} doped and is visible light active yet shows no visible light absorption or a shifted band edge. Fluoride is often used in the synthesis of these TiO_2 products. The source of the visible light activity is yet to be fully understood but some groups believe it is the absorption of infrared (IR) light, whereas others claim the visible light activity comes from surface activation occurring.[47] Czoska *et al.*[47] did an in-depth study of the experimental and theoretical electron paramagnetic behaviour of visible light active, fluoride doped, white TiO_2 using electron paramagnetic resonance (EPR) and density functional theory (DFT) calculations. They found through DFT calculations that there were many ways F^- and Ti^{3+} could interact at the defect sites. The experimental EPR led them to believe, due to a lack of hyperfine splitting, that the F^- was shared between two adjacent Ti^{3+} atoms. This leaves the Ti^{3+} centres in an octahedral arrangement. Although Ti^{3+} is present, the TiO_2 remains white due to the low concentrations of the defects. Even though a possible structure is given for the defect site, it is still a mystery as to how the white TiO_2 samples are visible light photoactive.

Next, we have blue TiO_2 that is truly self-doped as a result of oxygen vacancies. Many groups have shown blue and even black TiO_2 can be synthesised by reducing Ti^{4+} centres to Ti^{3+} during crystal growth. This can be achieved using many techniques such as combustion methods, reducing atmospheres and reducing agents in solution with the TiO_2 as it is crystallising.[48-53] Blue TiO_2 synthesised by groups such as Liu *et al.*[51], Xing *et al.*[53] *and Zuo et al.*[54] all show redshifts in the absorption edge and increased absorption throughout the visible range, see *Figure 2.14*. It should be noted that in some cases, rutile and anatase mixtures are formed due to the high temperatures of synthesis such as combustion. Therefore, when looking at shifts in the absorption edge the TiO_2 must be phase pure or the mixture of phases can shift the absorption edge as below in *Figure 2.14*. Blue TiO_2 synthesised by the aforementioned groups all show EPR active Ti^{3+} defect sites and are highly active for visible light photocatalysis. The authors claim their blue TiO_2 to be air stable and photocorrosion resistant, retaining their colour and activity after exposure to air and light. Between the groups, they commonly accept the blue or black colour have originated from bulk phase oxygen vacancies or interstitial Ti^{3+} atoms that have migrated inside the lattice. The most compelling evidence for their claims of bulk phase Ti^{3+} is the stability of the colour as bulk phase defects are not readily oxidised to Ti^{4+}.[48-53]

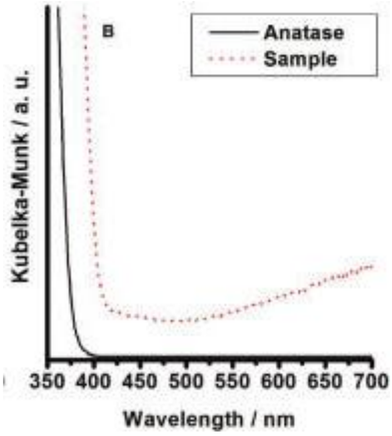

Figure 2.14 UV-Vis spectrum of blue TiO_2 (self-doped) synthesised by Zuo et al.[48]

Finally, the fluoride doped blue TiO_2 producers show the least coherence among the various researchers. These blue TiO_2 samples are synthesised in the presence of fluoride and other conditions that results in the reduction of Ti^{4+} to Ti^{3+}. Although all these TiO_2 samples synthesised using these conditions are blue in appearance, their ultraviolet-visible diffuse reflectance (UV-Vis) spectra differ from the simply reduced blue TiO_2 (oxygen deficient TiO_2) above. Also in some cases, the blue colour appears to only be a surface feature that can be removed by low-temperature calcination. The blue TiO_2 synthesised in this thesis appears to fall into this category.

2.4 Blue Rutile and Brookite Phase Titanium Dioxide

As aforementioned, there are 3 main phases of TiO_2 anatase, rutile and brookite. Above, blue anatase was discussed in some detail. However, as blue TiO_2 is formed by a Ti^{3+} defect it is possible to produce blue rutile and brookite theoretically. Because rutile is generally believed to be the least photoactive phase of TiO_2 there has been less research into producing a self-doped rutile phase material.[6] Likewise, brookite is very difficult to synthesise phase pure and there have been older reports that indicated it was photocatalytically inactive.[21] Yet in this thesis, both of these phases were synthesised phase pure and turned blue using the synthetic methods developed. The following will summarise any literature on the synthesis of self-doped/blue brookite and rutile. However, a more detailed introduction to blue rutile and brookite can be viewed in Chapter 6.

2.4.1 Blue Rutile

Blue rutile phase TiO_2 has been produced by combustion methods. The synthesised blue rutile may not have been the target phase of the synthesis, however, due to the thermodynamic stability of rutile and the harsh conditions of combustion methods used to synthesise blue anatase, rutile is often a by-product.[6] *Zuo et al.*[48] synthesised a mixture of blue anatase and rutile. Judging by the UV-Vis spectrum rutile was the dominant phase. EPR confirmed the presence of Ti^{3+}, believed to be due to oxygen vacancies. The rutile anatase mixture was active for hydrogen evolution under visible light only (>400 nm) light whereas the anatase standard was completely inactive. Hamdy *et al.*[55] also produced an 85:15 (rutile:anatase) mixture of blue rutile and anatase by combustion. Hamdy *et al.*[55] found that the band edge had been shifted to even longer wavelengths than commercial rutile indicating a reduced bandgap. It was also reported that the blue rutile anatase mixture was more photoactive for ketone degradation than P-25.

Grabstanowicz *et al.*[56] deliberately synthesised phase pure blue rutile by treating TiH_2 with H_2O_2 and calcining the yellow gel under argon or vacuum. The H_2O_2 was not in a stoichiometric excess; this left some TiH_2 present in the gel which reduced the surrounding Ti^{4+} to Ti^{3+} during the calcination. This produced blue rutile with Ti^{3+} defects as confirmed by EPR. The blue rutile was found to be photocatalytically active for the degradation of methylene blue.[56]

2.4.2 Blue Brookite

The synthesis of phase pure brookite is rare; the synthesis of phase pure blue brookite is even rarer.[21,57] One report of blue brookite has been found. Xin *et al.*[57] produced blue brookite by a peroxo-titanic acid and sodium borohydride gel synthesis followed by low-temperature calcination. It was found that the brookite was initially blue, becoming black upon low-temperature calcination and then back to blue when calcined at higher temperatures. The blue coloured brookite came from bulk phase Ti^{3+} characterised by EPR. Interestingly, the brookite was active for photocatalytic reduction of carbon dioxide to methane.[57]

Fluoride modified brookite TiO_2 has also been synthesised, however, it was not reported as being blue. Wang *et al.*[58] synthesised brookite using a known titanate method. The brookite was then mixed with NH_4F and calcined. The result was a brookite with surface Ti^{3+} defects and both nitrogen and fluorine doping (mostly at the surface). In contrast to the above, the brookite was found to be more photocatalytically active for hydrogen production before the treatment with NH_4F. Conversely, the same process was carried out on rutile and anatase phase TiO_2. It was found that the unmodified and modified brookite had superior photocatalytic activity for hydrogen production than either of the other phases.

2.5 Conclusion

Catalysts have had a huge impact on the world by improving industrial processes and photocatalysts may be the next great opportunity. Pressure to increase the efficiency of catalysts have pushed sizes down to the nano range to take advantage of the size effect. Photocatalyst catalyses reactions by capturing light and using the captured energy to perform reactions.

TiO_2 is a promising photocatalyst. It exists in 3 phases: anatase, rutile and brookite. Each phase is related to each other by different distortions of the TiO_6 octahedral. Generally, anatase is believed to be the most photoactive phase with rutile been relatively inactive and brookite rarely examined.

Many methods of morphology control have been used to try and improve the photocatalytic performance of $TiO_{2,}$ particularly around visible light photocatalysis. The methods used are either physical (shape, size *etc.*) or electronic (phase, doping, coupling *etc.*). However, most of these methods have some drawback such as photocorrosion or expensive synthesis.

Blue anatase phase TiO_2 offers a potential solution to many of the problems that come about from the other methods of manipulating the electronic properties of TiO_2. Blue TiO_2 is self-doped with Ti^{3+} defects that allow visible light absorption and visible light photocatalysis. However, there are still mixed opinions on the best methods of synthesising the most active blue anatase phase TiO_2. Also, the exact nature of the defect that causes the blue colouration is poorly understood.

Blue rutile and brookite phase TiO_2 have been synthesised but studied far less than blue anatase phase TiO_2. Yet, recent reports have indicated that both rutile and brookite show promise as visible-light photocatalysts.

Chapter 3 : Experimental

3.0 Reagents

All reagents were used as received. Reagents: 97 % titanium(IV) isopropoxide (TIPP) Sigma Aldrich reagent grade, oxalic acid Scharlau reagent grade, ammonium fluoride anhydrous Sigma Aldrich reagent grade, titanium tetrachloride Sigma Aldrich reagent grade, ammonia solution 30 % Sigma Aldrich reagent grade, 98 % sulphuric acid Sigma Aldrich reagent grade, 36 % hydrochloric acid Sigma Aldrich reagent grade, 30 % hydrogen peroxide Sigma Aldrich reagent grade, sodium fluoride Scharlau reagent grade, reactive blue dye 19 (RB-19) supplied by CI, methylene blue trihydrate chloride Sigma Aldrich reagent grade, ethanol anhydrous solvent grade, propanol anhydrous solvent grade and distilled water. Hydrothermal temperatures are reported +/- 2 °C.

3.1 Synthesis

3.1.1 Oxalic Acid Passivated Sol Synthesis

In a 250 ml beaker, 1.58 g (0.0125 mol) oxalic acid was dissolved in 28.0 g (0.6087 mol) ethanol; agitation was necessary to fully dissolve the oxalic acid. 14.2 g (0.05 mol) TIPP was added dropwise to the fully dissolved oxalic acid solution. The resulting solution was agitated to homogeneously disperse the TIPP. 180.0 ml distilled water was added to the ethanol solution forming a milky white solution. The solution was placed in a water bath (70-80 °C) and vigorously agitated with an overhead stirrer for approximately 60 minutes or until a transparent solution was achieved. The resulting sol was filtered through a Büchner filter and then diluted with water to a final volume of 180 ml. This particular sol will be referred to as TiO_2 0.25ox. Other sols were produced using 3.16 (0.025 mol), 4.74 (0.0375 mol) and 6.32 g (0.05 mol) oxalic acid. These sols are referred to as TiO_2 0.5ox, TiO_2 0.75ox, and TiO_2 1.0ox.

3.1.2 Hydrothermal Treatment of Oxalic Acid Sols

Hydrothermal treatment of the oxalic acid sols was performed in the following manner: First, the modifying solutions containing 0 to 1 equivalents NH_4F (with respect to mol Ti in 45.0 ml of the sol) was prepared by dissolving 0 g, 0.046, 0.093, 0.116, 0.139, 0.185, 0.231, 0.278, 0.324, 0.370, 0.417 and 0.463 g (0.000 – 0.0125 mol) NH_4F in 5 ml distilled water. 45.0 ml of the oxalic acid sol was transferred into a 75 ml Teflon-lined autoclave. 5.0 ml of the modifying solution was added to the 45.0 ml of sol. The autoclave was then sealed and placed in a preheated oven at 170-275 °C. The autoclave remained in the oven for 1-24 hours before being removed and allowed to cool to room temperature. Once cooled, the TiO_2 was separated by centrifugation (10 minutes 5000 RPM) and washed twice with 50 ml distilled water. Samples were named with respect to the number of equivalents of NH_4F to TiO_2 *i.e.* 0.25

equivalents NH_4F to 1 equivalent TiO_2 was named TiO_2 0.25F. Unless otherwise specified, the TiO_2 0.25ox sol was used as the precursor for NH_4F modified samples.

In a modification of the above method, oxalic acid TiO_2 sols were modified with both mineral acids and NH_4F at the same time. Briefly, a sol was modified as above with an NH_4F solution. Just before being sealed shut, either 0.05 mol H_2SO_4 (98%) or HCl (36%) was added to the sol. The autoclave was then sealed shut and placed in a preheated oven at 220 or 275 °C for a period of 24 hours before being removed and allowed to cool to room temperature. Once cooled, the TiO_2 was separated by centrifugation (10 minutes at 5000 RPM) and washed twice with 50 ml of distilled water. Samples were named with respect to the number of equivalents of NH_4F to TiO_2 and the acid used *i.e.* 0.5 equivalents NH_4F and 1 equivalent H_2SO_4 samples were named TiO_2 1H_2SO_4 0.25F. Unless otherwise specified, the TiO_2 0.25ox sol was used as the precursor for NH_4F modified samples.

3.1.3 Direct Hydrothermal Synthesis of Anatase Phase TiO_2

In a 75 ml Teflon-lined autoclave 3.55 g (0.0125 mol) TIPP was added to 45.0 ml distilled water. The liner was sealed and shaken to hydrolyse the TIPP. After being shaken, 0 g - 0.463 g (0 to 0.05 moles) of NH_4F pre-dissolved in 5.0 ml of distilled water was added to the autoclave along with the hydrolysed TIPP. The autoclave was then sealed shut and placed in a preheated oven at 150 – 270 °C. The autoclave remained in the oven for 24 hours before being removed and allowed to cool to room temperature. Once cooled, the TiO_2 was removed from the autoclave and isolated by centrifugation (10 minutes at 5000 RPM). The product was washed 3 times with distilled water (50 ml). The TiO_2 was then dried under vacuum for 24 hours.

Samples produced from the synthesis above were in two series of changing conditions. The first series (A) maintained a constant F:Ti ratio but varied the temperature of hydrothermal treatment. The second series (B) was carried out using the same temperature and examined the effect of varying the F:Ti ratio. Thus series (A) was synthesised with 0.0125 mol NH_4F (1:1 with mol TiO_2) added to the synthesis and then hydrothermally treated at 150, 170, 200, 220, 245 and 270 °C resulting in samples TiO_2 (A) 150, TiO_2 (A) 170, TiO_2 (A) 200, TiO_2 (A) 220, TiO_2 (A) 245, and TiO_2 (A) 270 respectively. Series (B) was synthesised at 270 °C with 0.001, 0.00125, 0.003125, 0.00625, 0.009375 and 0.05 mol of NH_4F added to the synthesis, resulting in samples TiO_2 (B) 0.1, TiO_2 (B) 0.25, TiO_2 (B) 0.5, TiO_2 (B) 0.75, and TiO_2 (B) 4 respectively. The resulting mol Ti to mol F^- was as such that the ratios were 1:0.1, 1:0.25, 1:0.5, 1:0.75, and 1:4 respectively. Table 3.1 below summarises the conditions and sample naming.

Sample name	TIPP (mol)	NH_4F (mol)	Equivalents TiO_2:NH_4F mol:mol	Temperature of hydrothermal treatment °C	Time (hours)
TiO_2 (A) 150	0.0125	0.0125	1:1	150	24
TiO_2 (A) 170	0.0125	0.0125	1:1	170	24
TiO_2 (A) 200	0.0125	0.0125	1:1	200	24
TiO_2 (A) 220	0.0125	0.0125	1:1	220	24
TiO_2 (A) 245	0.0125	0.0125	1:1	245	24
TiO_2 (A) 257	0.0125	0.0125	1:1	257	24
TiO_2 (A) 270	0.0125	0.0125	1:1	270	24
TiO_2 (B) 0.01	0.0125	0.000125	1:0.01	170	24
TiO_2 (B) 0.1	0.0125	0.00125	1:0.1	200	24
TiO_2 (B) 0.25	0.0125	0.003125	1:0.25	220	24
TiO_2 (B) 0.5	0.0125	0.00625	1:0.5	245	24
TiO_2 (B) 0.75	0.0125	0.009375	1:0.75	257	24
TiO_2 (B) 4	0.0125	0.050	1:4	270	24

Table 3.1 Table describing sample naming and conditions of series (A) and (B).

Two more series of anatase phase TiO_2 were synthesised as reference samples to gauge the impact of the NH_4^+ and F^- ions independently. The synthetic methods used were the same as above, however, the NH_4F was substituted for NH_4OH (series F) or NaF (series C). The following *Table 3.2* summarise the conditions and naming of the samples.

Sample name	TIPP (mol)	Modifier (mol)	Equivalents TiO_2:modifier mol:mol	Temperature of hydrothermal treatment °C	Time (hours)
TiO_2 (F) 170	0.0125	NH_4OH (0.0125)	1:1	170	24
TiO_2 (F) 220	0.0125	NH_4OH (0.0125)	1:1	220	24
TiO_2 (F) 245	0.0125	NH_4OH (0.0125)	1:1	245	24
TiO_2 (F) 270	0.0125	NH_4OH (0.0125)	1:1	270	24
TiO_2 (F) 0.1	0.0125	NH_4OH (0.00125)	1:0.1	270	24
TiO_2 (F) 4	0.0125	NH_4OH (0.05)	1:4	270	24
TiO_2 (C) 0.1	0.0125	NaF (0.00125)	1:0.1	270	24
TiO_2 (C) 1	0.0125	NaF (0.0125)	1:1	270	24

Table 3.2 Table describing sample naming and conditions of series (C) and (F).

3.1.4 Direct Hydrothermal Synthesis of Rutile Phase TiO_2

In a 75 ml Teflon-lined autoclave 0.395 g (0.003125 mol) oxalic acid was dissolved in 45.0 ml distilled water. 3.55 g (0.0125 mol) TIPP (or $TiCl_4$) was added dropwise to the dissolved oxalic acid. The liner was sealed and shaken to hydrolyse the TIPP. After being shaken, 0 g - 0.116 g (0 to 0.0125) mol of NH_4F pre-dissolved in 5.0 ml of distilled water was added to the autoclave along with the hydrolysed TIPP. The autoclave was then sealed shut and placed in a preheated oven at 270 °C. The autoclave remained in the oven for 24 hours before being removed and then allowed to cool to room temperature. Once cooled, the TiO_2 was removed from the autoclave and isolated by centrifugation (10 minutes at 5000 RPM). The product was washed 3 times with distilled water (50 ml). The TiO_2 was then dried under vacuum for 24 hours.

Samples produced from the synthesis above were named series (G). The oxalic acid was held constant at 0.25 equivalents. However, the NH_4F added to the synthesis was 0.00125, 0.003125, and 0.0125 mol. The resulting samples were called TiO_2 (G) 0.25ox0.1F, TiO_2 (G) 0.25ox0.25F and TiO_2 (G) 0.25ox1F respectively. Finally, in one particular sample, TIPP was substituted for $TiCl_4$ (0.0125 mol). The rest of the remaining conditions were identical to the synthesis of TiO_2 (G) 0.25ox0.1F. This sample was called TiO_2 (G) 0.25ox0.1F $TiCl_4$. Table 3.3 below summarises the conditions and sample naming.

Sample name	TIPP (mol)	Oxalic acid	NH_4F (mol)	Equivalents TiO_2:NH_4F mol:mol	Equivalents TiO_2:oxalic acid mol:mol	Temperature of hydrothermal treatment °C	Time (hours)
TiO_2 (G) 0.25ox0.1F	0.0125	0.003125	0.00125	1:0.25	1:0.1	270	24
TiO_2 (G) 0.25ox0.25F	0.0125	0.003125	0.003125	1:0.25	1:0.25	270	24
TiO_2 (G) 0.2ox1F	0.0125	0.003125	0.0125	1:1	1:0.25	270	24
TiO_2 (G) 0.25ox1F $TiCl_4$	0.0125 (As $TiCl_4$)	0.003125	0.00125	1:0.1	1:0.25	270	24

Table 3.3 Table describing sample naming and conditions of series (G).

3.1.5 Direct Hydrothermal Synthesis of Brookite Phase TiO_2

Briefly, in a 75 ml Teflon-lined autoclave 3.55 g (0.0125 mol) TIPP was added dropwise to 45.0 ml distilled water. The liner was sealed and shaken to hydrolyse the TIPP. After being shaken, 1.05 g – 4.20 g (0.025 to 0.1 mol) of NaF pre-dissolved in 5.0 ml of distilled water was added to the autoclave along with the hydrolysed TIPP. The autoclave was then sealed shut and placed in a preheated oven at 170 – 270 °C. The autoclave remained in the oven for 24 hours before being removed and allowed to cool to room temperature. Once cooled, the TiO_2 was isolated from the autoclave by centrifugation (10 minutes at 5000 RPM). The product was washed 3 times with distilled water (50 ml). The TiO_2 was then dried under vacuum for 24 hours.

Samples produced from the synthesis above were named series (Brk). The NaF added to the synthesis was 0.025, 0.05 and 0.1 mol. Table 3.3 below summarises the conditions and sample naming.

Sample name	TIPP (mol)	NaF (mol)	Equivalents TiO_2:NH_4F mol:mol	Temperature of hydrothermal treatment °C	Time (hours)
TiO_2 (Brk) 170 4	0.0125	0.05	1:4	170	24
TiO_2 (Brk) 220 4	0.0125	0.05	1:4	220	24
TiO_2 (Brk) 245 4	0.0125	0.05	1:4	245	24
TiO_2 (Brk) 270 4	0.0125	0.05	1:4	270	24
TiO_2 (Brk) 170 8	0.0125	0.1	1:8	170	24
TiO_2 (Brk) 220 8	0.0125	0.1	1:8	220	24
TiO_2 (Brk) 245 8	0.0125	0.1	1:8	245	24
TiO_2 (Brk) 270 8	0.0125	0.1	1:8	270	24
TiO_2 (Brk) 270 2	0.0125	0.025	1:8	270	24

Table 3.4 Table describing sample naming and conditions of series (Brk).

3.1.6 Direct Hydrothermal Synthesis of Organic Free Anatase Phase TiO_2

Briefly, in a 200 ml beaker 2.371 g (0.0125 mol) $TiCl_4$ was added dropwise to 45 g of distilled water ice. The rate of addition was slow enough to not cause any spontaneous hydrolysis of the $TiCl_4$. Once the ice had melted, a homogeneous $TiOCl_2$ solution was formed. This was neutralised to pH 7 by adding NH_4OH (30 %) dropwise while vigorously agitating. The precipitated ortho-titanic acid was washed 5 times with 50 ml of distilled water before being used in the hydrothermal synthesis. For each wash, the ortho-titanic acid was redispersed in 50 ml water and centrifuged out (10 minutes 5000 RPM). To hydrothermally treat the washed ortho-titanic acid, the ortho-titanic acid was redispersed into 45.0 ml distilled water and transferred into a 75 ml Teflon-lined autoclave. (0.0125 mol) of NH_4F (or NaF) pre-dissolved in 5.0 ml of distilled water was added to the autoclave along with the ortho-titanic acid. The autoclave was then sealed shut and placed in a preheated oven at 270 °C. The autoclave remained in the oven for 24 hours before being removed and allowed to cool to room temperature. Once cooled, the TiO_2 was removed from the autoclave and isolated by centrifugation (10 minutes 5000 RPM). The product was washed 3 times with distilled water (50 ml). The TiO_2 was then dried under vacuum for 24 hours.

3.2 Photocatalysis Experiment

3.2.1 Photocatalytic degradation of RB-19 under Xe broad spectrum light

Photocatalysis experiments using RB-19 were performed in collaboration with the Golovoko group with the help of Faridah Abu Bakar. The following procedure was used to test the photocatalytic performance of the synthesised TiO_2 samples:

A stock solution of RB-19 was first prepared. In a 25 ml glass vial, 80 mg of RB-19 ($1.2x10^{-4}$ mol) was weighed out. This was then washed into a 1 l volumetric flask using Milli-Q water (18.2 MΩ.cm) ensuring no RB-19 remained in the vial. The volumetric flask was made up to 1 l with Milli-Q water. The spectrum of the solution was then measured on a Cary 100 Bio UV-vis spectrometer. The absorption at 593 nm was approximately 0.7.

Before testing, the samples of TiO_2 were lightly ground by hand in a pestle and mortar. A photocatalytic slurry was prepared in a 160 ml quartz reaction tube by dispersing (ultrasonic bath for 5 minutes) 30.0 +/- 0.6 mg of TiO_2 into a 100 ml of the stock RB-19 solution. To this solution, 0.005 ml ($4.41x10^{-8}$ mol) 30 % H_2O_2 was added 5 minutes before the tube was placed in the photoreactor (described below). Once in the photoreactor, the slurry was stirred while being illuminated by a Ushio UXL-500D-O 500 W broad spectrum Xe lamp. 3 ml samples would be withdrawn at 15, 30, 45, 60, 90 and 120 minutes after the light was turned on. The total time of exposure to the light was 120 minutes. Each sample that was withdrawn from the reactor was centrifuged at 15,000 RPM for 3 minutes. Then the sample was transferred to a clean centrifuge tube and re-centrifuged. This process was repeated 2 times per sample to ensure all TiO_2 was removed. Remaining dye in the solution was monitored by UV-visible spectroscopy (UV-Vis). UV-Vis spectra were collected between 400-700 nm using a Cary 100 Bio UV-Vis spectrophotometer with Milli-Q water as the background. The RB-19's absorption maxima occurred at 593 nm and this peak was used to monitor the RB-19's concentration *via* Beer-Lambert's law. The degradation was calculated by dividing the absorption of the current sample by the absorption of the t=0 (when the light was turned on) to give a percentage of remaining dye.

3.2.1 Photocatalytic degradation of MB under Xe broad spectrum light

An alternative set of photocatalytic experiments were performed using methylene blue (MB). The method developed was a modification of the ISO standard (ISO10678-2010) for testing photocatalytic films.[59] The method used was as follows:

A stock solution of methylene blue was first prepared. In a 25 ml glass vial, 64 mg of methylene blue trihydrate ($5x10^{-5}$ mol) was weighed out. This was then washed into a 1 l volumetric flask using Milli-Q water (18.2 MΩ.cm) ensuring no MB remained in the vial. The volumetric flask was made up to 1 l with Milli-Q water. The spectrum of the solution was then measured on a Cary 100 Bio UV-vis spectrometer. The absorption at 660 nm was approximately 1.0.

Before testing, the samples of TiO_2 were lightly ground by hand in a pestle and mortar. A sample of 15 +/- 0.3 mg of TiO_2 was measured out and placed in a 25 ml glass sample vial. Approximately 20 ml of the stock MB solution was added to the TiO_2. This was then placed in an ultrasound bath for 3 minutes to disperse the TiO_2. The dispersed TiO_2 was then transferred to a 100 ml volumetric flask. The volumetric flask made up to 100 ml using the stock MB solution. This was then transferred to a 160 ml quartz tube. Care was taken to ensure the TiO_2 remained dispersed and did not settle out of solution at this point. A small magnetic stirrer bar was added to the quartz tube. The reaction tube was then placed in the photocatalytic reactor and magnetically stirred at 200 RPM. The photocatalytic mixture was stirred in the dark for 15 minutes, then a 3 ml sample was removed using a syringe from the outside of the reactor. The light was then turned on and samples were taken at 5, 10, 20, 30 and 45 minutes. Each sample was placed in a 3 ml centrifuge tube and centrifuged at 15,000 RPM for 2 minutes. The samples were then transferred to fresh centrifuge tubes and centrifuged at 15,000 RPM for a 2nd time. This process was then repeated for a third time. The remaining dye in the solution was monitored by UV-Vis. UV-Vis spectra were recorded between 400-700 nm using a Cary 100 Bio UV-Vis spectrophotometer, using Milli-Q water for the background measurement. The MB's absorption maxima occurred at 665 nm and this peak was used to monitor the MB's concentration *via* Beer-Lambert's law. The degradation was calculated by dividing the absorption of the current sample by the absorption of the stock solution to give a percentage of the remaining dye. This meant physically adsorbed dye was also included as "degraded dye".

There were two photocatalytic reactors used for the above experiments. One contained a Ushio UXL-500D-O 500 W broad spectrum Xe lamp, producing broad-spectrum light with the option of placing an Ocean Optics high pass filter in front of the light source. The high pass filter filtered out all wavelengths shorter than 395 nm (UV proportion of the light). The second reactor contained three 40 W UV LEDs. However, throughout the photocatalytic experiments reported here, only two LEDs were used simultaneously. There was the option to swap the UV LEDs for red 600 nm LEDs. Finally, each reactor consisted of a light-proof box, which had an external sampling tube and a magnetic stirrer inside the box to keep the TiO_2 suspended.

3.3 Characterisation

3.3.1 Synchrotron Powder X-ray Diffraction

The PXRD diffractograms were collected at the Australian Synchrotron. TiO_2 samples were packed into 0.3 mm glass capillaries. The capillaries were rotated while being irradiated and the diffraction pattern collected on a CCD detector spanning 80º 2ϴ. The patterns were analysed using Topas 4.2 (Bruker). A Rietveld refinement of a NIST standard LaB_6 660b was used to determine: the incident photon's wavelength (0.688650 Å), machine broadening and any additional convolutions resulting in an instrument profile. The resulting instrument profile was "fixed" and the samples were analysed using a Chebyshev 5th-degree polynomial background and two addition "peak phases" to account for air scattering. Structural files of anatase, rutile and brookite were fitted to the PXRD patterns, allowing refinement of relative phase percentage (wt/wt), crystallite size (Lorentzian and Gaussian), strain (Lorentzian and Gaussian), Ti occupancy, Bragg-reflexion intensity, scale, preferential orientation and lattice parameters. In the case of anisotropic crystallites displaying preferential orientation, two phases of the same lattice parameters, Bragg-reflexion intensity and Ti occupancies, were fitted with independently refining degrees of preferential orientation and crystallite size.

3.3.2 Lab Powder X-ray Diffraction

To collect the PXRD pattern of the sols the following procedure was used to prepare the samples: 20 ml of oxalic acid passivated TiO_2 sol was dried in the oven at 50 °C. The resulting glass was crushed to a fine powder in a pestle and mortar. PXRD was performed on a Philips PW3700 series diffractometer using Co-$K_{ά}$ radiation (λ =1.7889 Å). Scans were collected from 4° to 80 ° 2ϴ with a 0.01° step size and a count time of one second per step. The size and phase of the TiO_2 sols were determined by fitting the PXRD data with the Bruker software package EVA. The patterns used had internal reference intensity ratio values so phase percentage is reported on a wt/wt basis.

The as-synthesised TiO_2 from hydrothermal treatment of sols was characterised using the following methods: The dry washed powder was ground to a fine powder in a pestle and mortar. The dry powder was characterised on a Philips PW3700 series diffractometer using Co-$K_{ά}$ radiation (λ =1.7889 Å). Scans were recorded from 4° to 80° 2ϴ with a 0.01 step size and count time of one second per step. The size and phase of the TiO_2 samples were determined by fitting the PXRD data with the Bruker software package EVA. The patterns used had internal reference intensity ratio values so phase percentage is reported on a wt/wt basis.

For particular samples of the brookite series, a higher resolution scan was used. As above, the dry washed TiO_2 sample was ground to a fine powder in a pestle and mortar. The dry powder was characterised on a Philips PW3700 series diffractometer using Co-$K_{\acute{\alpha}}$ radiation (λ =1.7889 Å). Scans were recorded from 4° to 100° 2ϴ with a 0.005 step size and count time of 14 seconds per step. The patterns were analysed using Topas 4.2 (Bruker). A TiO_2 sample (TiO_2 (A) 270) pre-characterised using Synchrotron radiation was used to set the instrument profile to give the same result as the Synchrotron data. The resulting instrument profile was "fixed" and the samples were analysed using a Chebyshev 5th-degree polynomial background. Structural files of anatase, rutile and brookite were fitted to the PXRD patterns, allowing refinement of phase percentage (wt/wt), crystallite size (Lorentzian and Gaussian), Ti occupancy, Bragg-reflexion intensity, scale, preferential orientation and lattice parameters. In the case of anisotropic crystallites displaying preferential orientation, two phases of the same lattice parameters, Bragg-reflexion intensity and Ti occupancies, were fitted with independently refining degrees of preferential orientation and crystallite size.

3.3.3 Nitrogen Adsorption Isotherms

Surface area and porosity were measured by N_2 adsorption using a Micrometrics ASAP 2010. The following procedure was used: Approximately 0.200 g of TiO_2 sample was degassed at 300 ºC for 3 hours under high vacuum (3 μmm Hg). Degassed samples were then analysed at 77 ºK using 99.999 % pure N_2. The resulting isotherm was used to calculate surface area and porosity by Brunauer–Emmett–Teller (BET) theory and Barrett-Joyner-Halenda (BJH) theory which was built into the Micrometrics software package.

3.3.4 Scanning electron microscopy

Scanning electron microscopy (SEM) was performed at Callaghan Innovation on an FEI Nova NanoSEM. Samples were prepared by blowing a small amount of TiO_2 powder over conductive carbon pads.

Alternatively, samples were analysed at Canterbury University using a JEOL JSM 7000F SEM. Samples were prepared by ultrasonically dispersing TiO_2 in methanol and then dropping a small sample of the dispersed TiO_2 onto a single crystal silicon wafer. The samples were dried under vacuum before being analysed in the SEM.

3.3.5 Transmission electron microscopy

Transmission electron microscopy (TEM) was performed at Victoria University using a JEOL 2010 TEM in collaboration with Dr Richard Tilley (Victoria University). TiO_2 samples were prepared by ultrasonically dispersing finely ground TiO_2 powders into methanol and then depositing them onto

Formvar/carbon coated copper 50 mesh grids. Samples were dried under heat lamps before being imaged.

3.3.6 Ultra-Violet Diffuse Reflectance Spectroscopy

Ultra-violet diffuse reflectance spectroscopy (UV-Vis-DRS) was performed on a GBC Cintra 4040 spectrometer at the University of Canterbury. The diffuse reflectance sphere was used as supplied by the manufacturer. Spectra were recorded from 300 nm to 800 nm. To prepare a TiO_2 sample, TiO_2 was lightly ground in a pestle and mortar and then pressed into a small cup using a glass slide to make a flat surface. A Teflon reference cell was used to define the background.

3.3.7 Synchrotron Soft X-ray Spectroscopy

X-ray photoelectron spectroscopy (XPS) and Ultraviolet photoelectron spectroscopy (UPS) was performed in collaboration with Dr Gunther Anderson.

Synchrotron X-ray photoelectron spectroscopy (XPS) and valence band spectroscopy (VBS) was performed at the Australia Synchrotron on their soft X-ray beamline. TiO_2 samples were dispersed in methanol and deposited on silicon wafers. Spectra were collected using 4 different energies for the incident X-rays: 100 eV for the valence band spectroscopy, 580.0, 1265.0 and 1486.4 eV for the XPS and depth profiling. The built-in gold reference standard or the Ti2p peaks was used to references the incident X-ray energies and to account for any charging. Spectra were collected using a SPECS Phoibos 150 hemispherical analyser. The collected spectra were analysed by fitting the peaks with the software package CasaXPS.

The XPS spectra were fitted using the following procedure: The energy of the incident X-rays was normalised by either looking at the gold reference standard or taking the most dominant peak (generally Ti2P) and adjusting the incident X-ray's energy until that peak was aligned with the literature value (458.2 eV $Ti2P_{3/2}$). An offset Shirley background was fitted to the data with the endpoints fixed at specific energies to make each spectrum directly comparable. Following this, pseudo-Voigt peaks were fitted and refined using the least-squares method. The peak positions were allowed to refine. However, the relationship between the area of the spin-up and spin-down peaks was fixed so that the area of the $2P_{1/2}$ equalled half the area of the $2P_{3/2}$ peak.

For valence band spectroscopy, incident X-ray energy was normalised using the built-in gold reference standard. Following this, the intensity was normalised by looking at the intensity of the area around 17 eV. At 17 eV there were no peaks from the TiO_2 or Si wafer, so it was effectively normalising to the background noise intensity. After normalising, the spectra were analysed by looking at the peak intensity of specific peaks *i.e.* the O 2P non-bonding and bonding peaks as well as the Ti^{3+} 3d peak. The slope of the O 2P leading edge was fitted with a straight line and the X-intercept recorded to estimate band bending.

Near edge X-ray absorption fine structure (NEXAFS) spectra were collected at the Australian Synchrotron. Spectra were normalised by: First dividing the collected spectra by the grounding current of the inline gold reference. Then the pre-edge background was subtracted. Then the spectra were normalized so the post edge after the last transition occurred equalled 1. The spectra collected were: fluorescence yield, grounding current and partial electron yield. Spectra were analysed by looking at the ratios of peak intensities between the L_3 t_{2g} e_g and L_2 t_{2g} e_g.

3.3.8 Mass Spectrometry of Gas

To analyse the gases released from the hydrothermal syntheses, a syringe was used to sample the gases released from the autoclave. The contents of the syringe were analysed using an Ametek dymaxion (100 mass units model) mass spectrometer. Masses were measured from 0 to 50 atomic mass unit; count time per atomic mass unit was 500 ms and each point was averaged 12 times.

3.3.9 Electron Paramagnetic Resonance

Electron paramagnetic resonance (EPR) measurements were performed using a JOEL JES-FA200 at the University of Auckland. To analyse the samples, freshly prepared TiO_2 samples were placed in a glass capillary tube (3 mm). The measurements were performed at 220 °K under a nitrogen stream with no light exposure. No internal standard was added to the TiO_2 samples so quantitative analysis was not possible.

3.3.10 Ion Beam Analysis

Ion beam analysis was done at GNS in collaboration with Dr John Kennedy. Freshly prepared samples were split into 2 groups: one to be sent as-synthesised and the other to be washed with 10 molar NaOH. To wash the samples with NaOH, a stock solution of 10 molar NaOH was prepared in distilled water. 0.5 g of sample was added 50 ml NaOH in a small beaker and left stirring for 2 hours. After stirring for 2 hours, samples were centrifuged at 5000 RPM for 10 minutes to recover the TiO_2. The TiO_2 was then re-dispersed in 50 ml of distilled water and centrifuged out again. This process was repeated until the spent wash water had a pH of 7. The samples were then sent to GNS where they were analysed using particle-induced gamma-ray emission spectroscopy (PIGE).

3.3.11 Raman Spectroscopy

Raman spectroscopy was performed at the University of Victoria in collaboration with Prof Eric Le Ru. The instrument used was a Jobin-Yvon T64000. Spectra were collected using the red He-Ne (633 nm) laser with an 1800-line grating. The instrument was set up to collect for a period of 5 seconds per scan and then performed 10 scans averaging the results. Spectra were recorded from 75 to 750 wavenumbers (cm^{-1}). Before using the instrument, the instrument was calibrated using a silica NIST standard.

To prepare the samples, as-synthesised dry TiO_2 powders were simply placed on a microscope slide and then pressed flat using a small metal spatula. Under the microscope, the laser was aimed at a thick proportion of each sample and focused while collecting a live spectrum, maximising the number of counts per second.

To analyse the data, spectra were normalised using the most intense peak at approximately 150 cm^{-1}. Originpro was used to fit simple pseudo-void peaks to each of the modes seen in the spectra. To analyse the samples, intensity, position and FWHM of peaks were compared between samples.

3.3.12 Dynamic Light Scattering

Sols were particle sized on a Malvern Nano ZS. The colloidal sols were diluted tenfold with Milli-Q water. The samples were measured allowing the built-in auto optimiser to set the measurement conditions.

Chapter 4 : Oxalic Acid Passivated Sols and Hydrothermal treatment

4.0 Introduction:

In this chapter, TiO_2 sols were synthesised using oxalic acid as both a hydrolysis catalyst and passivating agent. These TiO_2 sols were hydrothermally treated in the presence of NH_4F and mineral acids to study the influence of the modifying agent on the morphology of the particles produced. As an unexpected consequence of the treatment under hydrothermal conditions, blue coloured TiO_2 was formed. Detailed characterisation of obtained materials was performed with an aim to understand factors inducing such colour. Finally, a sol-less synthesis was developed to replicate the same blue colour while producing a phase pure product for a more in-depth study (Chapter 5).

4.0.1 Oxalic acid passivated TiO_2 Sols

TiO_2 sols are a colloidal suspension nanoparticulate titanium dioxide. TiO_2 particles (colloids) with the size ranging from only a few nanometres to a few hundred nanometres can form a suspension where the repulsive forces between particles are enough to prevent aggregation producing a stable suspension.[60] Typically, the size of the particles is so small, the interaction with visible light rarely occurs, resulting in a transparent solution. Sols are often used as precursors when synthesising larger particles as they offer a controlled number of nucleation sites. Alternatively, they can also be used to form thin coatings over substrates.[60-62] Sols can be synthesised by hydrolysing a titanium-containing precursor in the presence of capping or passivating agents such as organic acids, mineral acids and bases.[22,62] Typically, the acids and bases used as the capping agents also catalyse the hydrolysis reaction. The capping layer on the surface of the particles changes the zeta potential of the TiO_2 producing the repulsive forces necessary to stabilise the sol.[60] TiO_2 sols have been synthesised previously mostly using mineral acids.[62,63] Alternatively, Kemmitt *et al.*[61] produced a TiO_2 sol passivated with oxalic acid. The oxalic acid is easily thermally or photocatalytically oxidised and removed from the surface of the particles. These sols offer the advantage of being able to retrofit photoactive coatings to sensitive substrates.[61] This chapter investigates the use of these stable sols as a consistent starting material for the morphologically controlled growth of the larger crystals.

4.0.2 Hydrothermal Treatment of Oxalic Sols Modified with NH_4F

Throughout the literature, fluoride ions have been used successfully to control the morphology of the TiO_2. The fluoride ions offer two advantages: firstly, the F^- ion tends to hold the anatase phase by stabilising the anatase crystal facets.[28] Secondly, the {001} facet is preferentially stabilised resulting in higher percentages of coverage than the other facets typical of natural anatase.[27-29,64] Typically, either HF or TiF_4 is the source F^- ions in the hydrothermal syntheses of TiO_2, where TiF_4 forms HF upon contact with water.[29,64] However, HF is rather dangerous and unpleasant to work with.[65]

Ammonium fluoride (NH_4F) in lieu of HF was used in this work due to the fact the F^- ion should have a similar effect as previously reported; however, the dangers of HF are avoided.[27-29,64] Several researchers have used NH_4F as a morphology directing agent. Ye *et al.*[66,67] and Yu *et al.*[32] both found that NH_4F could be used to ensure the TiO_2 produced was 100 % anatase. Yet far more interestingly, both research groups found that NH_4F could control the morphology, so the resulting TiO_2 particles produced were full or hollow spheres, see *Figure 4.1*. The proposed mechanism by both groups is that the NH_4F disassociates and the resulting F^- ions dissolve the more amorphous content in the centre of the spheres depositing it onto the outside spheres.[32] Interestingly and against what would be predicted, as NH_4F fully dissociates into NH^{4+} and F^- ions and it is the binding of the F^- ion to the {001} which inhibits growth in the [001] direction, enhancing the {001} facet exposure.[27] There are no literature reports of increased coverage of the {001} facet when using NH_4F compared with when using HF.[32,66-69]

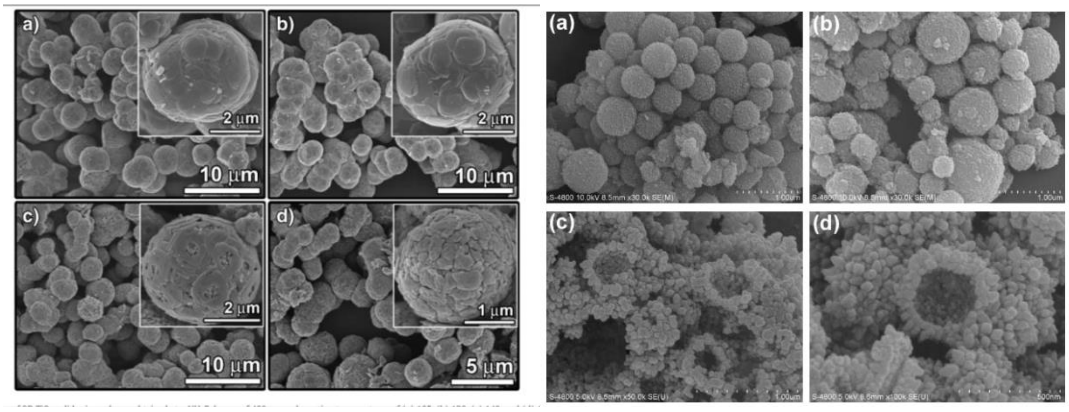

Figure 4.1 Hollow TiO_2 spheres synthesised by 2 different research groups. Left: Ye et al.[66,67] Right: Yu et al.[32] Both using NH_4F as a morphology directing agent.

In the following chapter, the effects of NH_4F as a modifying agent when hydrothermally treating oxalic acid passivated TiO_2 sols is explored.

4.1.0 Results and Discussion:

4.1.1Characterisation of Oxalic Acid Stabilised TiO_2 Sols

The oxalic acid passivated TiO_2 sols varied in turbidity and stability depending on the oxalic acid content. For the purpose of this discussion, different sols will be labelled as TiO_2 “X”ox, where “X” corresponds to the molar equivalents of oxalic acid (ox) with respect to the Ti. The TiO_2 0.25ox sols were translucent, interacting with visible light to produce a light blue reflected colour and orange transmitted light typical of sol particles (the Tyndall effect). The TiO_2 0.25ox sols also showed good stability against agglomeration for several months. As the oxalic content increased from 0.25 equivalents to 0.5 equivalents, the sols became increasingly more transparent and colourless but the stability decreased with TiO_2 0.5ox sols precipitating within weeks. Dynamic light scattering (DLS) indicated that the TiO_2 0.25ox sols consisted of smaller particles than the TiO_2 0.5ox sols with average particle sizes of 4 nm to 6 nm respectively, see *Figure 4.2*. DLS also indicated that there was a degree of agglomeration within the sols, although not shown here. The TiO_2 0.25ox sols contained 62 nm agglomerates and the TiO_2 0.5ox sols contained smaller 11 nm agglomerates. The difference in size of these agglomerates may explain the change in transparency of the sols. When the oxalic acid concentration was increased to 1 equivalent (TiO_2 1.0ox), the sols precipitated a white powder determined to be titanium oxalate, ($Ti_2O_3(H_2O)_2(C_2O_4).3H_2O$) by powder X-ray diffraction (PXRD), JCPDS card number 00-054-0330. These sols would continue to precipitate titanium oxalate over several days.

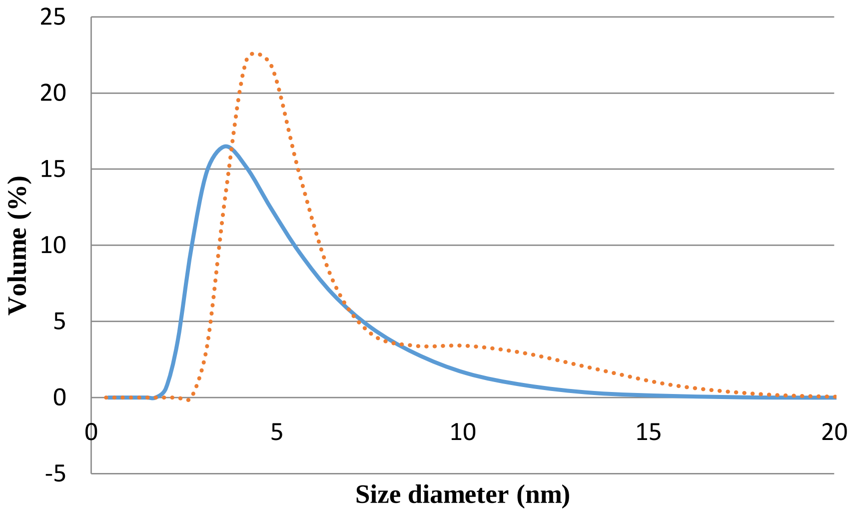

Figure 4.2 DLS results showing the particle size distribution within the sols synthesised with different equivalences of oxalic acid: Blue solid TiO_2 0.25ox and red dashed TiO_2 0.5ox.

PXRD on the dried sols showed that TiO_2 crystallites produced were a mixture of brookite, rutile and anatase the phases, see *Figure 4.3*. The PXRD diffractograms (S1) were fitted with the software package Eva (Bruker) using the JCPDS cards: anatase (078-2486), rutile (087-0920) and brookite (076-1937) patterns. This gave the relative phase composition on a percent wt/wt basis. Brookite was the most dominant phase accounting for over 60 % of the TiO_2 produced in all sols. The brookite crystallites were extremely small and a precursor to the formation of anatase and rutile.[70] PXRD also showed that the anatase phase content decreased with increasing oxalic acid content from 30 % to 7 % for TiO_2 (0.25ox) and TiO_2 (0.5ox) respectively. The bidentate binding of oxalic acid to the surface of anatase locks the structure suppressing the formation of rutile phase TiO_2.[71] While at the same time, the acidic conditions favour the nucleation of rutile phase TiO_2.[18] Furthermore, the presence of alcohol favours the nucleation of anatase.[72] This is because both alcohols and H^+ ions bind to the TiO_6 building blocks distorting the polymeric chains resulting in the preferential nucleation of specific phases.[18,72] However, rutile formation was not fully supressed as all sols examined here contained a small amount of rutile phase TiO_2.

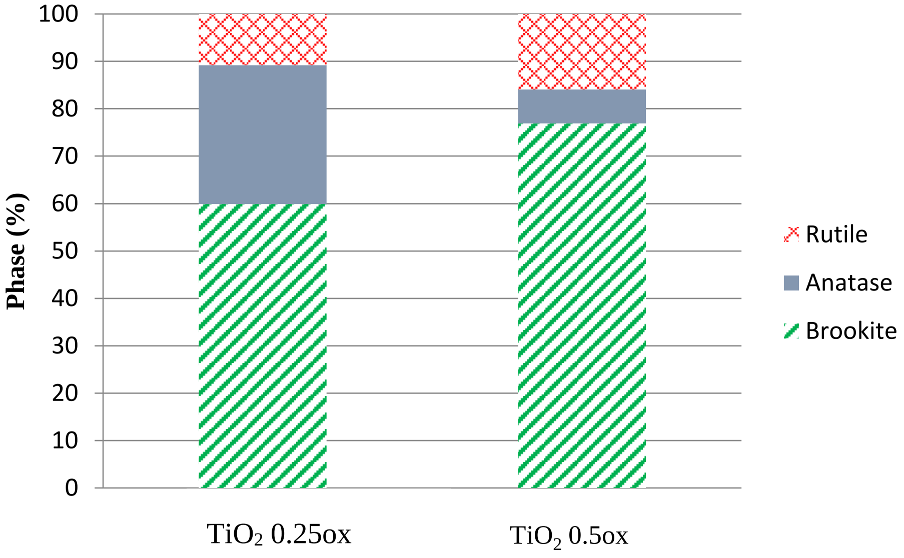

Figure 4.3 The phase of TiO_2 as calculated by PXRD within sols synthesised with different equivalences of oxalic acid: Left TiO_2 0.25ox and right TiO_2 0.5ox.

4.1.2 The Hydrothermal Treatment of Oxalic Sols and the Effects of Temperature and Oxalic Acid Concentration

The hydrothermal treatment of oxalic acid sols between 85 and 275 °C was investigated. PXRD on the resulting white precipitated TiO_2 showed that only anatase and rutile phase was obtained after hydrothermal treatment for 24 hours. Brookite phase was lost as it is too unstable at these temperatures.[70] *Figure 4.4* shows the relative ratios of anatase and rutile for the products prepared from the TiO_2 0.25ox and the TiO_2 0.5ox sols after 24 hours of hydrothermal treatment at various processing temperatures. At temperatures up to 140 °C the TiO_2 0.25ox sol maintains its composition of between 50 % and 60 % anatase phase. This changed abruptly around 170 °C where the only phase produced was rutile. All preparations above this processing temperature and up to 275 ºC (the maximum temperature examined) resulted in phase pure rutile.

The hydrothermal treatment of the TiO_2 0.5ox sols also resulted in a high anatase phase content in the lower temperature range. The TiO_2 0.5ox sols also demonstrated an abrupt conversion to rutile although in this case, the transformation occurs at a slightly lower temperature (at 140 ºC less than 2% anatase remained). However, the biggest impact of the oxalic acid concentration was observed above this temperature. A gradual reconversion of the rutile back to anatase occurred for the TiO_2 0.5ox sols hydrothermally treated at temperatures >170 °C. In contrast, the TiO_2 0.25ox sols remained as rutile. For confirmation, a sol was synthesised with higher oxalic acid content, one equivalent (TiO_2 1.0ox), then was hydrothermally treated at 220 ºC for 24 hours, which resulted in > 70 % anatase (the remainder was rutile), confirming that the reappearance of anatase is related to the initial oxalic acid concentration.

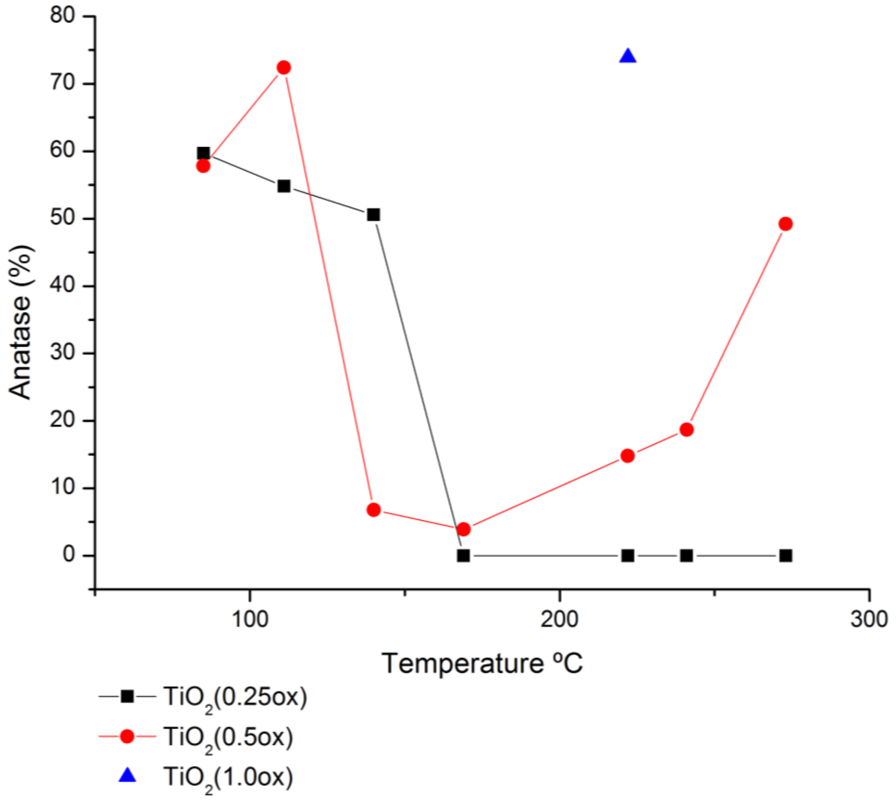

Figure 4.4 Anatase phase composition of TiO_2 as determined by PXRD, produced by the hydrothermal treatment of oxalic acid sols, with increasing temperatures from 85 ºC to 275 ºC. Hydrothermal treatment was for 24 hours. Note: (▲)-TiO2 (1.0ox) is only one point. Note: Lines have been added to guide the eyes and not link to results.

At the lower temperatures, the surface stabilisation from the bidentate binding of oxalic acid reduces the surface energy, particularly on smaller particles favouring the anatase phase formation.[72,73] However, the higher temperature syntheses contain no oxalic acid as it decomposes below 170 ºC. The onset decomposition temperature of oxalic acid is ~126.6 ºC (gas phase).[74] The oxalic acid decomposes into carbon dioxide and formic acid.[74] Then in a second step, at higher temperatures and catalysed by TiO_2, formic acid decomposes into carbon dioxide and water.[75] The decomposition of oxalic acid and formic acid has been confirmed with Fourier transform infrared spectroscopy (FT-IR) by looking for the disappearance of the $C=O_{str}$ at 1733 cm^{-1} in the dry powders post hydrothermal treatment, see *Figure 4.5*.[61] The disappearance of the C=O stretch first occurred in samples that have been hydrothermally treated at temperatures above 170 ºC. This coincides with the divergent behaviour between low oxalate (0.25ox) and high oxalate (0.5ox and above) content sols, which initiate the reversion to the anatase phase. It is well-known rutile phase is more thermodynamically stable than anatase for bulk materials.[6] So, it is somewhat surprising that this transformation occurs, although there are precedents in the literature. The perchlorate ion mediated transformation of rutile to anatase has been described as due to the thermal elimination of synthetically included hypochlorite ions.[76] However, rutile transforming into anatase seems unlikely. An alternative mechanism is proposed that the hydrothermal processing and the *in-situ* generation of CO_2 during the oxalic acid decomposition results in carbonic acid. The carbonic acid may dissolve the small rutile crystallites and re-precipitate them as anatase. This would also explain why the size of the rutile crystallites in 275 °C sample (0.5 OX) is decreasing and the size of the anatase is increasing, see *Figure 4.6*.

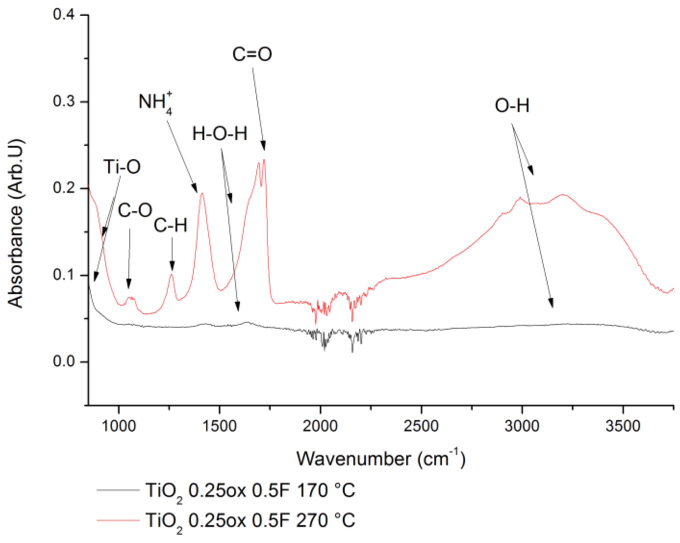

Figure 4.5 FT-IR spectra of washed TiO_2 powder synthesised at 170 and 270 °C from modified oxalic acid sols. The spectra show the disappearance of the C=O stretch with increased temperatures of hydrothermal treatment.

Estimates of the crystallite sizes (based of the PXRD peak broadening (*Section 3.3.2*)) of the anatase and rutile phase produced by the hydrothermal treatment of the oxalic acid sols show some similarities between the two sols, see *Figure 4.6*. Please note: some of the points in *Figure 4.6* have been removed as there was an insufficient proportion of that phase for accurate sizing. The growth of rutile crystallites is very rapid between 85 ºC and 170 ºC. Above this temperature, the oxalic acid has fully decomposed and the rutile crystallites remain a constant size at all processing temperatures above this. The anatase crystallites remain small except in the case of the TiO_2 0.5ox sols above 170 ºC where the anatase phase crystallites grow at the expense of the rutile phase. The higher oxalic acid content sol, TiO_2 1.0ox, results in only marginally larger anatase crystallites of *ca.* 24 nm when hydrothermally treated at 220 ºC compared to *ca.* 20 nm in the TiO_2 0.5ox sols.

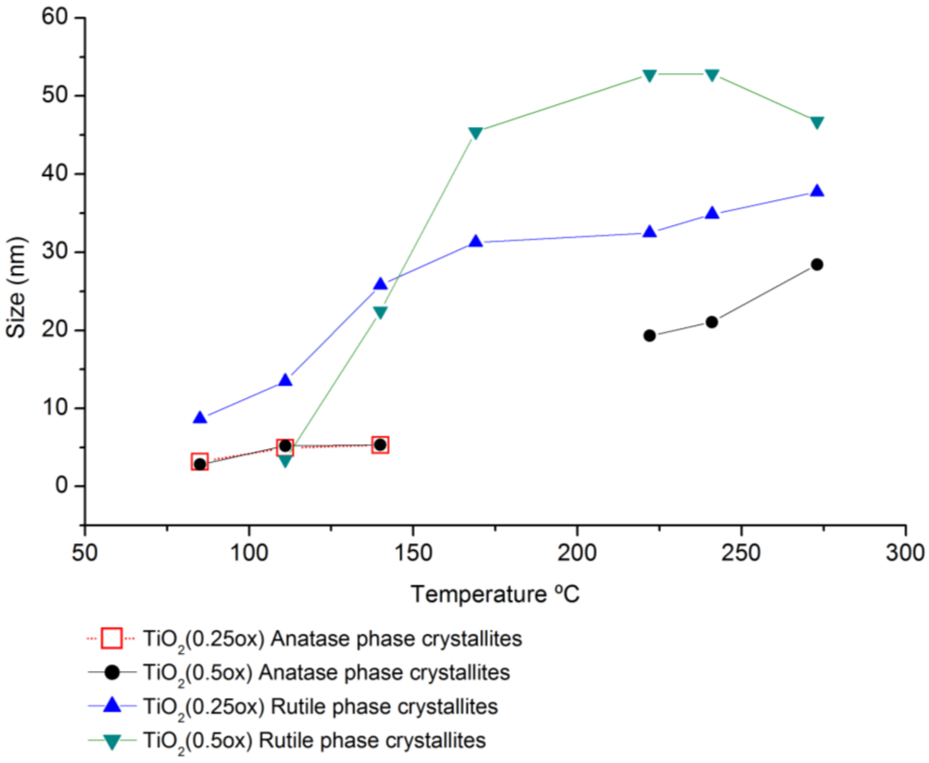

Figure 4.6. Crystallite sizes as determined using the Scherrer equation from PXRD of TiO_2 produced by the hydrothermal treatment of oxalic acid sols with different equivalencies of oxalic acid and at different temperatures from 85 ºC to 275 ºC. All sols were hydrothermally treated for 24 hours. Note: Lines have been added to guide the eyes and not link to results.

The time dependence of phase and crystallite size evolution was also explored for the TiO_2 0.25ox sol. In *Figure 4.7*, it is clear from the PXRD data that the majority of the change to the TiO_2 happens early on in the hydrothermal treatment process. Within the first 4 hours, the anatase phase TiO_2 has completely disappeared along with the brookite phase TiO_2. Also, the rutile phase crystallites grow to their full size within 8 hours. FT-IR spectra confirm the decomposition of the oxalic acid in the solution within the first hour *via* the disappearance of the $C{=}O_{str}$ at 1733 cm^{-1}; the solution also released gas when first removed from the autoclave suspected to be CO_2. This rapid change in phase composition supports the above observation that the TiO_2 in the TiO_2 0.5ox sols converts to rutile first and then back to anatase. The initial period could be affected by the actual temperature profile, as it has been observed that the autoclaves do not reach their final target temperature until approximately 2 hours into the hydrothermal treatment, due to slow heat transfer from the oven.

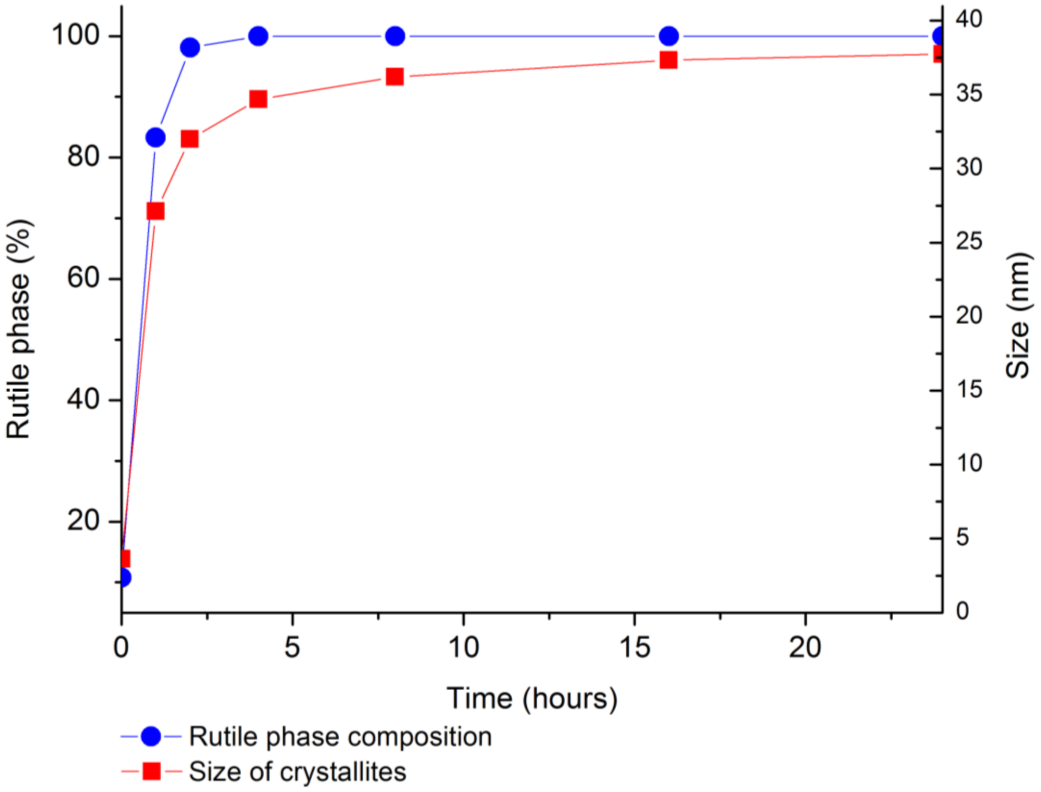

Figure 4.7 The rutile phase composition as determined by PXRD and the size of the rutile crystallites as determined using the Scherrer equation for TiO_2 produced by the hydrothermal treatment of TiO_2 0.25ox sols at 275 ºC. Hydrothermal treatment was performed for 0-24 hours.

The scanning electron microscopy (SEM) images of TiO_2 produced at 275 ºC show the morphologies of the crystallites formed by the hydrothermal treatment of TiO_2 0.25ox and TiO_2 0.5ox sols, *Figure 4.8* left and right respectively. The crystallite sizes observed are largely consistent with the Scherrer crystallite size data shown in *Figure 4.7* above. However, the PXRD data provide a single dimension averaged for a theoretical spherical particle whereas the large aspect ratio of the elongated rutile rods can result in significantly different dimensions observed in the SEM. For example, rutile particles calculated as 40 nm diameter from PXRD data can be observed (SEM) as rods 100 nm long x 20 nm wide. The rutile phase from TiO_2 0.25ox exhibits elongated rods which are observed clearly in all preparations from 170 ºC to 275 ºC (S2). Although the sizes do not vary significantly across this temperature range, the aspect ratio of the rods decreases slightly. By contrast, the mixed anatase/rutile phase crystallites from TiO_2 0.5ox show the smaller irregularly shaped anatase crystallites covering the residual rutile rods, *Figure 4.8* right.

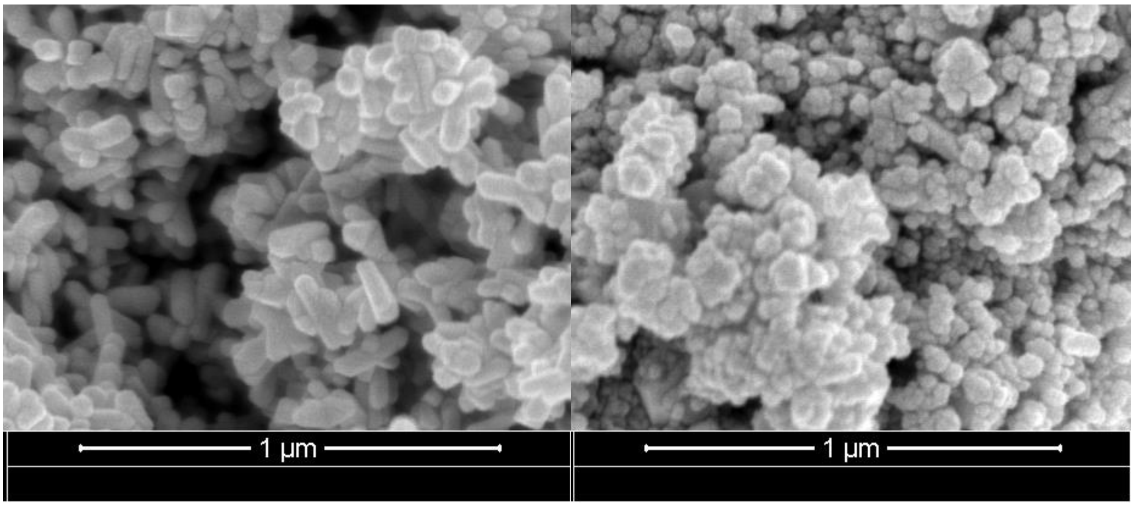

Figure 4.8 SEM image of TiO_2 produced by the hydrothermal treatment of TiO_2 (0.25ox) (left) and TiO_2 (0.5ox) (right) sols. Both were hydrothermally treated at 275 ºC for 24 hours.

4.1.3 Hydrothermal Treatment of Oxalic Sols Modified with NH_4F

The oxalic acid passivated TiO_2 sols showed promise as a starting material for growing TiO_2 nanocrystals hydrothermally (see *Section 4.1.2*). Yet, the control over the morphology of the particles produced was limited as the phase composition often drifted towards rutile, the least photoactive phase of TiO_2.[6] The 0.5 equivalent oxalic acid sols were disregarded as a starting material because of the observed reverse phase transformation adds unnecessary complications. Here, 0.25ox sols were modified with different amounts of NH_4F in an attempt to direct the morphology of the TiO_2. For the purpose of this discussion, different samples will be labelled as TiO_2 “X”ox “Y”F, where “X” corresponds to the molar equivalents of oxalic acid (ox) and “Y” to the molar equivalents NH_4F add as a modifier with respect to the Ti.

The phase of TiO_2 synthesised showed a strong dependence on the number of equivalents of NH_4F added to the synthesis when hydrothermally treated at 270 °C. When the line-profiles of the PXRD diffractograms were fitted, the results revealed that at less than or equal to 0.25 equivalents of NH_4F the TiO_2 produced was phase pure rutile, see *Figure 4.9*. As a greater ratio of NH_4F was added, anatase phase TiO_2 began to dominate. Further addition of NH_4F resulted in the anatase phase content remaining stable at approximately 60 %. The literature states that when NH_4F is present anatase phase would dominate.[66] Although, as previously reported in *Section 4.1.2* above, the 0.25 equivalent oxalic acid sols favour rutile phase at the higher temperature of hydrothermal treatment.[77] It would appear that above 0.25 equivalents NH_4F, the F^- ions suppress rutile phase formation favoured by oxalic acid (alone).

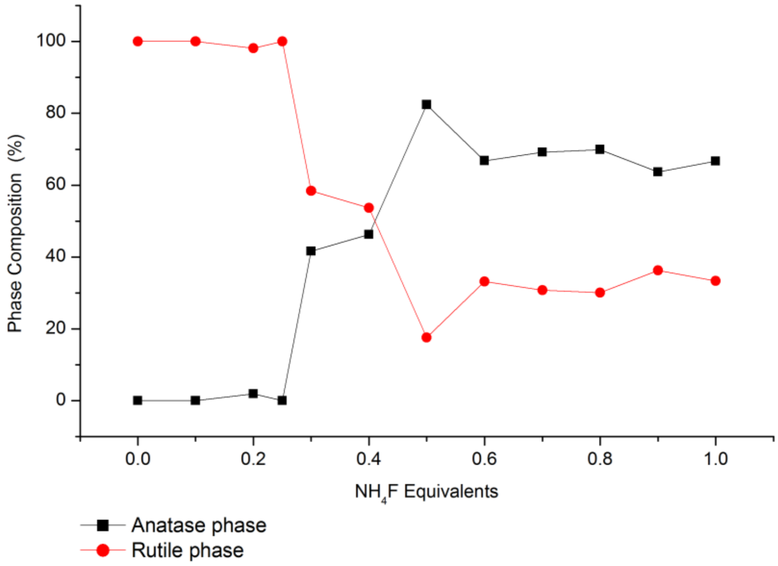

Figure 4.9 Phase of TiO_2 produced with 0 - 1 equivalents of NH_4F as determined using PXRD. Note: Lines have been added to guide the eyes and not link to results.

We have shown previously that the oxalic acid content influences crystallite sizes (*Section 4.1.2*).[77] Here we found the concentration of NH_4F also influenced the crystallite sizes of each phase independently. *Figure 4.10* shows the rutile phase crystallites grew larger with increasing NH_4F equivalency (up to *ca.* 82 nm) until anatase phase TiO_2 begun to appear at >0.25 equivalents NH_4F. This could be due to a lack of TiO_2 building blocks available to grow the rutile crystals as the anatase phase began to grow. Coincidentally, the growth of anatase phase crystallites was also suppressed by increasing NH_4F content. A change in size was observed from *ca.* 33 to 19 nm with the NH_4F ratio increasing from 0.5 to 1 equivalents respectively. The growth of both rutile and anatase crystallites appeared to be equally suppressed between 0.25 and 1 equivalents of NH_4F, as indicated by the near equal negative gradient between the size of the crystallites, see *Figure 4.10*. This could be due to etching effects where the F^- dissolves the precipitated TiO_2 reducing crystallite size or F^- binding to the surface and suppressing growth.[29] It was reported by Wang *et al.*[29] that the selective {001} facet etching occurred when the concentration of F^- increased from 0.028 $molL^{-1}$ to 0.056 $molL^{-1}$. Whereas, the F^- concentration used in the synthesis reported here ranges from 0.025 $molL^{-1}$ at 0.1 equivalents to 0.25 $molL^{-1}$ at 1 equivalent. The excessively high concentrations of F^- could etch more than just the {001} facet of the anatase phase crystallites.

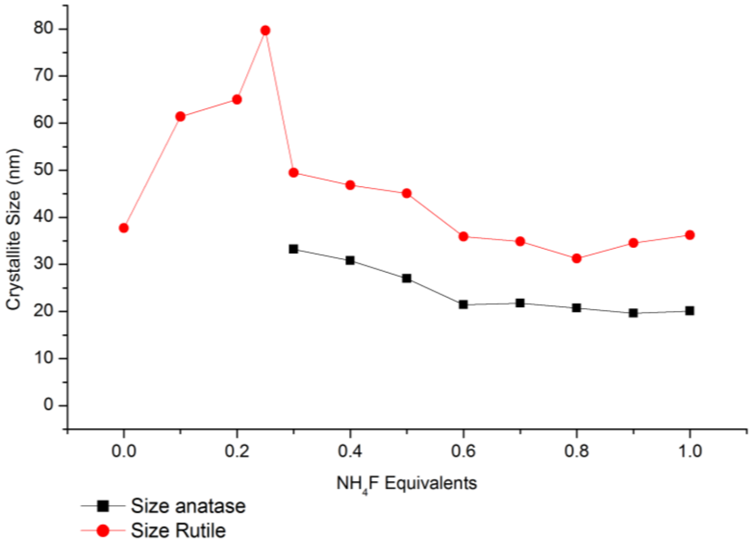

Figure 4.10 Size of crystallites produced with 0 - 1 equivalents of NH_4F as determined by line broadening using PXRD. Note: Lines have been added to guide the eyes and not link to results.

The time dependence of the phase change during hydrothermal treatment was examined at four different equivalency of NH_4F. *Figure 4.11* shows the anatase phase content of TiO_2 produced with respect to the time of hydrothermal treatment at 270 °C. When no NH_4F is present during the hydrothermal treatment of a 0.25 oxalic acid sols, full conversion to rutile occurs within the first 2 hours. Yet, with 0.25 equivalents of NH_4F, conversion to rutile is significantly slowed, the full conversion to rutile is only observed after 24 hours. Interestingly, the highest retention of anatase phase occurred at 0.5 equivalents of NH_4F and remained true throughout the 24 hour time period. Above this level at 1 equivalent of NH_4F, more conversion of anatase to rutile occurred. This result agrees with what was observed above in *Figure 4.9*, based on a separate set of experiments, where the 0.5 equivalent NH_4F resulted in the highest anatase retention. Nonetheless, this result was unexpected as the literature states that the fluoride ions should help retain anatase phase TiO_2.[27,28,64] It also appears that in *Figure 4.11* there was a general trend towards the conversion to rutile, the addition of NH_4F only retards the conversion. Future work may reveal that increasing the processing time results in full conversion to rutile even at higher equivalency of NH_4F. Of course, rutile is the more thermodynamically stable phase so when possible, anatase should convert to rutile.[6] It has been reported that the doping of anatase with F^- increases the temperature of calcination required to initiate the phase transformation to rutile.[78] These results also corroborate that the presence of F^- during the hydrothermal treatment of anatase also increases the activation energy required to convert anatase to rutile and hence slows the conversion.

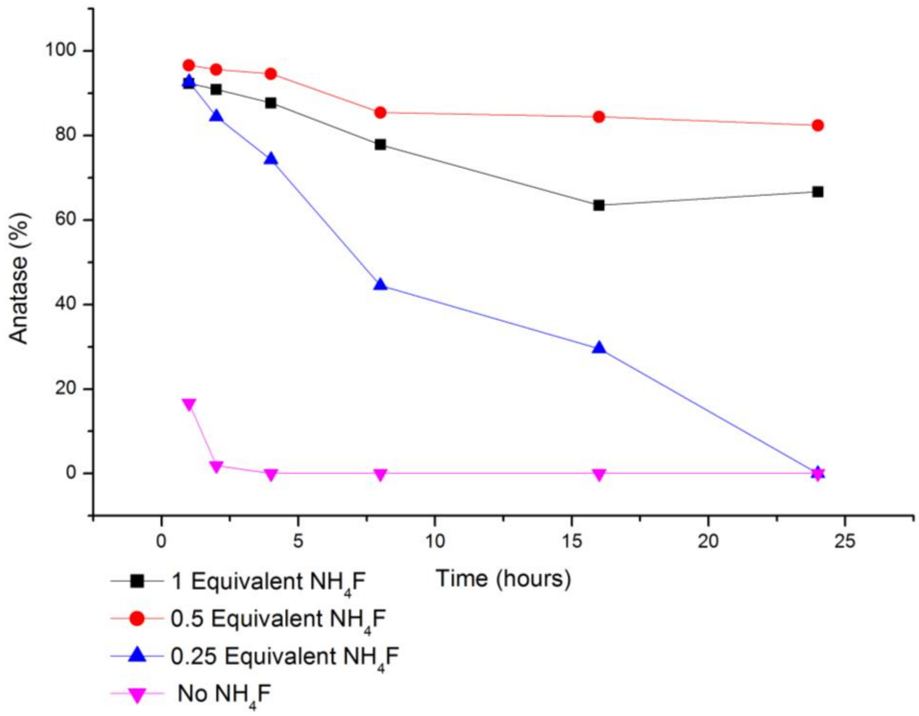

Figure 4.11 Percentage anatase phase of TiO_2 produced with 0, 0.25, 0.5 and 1 equivalents of NH_4F verse time of hydrothermal treatment at 270 °C as determined by PXRD. Note: Lines have been added to guide the eyes and not link to results.

The evolution of crystallite size with time during hydrothermal treatment with various equivalents of NH_4F was also investigated. It was observed that at 0.25 equivalents of NH_4F both anatase and rutile crystals grew to a much larger size and much faster than any other case examined, see *Figure 4.12*. Also observed is that for both anatase and rutile phase crystallites the 1 equivalent NH_4F series produced smaller crystallites than the 0.5 and 0.25 equivalents. Unlike the hydrothermal treatment of an unmodified oxalic acid sol, crystals in the modified sols continued to grow over the full 24 hour period tested. Whereas in the unmodified sols, the rutile phase crystallites grew to their full size within 4 hours. It has been proposed in the literature that the formation of $TiOF_2$ enables the titanium to dissolve and re-hydrolyse on the surface of larger particles, resulting in the growth of crystallites.[79-81] However, trends shown in *Figure 12* imply at higher concentrations of NH_4F crystallite growth is suppressed. Yet, the fact that NH_4F can form a buffer solution with the oxalic acid present in the sols was not considered in the above discussion. It can be seen in *Figure 4.13* that as more NH_4F is added to the sol the pH becomes closer to neutral. Also, the change in pH observed from the decomposition of the oxalic acid decreases as the NH_4F content increases. It could be hypothesised that in order to solubilise Ti ions from the dissolution of smaller particles for the growth of larger particles by forming $TiOF_2$, the H+ ions are required. This is because the H+ ions are the species which actually attack the TiO_2 as per the *Equation 4.1* below.

$$TiO_2 + H_3O^+ \rightarrow TiO(OH)_2 + H^+ \qquad (1)$$

$$TiO(OH)_2 + 2H^+ + 2F^- \rightarrow TiOF_2 + 2H_2O \qquad (2)$$

Equation 4.1 Possible equations for the reaction of TiO_2 *to* $TiOF_2$

When an excess of NH_4F is added to the sols the concentration of H+ ions drops significantly making it harder to solubilise the titanium, therefore, decreasing the growth of the crystals. Also, the pH may influence the phase of TiO2 produced. It has been shown that acidic conditions favour the formation of rutile phase TiO2 whereas basic conditions favour the formation of anatase.[82] This could explain the formation of rutile in lieu of anatase at lower NH_4F concentrations.

On the other hand, the NH_4^+ could form ammonium titanate and be driving crystal growth. Ammonium titanate can form when NH_4OH reacts with a TiO_2 precursor or near amorphous material. The NH_4^+ ions simply act as a charge balancing species between layers of TiO_6 octahedra.[83] It is feasible that the ammonium titanate facilitates the mass transport of TiO_2 material, as single sheets in solution, resulting in the growth of crystallites. The growth rate suppression at higher concentrations may be due to the more efficient TiO_2 surface coverage by F^- inhibiting growth.[84]

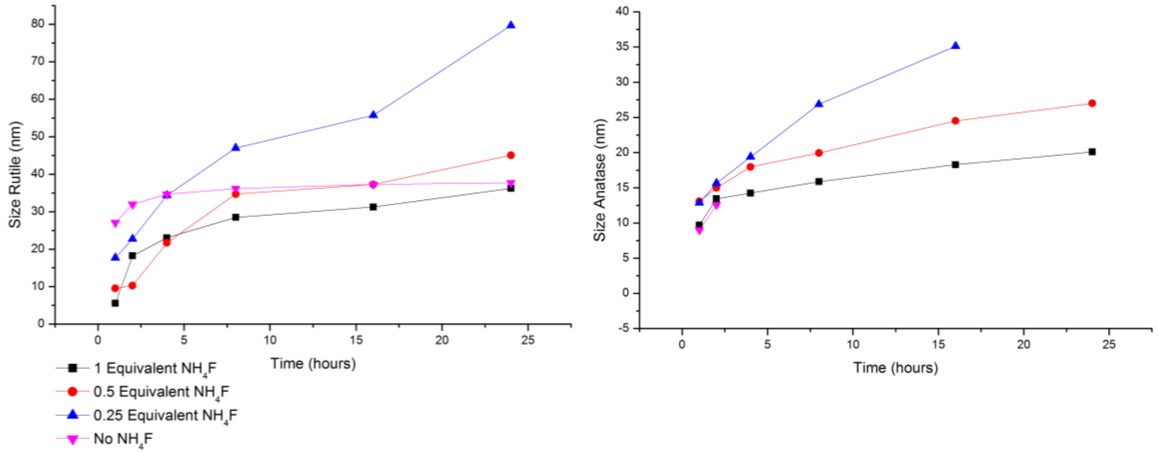

Figure 4.12 Size of rutile (left) and anatase (right) phase crystallites produced with 0, 0.25, 0.5 and 1 equivalents of NH_4F *verse time of hydrothermal treatment at 270 °C as determined by line broadening in PXRD. Note: Lines have been added to guide the eyes and not link to results.*

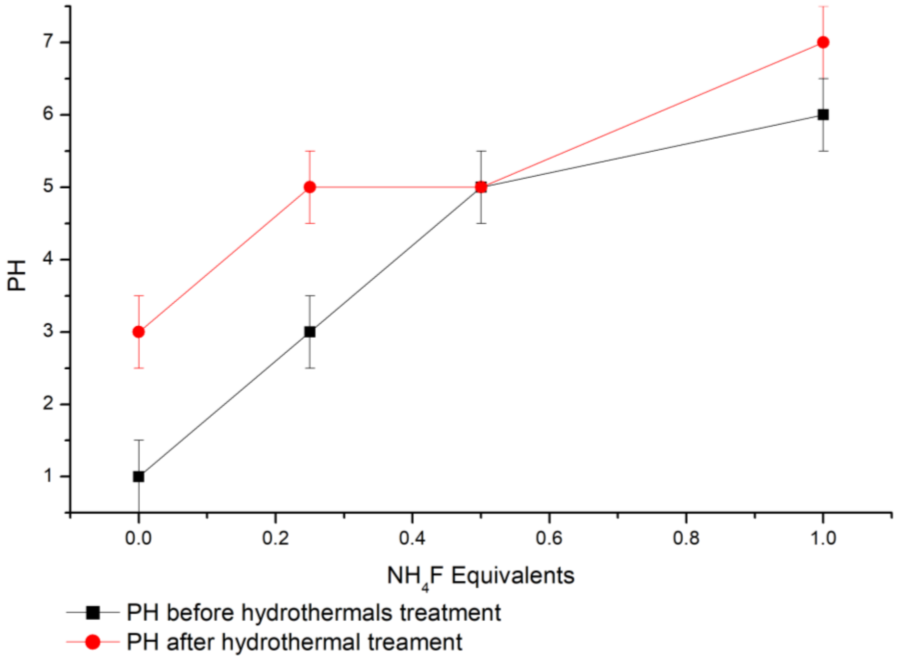

Figure 4.13 Depicting the pH of the oxalic acid sols after modification with NH_4F before and after hydrothermal treatment. Note: Lines have been added to guide the eyes and not link to results.

To continue the investigation into how the ratio of NH_4F, time and temperature of hydrothermal treatment influences the phases and size of crystallites produced, the following series of experiments were carried out. The series looked at how the phase composition and size of crystallites changed over time at different processing temperatures using the 0.5 equivalents of NH_4F modified TiO_2 0.25ox sol. It was found by PXRD that the composition of the TiO_2 produced is relatively constant (83-93% anatase for all temperatures) after 24h of hydrothermal treatment. There is only a slight progression towards rutile phase at processing temperatures greater 245 °C, see *Figure 4.14* left. Also at 90 °C, there is a progression towards anatase, this is actually due to the disappearance of brookite phase. As expected, the size of crystallites produced continues to increase with time and temperature, see *Figure 4.14* right. The fact that the phase composition remains relatively constant suggests that conditions within the solution *i.e.* F^- ions and pH are preventing the interconversion of the anatase phase to rutile, the more thermodynamically stable phase.[6] The fact that increasing the temperature made very little difference to the final phase composition implies that it is not a lack of kinetic energy that is preventing the anatase converting to rutile rather the additives. F^- ions have been shown to stabilise anatase throughout the literature.[78,84] Yet, the growth of crystallites implies smaller crystallites must be sacrificed to free up building material for the larger crystals. This supports the idea that either the F^- ion or NH_4^+ ion must aid in the dissolution of smaller crystals to be deposited on larger crystals. Clearly, the data shows temperature speeds up this process, see *Figure 4.14* right.

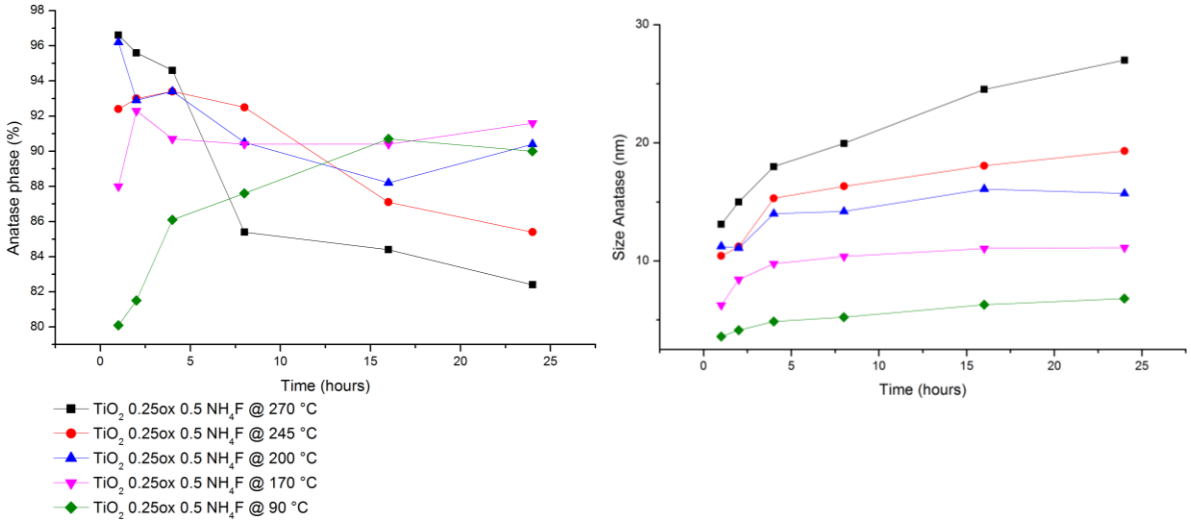

Figure 4.14 Left: Anatase phase composition. Right: Anatase phase crystallites sizes produced with 0.5 equivalents of NH_4F verse time of hydrothermal treatment at 95, 170, 220, 245 and 270 °C as determined by PXRD. Note: Lines have been added to guide the eyes and not link to results.

Scanning electron microscopy (SEM) was used to investigate how the shape of the particles was influenced by the amounts of NH4F modifier. SEM images revealed that the rutile particles produced in the absence of NH_4F were elongated rods similar to ones reported earlier, see *Figure 4.8*.[77] Conversely, when 0.25 equivalents of NH_4F was added the shape of the rutile crystallites dramatically changed to isotropic pyramid-like formations. Compare top left and top right images in *Figure 4.15*. In the case of high concentrations of NH_4F (1 equivalent), the shape of the anatase crystallites produced did not show any well-defined anisotropic shape. This is in part due to the very small size of the crystallites, making it very difficult to accurately resolve the crystallite's shape. Nonetheless, it can be seen in *Figure 4.15* (bottom image), that the rutile present amongst the anatase crystallites is of a similar shape to those observed in sample TiO_2 0.25ox 0.25F (the assignment based on the crystallite sizes according to PXRD). Clearly, the F^- ion is binding to a facet of the growing rutile phase crystallites and inhibiting growth in specific crystallography directions. Judging by the shape of crystallites observed in the SEM images and most common facets of rutile reported in the literature, the unmodified crystals (TiO_2 0.25ox), are elongated in the [001] direction exposing the {101} facet at the top and the {110} along the sides.[85] Yet, the fluoride-modified rutile (*Figure 4.15* top right) is no longer elongated and exposes a much greater proportion of the {101} facet.[85] Wu *et al.*[86] reported that fluoride binds to the {101} facet stabilizing it, which influences the shape of rutile particles.

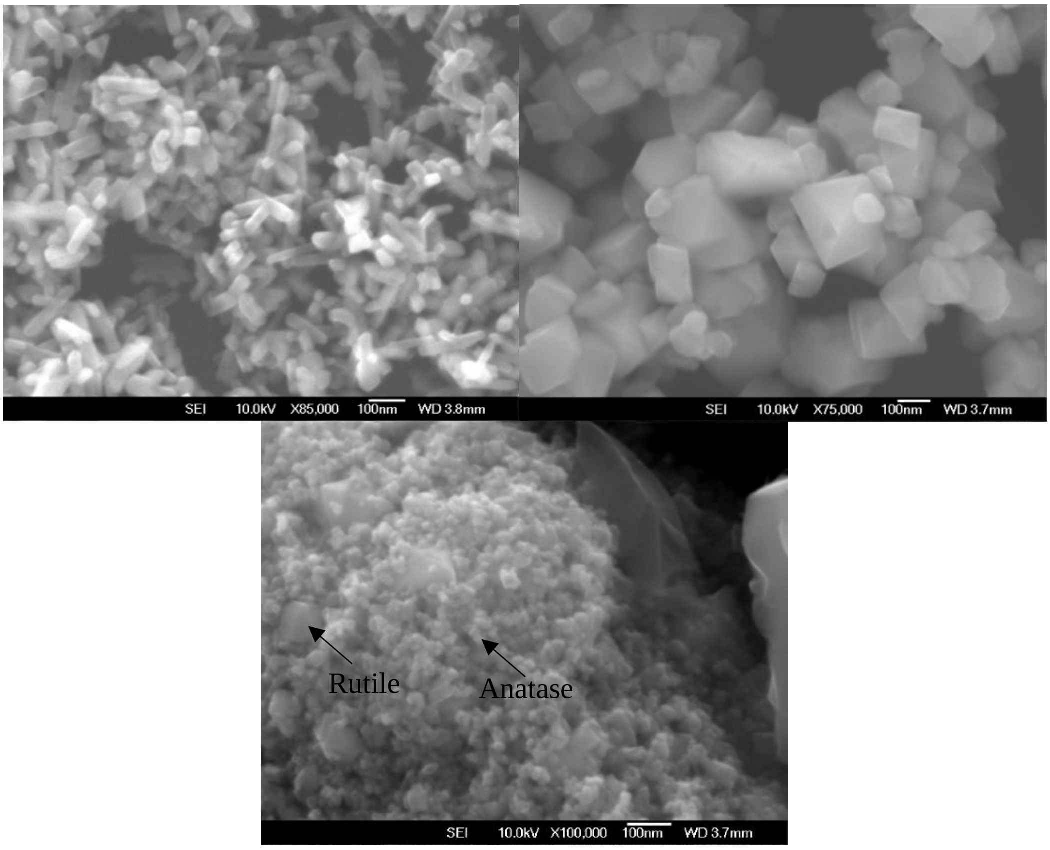

Figure 4.15 SEM images of TiO_2 synthesised. Top left: 0 equivalents (TiO_2 0.25ox 0F). Top right: 0.25 equivalents NH_4F (TiO_2 0.25ox 0.25F). Bottom: 1 equivalent NH_4F (TiO_2 0.25ox 1F).

It is proposed from the above experimental evidence that the composition of the final product is in part controlled by the modifying agent and the initial composition of the oxalic acid sol. The sol starts as a mixture of anatase, rutile and brookite, see *Figure 4.3*. During hydrothermal treatment amorphous material and/or smaller particles are dissolved and re-precipitated or hydrolysed onto the surface of larger particles enabling them to grow through "Ostwald's ripening"- like process.[87] When less than 0.25 equivalents of NH_4F is added to the sol, the product tends towards rutile phase TiO_2 during the hydrothermal treatment. However, the final size of the rutile crystallites increases as the amount of NH_4F gets closer to 0.25 equivalents. The size of the rutile crystallites peaks just before anatase phase begins to coexist, see *Figure 4.9* and *Figure 4.10*. This observation suggests the number of individual crystals growing reduces up until that point, allowing more material to go into each individual crystal increasing their size. Importantly, in the case of less than 0.25 equivalents of NH_4F, rutile grows at the expense of anatase. This can be seen in *Figure 4.11* where after the 1st hour the 0.25, 0.5 and 1 NH_4F equivalent sols all have approximately the same anatase phase content. Though, as the hydrothermal treatment continues the rutile crystals grow and consume all the anatase phase in the TiO_2 0.25ox 0.25F sample. Rutile growing at the expense of anatase can also be observed in the case of the unmodified sol, see *Figure 4.7*. Evidence of this can be seen in the first 2 hours of hydrothermal treatment where the anatase phase is disappearing the rutile grows extremely quickly. Yet, once the anatase phase has been consumed the growth rate of rutile plateaus. Also when comparing the unmodified sol, 0.25, 0.5 and 1 NH_4F equivalent samples, *Figure 4.7* and *Figure 4.10*, it can be seen that the NH_4F slows growth of both anatase and rutile crystallites above 0.25 equivalents. The slower growth rate could be explained by either the F^- ion binding to specific facets, which is evident from the change in shape of rutile crystals, slowing the rate at which dissolved building material can precipitate onto each crystal. The more efficient growing surface blockade by F^- could be coinciding with less efficient digestion of sacrificial species (amorphous or smaller TiO_2 particles) due to the increasing amounts of the NH_4F neutralising the pH resulting in less efficient H^+ attack. Noteworthy, that NH_4F once present, increases the final crystallite size achievable by the crystallites up to the maximum observed at 0.25 equivalents. Conversely, as the NH_4F ratio increases to 0.3 equivalents, the maximum size achieved by rutile crystallites is reduced while anatase phase appears in the final product for the first time. Suppression of the final crystallite size at high NH_4F ratios is true for both rutile and anatase; compare the final points *Figure 4.12* on and *Figure 4.10*. By combining these two observations we came to the conclusion that: initially, NH_4F in the synthesis mixture allows for the formation of $TiOF_2$ at low pH, which speeds up the transportation of the titanium building blocks, allowing rutile crystals to grow larger. However, as more NH_4F is added the pH is neutralised which reduces the formation of $TiOF_2$.

Between 0.25 and 0.5 equivalents of NH_4F, there is a shift towards favouring anatase as the most dominant phase. What appears clear from *Figure 4.14,* is the anatase is not being consumed *via* dissolution and re-deposition of Ti ions onto the growing surface of the rutile crystals. Instead, the anatase phase is preserved because the growth of the rutile crystals has been suppressed. The suppression may come from the surface of the rutile being saturated with F^- ions, making it incapable of growing. Even though anatase is favoured, the dissolution of rutile never occurs as rutile is not dissolvable by HF.[17] This means the rutile phase crystallites initially present in the sol, see *Figure 4.3,* remains and only grow from amorphous material or coalescence of other rutile crystallites. Hence, the product of the sols is never 100 % anatase.

The idea of the F^- ions binding to specific facets and slowing growth is supported by the change in particle shape observed in the rutile phase, see *Figure 4.15*. The rutile produced shifts from elongated rods which are most likely elongated in the [001] direction (the natural direction rutile grows), to bi-pyramidal shaped crystals with a compressed [001] axis.[85,88-90] The idea that F^- binds to the surface of rutile was also proposed by Wu *et al.*[86]

4.1.4 Hydrothermal Treatment of Oxalic Sols Modified with Mineral Acids and NH_4F

In order to investigate the role of pH in the hydrothermal treatment of oxalic acid passivated sols, mineral acids namely sulphuric acid (H_2SO_4) and hydrochloric acid (HCl) were added to the sols in combination with NH_4F. For the purpose of this discussion, different samples will be labelled as TiO_2

“X”HCl “Y”F, where “X” corresponds to the molar equivalents of mineral acid (either HCl or H_2SO_4) and “Y” to the molar equivalents NH_4F add as a modifier with respect to the Ti.

The addition of one equivalent the H_2SO_4 reduced the pH to less than one, the addition of NH_4F made very little difference to the starting or ending pH. However, as can be seen below in *Figure 4.16* (left), PXRD showed the full conversion to rutile still occurred when starting mixture contained less than 0.25 equivalents NH_4F. Anatase phase was retained as the addition of NH_4F was increased above 0.25 equivalents. Unlike the NH_4F modified sols above (*Section 4.1.3*), there did not appear to be any optimal NH_4F level which resulted in the maximum retention of anatase between the conditions tested. In fact, the anatase phase dominance appeared to increase monotonically with the addition of more NH_4F. The pH remained less than one despite 1 equivalent on NH_4F being added to the synthesis. As for the size of crystallites produced, the NH_4F seemed to suppress the growth of rutile as the concentration was increased. On the other hand, between the only two points tested, the size of the anatase crystallites seemed unaffected by the increasing NH_4F concentration, see *Figure 4.16* (left). This is in contrast to what was observed above, where the addition of NH_4F suppressed the growth of anatase phase crystallites, see *Figure 4.10*. This would support the theory that the addition of more NH_4F suppressed growth by increasing pH in the earlier study without strong acids.

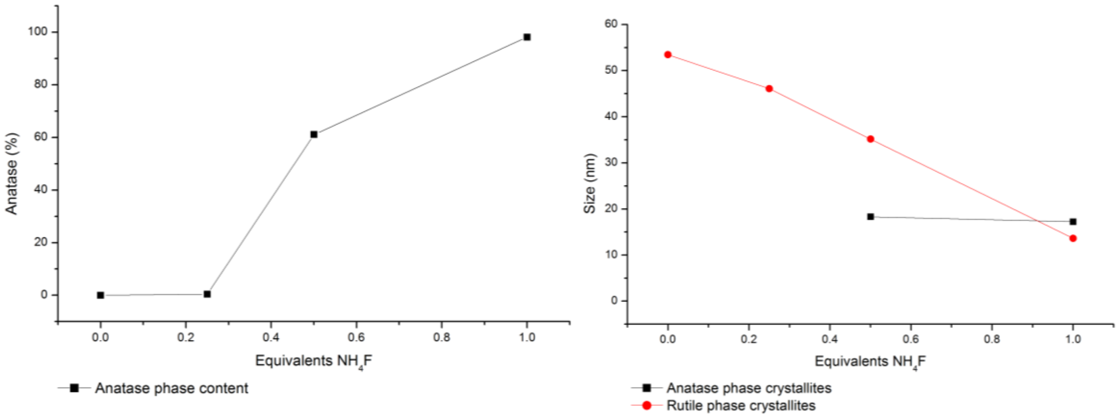

Figure 4.16 Left: Anatase phase composition. Right: anatase/rutile phase crystallites size (right) produced with 1 equivalent H_2SO_4 and 0, 0.25, 0.5 and 1 equivalents of NH_4F hydrothermal treatment at 220 °C as determined by PXRD. Note: Lines have been added to guide the eyes and not link to results.

In the same fashion as above, HCl at one molar equivalent to Ti was added to the TiO_2 0.25ox sols to reduce the pH below one. The pH did not appear to change before or after hydrothermal treatment nor did it change with the addition of NH_4F, always remaining below 1. As above with the H_2SO_4 modified sols, the HCl modified sols initially converted to rutile when no NH_4F was present. However, as the amount of NH_4F added to the sols was increased the product produced shifted towards anatase, see

Figure 4.17 (left). Yet, at one equivalent of NH_4F the anatase phase content was only 64 % as opposed to 98 % with the H_2SO_4. The crystallite size of the rutile and anatase was not significantly reduced with increasing concentrations of NH_4F, unlike in the case of use of H_2SO_4 and non-acid modified sols above, see *Figure 4.17* (right). Diprotic acids such as H_2SO_4 have been shown to be selective towards anatase phase as the SO_4^{2-} ion locks the surface of the anatase phase structure by bidentate bonding, whereas monoprotic acids, with monodentate Cl- ions, do not impose selectivity in phase formation.[82,91,92] This explains the higher anatase phase content of the H_2SO_4 modified sols above, see *Figure 4.16*.

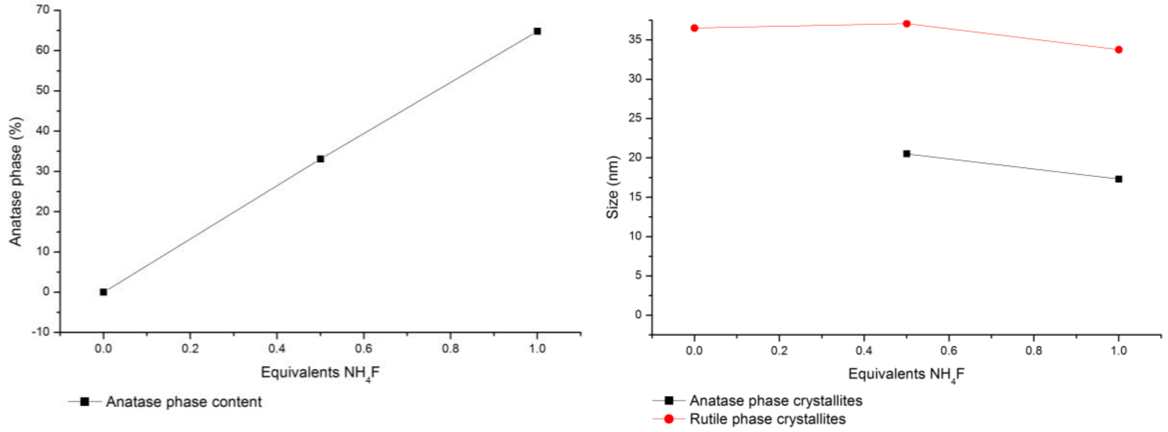

Figure 4.17 Left: PXRD results showing anatase phase composition. Right: Anatase/rutile phase crystallites size (right) produced with 1 equivalent HCl and 0, 0.5 and 1 equivalents of NH_4F hydrothermal treatment at 220 °C. Note: Lines have been added to guide the eyes and not link to results.

When the temperature of hydrothermal treatment was increased from 220 to 270 °C there was an abrupt shift in the phase produced and crystallite sizes produced. With the H_2SO_4 modified sols at 1 equivalent NH_4F, PXRD showed anatase remains the dominant phase, however, the crystals grew to a massive 125 nm as opposed to 20 nm seen at 220 °C for the same conditions, see *Table 4.1*. Secondly, in the HCl modified sols, there was a change from 60 % anatase to 100 % rutile, the size also increased to 87 nm as opposed to 35 nm. The experimental observation was made that the H_2SO_4 began to decompose at this temperature or due to contact with steel (Teflon seal could have failed), as there was a putrid smell coming from the autoclaves and the TiO_2 took days to become odour free.

Sample	Phase (%)	Size anatase (nm)	Size rutile (nm)
TiO_2 $1H_2SO_41F$ (24 hours @ 270 °C)	Anatase 87	125	51
TiO_2 1HCl 1F (24 hours @ 270 °C)	Rutile 100	-	87

Table 4.1 Table showing the PXRD results from samples produced with one equivalent of either HCl or H_2SO_4, and one equivalent of NH_4F hydrothermal thermally treated at 270 °C for 24 hours.

SEM showed that not only does the combination of mineral acids and NH_4F have a massive effect on the phase of TiO_2 produced, but it also strongly affects the shape and size of crystals. SEM images of the H_2SO_4/NH_4F modified TiO_2 showed that at 1 equivalent of H_2SO_4 and NH_4F at 220 °C, the anatase particles were small with no distinct shape, much like the products of the hydrothermal treatment of the non-acid modified sols discussed above, see *Figure 4.18* top left and *Figure 4.15*. However, if the temperature was increased to 270 °C, the crystals were much larger and showed a lozenge shape typically seen in HF modified hydrothermal synthesises, see *Figure 4.18* top right.[29,35,93] When H_2SO_4 was substituted for HCl under the same conditions (220 °C, 1 equivalent of acid and NH_4F) the anatase particles appeared to have a similar shape and size as the H_2SO_4 modified synthesis, see *Figure 4.18* top and bottom left. In contrast, when the temperature was increased to 270 °C, the rutile crystals produced showed a bi-pyramidal shape, see *Figure 4.18* bottom right. The general morphology of the bipyramidal rutile appears very similar to that seen above in *Figure 4.15*, where oxalic acid sols were modified with 0.25 NH_4F equivalents and hydrothermally treated at 270 °C, the only difference was the particles produced here were much larger.

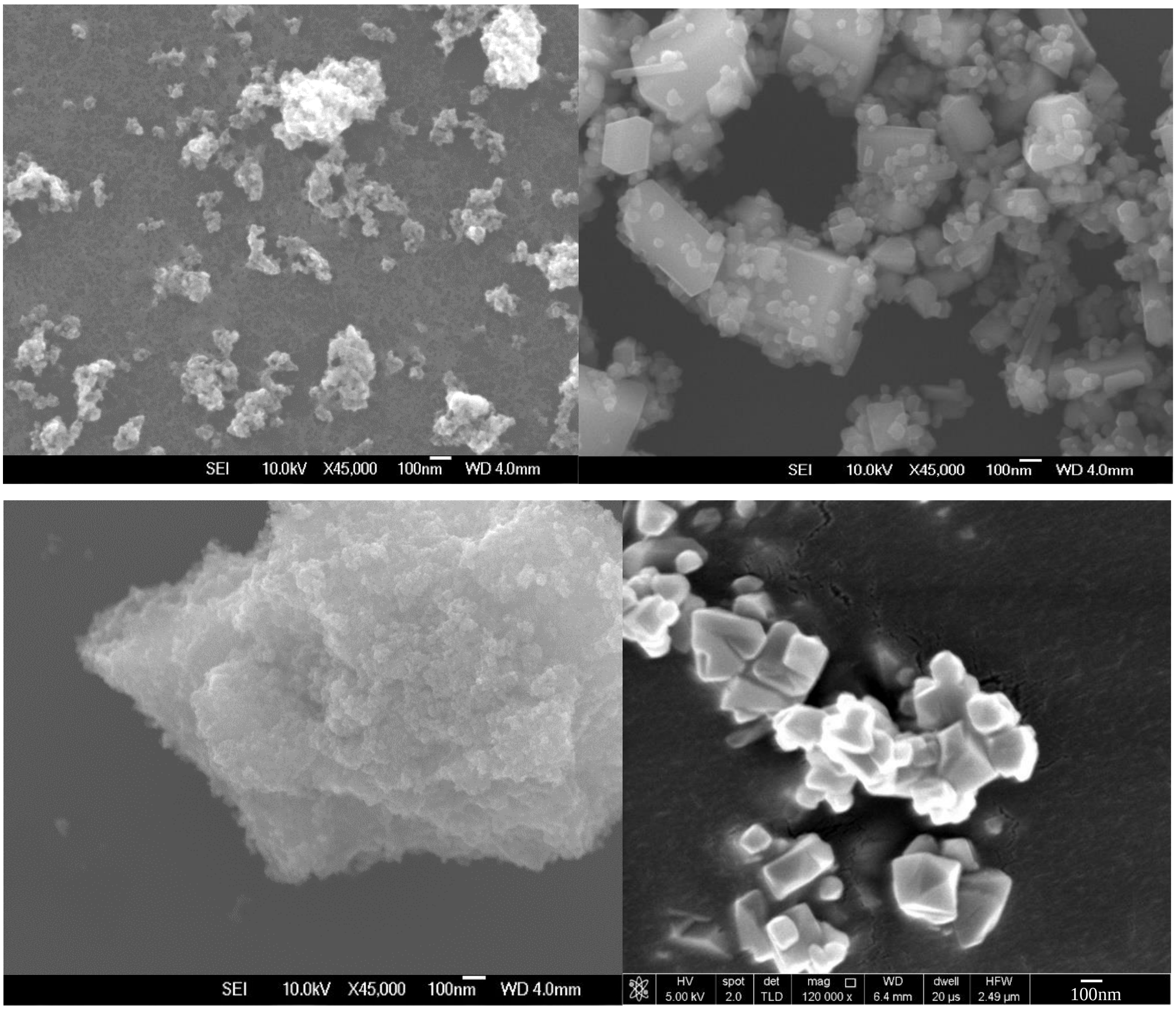

Figure 4.18 SEM images of TiO_2 samples: Top left: TiO_2 $1H_2SO_4$ 1F hydrothermal treatment at 220 °C. Top right: TiO_2 $1H_2SO_4$ 1F hydrothermal treatment at 270 °C. Bottom left: TiO_2 1HCl 1F hydrothermal treatment at 220 °C. Bottom right: TiO_2 1HCl 1F hydrothermal treatment at 270 °C. Note: Bottom left image was done on a different SEM, however, scales are similar.

The addition of mineral acids and NH_4F to the hydrothermal treatment of oxalic acid sols lowered the pH and dramatically change the morphology of the particles produced. When the pH was lowered by the addition of H_2SO_4 or HCl, anatase phase was favoured with increasing NH_4F equivalents. No peak anatase phase retention or plateau was observed unlike sols modified purely with NH_4F. The fact that a phase pure anatase product was produced with H_2SO_4 supports the theory that the TiO_2 is dissolved and re-precipitated as the sol start as *ca.* 10 % rutile. Note: Hot H_2SO_4 can dissolve rutile whereas HF cannot.[17,94] The HCl modified sols showed the same behaviour as the H_2SO_4 modified sols where the anatase phase content was dependent on the NH_4F concentration. However, given the same acid and NH_4F equivalencies, HCl modified sols did not favour the formation of anatase phase as strongly. Within the conditions tested, the maximum anatase phase content achieved using HCl was only 66 %

whereas it was >98 % for H_2SO_4 modified sols under the same conditions. It is known from the literature that H_2SO_4 will preferentially precipitate anatase phase under hydrolytic conditions, whereas HCl and other monoprotic acids, can precipitate both anatase and rutile phases under hydrolytic conditions.[82,91,92] This suggests that the acid anion was also directing the morphology. Therefore, changes in morphology cannot be solely related to pH changes and the formation of $TiOF_2$ *via Equation 4.1* as suggested above. The anatase phase crystallites were larger in the acid-modified sols when compared to the non-acid modified sols *i.e*. 15.7 nm non-acid modified *vs* 18.5 and 20.5 nm for H_2SO_4 and HCl modified samples. This increase in size is approximately 24 %. This could suggest the TiO_2 building blocks were more agile due to the possible formation of $TiOSO_4$ or $TiOCl_2$ stabilising the TiO_2 in solution facilitating the dissolution and re-precipitation of TiO_2 building blocks.

Hydrothermally treating at very high temperatures (270 °C) resulted in different TiO_2 morphologies being produced with respect to the acid used. The particles produced from the H_2SO_4 modified synthesis were mostly anatase phase (86.7 %). More astonishingly, the crystallites were very large, over 125 nm as determined PXRD. The crystallites showed a lozenge shape morphology commonly seen with HF modified TiO_2.[29,35,93] The lozenge shape observed *via* SEM suggests that the exposure of the {001} facet has been enhanced due to F^- ions binding to the crystal facet inhibiting growth in the [001] direction.[28,29] However, when HCl was used instead of H_2SO_4, the morphology produced was very different. The crystallites were phase pure rutile, yet, like the H_2SO_4 modified TiO_2, the crystallites were very large, *i.e.* 87 nm as determined by PXRD. The reasons for the different morphologies produced between the H_2SO_4 and HCl modified TiO_2 is not yet fully understood. However, as with the lower temperature experiments, the phase difference is probably due to phase stabilising by the acid.[82,91,92] Therefore, the HCl allowed the formation of rutile phase whereas the H_2SO_4 prevented the conversion of anatase to rutile. The dramatic change in the morphology observed with the H_2SO_4/NH_4F could be due to the *in-situ* formation of HF as per *Equation 4.2*. Note: Commercially, NaF and concentrated H_2SO_4 are used to synthesise HF. However, this would not explain why at 220 °C there appeared to be no HF affect as per the literature, whereas, at 270 °C the particles looked near identical to those synthesised by Wang *et al.*[29] using HF. Conversely, it is reported that the lozenge shape crystallites are produced due to the stabilisation of the {001} facet due to F^- ions binding to the facet, not the binding of HF to the {001} facet. Therefore, as HF is a weak acid, the presence of mineral acids should shift the equilibrium to the reagents (*Equation 4.2* (2)), reducing the F^- concentration present in the solution. Within the autoclave, the decomposition of H_2SO_4 was observed. Perhaps the decomposition of the H_2SO_4 resulted in a secondary reaction taking place with the NH_4F resulting in the *in-situ* formation of HF. Unfortunately, no further experimentation was carried out using high temperatures and H_2SO_4 as it was inherently unsafe to have acid decomposing in a stainless-steel autoclave at over 200 bar steam pressure.

$$H_2SO_4 + NH_4F \rightarrow (NH_4)_2SO_4 + HF \qquad (1)$$

$$HF + H_2O \rightarrow H^+ + F^- \qquad (2)$$

Equation 4.2. H_2SO_4 NH_4F equilibrium.

4.1.5 The Blue Coloured TiO_2 Produced

The modification of oxalic acid sols with NH_4F had resulted in changes in phase, crystal shape and size of the TiO_2 produced. However, the most interesting effect of the NH_4F, when compared to the non-modified oxalic acid sols, was that the TiO_2 produced was blue! All samples produced, bar the low-temperature samples, were a light to dark blue colour depending on the conditions used.

To study how the blue colour had affected the bandgap and the spectral properties of the TiO_2 produced, ultraviolet-visible - diffuse reflectance spectroscopy (UV-VIS DRS) was used to spectrally characterise a series of the blue TiO_2 modified with varying NH_4F equivalencies (hydrothermally treated at 270 °C for 24 hours). UV-VIS DRS results shown in *Figure 4.19* below, revealed all the TiO_2 produced had a shifted absorption edge compared to the anatase standard, but only NH_4F modified TiO_2 absorbed a proportion of visible wavelengths. The visible light absorption grew stronger as the wavelengths lengthened extending towards the infrared (IR) region. This absorption of red light produced the blue colour observed. It should be noted that the TiO_2 synthesised with no NH_4F added to the synthesis was white, yet, the absorption shoulder remained shifted. As NH_4F was introduced into the synthesis, the TiO_2 absorbed more red light deepening the blue colour observed. It appeared that the TiO_2 modified with 0.5 equivalents NH_4F absorbed the most red-light and therefore was the bluest. TiO_2 modified with 0.25 and 1 NH_4F equivalent absorbed roughly the same amount of red light, however, at approximately 450 nm the 1 equivalent NH_4F modified TiO_2 absorbed less light. The shifted absorption edge and hence band gap is due to the phase of TiO_2 produced. As there was a mixture of anatase and rutile, samples with more rutile showed a red-shifted absorption edge relative to the pure Aldrich anatase (the reference sample). This is because rutile has a smaller band gap compared to anatase, 3.0 eV *vs* 3.2 eV respectively and a high absorption extinction coefficient.[6] However, the phase change does not explain the red-light absorption.

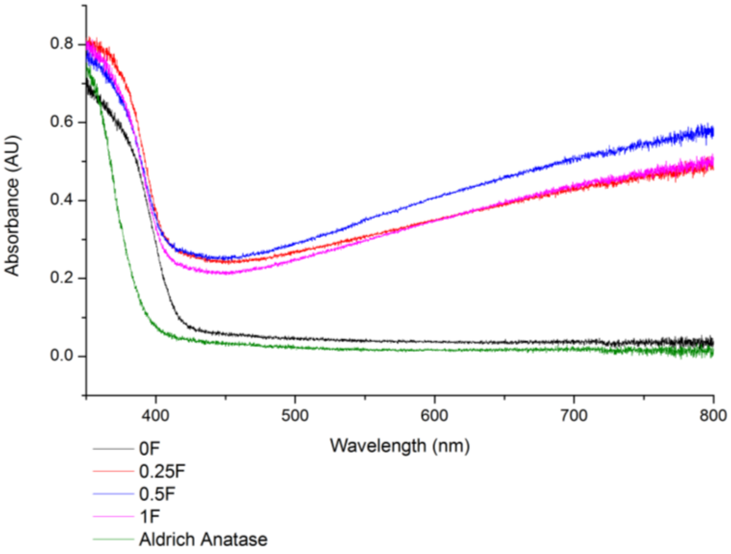

Figure 4.19 UV-Vis DRS results showing a shift in the bandgap and red light absorption of samples synthesised with 0, 0.25, 0.5 and one equivalent of NH_4F.

Blue TiO_2 has previously been synthesised by other groups where reducing conditions have been used to produce Ti^{3+} defects.[48] In literature reported syntheses, reducing conditions were induced by adding reducing gases or reducing agents.[53,95] Conversely, in the synthesis reported here, no reducing agents were deliberately added. Previously reported above in *Section 4.1.1*, it was noticed the oxalic acid decomposes at the high temperatures used for the hydrothermal synthesis.[77] Gas is released from the autoclave when it is first opened after a high-temperature hydrothermal treatment. It was suspected that the decomposition of oxalic acid could be responsible for inducing the reducing conditions necessary to reduce Ti^{4+} to Ti^{3+} and hence produce the blue TiO_2.[53,95]

To investigate what could potentially be causing the reducing conditions, mass spectrometry (MS) was used to analyse the gases released from the hydrothermal synthesis. Looking at the mass spectrum below in *Figure 4.20* (which has had the mass spectrum of air subtracted), it can be seen that there are many decomposition products present. First, there is more CO_2 present than in air, this confirms what had been suspected earlier in *Section 4.1.1*, that the oxalic acid decomposes to form CO_2 and water.[77] Secondly, there are traces of organic decomposition compounds with masses ranging from 40 and 45 $gmol^{-1}$. These peaks also appear lower in the spectrum as doubly charged masses. Lastly and most importantly, the presence of hydrogen was detected. H_2 is a well-known reducing agent that has been used to synthesise blue TiO_2 before.[95]

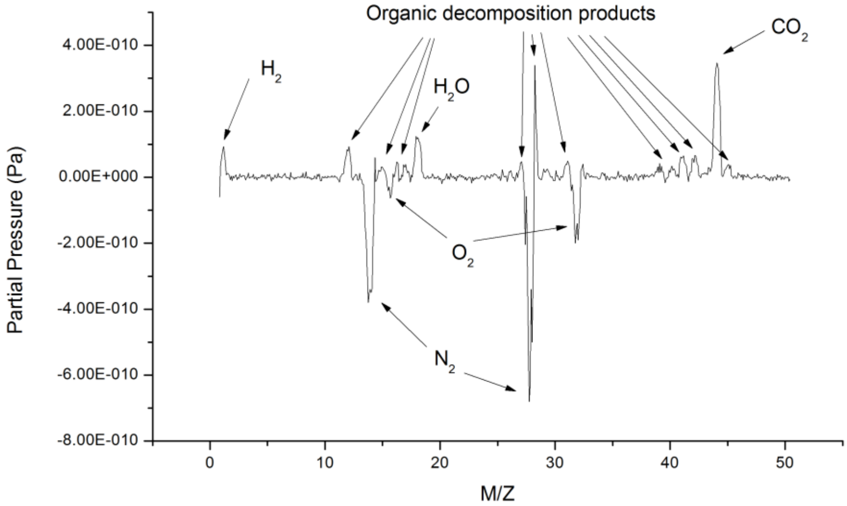

Figure 4.20 Mass spectrometry results of gas released from autoclave after hydrothermal synthesis. Note: The mass spectrum of air has been subtracted from the spectrum released from the autoclave above to make decomposition components more obvious.

Above it was observed that the blue TiO_2 shows a shifted absorption band and an absorption tail extending through the visible light region into the IR region. The initial shift in the absorption edge can be explained by the phases produced. Rutile phase TiO_2 has a smaller bandgap *ca.* 3.0 eV than anatase phase TiO_2 *ca.* 3.2 eV.[6] So the samples produced with 0 and 0.25 equivalents of NH_4F were rutile phase TiO_2, therefore, the band gap reduced and hence absorption shoulder shifted to longer wavelengths. However, the other sample synthesised with 0.5 and 1 equivalents of NH_4F were >80 % anatase phase. Though, due to the high extinction coefficient of rutile, even though the sample is only 20 % rutile, the band gap of rutile is observed.

However, the phase change does not explain the absorption of red-light. Blue TiO_2 has previously been synthesised by other groups where reducing conditions have been used to produce Ti^{3+} defects.[48] In other papers, reducing conditions were induced by adding reducing gases or reducing agents.[53,95] In the synthesis reported here, no reducing agents were added deliberately, but as seen above in *Figure 4.20*, hydrogen was produced as a decomposition product of either the oxalic acid or the isopropanol/ethanol mixture present in the sols.

It is proposed that the elevated temperatures thermally decompose the organic components (ethanol, propanol and oxalic acid) to produce hydrogen and other products. At the high temperatures and high pressures inside the autoclave, the hydrogen reduces some Ti^{4+} to Ti^{3+} which is incorporated into the growing crystallites turning the TiO_2 blue. Conversely, hydrogen was also detected in the synthesis of non-NH_4F modified TiO_2, yet blue TiO_2 was not formed. It is suspect that the presence of the F^- ion is necessary to either assist in the formation or stabilise the Ti^{3+} defect; possibly by occupying a vacant oxygen site, thus maintaining charge neutrality. This is a particularly interesting phenomenon; however, a mixed phase system is not ideal for studying the nature of the defect causing the blue colour, particularly since the blending of phases can mask changes in the band gap *etc*. Therefore, another synthesis route needed to be developed (see *Section 4.16* below) to study the defect in a phase pure product.

4.1.6 The Development of the Sol-Less Hydrothermal Synthesis of Phase Pure TiO_2

In order to characterise and study the defect that could be causing the blue colouration to the TiO_2 produced by the hydrothermal treatment of NH_4F modified oxalic acid sols (Chapter 4), it became evident that it was necessary to develop a synthesis that produced a phase pure product using similar processing conditions. The following explores and validates the synthesis of TiO_2 using the sol-less method.

The hydrothermal treatment (270 °C for 24 hours) of titanium isopropoxide (TTIP) in water modified with NH_4F, produced a blue TiO_2 that was phase pure anatase. It can be seen below in *Figure 4.21* that PXRD results showed when TTIP was hydrothermally treated in the presence of NH_4F (0-1 equivalents), a phase pure anatase or very nearly phase pure anatase (>98%) was produced (unlike the equivalent modified oxalic acid sol series, see *Figure 4.9*). Interestingly, it can also be seen that the crystallite size (calculated using PXRD) decreased with increasing NH_4F content (*Figure 4.21*), thus showing crystallite growth was suppressed by the addition of NH_4F (the same effect was seen in the hydrothermal treatment of NH_4F modified OX sols above, see *Figure 4.12*). The anatase phase crystallites grew larger in an NH_4F free environment when compared to modified oxalic acid sols *i.e. ca.* 67 nm for unmodified sol-less anatase *vs ca.* 30 nm for TiO_2 0.25ox 0.3F. This is because there was no phase change to rutile to consume available building material and no F^- to suppress growth. Once NH_4F was present in the synthesis, crystallite sizes were similar to those measured in the NH_4F modified OX sols *i.e. ca.* 22 nm sol-less synthesis at 0.5 equivalent NH_4F (270 °C, 24 hours) *vs ca.* 27 nm for TiO_2 0.25ox 0.5F. Thus, the sol-less synthesis produces a product with properties (based on PXRD) similar to NH_4F-modified OX sols when hydrothermally treated using the same process conditions. Furthermore, the phase pure anatase produced was blue (see Chapter 5).

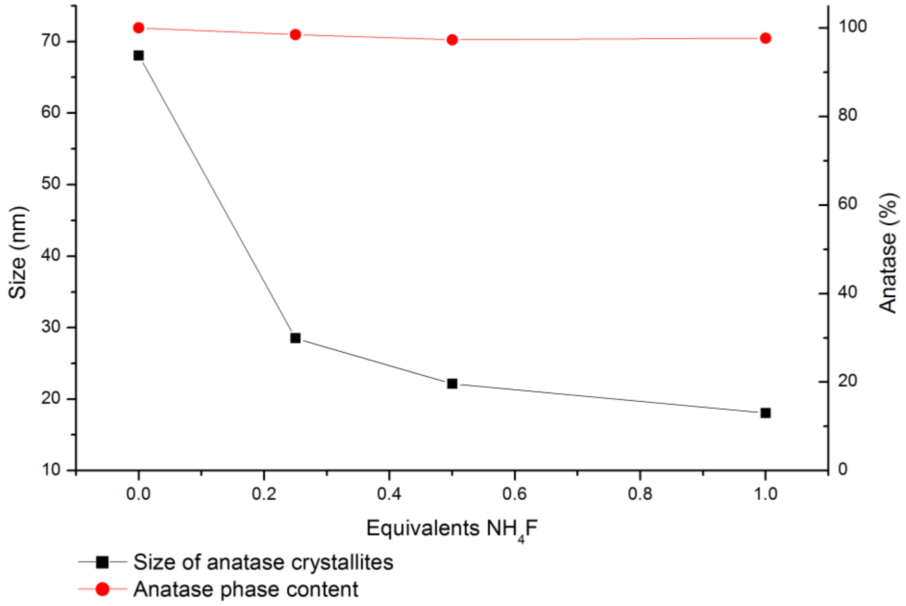

Figure 4.21 Anatase phase composition and size of crystallites as determined by PXRD for TiO_2 *synthesised using the sol-less method modified with 0 to 1 equivalents* NH_4F*. Samples were hydrothermally treated at 270 °C for 24 hours. Note: Lines have been added to guide the eyes and not link to results.*

For contrast, OX was added as a modifying agent into the sol-less synthesis. The mixture was hydrothermally treated at 220 °C for 24 hours. A white TiO_2 product was obtained and this was analysed by PXRD to reveal the addition of OX caused rutile to become the dominant phase, see *Figure 4.22*. Fascinatingly, peak rutile phase dominance within the conditions tested was at 0.25 equivalents oxalic acid. At 0.5 equivalents oxalic acid, the anatase phase content had increased slightly. This could be evidence towards the findings in *Section 4.1.2*, where high-pressure CO_2 incorporation leads to a reverse phase transformation of rutile to anatase. In contrast to what was seen with the anatase above in *Figure 4.21*, the rutile phase crystallites produced tended to be smaller in the sol-less synthesis *ca*. 28 nm for the sol-less synthesis *vs* 33 nm for a modified OX sol, processed using the same OX concentration and hydrothermal conditions. Increasing the oxalic acid content to 0.5 equivalents appeared to favour the formation of larger rutile crystallites *i.e*. *ca*. 33 nm. The same effect was observed when hydrothermal treating OX sols at 0.5 equivalents OX above in *Figure 4.6*. As the reverse phase transformation was more prevalent, consuming TiO_2 building material.

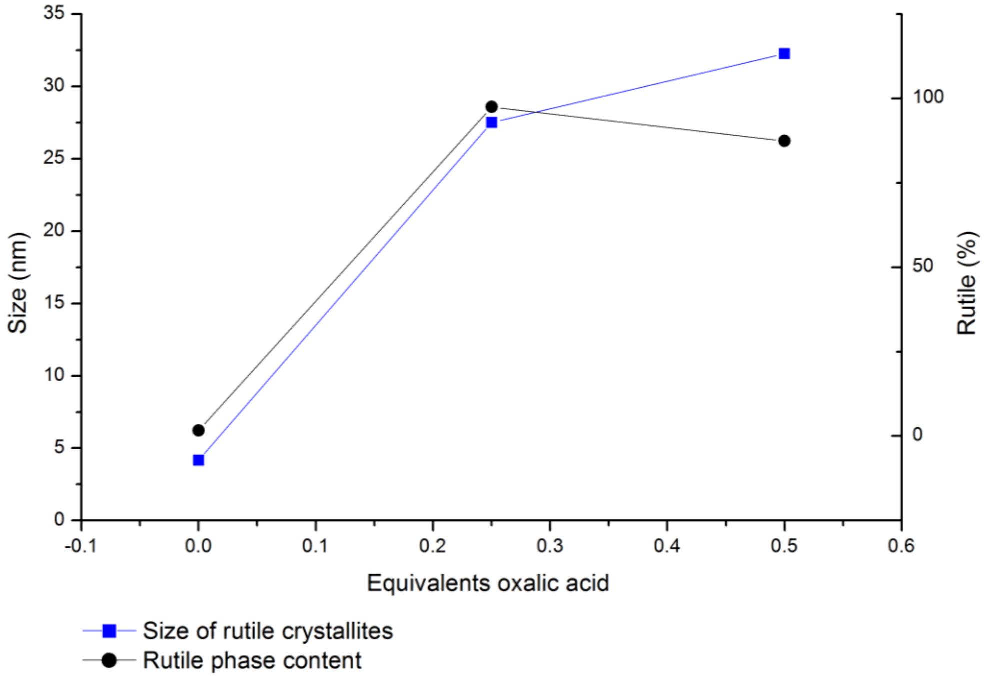

Figure 4.22 Rutile phase composition and size of crystallites as determined by PXRD for TiO_2 *synthesised using the sol-less method modified with 0 to 0.5 equivalents oxalic acid. Samples were hydrothermally treated at 220 °C for 24 hours. Note: Lines have been added to guide the eyes and not link to results.*

To check the morphology was consistent between the sol-less synthesis and the oxalic acid sol synthesis, SEM was used to observe the shape and size of crystallites produced from the sol-less synthesis. It can be seen below in *Figure 4.23*, the particles produced from an unmodified sol-less synthesis are relatively small and show no discernible shape. Likewise, when NH_4F is added the particles are very small and show no discernible shape. Yet, if 0.25 equivalents OX (with respect to the Ti) is added, the particles produced are rod-like with a high aspect ratio. This shows that the general shape and size of the particles is fairly consistent with those that were produced using the OX sols as a Ti precursor.

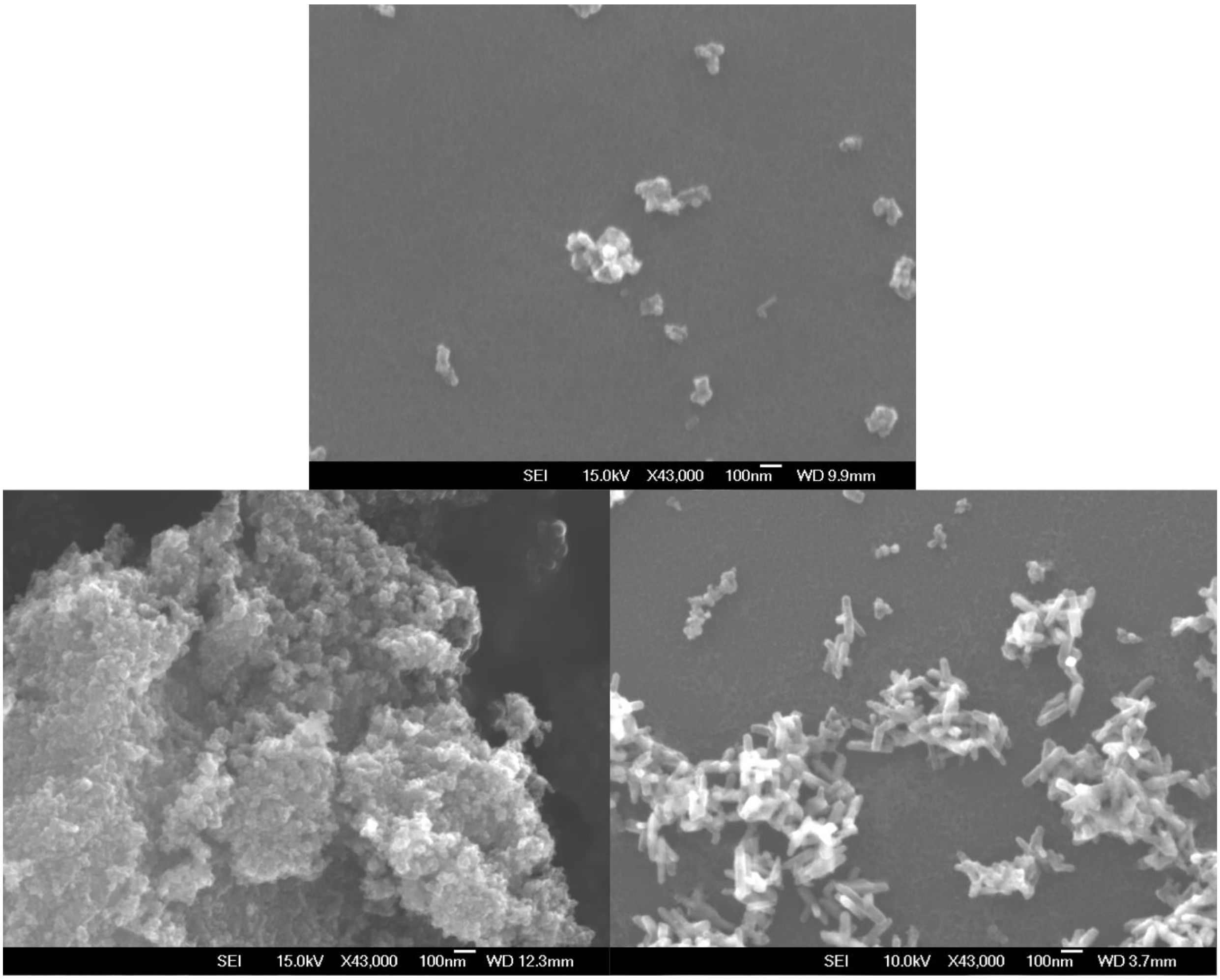

Figure 4.23 SEM images. Top: Sol-less unmodified. Bottom left: Sol-less modified with NH_4F*. Bottom right: Sol-less modified with 0.25 oxalic acid.*

The sol-less synthesis appeared to produce phase pure anatase even in the presence of NH_4F. Also, the synthesis could be manipulated by the addition of OX to produce near phase pure rutile. In general, the shape, size and general morphology of particles produced followed the same trends as OX modified sols. This suppression of growth at high equivalencies of NH_4F was also observed. The only slight difference that was noted, was that in general, the particles were larger in the sol-less synthesis when compared to an oxalic acid sol. This could be due to the number of nucleation sites generated with the addition of the TTIP to the water. This was done with a pipette in an uncontrolled manner. It is known when neutralising $TiOCl_2$ solutions to produce nuclei for the sulphate process, the addition time (drop time) and the D50 mixing time of the vessel, ultimately controls the number of nucleation sites and the phase of the nuclei.[96] This could lead to different crystallite sizes being produced during the hydrothermal treatment as the particles grow through an “Ostwald’s ripening” type process.[87] Nevertheless, it is believed that the sol-less synthesis could be used to study the formation of the blue colouring defects without having a mixed phase system.

4.3 Conclusions:

In conclusion, TiO_2 sols were synthesised using oxalic acid as a passivating agent. Characterisation of the sols by PXRD and DLS showed that the phase composition and aggregate sizes were highly dependent on the ratio of oxalic acid to TiO_2 used in the synthesis. The product produced by hydrothermally treating these sols also showed a high dependence the oxalic acid to TiO_2 ratio. At 0.25 equivalents of oxalic acid, the TiO_2 produced abruptly changed to rutile phase when hydrothermally treated at temperatures greater than 170 °C. The rutile crystallites grew into rod-shaped particles elongated along the [001] direction. At 0.5 equivalents oxalic acid, the TiO_2 produced at low temperatures was rutile phase. However, at higher temperatures (>170 °C), the decomposition of oxalic acid to CO_2, in combination with the high pressures of the autoclave, led to a reverse phase change of rutile to anatase. Although no conclusive mechanism was identified.

NH_4F (0-1 equivalent with respect to Ti) was added to TiO_2 0.25ox sols as a modifying agent. These were hydrothermally treated at processing temperatures ranging from 170 and 270 °C for 0-24 hours. It was clear that the NH_4F had an effect on the phase produced. Where at 0.25 equivalents NH_4F and below, phase pure rutile was produced. Conversely, any ratio of 0.3 equivalents NH_4F or above, a mixture of anatase and rutile was produced. The NH_4F also affected the size of crystallites produced. At low concentrations, the growth of rutile crystallites was enhanced whereas, at higher concentrations, the growth of both anatase and rutile crystallites was suppressed. The NH_4F changed the shape of the rutile produced from elongated rods to bi-pyramidal crystals exposing a greater percentage of the {101} facet. The shape of anatase crystallites seemed unaffected by the addition of NH_4F.

It was found that lowering the pH with mineral acids (H_2SO_4 and HCl) had an impact on the phase and morphology of crystals produced. However, it became evident that pH alone is not responsible for controlling the phase. What became apparent, is that lowering the pH results in larger crystallites being produced (given the same conditions as the non-acid modified system). This is thought to be due to the *in-situ* formation of $TiOSO_4$ or $TiOCl_2$ increasing the mobility of TiO_2 building material. It was also clear that the choice of acid had an impact on the phase produced. H_2SO_4 preferentially favoured the formation of anatase whereas HCl could precipitate both anatase and rutile depending on the temperature of hydrothermal treatment. Hydrothermally treating at 270 °C with acid-modified systems caused an abrupt change in morphology compared to when treated at 220 °C. The HCl modified sols precipitated very large rutile crystallites showing the same bi-pyramidal shape observed in the solely NH_4F-modified sols. On the other hand, H_2SO_4 appeared to thermally decompose resulting in the *in-situ* formation of HF. The HF resulted in the growth of large anatase crystallites exposing a higher percentage of the {001} facet.

It was proposed that at low concentrations of NH_4F, the rutile grew at the expense of anatase through a $TiOF_2$ mediated process. Whereas, at higher concentrations of NH_4F, the growth of rutile was suppressed due to surface coverage of F^-. It appeared the rutile crystallites initially present in the oxalic acid sol never disappeared, but their growth was suppressed.

Hydrothermally treating the sols in the presence of NH_4F produced blue TiO_2. UV-VIS DRS characterisation showed that the blue TiO_2 synthesised from NH_4F-modified oxalic acid sols absorbed red visible light making the TiO_2 appear blue. Also, it was found that the absorption shoulder (in a mixed phase system) shifted to that of rutile, due to the high extinction coefficient of rutile. MS of the gases released from the autoclaves after the hydrothermal treatment showed that the decomposition of the organic reagents present in the autoclave produced a small amount of H_2 gas. It is suspected that this H_2 gas reduces Ti^{4+} to Ti^{3+} and generated Ti^{3+}defects within the crystals causing the blue colour. It is also suspected that F^- ions are necessary to either assist in the reduction of Ti^{4+} or stabilise the Ti^{3+} produced as reducing conditions alone did not produce blue TiO_2.

Finally, TiO_2 was successfully hydrothermally synthesised without using OX sols as a precursor. Adding TIPP to water and hydrothermally treating the mixture, produced white or blue anatase depending on the conditions. Also, it was found that the addition of a small amount of OX shifted the phase composition of the product to rutile. SEM images and PXRD line profiles showed the particles produced using the sol-less synthesis had relatively consistent morphology when compared to the equivalent hydrothermal treatment of OX sols but the produce was phase pure. Finally, it was concluded that this method could be used to synthesise phase pure blue anatase and rutile TiO_2 ideal for studying the nature of the blue colouring defect.

Chapter 5 : Defect Characterisation in Blue Anatase

5.0 Introduction:

The formation of the blue coloured TiO_2 is a very interesting yet poorly understood phenomenon. The mixed phase blue TiO_2 synthesis of which using oxalic acid sols was discussed in Chapters 4, made for a difficult system to study as the mixture of phase would have obscured subtle changes in the band-gap and electronic features of the blue TiO_2. On the other hand, the sol-less method produced a phase-pure blue anatase that is ideal for studying. In the following chapter, blue phase-pure anatase was used as a model system to study the structural defects causing the blue colouration.

Blue and black TiO_2 has been reported by many groups in the literature.[46] There have been many synthetic methods developed for synthesising blue or black TiO_2 reported.[46] However, each method appears to produce a slightly different "blue TiO_2". Also, the characterisation methods and conclusions that are drawn vary from paper to paper.[46] The following introduction summarises some of the characterisation methods used and the reported structural defects believed to cause the blue colouration.

5.1.1 Ultraviolet-visible light diffuse reflectance spectroscopy

Ultraviolet-visible light diffuse reflectance spectroscopy (UV-VIS DRS) is a useful tool for studying coloured TiO_2. UV-VIS DRS can be used to measure changes in the band gap of TiO_2 using Tauc plots. Also, absorption of visible light can be used to estimate the energy of any other transitions possible due to defects or dopants. Many research groups who have reported synthesising blue or black TiO_2, yet, there is little constancy among the UV-Vis spectra reported.[4655,9797,98] For a start, often blue/black TiO_2 synthesised is a mixture of phases, mainly anatase and rutile.[55,99] Secondly, depending on the synthetic conditions used, the coloured TiO_2 does not always show an altered absorption edge.[51,98] Lastly, some blue coloured TiO_2 samples show increased absorption throughout the visible range, whereas others only show increased absorption of the red and infrared light.[97,98]

5.1.2 Electron Paramagnetic Properties of the Blue TiO_2

Countless reports in the literature on blue, black and doped TiO_2 use electron paramagnetic resonance (EPR) and to a lesser extent, superconducting quantum interference devices (SQUID), to prove the existence of either surface or bulk Ti^{3+} defects.[47,51,100-102] SQUID and EPR measure the magnetic properties of the unpaired electrons. In EPR, the exact position of the peak indicates whether the unpaired electron belonging to the Ti^{3+} is surface or bulk *i.e.* $g = 1.96$ for bulk and $g = 2.02$ surface Ti^{3+}.[53,97,103] However, the exact position and profile of the Ti^{3+} signals vary greatly between blue, black and white TiO_2 synthesised using different methods.[100] Both SQUID and EPR can identify paramagnetic behaviour and how it changes with temperature.[47,101] Both SQUID and EPR can also quantify Ti^{3+}, but EPR requires an internal standard, whereas SQUID measurements can approximate the number of defects using the Brillouin Function and the Bohr magneton.[104-106] Finally, SQUID can be used to determine if there is any ferromagnetic behaviour.[102]

Czoska *et al.*[47] used EPR to study the nature of the (F^- - Ti^{3+}) defect. This is by far is the most detailed EPR study of Ti^{3+} in F^- doped TiO_2. Czoska *et al.*[47] first showed that TiO_2 reduced in an oxygen deficient environment produced a broad peak in EPR spectrum, and that obtained material would react instantly upon contact with air producing superoxide radicals as evidenced by characteristic EPR signature, see *Figure 5.1* left. Secondly, Czoska showed that F^- doped TiO_2 shows a sharp peak at $g = 1.99$ and $g = 1.96$ *Figure 5.1* right (a). Lastly, the authors showed that surface F^- does not result in paramagnetic centres, see *Figure 5.1* right (b).

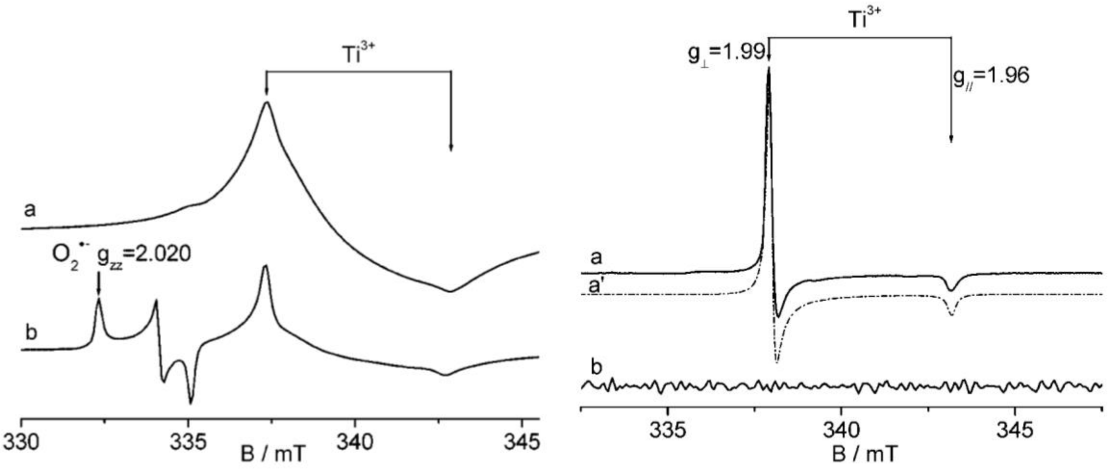

Figure 5.1 Left: Shows (a) annealed TiO_2 and (b) annealed TiO_2 after exposure to air at room temperature. Right: (a) F-doped TiO_2, (a') theoretical spectrum of F^- doped TiO_2 and (b) TiO_2 with only surface F^-. Reproduced from Czoska *et al.*[47]

Furthermore, Czoska *et al.*[47] used modelling to understand the EPR results. By looking at the coupling of electrons in the EPR spectrum and XPS results, it was concluded that a Ti-F-Ti bond was formed. The F^- substitutes for an oxygen forming a Ti-F-Ti bond and the extra electron is located on the adjacent Ti^{4+} reducing it to Ti^{3+}, see *Figure 5.2*. The resulting TiO_2 has the formula $Ti^{4+}_{(1-x)}Ti^{3+}_{x}O^{2-}_{(2-x)}F^{-}_{x}$. Interestingly, the F^- doped TiO_2 showed no changes in its UV-DR spectrum. Yet, the theoretical modelling suggested that the defect would introduce a state 0.6 eV above the edge of the valence band. This would result in the absorption of infrared light.[47] Lastly, Czoska *et al.*[47] determined the number of unpaired electrons to be 10^{17} spins/g. If it is assumed that each unpaired electron is located on a Ti^{3+} defect, then it is calculated that the concentration of Ti^{3+} is 0.008 atomic % with respect to Ti^{4+}.

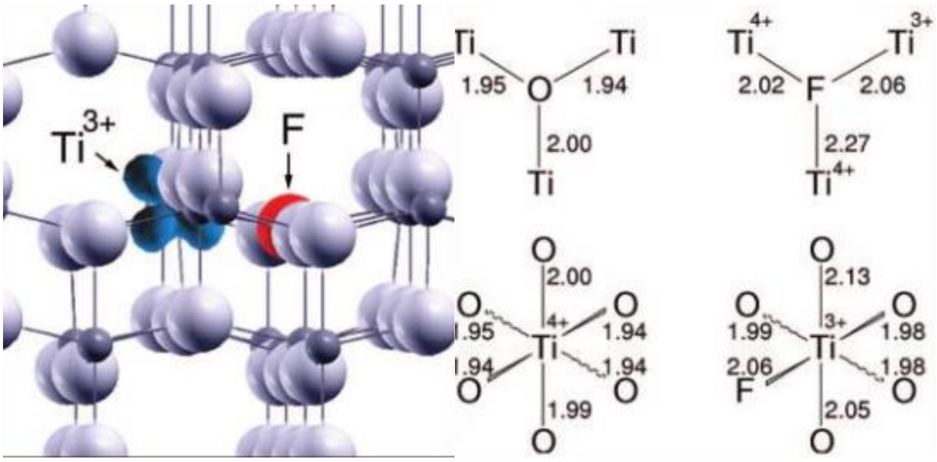

Figure 5.2. A model of the Ti^{3+} F^{-} defect proposed by Czoska et al.[47] *after in-depth EPR study.*

SQUID has been used to study both oxygen and titanium vacancies.[101,102] Zhou *et al.*[101] showed that bombarding a single crystal of rutile with 2 MeV oxygen molecules can generate oxygen vacancies in the crystal. Zhou *et al.*[101] also showed with SQUID, that the Ti^{3+} can be detected at low temperatures as there is a transition from diamagnetic behaviour to paramagnetic behaviour, due to the localisation of electrons. Interestingly, Zhou *et al.*[101] found that the number of defects increased with increasing bombardment to a critical point, then suddenly, the number of defects began to decrease with continued bombardment, see *Figure 5.3*. This effect was explained by the number of defects increasing to a critical point where it became energetically favourable to rearrange into a different crystal structure rather than maintaining the defects. Zhou *et al.*[101] and Wang *et al.*[102] both deliberately synthesised TiO_2 crystals containing defects; both reported hysteresis in the magnetic profile of their as-synthesised TiO_2, see *Figure 5.3*. The hysteresis indicates ferromagnetism. Wang *et al.*[102] explained the ferromagnetism as due to the formation of Ti vacancies, whereas, Zhou *et al.*[101] did not believe they had any titanium vacancies.

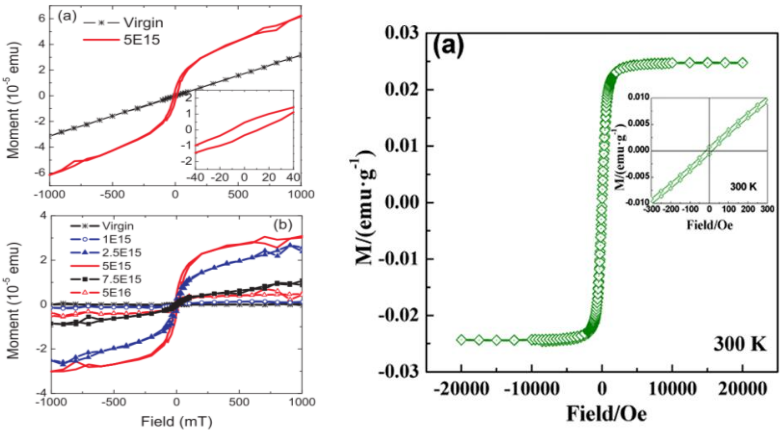

Figure 5.3 SQUID results of a single rutile crystal that has been reduced using ion bombardment, reproduced from Zhou et al.[101]

5.1.3 Raman Spectroscopy Study of Blue TiO_2

Raman spectroscopy examines the vibrational modes of chemical bonds.[107] Several previous reports have used Raman spectroscopy to identify features of TiO_2, particularly doped TiO_2 and blue/black TiO_2. Raman spectroscopy looks at the inelastic scattering of photons from vibrational states. Raman spectroscopy's selection rules are the opposite of infrared spectroscopy, thus making modes that are hardly visible in infrared spectroscopy particularly intense in Raman spectroscopy. Raman spectroscopy can identify: phase, shape, quantify disorder and predict the size of inorganic crystallites with Raman active vibrational modes.[107-109] Since so many elements of morphology can change the observed Raman spectrum, it is important to understand how factors such as size and shape can influence the Raman spectrum when trying to pinpoint the features of the spectrum which originate due to the presence of the electronic defects. The following summarises some of these influences:

- Previous studies have reported that pure anatase phase TiO_2 shows 6 active vibration modes with are observed as peaks in the Raman spectrum located at: 144 cm^{-1} E_g, 197 cm^{-1} E_g, 399 cm^{-1} B_{1g}, 513 cm^{-1} A_{1g}, 519 cm^{-1} B_{1g}, and 639 cm^{-1} E_g, see *Figure 5.4*.[108] When interpreting TiO_2 spectra, it should be noted that the second B_{1g} peak and A_{1g} peaks overlap. However, the majority of the intensity at 513 cm^{-1} is attributed to the A_{1g} mode.[108]
- The intensity, FHWM and position of peaks are sensitive to the size of the crystallites. In a study by Choi *et al.*[108], the authors showed that the peaks in the spectrum of anatase experience a blue shift as the crystallites become smaller. The peaks also broaden as the crystallites become smaller, see *Figure 5.4*. Such shifts and broadening of peaks is due to the confinement of the phonon. As the particle's size decreases below 20 nm the phonon experiences confinement due to the Heisenberg uncertainty principle. This results in the phonon's momentum distribution

increasing as its position becomes confined. This distribution of momentum results in asymmetric peak broadening, shifting the centre of the peak.[108]

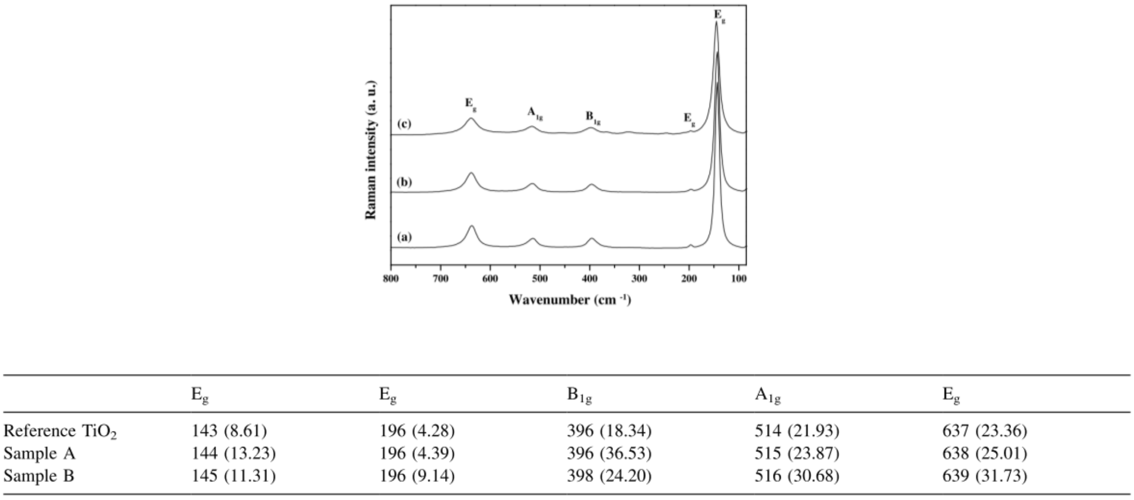

	E_g	E_g	B_{1g}	A_{1g}	E_g
Reference TiO_2	143 (8.61)	196 (4.28)	396 (18.34)	514 (21.93)	637 (23.36)
Sample A	144 (13.23)	196 (4.39)	396 (36.53)	515 (23.87)	638 (25.01)
Sample B	145 (11.31)	196 (9.14)	398 (24.20)	516 (30.68)	639 (31.73)

Figure 5.4 Top: Raman spectra of TiO_2 samples of different sizes. Bottom: Table of fitted modes. Reproduced from Choi et al.[108]

- The exposed facets of TiO_2 crystals also change the relative intensity of peaks corresponding to the Raman active modes; hence, the shape of crystallites can be estimated. Zhang *et al.*[109] showed that the intensity of the B_{1g}, A_{1g} and E_g peaks is influenced by the relative proportion of the exposed {001}, {111} and {101} facets, see *Figure 5.5*. This is due to the variation in relative ratios of Ti_{5c}, Ti_{6c}, O_{2c} and O_{3c} (where “c” donates the coordination number) present at the various facets.[109]

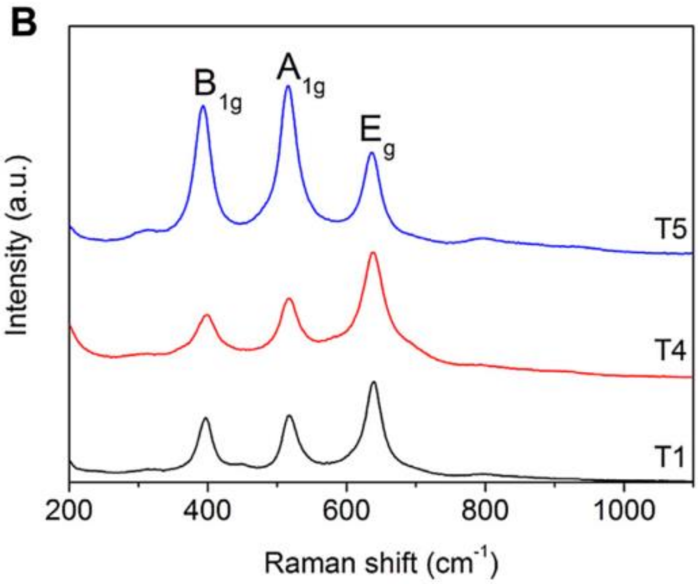

Figure 5.5 Raman spectra from Zhang et al.[109] *showing peak intensities as a function of the surface enrichment with the particular facets. Note: Sample T5 = 70 % {0 0 1}, T4 = 70 % {1 1 1} and T1 = 95 % {1 0 1}.*

Only once the aforementioned effects have been accounted for the Raman spectroscopy can be used to identify features of the spectrum that are related to the colour causing defects. Below are two examples of the changes in Raman spectra that have been observed in blue or black TiO_2 when compared with white TiO_2.

First, the broadening and blue shifts of Raman peaks are not only affected by the particle size but also disorder within its lattice. In a study by Naldoni *et al.*,[49] the authors reported black TiO_2 (with particles large enough such that size effects become insignificant) exhibiting blue-shifted and broadened peaks which was attributed to the increase in the disorder within the crystals with the formation of the larger numbers of defects, see *Figure 5.6*.[49]

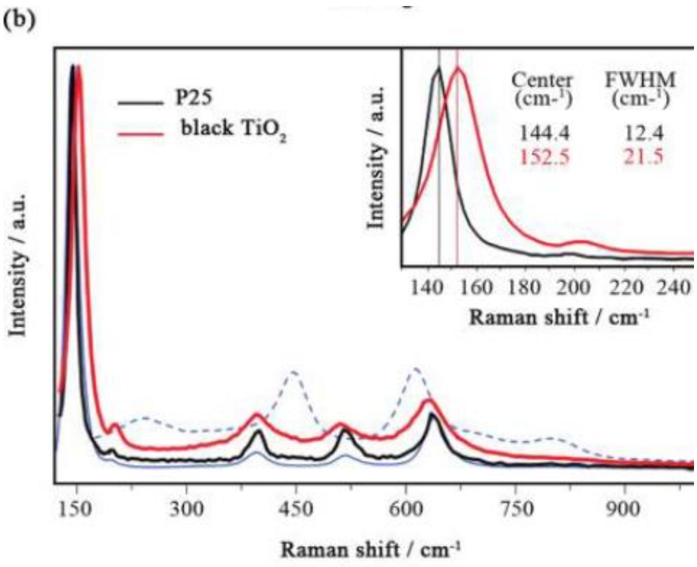

Figure 5.6 Raman spectra of white and black TiO_2 from Naldoni et al.[49]

Lastly, the relative peak intensity can be proportional to the number of atoms involved in the Raman mode motion. Studies by Wei *et al.*[95] of oxygen vacancies in F^- doped TiO_2 showed the reduced intensity of specific modes *i.e.* the A_{1g} and B_{1g} in pure anatase phase TiO_2 upon hydrogenation, see *Figure 5.7*. As the size and shape of the TiO_2 crystallites did not change significantly with the treatment, the shift in the E_g peak and changes in the relative intensities of the B_{1g} and A_{1g} modes, is due to the formation of oxygen vacancies, see *Figure 5.7*.

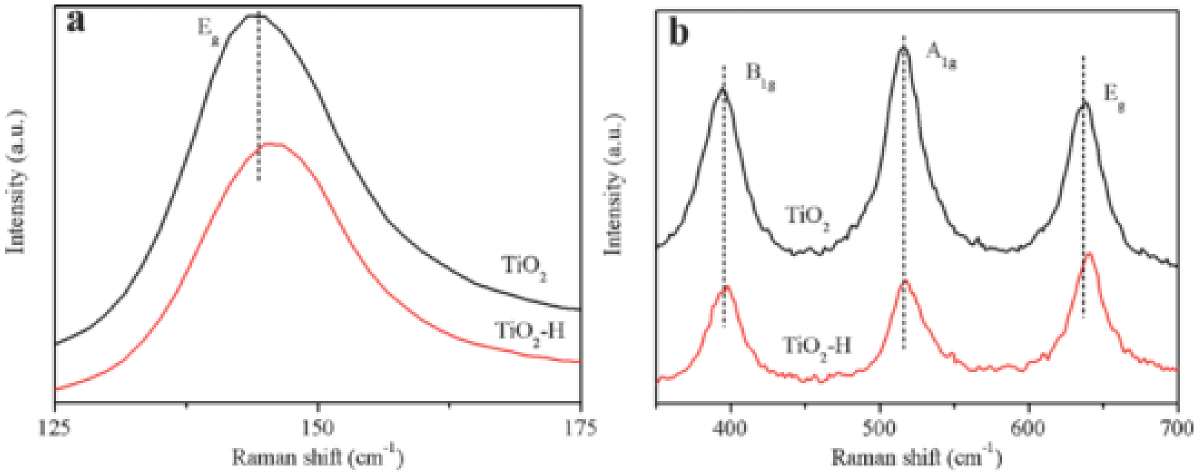

Figure 5.7 Raman spectra of F^- doped TiO_2 before and after reductive H_2 treatment from Wei et al.[95]

5.1.4 Synchrotron Powder X-ray Diffraction study of Blue TiO_2

Powder X-ray diffraction is a powerful tool for examining the phase, size, shape, stress and lattice features of crystallites. With the power, tunability and resolution of synchrotron radiation, it is possible to determine with an extremely high precision all features of nanocrystals using a Rietveld refinement of the PXRD pattern.[110]

In the past, PXRD has been extensively been used for the generic analysis TiO_2.[6] However, only a limited number of reports have used PXRD to pinpoint the signs of defects, particularly in blue or black TiO_2.[49,53,102,111,112] Below is a summary of some of the findings based on the PXRD studies reported for coloured TiO_2:

- Wang *et al.*[111] studied changes in the lattice parameters of the blue anatase. It was reported that the lattice of anatase phase TiO_2 contracted as the anatase became darker blue. The observation of the [101] diffraction peak shifting to higher angles indicated the lattice was contracting (although the shift was not quantified). The contractions were postulated to be due to the formation of oxygen vacancies, the oxygen vacancies reduced the Ti to Ti distance.
- Xing *et al.*[53] also used PXRD to study changes in the lattice of blue TiO_2. However, unlike Wang *et al.*[111], Xing found there were no changes in the lattice spacing with increasing Ti^{3+} doping (deepening colouration).
- Naldoni *et al.*[49] used synchrotron PXRD to study the structural defects of black TiO_2. The authors found that the lattice spacing contracted around 1 - 4 % with the introduction of oxygen vacancies. Also, it was reported that the occupancy of the O atoms in the lattice was only 0.95 indicating 5 % of the lattice oxygen sites were vacant.
- Xu *et al.*[112] studied the effects of lattice distortion and how it encouraged the formation of Ti^{3+} defects and enhanced photocatalytic activity. It was found that Cl^- ions added to the synthesis mixture resulted in the distorted lattice of the anatase formed, but did not dope the anatase. The distortion caused by the Cl^- shifted the [101] and [004] peak to lower angles (*i.e.* longer bond distances). Introducing Ti^{3+} defects by reduction alone (with ethyl glycol and with no previous distortion induced using Cl^- ions) also shifted the [101] and [004] peaks to lower angles but to a lesser extent than the Cl^-. Interestingly, it proved to be possible to reduce the already distorted crystals (Ti^{4+} to Ti^{3+} with ethyl glycol) to a greater extent (as shown by the Ti^{3+} detected using XPS) compared to undistorted crystals. Both the reduced and distorted crystals showed approximately a 0.5° shift of the [101] and [004] peaks to lower diffraction angles compared to the anatase control. Finally, the both distorted and reduced sample showed the greatest photocatalytic activity in the degradation of rhodamine B dye and phenol under visible light.

When studying lattice distortions caused by Ti^{3+} or oxygen vacancies, it is important to consider that there may also be Ti vacancies.[43,102,113] The presence of Ti vacancies also distorts the lattice. The following is an example of how one may expect the lattice to change in the case of Ti vacancies:

- Wang *et al.*[102] studied the changes in the lattice dimensions using DFT modelling and compared them to experimental results. They found the introduction of a titanium vacancy into a small TiO_2 particle with the formula $Ti_{15}O_{32}$, caused the (*a*) and (*b*) lattice dimensions to expand (lightly) and the (*c*) to heavily contract. On the other hand, they found the introduction of interstitial O, cause the *c* lattice dimension to expand.

5.1.5 Synchrotron Soft X-ray Study of Blue TiO_2

Synchrotron X-ray photoelectric spectroscopy (XPS) is an advanced technique that looks at the binding energy of inner core electrons. With high-resolution detectors and a variable incident X-ray energy source available at synchrotrons, it is possible to detect very small differences in chemical environments by looking at the shifts in the binding energy of core electrons. Secondly, with the tuneable incident X-ray energy source, it is possible to effectively depth profile the chemical environments from the surface of particles to the inner core.[114,115] This is achieved by changing the incident radiation energy, which in turn changes the mean-free-path of the photo-ejected electrons. The mean-free-path and its relationship to the incident ration energy for TiO_2 have been determined experimentally using reflection electron energy-loss spectroscopy, for TiO_2 the mean free path varies from *ca.* 0.46 nm at 250 eV to 2.8 nm at 2000 eV.[114]

Throughout the literature, XPS has been extensively used to study blue and black TiO_2.[49,51-53,98] There are several ways a soft X-ray beamline can be used to study the chemical environments within TiO_2 particles. First, survey scans give a quantitative atomic composition of the surface layer of TiO_2.[98] Secondly, high-resolution scans of the Ti2p, O1s and F1s core electron energy levels can reveal subtle differences in the chemical environments of each atom.[50,52,115] Thirdly, low energy X-rays can be used to study the band edge (valence band spectroscopy).[99,116,117] Finally, the absorption of X-rays can be used to study the fine structure of the bonding within a particle using a method called near-edge X-ray absorption spectroscopy (NEXAFS).[49,115,116] However, it must be noted that all the aforementioned techniques are only analysing the outer-shell of the particles. This is due to the maximum energy used to analyse the samples *ca.* 1486.7 eV and the approximate mean-free-path *ca.*2 nm, relative to the mean particle size *ca.* 20 nm.[114]

Throughout the literature, depending on the method of synthesis, a survey scan will reveal different chemicals present. With TiO_2 synthesised using any method, it is normal to detect Ti, O and C. However if F^- was used during the synthesis it will be detected in the survey scan unless the TiO_2 was washed with a base *e.g.* KOH.[115] Finally, the case of a reducing agent being used *e.g.* $NaBH_4$, these will also be detected on a survey scan.[53]

A high-resolution scan of the Ti2P region can reveal the oxidation state of the Ti atoms present in the TiO_2. In particular, researchers often look for the evidence of Ti^{3+} when studying blue or black TiO_2. Two different properties of the spectrum can indicate the presence of the Ti^{3+}. Firstly, as seen in *Figure 5.8* left, the Ti^{3+} can be observed as a shoulder at a lower binding energy on the Ti^{4+} peak (positioned at 458.7 eV). Typically, the Ti^{3+} shoulder is positioned at anywhere between 0.7 and 1.0 eV lower than the Ti^{4+} peak.[111] Secondly, evidence of Ti^{3+} also appears in the literature in the form of a shift of the Ti^{4+} peak, see *Figure 5.8* right.[53,55] Interestingly, the reporting of Ti^{3+} in blue TiO_2 and black TiO_2 is very irregular. Some researchers, such as Wang *et al.*[111], X. Liu *et al.*[51] and M. Xing *et al.*,[53] do not report the quantity of Ti^{3+} despite having an extremely well-defined shoulder on the Ti^{4+} peak. On the other hand, other researchers (for example, Naldoni *et al.*[49]) who have produced black TiO_2, clearly containing large amounts of Ti^{3+} (as evident by EPR), report that the XPS spectra of the Ti2P region show no evidence of Ti^{3+}.[49] On the other hand, researchers producing white TiO_2 have claimed Ti^{3+} exceeding 10 %.[118] The large variation in reported Ti^{3+} content is due to the presence of surface Ti^{3+}. Since XPS is more sensitive to the surface atoms than the bulk atoms, the results can be extremely skewered when trying to accurately quantify bulk Ti^{3+}.

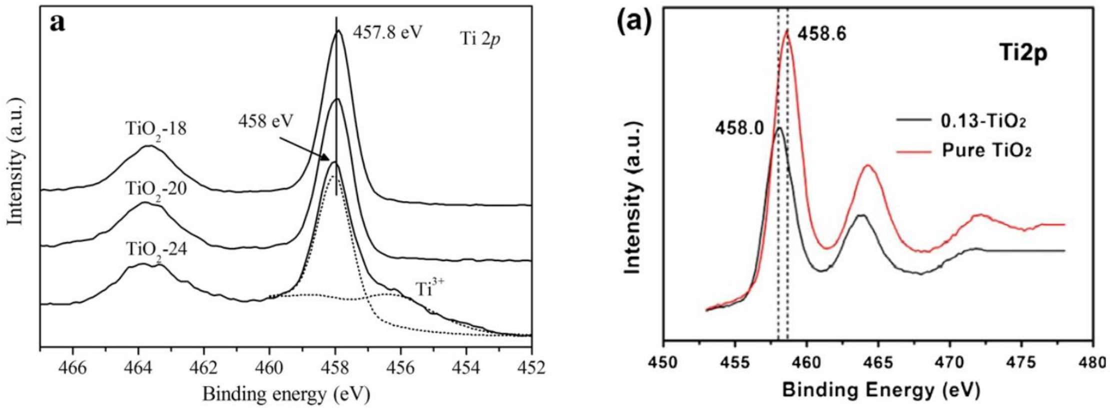

Figure 5.8 Left: XPS spectrum of the Ti2P peak of blue and white TiO_2 synthesised by W. Wang et al.[111] *Right: XPS spectrum of the Ti2P peak of blue and white TiO_2 synthesised by M. Xing et al.*[53]

The use of valance band spectroscopy in studying blue or black TiO_2 is uncommon. However, Naldoni *et al.*[49] used valence band spectroscopy to look at the density of states (DOS) of black TiO_2 and compared it to P-25. As can be seen in *Figure 5.9*, the black TiO_2 showed a significantly altered DOS. The onset of absorption was shifted to 0.6 eV compared to 1.23 eV for P-25. Secondly, the band tail shifted to -0.3 eV. This shift was attributed to the surface hydrogenation of the black TiO_2. The observed shift would narrow the band gap to 1.85 eV assuming the conduction band did not move. This would result in absorption of NIR light and indeed the black TiO_2 was shown to absorb NIR light *via* UV-VIS DRS.

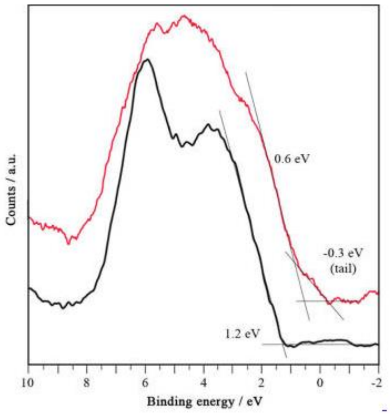

Figure 5.9 Valance band spectra of white (black line) and black TiO_2 (red line) showing the changes in the DOS introduced by hydrogen reduction. Reproduced from Naldoni et al.[49]

NEXAFS is quite an uncommon characterisation technique due to strict pre-requisite of access to synchrotron light source, yet it allows a qualitative interpretation of electronic states. However, it has also been used in the characterisation of blue and black TiO_2. Naldoni *et al.*[49] used electron energy loss near-edge structure (EELS) (a technique that looks at the same transitions as NEXAF) to study black TiO_2. Naldoni *et al.*[49] observed there was a 20 % decrease in the L_2 splitting, see *Figure 5.10*. This was attributed to the presence of Ti^{3+} defects.

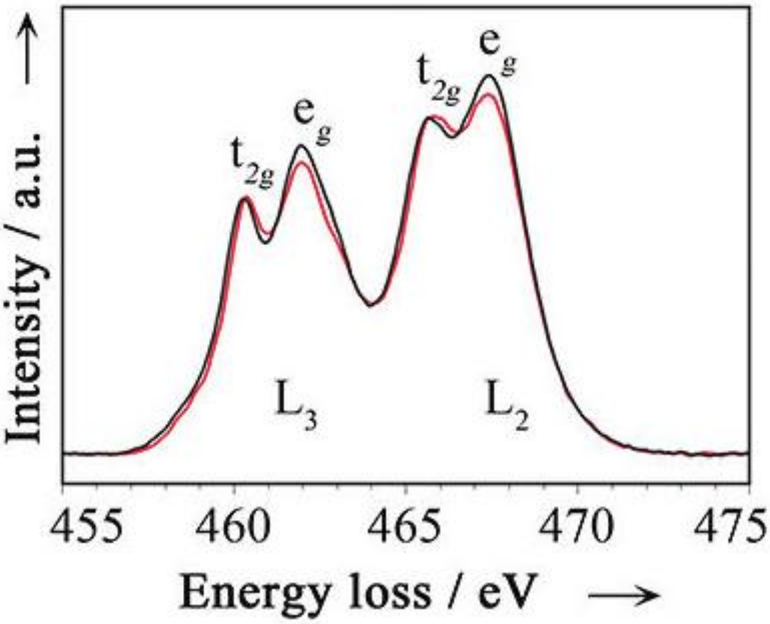

Figure 5.10 The EELS (similar to NEXAFS) spectrum of white (black line) vs black (red line) TiO_2. reproduced from Naldoni et al.[49]

5.1.6 Electron Microscopy Study of Blue TiO_2

In the study of blue TiO_2 and the defects associated with the blue colour, electron microscopy (SEM, TEM and HRTEM) have been used to look at the size, shape, type of the exposed facets and the surface disorder of the coloured nanoparticles. Of cause, besides the fact that the TiO_2 is blue, the shape, size and exposed facets also have an impact on the bandgap, photocatalytic activity, surface chemistry and electronic structure of the TiO_2. Thus, it is important to understand the crystals' morphology. Several theories and the work of other groups are summarized in the following section:

- In many cases, the size of crystallites observed in SEM and TEM disagrees with the size determined using PXRD line broadening. Abu Bakar *et al.*[119] is just one example of how PXRD can disagree with SEM observations. Particles in *Figure 5.11* left look like rice grains of approximately 100 nm x 30 nm wide. However, these rice grains were reported to be only 20 x 30 nm when analysed by PXRD, see *Figure 5.11* right. These findings can be explained by looking at what each method measures exactly. The PXRD gives *an estimate* of the crystalline domain sizes while SEM and low magnification TEM provide means of *direct imaging of the overall shape* of the entire particle. Therefore, many small crystalline domains within a larger particle can be crystallographically aligned but their lattices are slightly offset from one another. Using PXRD, these particles are detected as multiple small crystalline domains rather than one large crystalline particle. Whereas SEM is taking a relatively low-resolution image of the electrons interacting within a pocket near (the interaction volume is proportional to the accelerating voltage) the surface of the particle, observing the small aggregated crystals as on large particle.[120] The grains themselves can be aligned so closely that even with TEM you will not necessarily see the individual crystallites making up the larger particles.

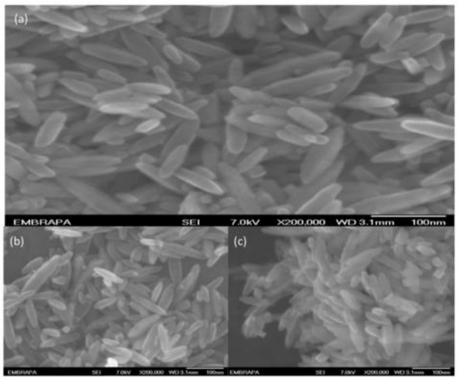

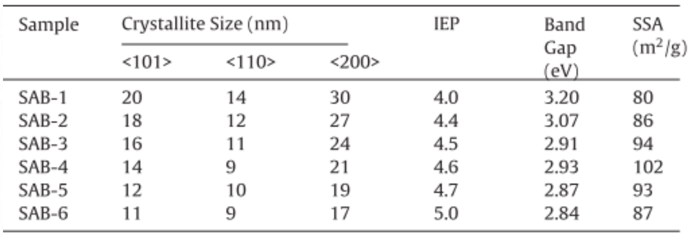

Sample	Crystallite Size (nm)			IEP	Band Gap (eV)	SSA (m^2/g)
	<101>	<110>	<200>			
SAB-1	20	14	30	4.0	3.20	80
SAB-2	18	12	27	4.4	3.07	86
SAB-3	16	11	24	4.5	2.91	94
SAB-4	14	9	21	4.6	2.93	102
SAB-5	12	10	19	4.7	2.87	93
SAB-6	11	9	17	5.0	2.84	87

Figure 5.11 Left: SEM image of rice grain like particles. Right: Crystallite size of rice grain like particles as determined using Scherrer equation for PXRD data analysis. Reproduced from Abu Bakar et al.[119]

- Fluorine is a well-known shape modifying agent for TiO_2, particularly anatase.[28] Yang *et al.*[27] was the first to show the ability of F^- ions to modify the shape of anatase crystals. Yang *et al.*[27] observed that the F^- ion selectively binds to the {001} facet of anatase forcing growth in the other planes, namely the [100] and [010].[27] Since Yang *et al.*,[27] many other researchers have found that F^- can modify the shape of anatase phase crystals.[29,35,93] Gordon *et al.*[98] produced shaped anatase crystals that were also blue. It can be seen below in *Figure 5.12* that Gordon *et al.*[98] produced anatase crystallites with a varying exposure of the {001} facet by using TiF_4 (that forms HF *in-situ*) in combination with Cl^- ions. However, Gordon *et al.*[98] did not find the correlation between the shape of the crystals and their colour of the TiO_2.

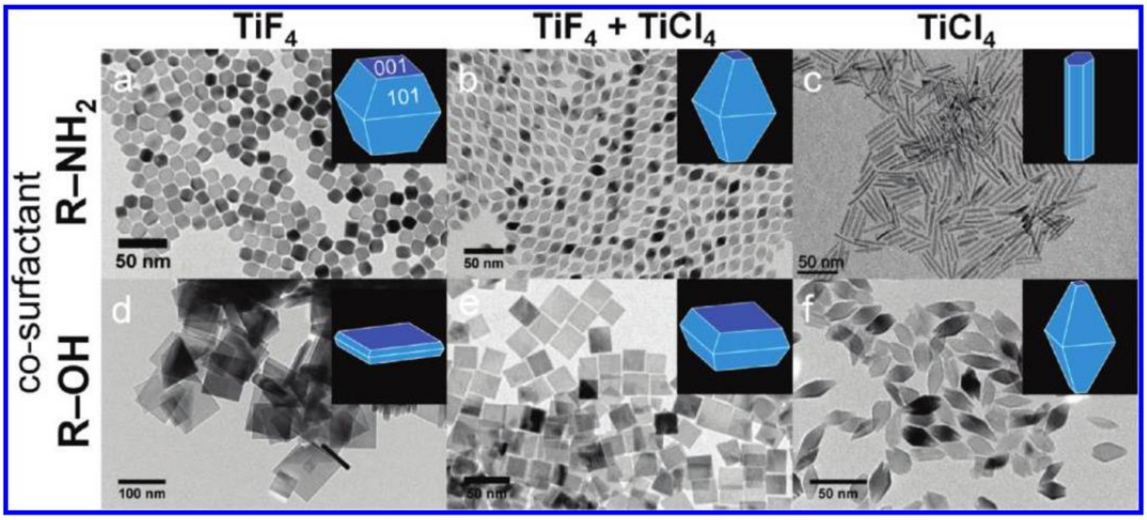

Figure 5.12 TEM images of blue anatase with different crystallite shapes (inserts show geometric models for each type of morphology). Reproduced from Gordon et al.[98]

- On the other hand, NH_4F has been found to produce hierarchical structures *i.e.* microspheres that can be either solid or hollow.[32,66,67] Yu *et al.*[32] found that adding NH_4F to a hydrothermal synthesis of TiO_2 resulted in the formation of microspheres, see *Figure 5.13*. These microspheres were made of small crystallites aggregated into particles which were then aggregated again into the observed hollow spheres. Yu *et al.*[32] found that by changing the molar ratio of NH_4F and TiO_2 from 0 to 2, the size of the spheres and whether they were hollow or not could be controlled. However, Yu *et al.*[32] did not report the TiO_2 to be blue or black. The temperature used for the hydrothermal treatment was lower than 170 °C. So, as per Chapter 4, the organics would not have decomposed to produce the reducing conditions necessary for the formation of blue TiO_2.[32,121] Furthermore, Yu *et al.*[32] did not report any enhanced exposure of the {001} facets when using NH_4F.[32]

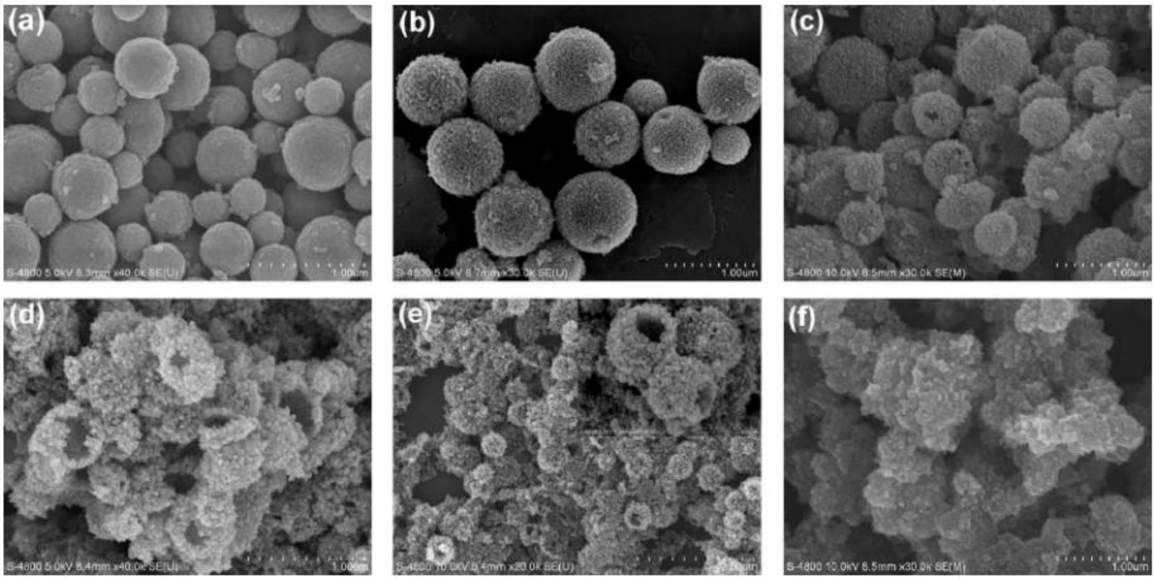

Figure 5.13 SEM image of microspheres synthesised in the presence of NH_4F. The molar ratio was 0 (b), 0.25 (c), 0.5 (d), 1 (e) and 2 (f). Sample (a) was the amorphous microsphere before hydrothermal treatment. Reproduced from Yu et al.[32]

- Chen *et al.*[122] produced black TiO_2 by reducing anatase particles in a hydrogen atmosphere. Using HRTEM Chen *et al.*[122] found that the crystals had a shell-like structure around the outside of the crystals, see *Figure 5.14*. This disordered layer was believed to be where the hydrogen had penetrated into the crystal and caused the reduction of the Ti^{4+} to Ti^{3+}. The disordered layer was responsible for the black colour observed. Multiple researchers studying black TiO_2 have found the same disordered layer around the outside of the particles.[122,123]

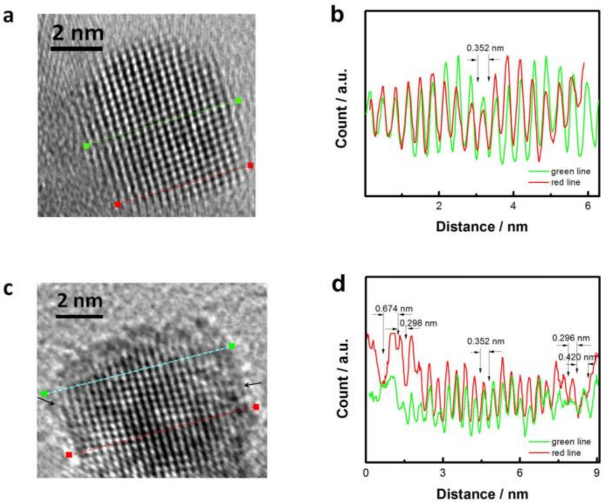

Figure 5.14 HRTEM images of unmodified and black TiO_2 showing a disordered shell around the outside of the crystal believed to be responsible for the colour. Reproduced from Chen et al.[122]

- Furthermore, Naldoni *et al.*[49] demonstrated that electron diffraction on single particles can be used to determine the presence of any disorder in the outer layer of the black TiO_2. As can be seen below in *Figure 5.15*, TEM electron diffraction on a single crystal will show bright points from the lattice diffraction. However, in between these points, there is a haze caused by the disordered layer on the surface of the particles. Again the disordered outer layer was reported to be due to the hydrogen reducing Ti^{4+} to Ti^{3+}.

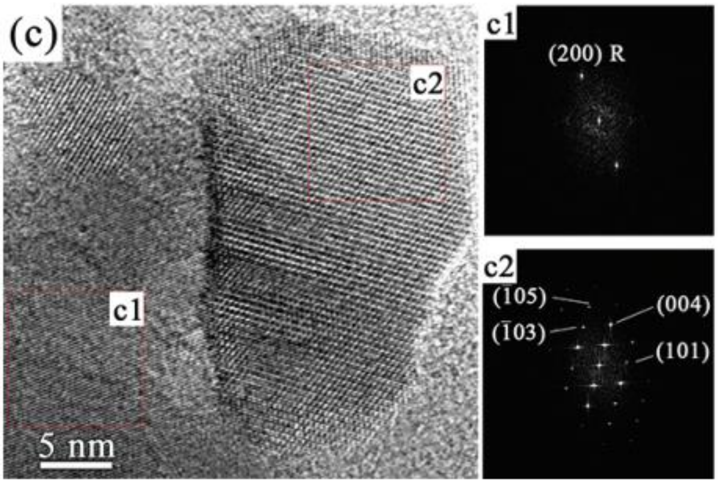

Figure 5.15 HRTEM image of black TiO_2 and its electron diffraction pattern. The haze in the electron diffractogram around the bright points is believed to be caused by the disordered layer surrounding the particles. Reproduced from Naldoni et al.[49]

5.1 Results and Discussion:

5.1.1 Synthetic Clues

Blue TiO_2 was initially synthesised by accident in Chapter 4, so in order to understand the importance of each variable, series of synthetic conditions were evaluated. Understanding the synthesis conditions that result in blue TiO_2 will help in understanding the conditions that cause the colour change.

The sets of synthetic variables chosen to examine were: temperature, NH_4F concentration, F^- ion source, the presence of organic substances (alcohols) and the effects of NH_4OH. Each of these variables was tested in a series of experiments (A), (B), (C) and (F). A brief description of each of these series follows:

- Series (A): The temperature of hydrothermal treatment ranged from 150 to 270 °C, hydrothermal treatment time was fixed at 24 hours and the NH_4F to TiO_2 molar ratio was fixed at 1:1.
- Series (B): The number of equivalents of NH_4F to TiO_2 (molar ratio of $NH_4F:TiO_2$) was varied from 0.01 to 4. Each sample was hydrothermal treatment at 270 °C for 24 hours.
- Series (C): This series examined whether the source of F^- ions was important so, NH_4F was substituted for NaF. The same conditions sets as series B was used.
- Series (F): This series examined whether the NH_4^+ ion played an important role in the synthesis. Series (F) combined the condition sets from both series (A) and (B) above but with the NH_4F being substituted for NH_4OH.In the first part of series (F), the temperature of hydrothermal treatment ranged from 170 to 270 °C, hydrothermal treatment time was fixed at 24 hours and the NH_4OH to TiO_2 molar ratio was fixed at 1:1. In the second part of series (F), the number of equivalents of NH_4OH to TiO_2 (molar ratio of $NH_4OH:TiO_2$) was varied from 0.1 to 4. Each sample was hydrothermal treatment at 270 °C for 24 hours.
- Blank experiments (blank): To test the importance of the organic reagents and the NH_4F, two additional experiments were carried out: First, an amorphous TiO_2 was produced using $TiCl_4$ precursor and substituted for TIPP in a series (A) experiment. The conditions used were 270 °C for 24 hours at 1 equivalent NH_4F. Secondly, a sample completely free of F^- and NH_4^+ ions was produced by hydrothermally treating TIPP in water. The conditions used were 270 °C for 24 hours.

All the different conditions and naming scheme for samples are summarised below in *Table 5.1*:

Series	**TiO_2 precursor**	**Modifier**	**Concentration range**	**Temperature range**	**Organics?**	**Samples naming**
A	Titanium isopropoxide	NH_4F	1-1	150 to 270 °C (150, 170, 200, 220, 245, 257 and 270)	Isopropanol	TiO_2 (A) XXX, where XXX donates the temperature of hydrothermal treatment.
B	Titanium isopropoxide	NH_4F	1 – 4 (0.01, 0.1, 0.25, 0.5, 0.75 and 4)	270 °C	Isopropanol	TiO_2 (B) XXX, where XXX donates the molar equivalents of NH_4F relative to Ti.
C	Titanium isopropoxide	Na_4F	0.01 – 4 (0.01, 0.1, 1 and 4)	270 °C	Isopropanol	TiO_2 (C) XXX, where XXX donates the molar equivalents of NaF relative to Ti.
F	Titanium isopropoxide	NH_4OH	0.01– 4 (0.01, 0.1, 1 and 4)	170 to 270 °C (170, 220, 245, and 270 °C)	Isopropanol	TiO_2 (F) XXX, where XXX donates the temperature of hydrothermal treatment or if XXX is 0.1 or 4 it donates the molar ratio of NH_4OH to Ti.
F free blank	Titanium isopropoxide,	-	0	270 °C	Isopropanol	TiO_2 (Blank) F free
Carbon free blank	Titanium tetrachloride	NH_4F	1	270 °C	-	TiO_2 (Blank) C free

Table 5.1 Table showing different synthesis conditions and sample naming system of different series

The colour of the TiO_2 produced was highly depended on the synthetic conditions used. It can be seen in *Table 5.2* below that the colour of the TiO_2 synthesised changes between series and within series of experimental conditions tested.

First of all, it was clear from series (A) that the temperature of hydrothermal treatment had an impact on the colour. It can be seen in *Table 5.2* below that TiO_2 synthesised at 150 and 170 °C had a stark white colour. However, as the temperature increased from 200 to 220 °C the TiO_2 became a faint blue. Following this, the TiO_2 became progressively deeper blue in colour until it became a dark blue at 270 °C.

Secondly, it was clear from series (B) that the colour was also dependent on the number of equivalents of NH_4F added to the synthesis. Unlike series (A), the colour of the TiO_2 produced in series (B) appeared more complicated. At very low concentrations of NH_4F (0.01 equivalents of NH_4F), the TiO_2 appeared white. At 0.1 to 0.75 equivalents of NH_4F, the TiO_2 produced was very dark in colour. Finally and unexpectedly, the intensity of the blue colour reduced as the concentration of NH_4F was increased to 4 equivalents (relative to Ti).

From series (C) it became clear that substituting NH_4F for NaF still produced blue TiO_2. Initially, the TiO_2 produced at low equivalency (0.01 equivalents of NaF) was white. However, the blue colour progressively became more intense as the number of equivalents of NaF increased from 0.1 to 4.

Series (F) demonstrated that NH_4OH and most likely the NH_4^+ ion itself had no impact on colour. All the TiO_2 synthesised in series (F) was white.

The blank samples confirmed that both the F^- ions and an organic source were critical to the formation of the blue colour. The fluoride-free blank was white, and although not absolutely white, the carbon-free blank was only the “faintest” blue (when compared to series (A)).

The results show that temperature, F^- ions and organics are certainly key factors in the formation of blue TiO_2. Temperature is necessary to decompose the organics, which produces the reducing conditions (H_2 gas) needed to reduce Ti^{4+} to Ti^{3+} (discussed in more detail *Section 5.1.3*).[121] Exactly why the F^- ions are important is not known yet. It is hypothesised that F^- ions may stabilise the Ti^{3+} centres and maintain charge neutrality. The investigation will continue through this chapter.

Series	**Colour**						
A (Temperature of hydrothermal treatment)	White 150 °C	White 170 °C	Faint blue 200 °C	Faint blue 220 °C	Light blue 245 °C	blue 257 °C	blue 270 °C
B (Number of NH_4F equivalents)	White 0.01	Dark Blue 0.1	Dark Blue 0.25	Dark Blue 0.5	Dark Blue 0.75	Light blue 4	
C (NH_4F substituted for NaF)	White 0.01	Faint blue 0.1	Faint blue 1	Blue 4			
F (NH_4OH substituted for NH_4F)	White 170 °C	White 220 °C	White 245 °C	White 270 °C	White 0.01	White 0.1	White 1
F free Blank	White 270 °C						
Carbon-free blank	Very faint blue 270 °C 1						

Table 5.2 Table showing the colour of the TiO_2 produced from series tested above in Table 5.1

5.1.2 Ultraviolet-Visible Light Diffuse Reflectance Spectroscopy

Expanding on the visual results above, ultraviolet-visible light diffuse reflectance spectroscopy (UV-Vis DRS) was used to measure the light absorbing properties of the blue TiO_2. This allowed quantification of the blue colour and allowed comparison to the literature.

A phase pure blue anatase sample was compared to a phase pure white anatase sample synthesised with no added fluoride. Note: *Section 5.1.6* confirms the phase purity by PXRD. It can be observed below in *Figure 5.16* that the blue TiO_2 absorbs red light ranging from approximately 450 nm to 625 nm. This absorption of red light gives the appearance of the blue colour as blue light is preferentially reflected. Furthermore, it should also be observed that the absorption band edge at approximately 325 nm does not appear to be shifted in any way. The lack of a shift in the absorption band edge shows the TiO_2 has retained the band gap of pure anatase (3.2 eV).[6] To confirm, a Tauc plot of the optical absorption spectra was analysed, see *Figure 5.17*. When a line is extended from the point of inflexion to where $(\alpha h\nu)^2$ equals zero, the optical bandgap can be calculated from the x-axis intercept.[117,124] The fluorine-free blank had a bandgap of 3.20 eV. This bandgap is typical of phase pure anatase not displaying any size effects.[6] When the same method was applied to the blue sample (TiO_2 (A) 270 in *Figure 5.17* below), the same bandgap of 3.20 eV was determined. From this information, it can be stated that the bandgap remained unaffected by the blue colouring defects. However, the blue colouring defects were responsible for absorbing red and possibly IR light. The blue TiO_2 spectrum seen below in *Figure 5.16*, closely resembles spectra reported by Gordon *et al.*[98] who synthesised fluoride-modified blue TiO_2 solvothermally.[98] Gordon *et al.*[98] also reported that the band gap did not change. This is unlike black TiO_2 or other heavily-dopped blue TiO_2 where the band gap reduces due to intermediate states between the conduction and valence bands caused by the defects.[49,51,53,99,124-126]

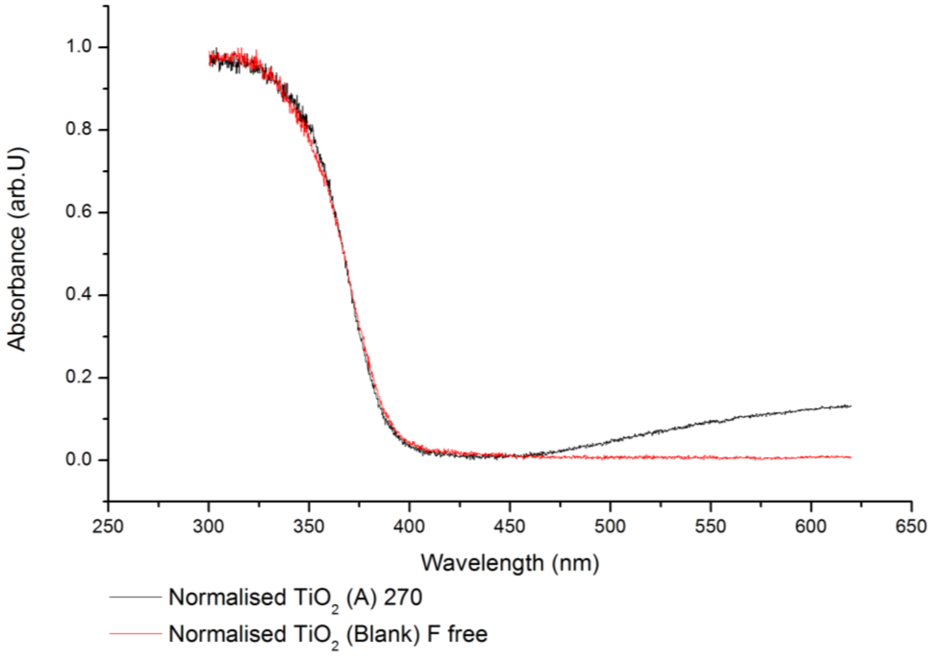

Figure 5.16 Results from UV-Vis-DR spectra showing blue TiO_2 *(A) 270 vs* TiO_2 *(Blank) F free.*

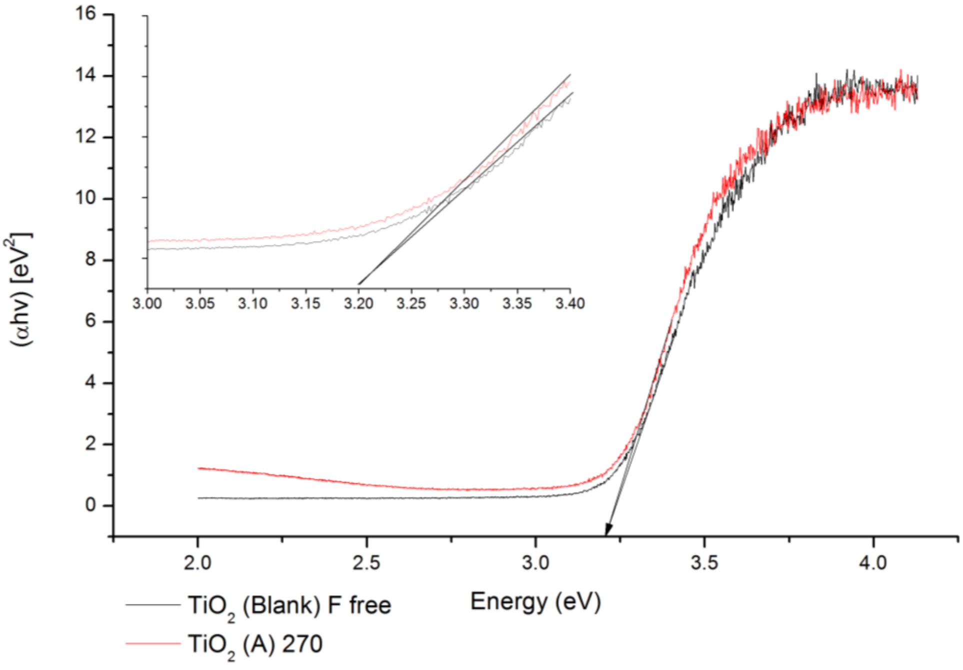

Figure 5.17 Tauc plot of F^- *free blank vs blue* TiO_2 *sample* TiO_2 *(A) 270. Inset showing close-up of the point of inflexion and where* $(\alpha h\nu)^2$ *equals zero corresponding to the bandgap.*

The blue colour of the TiO_2 developed and darkened with increasing temperature of hydrothermal treatment. Below in *Figure 5.18*, it can be seen that the absorption of red light at 450 to 625 nm increases moving through series (A), from lower hydrothermal treatment temperatures (150 °C) to higher temperatures (270 °C). This darkening correlates with what was observed in the experimental *Section 5.1.1* above. The absorption of 620 nm light was plotted against the temperature of hydrothermal treatment. As can be seen below in *Figure 5.19*, samples synthesised at 150 and 170 °C show no absorption at 620 nm. Though, as the temperature of hydrothermal treatment increased from 200 to 270 °C, the absorption of 620 nm light increased from 0.017 to 0.132. Thus, the minimum onset temperature for the formation of defects appears to be 200 °C.

Also, it was observed that the absorption edge redshifts with increasing temperature of hydrothermal treatment, see in *Figure 5.18*. *Figure 5.20* shows a Tauc plot of a sample synthesised at 170 °C *vs* a sample synthesised at 270 °C. The corresponding bandgaps were determined as 3.15 eV and 3.20 eV respectively. The observed change in the bandgap can be explained by size effects.^{6} The smaller crystallites synthesised at lower temperatures show a larger bandgap than the larger more crystalline crystallites synthesised at higher temperatures (*i.e.* 270 °C).^{6} Bandgap widening due to size effects was very prevalent in TiO_2 synthesised at 170 °C or below, however, signs of band gap widening could be observed in most samples synthesised up to 270 °C.

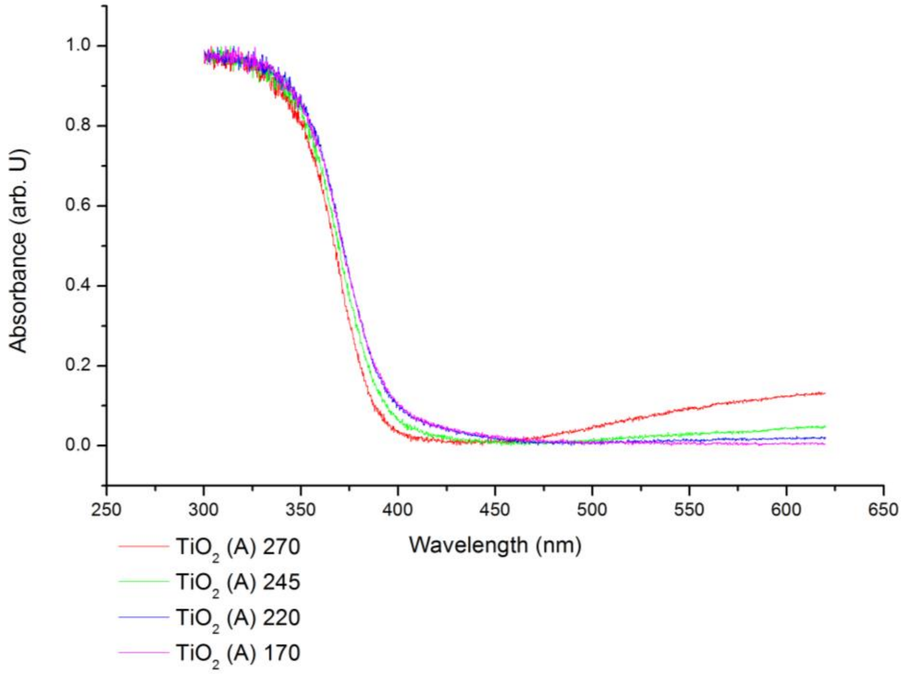

Figure 5.18 UV-Vis DR spectra of TiO_2 synthesised in series (A) with increasing temperature of hydrothermal treatment. Note: Not all of the samples in series (A) are shown to simplify the figure.

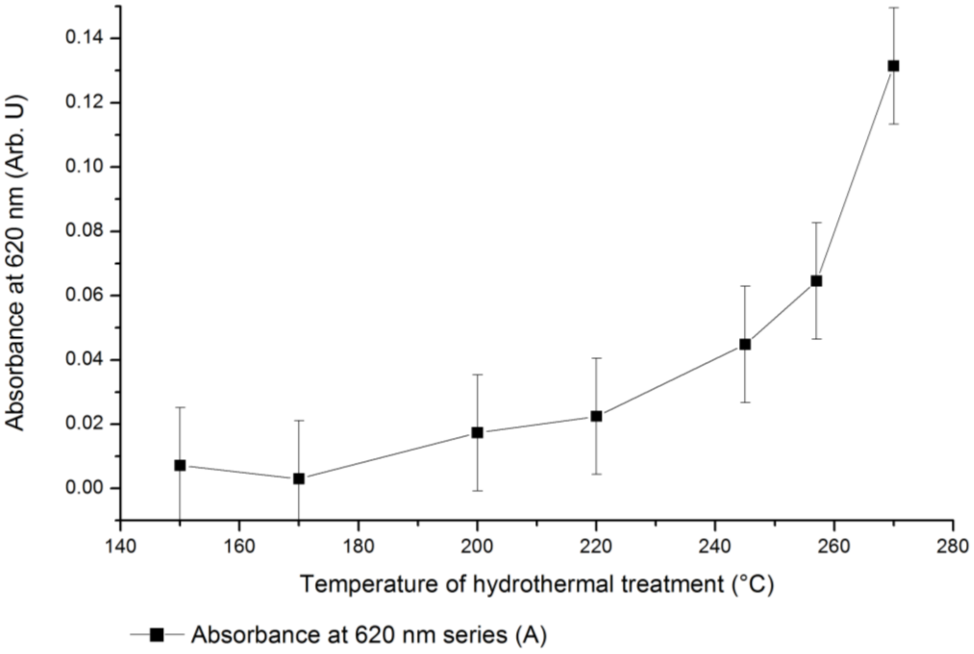

Figure 5.19 Graph displaying the absorption at 620 nm as determined by UV-Vis DRS of TiO_2 synthesised in series (A) with increasing temperature of hydrothermal treatment. Note: Error is calculated based on sample reproducibility (e.g. by making several separate batches of materials and recording their UV-Vis DR spectra).

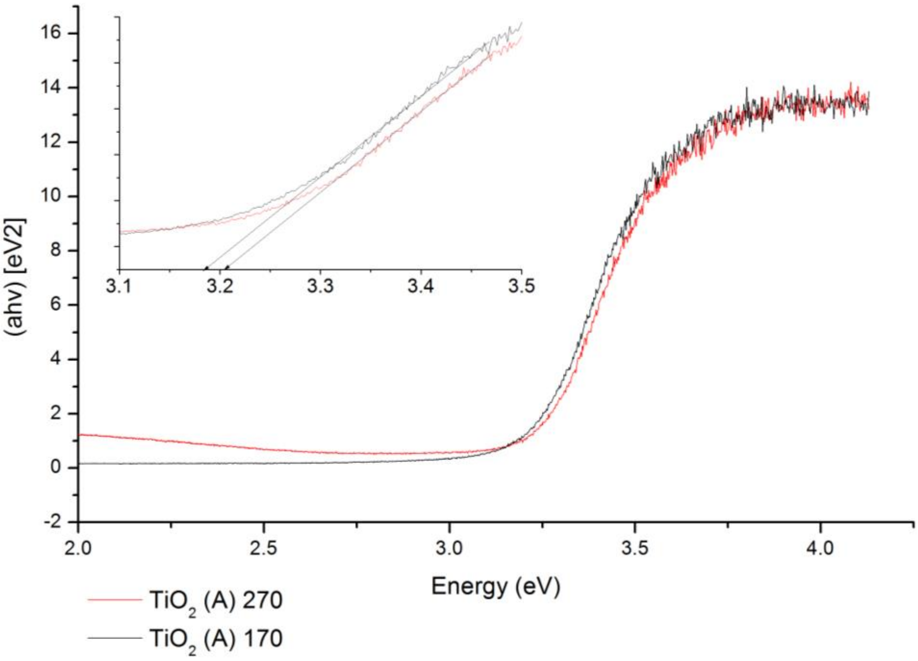

Figure 5.20 Tauc plot of TiO_2 (A) 170 vs TiO_2 (A) 270. Inset close-up of the point of inflexion and showing where $(\alpha h\nu)^2$ equals zero corresponding to the value of the bandgap.

The colour of the TiO_2 also showed a dependency on the number of equivalents NH_4F added to the synthesis mixture (series (B)). As can be seen in *Figure 5.21*, the TiO_2 as-synthesised in series (B) has a high level of absorbance at 620 nm. Remarkably, the absorbance does not increase linearly with the number of equivalents of NH_4F added to the synthesis mixture. Instead, the absorption peaks at 0.25 equivalents NH_4F with an absorption of *ca.* 0.25. Either side of this point the absorption decreases. At 0 and 0.01 equivalents NH_4F, there is very little absorption at 620 nm *i.e.* less than 0.05. This decrease in adsorption was expected as it is known that the NH_4F is a key component responsible for producing the blue colouring defects. Though, the decreasing absorption of sample synthesised at greater equivalents of NH_4F was not expected. Astonishingly, the blue colour has almost disappeared at 4 equivalents NH_4F *i.e.* the absorption of the sample made using 4 equivalents is nearly identical to the sample synthesised at 0.01 equivalents. If the absorption at 620 nm was purely dependent on the number of defects, one would expect the absorption to increase as the number of NH_4F equivalents increased. Clearly, this does not appear to be the case, so something else is affecting the colour or number of defects.

A possible explanations for the enhanced absorption at 0.25 equivalents NH_4F and the lack of absorption at 4 equivalents NH_4F may be, four Ti^{3+} defects may be substituted for one Ti vacancy to maintain charge neutrality.[43] This hypothesis is supported by the decreasing Ti occupancy as determined by PXRD (*ca.* down to 91%) with increasing concentration of NH_4F (*Section 5.1.6*). The reduced number of Ti^{3+} defects would reduce the red light absorption. Although this phenomenon cannot be found specifically in the literature, it has been reported by Zhou *et al.*[101] that when irradiating a single rutile crystal with 2 MeV O ions to generate Ti^{3+} defects. Initially, irradiation results in point defects that give rise to a small additional diffraction peak near [330] diffraction peak in PXRD diffractogram. Further prolonged exposure to the O ion flux results in the sudden disappearance of the peak as the point defects accumulate and develop into a dislocation defect.

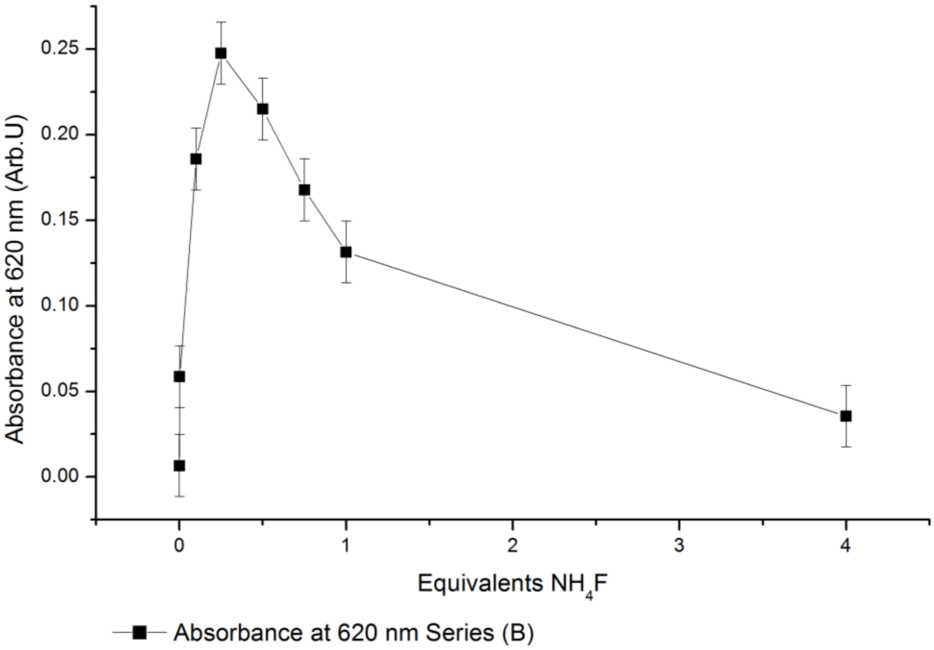

Figure 5.21 Graph displaying the absorption at 620 nm as determined by UV-Vis DRS of TiO_2 *synthesised in series (B) with increasing number of equivalents* NH_4F *added to the synthesis mixture. Note: Error is calculated based on sample reproducibility (e.g. by making several separate batches of materials and recording their UV-Vis DR spectra).*

Series (C) demonstrated that the blue TiO_2 could be produced using NaF in place of NH_4F. It can be seen in *Figure 5.22* that TiO_2 synthesised using NaF absorbed red light similarly to the NH_4F-modified TiO_2. From 0.01 to 1 equivalents NaF, the colour of the TiO_2 produced was only a light blue. When compared to series (A), the absorption at 620 nm was considerably lower, only *ca.* 0.024 for 1 equivalent NaF whereas it was *ca.* 0.131 for the equivalent NH_4F sample (TiO_2 (A) 270). Also, it can be seen in *Figure 5.22*, that the absorption edge did not change for samples synthesised with one or fewer equivalents of NaF. Conversely, when 4 equivalents of NaF was used there was a noticeable shift in the band edge to shorter wavelengths. This shift in absorption edge was found to be due to the formation of brookite which will is discussed later in Chapter 6. Lastly, when looking at the absorption at 620 nm in *Figure 5.23*, it can be seen that unlike series (B), the absorption appears to increase linearly with the number of equivalents of NaF added to the synthesis mixture. As above, the substitution of Ti^{3+} defects for Ti vacancies may result in reduced red light adsorption. If this scenario is true, then the greater number Ti vacancies in series (C) as determined by PXRD (*Section 5.1.6*) explains the reduced red light adsorption.

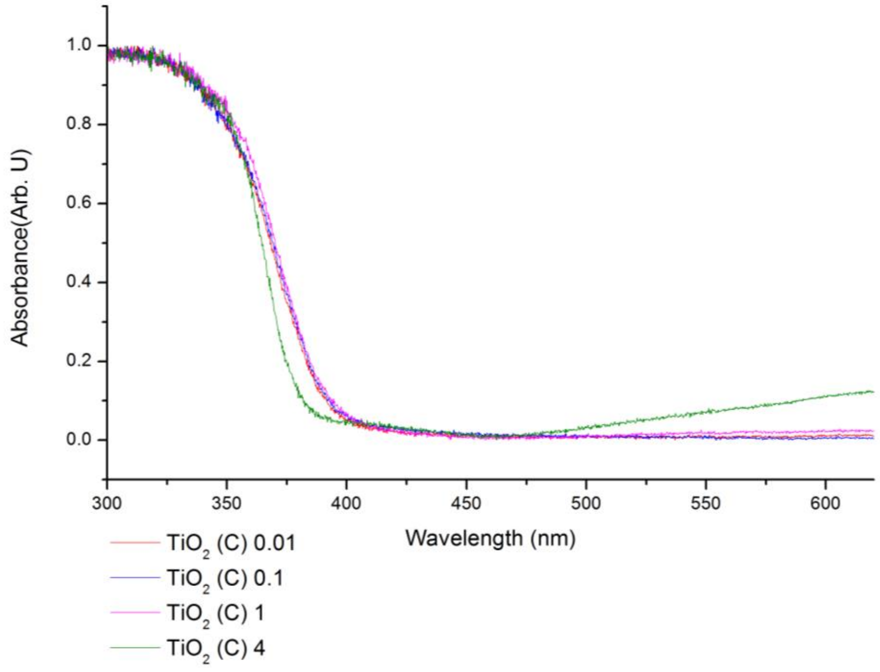

Figure 5.22 UV-Vis DR spectra of TiO$_2$ synthesised in series (C) with increasing number of equivalents of NaF added to the hydrothermal synthesis mixture.

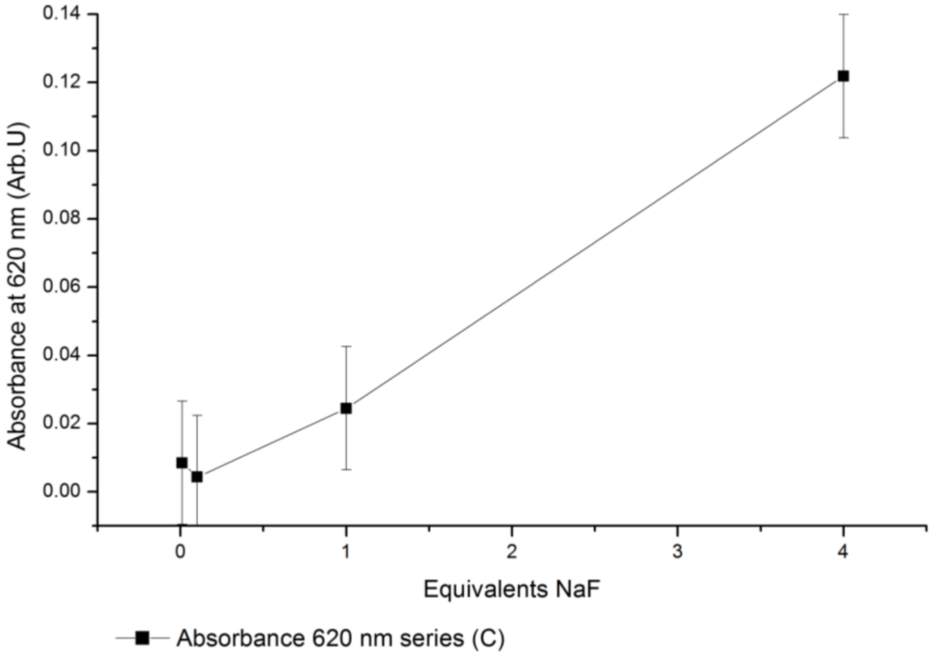

Figure 5.23 Graph displaying the absorption at 620 nm as determined by UV-Vis DRS of TiO$_2$ synthesised in series (C) with increasing number of equivalents NaF added to the synthesis. Note: Error is calculated based on sample reproducibility (e.g. by making several separate batches of materials and recording their UV-Vis DR spectra).

When NH_4OH was substituted for NH_4F, the TiO_2 produced was white with no signs of red light absorption. As can be seen in *Figure 5.24* below, the TiO_2 synthesised at 170 to 270 °C showed no absorption at 620 nm. Secondly, the band edge appears constant, in all the samples. The TiO_2 synthesised with different ratios of NH_4OH also showed consistent spectra with no absorption around 620 nm (Figure S3). Beyond a doubt, the NH_4OH does not produce colour-causing defects.

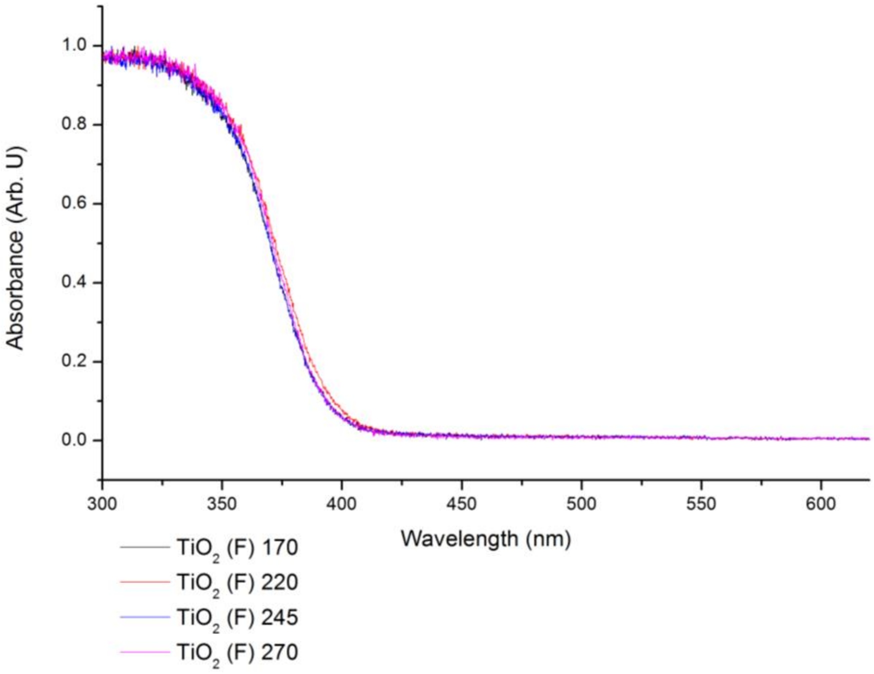

Figure 5.24 UV-Vis DR spectra of TiO_2 synthesised in series (F) with increasing temperature of hydrothermal treatment.

When examining the UV-DR spectra of the blank samples, it becomes clear that both F^- ions and organics (isopropanol is a by-product of TIPP hydrolysis) are key to the formation of the blue TiO_2. Sample TiO_2 (Blank) F free in *Figure 5.25* shows that when no source of F^- ions are present, then the TiO_2 produced is white (absorption at 620 nm *ca.* 0.0068). When the organics source is removed, as in sample TiO_2 (Blank) C free, it can be seen that there is very little absorption at 620 nm *ca.* 0.02855. Although this is higher than the (Blank) F free sample, it is still considerably lower than a sample synthesised with organics at the same temperature and NH_4F ratio *i.e.* TiO_2 (A) 270 *ca.* 0.13145. The organics free sample (TiO_2 (Blank) C free) was synthesised using $TiCl_4$ as opposed to $Ti(OC_3H_8)_4$, thus eliminating the presence of isopropanol. However, the Teflon liner or distilled water may have contained traces of organics, as it is near impossible to completely avoid contamination with adventitious hydrocarbons. Thus, the traces of organics may explain the slight blue tinge.

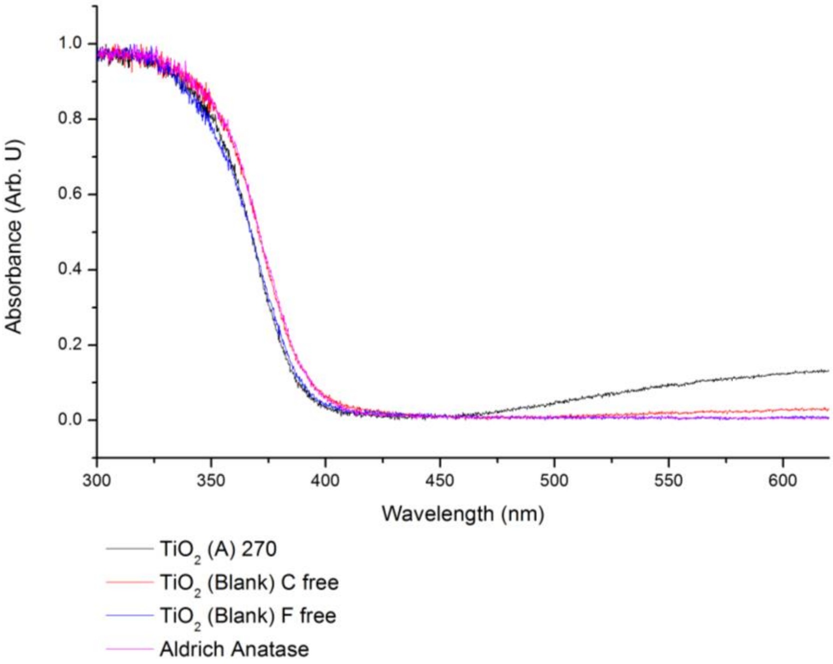

Figure 5.25 UV-Vis DR spectra of TiO_2 *synthesised in series (Bank) compared to Aldrich anatase.*

The blue colour observed and the corresponding UV-DR spectra most closely resemble the spectra reported by Gordon *el al.*[98] Gordon *et al.*[98] proposed the red light and NIR adsorption was due to Ti^{3+} defects. The energy band from the Ti^{3+} defects was positioned just below the conduction band facilitating the transition of the electrons localized on the Ti^{3+} defects to the conduction band resulting in red light absorption. The energy position of the defect was not reported by Gordon *et al.*[98], nonetheless, other authors have reported the Ti^{3+} defects to lie between 0.68 and 1.18 eV below the conduction band of non-dopped TiO_2.[49,103] On the other hand, it was also proposed by Gordon *et al.*[98] that the free electrons residing in the conduction band could also change state or act as a localized surface plasmon resulting in the absorption of NIR light. localized surface plasmons have been observed in highly conductive doped-metal oxides, however, this seems unlikely as the colour would have a size dependency which was not reported.[98] Furthermore, it has been shown by Guo *et al.*[127] using DFT calculation of F^- dopped TiO_2 that the absorption of red light between 600 and 700 nm is as a result of Ti3d transition to Ti3d states. Moreover, it was reported that O vacancies cause red light absorption centred at 520 nm whereas, the absorption maximum was at 670 nm for F-doped TiO_2.[127] The Ti3d transition to Ti3d states is in good agreement with the blue TiO_2 reported here as the absorption maximum is centred beyond 600 nm and Ti3d electrons were detected *via* valence band spectroscopy in the NH_4F-modified TiO_2. Although, the transitions described by Guo *et al.*[127] are hard to comprehend making the conclusions drawn questionable.

5.1.3 Identifying the Reducing Agent

The NH_4F modified oxalic acid sols (Chapter 4), the synthetic clues and the UV-Vis DRS results above have all suggested that organics, temperature and an F^- ion source are important in the synthesis of blue TiO_2. To start narrowing down on why these keys synthetic conditions are important a study was carried out to examine how the organic components assisted in the formation of blue colouring defects. When reviewing the literature, the synthesis of blue or black TiO_2 commonly uses a reducing agent to generate Ti^{3+} defects by reducing Ti^{4+}.[46,121] However, in the current synthesis, no reducing agents were added. Yet, it had been noticed that there was a release of gas from the autoclaves after the hydrothermal treatment. This was also observed with the NH_4F modified oxalic acid sols, which was found to be due to the oxalic acid decomposing.[121] Oxalic acid could have been acting as a reducing agent along the H_2 gas as oxalic acid can reduce metal dioxides *e.g.*MnO_2.[128] However, no oxalic acid was added in the experiments discussed in this chapter. The following experiments were carried out in an attempt to identify the potential reducing agent formed within the synthesis media. Mass spectrometry was used to analyse the gas released from the autoclaves. IR spectroscopy was used to analyse the remaining mother liquor to look for the disappearance of certain organic groups.

To start the identification process, a 0-120 M/Z survey scan using mass spectrometry was used to analyse the gas released from the autoclave after the synthesis of sample TiO_2 (A) 270, which was blue. The survey spectrum showed no species with a mass greater than 44 g/mol were present, see *Figure 5.26*. These results were very similar to the ones obtained in the case of oxalic acid modified sols (Chapter 4).[121]

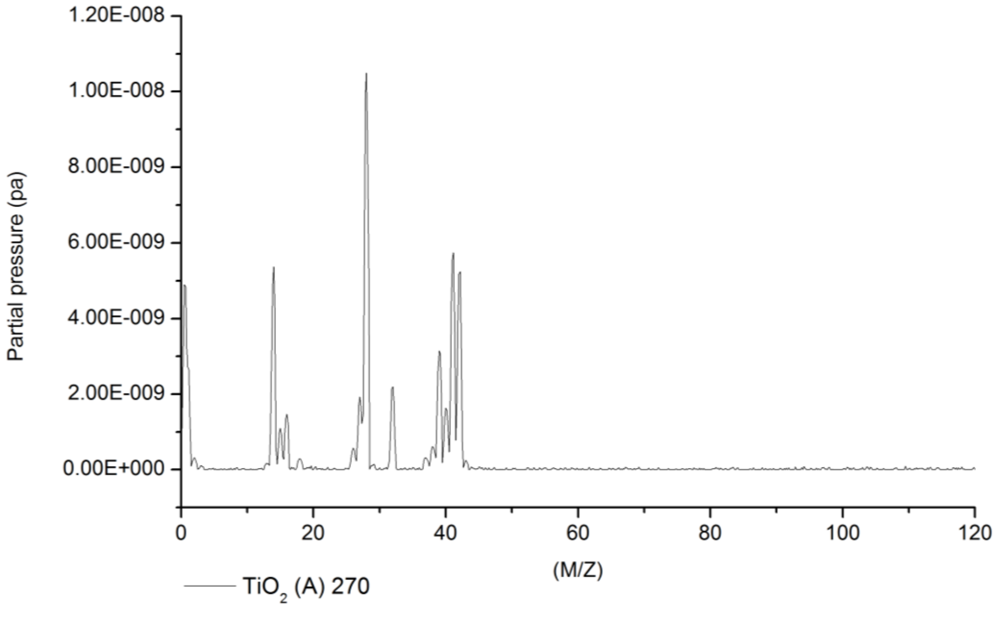

Figure 5.26 Mass spectra of gas released from autoclave after the synthesis of TiO_2 (A) 270.

High-resolution mass spectrometry clearly showed a complex mixture of compounds was present in the gas released from the autoclaves. As can be seen below in *Figure 5.27*, the gases released from the autoclaves contains many molecules with molar masses ranging from 1 to 43. Peaks at 1 and 2 M/Z are H_2 gas. The H_2 gas is most probably the reducing agent that causes the Ti^{4+} to be reduced to Ti^{3+}.[46] The origin of H_2 is the decomposition of the isopropanol released from the titanium isopropoxide during hydrolysis. Evidence for the decomposition of isopropanol can be seen in *Figure 5.27* as masses ranging from 37 to 44 g/mol; it is somewhat surprising that there is no peak for the isopropanol itself with a molecular weight of 60.096 g/mol. Although it is clear from the IR spectra below (*Figure 5.29*), not all the isopropanol decomposed. However, the autoclave was allowed to cool to room temperature before being opened to collect the reaction gases. There was still considerable pressure inside the autoclave, as indicated by a loud hiss when the seal was broken due to the decomposition products. So it is thought that the vaporization of isopropanol into the gas phase was suppressed (to below the detection limit) due to the head pressure and relatively low concentration of isopropanol *ca.* 20 %. Possible compounds for these masses based on the mass and available elements are listed in *Table 5.3*; ionization was soft so no fragmentation is expected. These compounds contain only hydrogen, carbon and oxygen, they also contain functional groups such as alkanes, alkenes, alkynes or epoxides. In order to form these compounds from isopropanol, H_2 or H_2O liberation must occur.[129,130] Loss of water from isopropanol *via* dehydrogenation reaction would form propene with a molecular weight of *ca*. 42 g/mol, one of the masses detected, see *Table 5.3*. Alternatively, the organic molecules themselves could have acted as the reducing agent *e.g.* ethylene glycol has been used as a reducing agent.[112]

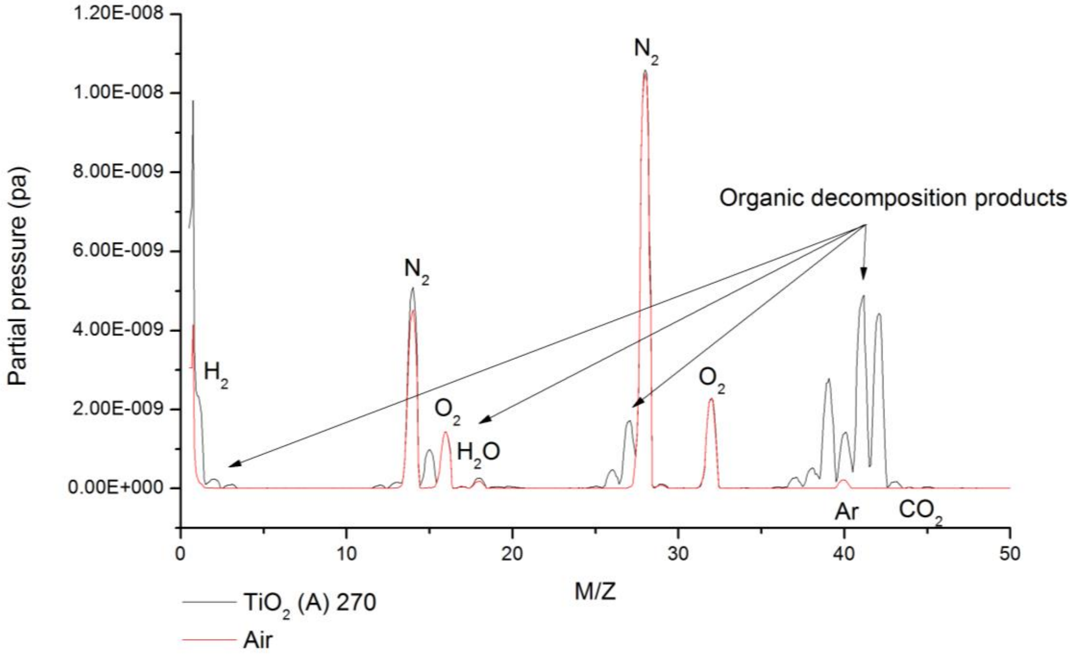

Figure 5.27. High-resolution mass spectrum of gas released from autoclaves after hydrothermal synthesis of sample TiO_2 (A) 270. A high-resolution spectrum of air has also been included to help show what is not found in air. Note: As the mass spectrometer used was an industrial unit used to analysis gas emissions, the units reported are the partial pressures of the gases inside the manifold.

Molecular Formula	**Mass (g/mol)**
C_3H_2	38
C_3H_4	40
C_2H_2O	42
C_3H_6	42
C_3H_8	44

Table 5.3 Table showing possible molecules for masses between 38 and 44 g/mol.

By comparing the mass spectroscopy results of the gas released from the synthesis of TiO_2 (A) 270, TiO_2 (A) 170, TiO_2 (Blank) F free and TiO_2 (Blank) C free in *Figure 5.28*. It becomes evident that the NH_4F does not alter the composition of the gases released during the hydrothermal synthesis; to reach this conclusion one has to compare samples TiO_2 (Blank) F free *vs* TiO_2 (A) 270. Furthermore, the low-temperature synthesis of TiO_2 (A) 170 does not result in any detectable decomposition products of the isopropanol and hence no hydrogen gas was detected. This explains the lack of blue colouration of TiO_2 observed with low-temperature syntheses; no Ti^{3+} defects were formed by the reduction of Ti^{4+} by H_2. Lastly, it can be seen that the carbon-free sample TiO_2 (Blank) C free, also lacks detectable organic decomposition products. This explains the significantly reduced blue colouration when compared to TiO_2 (A) 270.

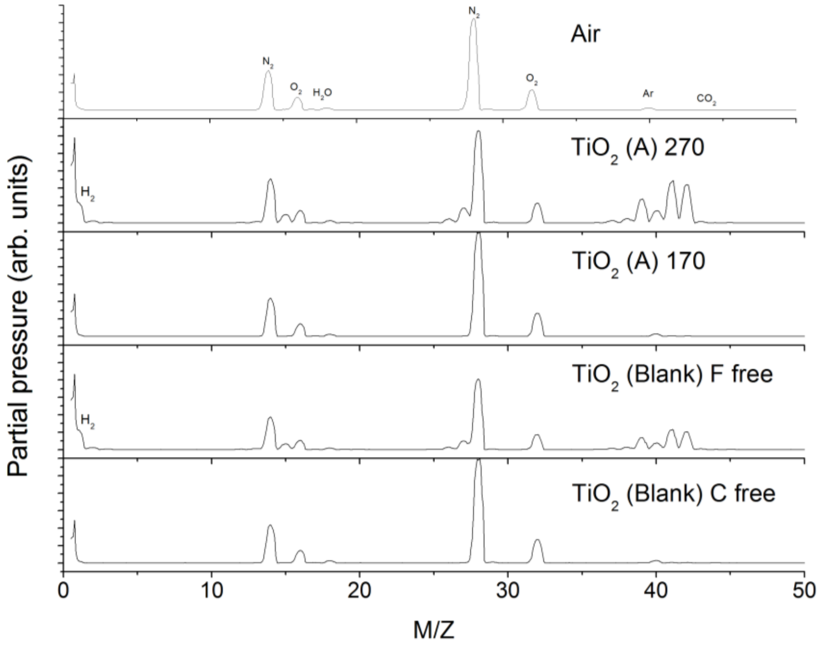

Figure 5.28 Mass spectra of air and the gases released from autoclaves used to make TiO_2 (A) 270, TiO_2 (Blank) F free and TiO_2 (A) 170.

To ensure there was no other chemistry going on in the liquid that could explain the reducing conditions, FT-IR was used to inspect the composition of the spent hydrothermal fluid. First of all, it can be observed in *Figure 5.29*, that the decanted solution of sample TiO_2 (A) 270 contained only the peaks expected from a mixture of NH_4F and isopropanol, no new peaks were observed. The lack of IR-signatures of any new chemical functional groups in solution and the mass spectrometry results confirm that no F^- or N-containing organic compounds were formed. Hence, H_2 is the most likely reducing agent. Interestingly, the peaks in the IR spectra corresponding to the isopropanol still exist, although their intensity is reduced, suggesting not all the isopropanol decomposed.

The H_2 is in the gas phase at room temperature and atmospheric pressure, however, under 200 atm of steam pressure and at 270 °C, it is expected that some of the H_2 gas would dissolve into the solution.

The H_2 reduces Ti^{4+} to Ti^{3+} as per the *Equation 3* below. High-pressure H_2 gas has been used in the synthesis of blue and black TiO_2.[46,49,51,99,131]

$$Ti^{4+} + e^- \rightarrow Ti^{3+} \qquad (1)$$

$$H_2 + O^- \rightarrow HO_2 + e^- \qquad (2)$$

$$H_2 + 2TiO_2 \rightarrow Ti_2O_3 + H_2O \qquad (3)$$

Equation 3 H_2 reduction of Ti^{4+}

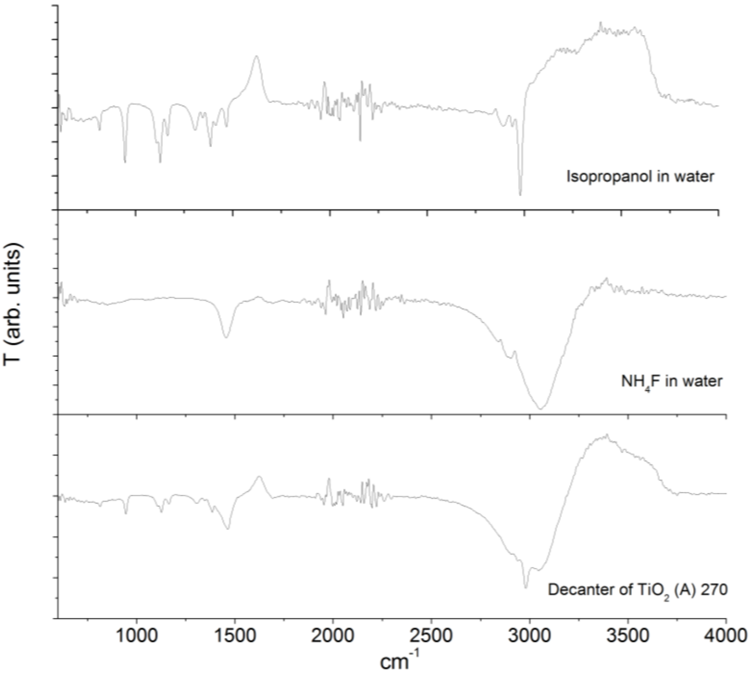

Figure 5.29 FT-IR spectra of standard solutions made with: isopropanol in water, NH_4F in water and decanted mother liquor from the synthesis of sample TiO_2 (A) 270.

5.1.4 Electron Paramagnetic Properties of the Blue TiO_2

To further understand the potential presence of Ti^{3+} defects and/or oxygen vacancies in the as-synthesised blue TiO_2. SQUID and EPR were used to look at the magnetic properties of the blue TiO_2. The SQUID study was carried out in collaboration with Dr Shen Chong at Callaghan Innovation (who did the measurement and analysis of the data). EPR was performed at Auckland University in collaboration with Associate Professor Geoff Waterhouse.

EPR results showed that there were paramagnetic electrons present in the blue TiO_2 sample (TiO_2 (A) 270), but not in white TiO_2 sample (TiO_2 (A) 170), see *Figure 5.30*. These paramagnetic electrons are associated with Ti^{3+} defects.[47,53,97,103] It can be seen in *Figure 5.30*, that there is a spin coupling signal at g = 1.967 present in the blue TiO_2 sample (TiO_2 (A) 270). On the other hand, there is no coupling signal present in white TiO_2 sample (TiO_2 (A) 170), despite both samples being synthesised in the presence of NH_4F. The coupling signal detected in the TiO_2 (A) 270 sample does not match any exact g values reported in the literature but, it is extremely close to the g = 1.960 reported as bulk Ti^{3+}.[47,53,97,103] Also it should be noted that the peak is very broad when compared to those reported in the literature.[47] This is most likely caused by the temperature of the measurement. EPR is generally performed at 77 K but, here it was performed at 200 K using a stream of cold N_2 gas from evaporating liquid N_2. This was because the machine was not designed to take liquid N_2. Both samples display a very broad signal at g =2.05, see *Figure 5.30*. This signal is due to O_2^- and is often found in TiO_2 after exposure to air and light.[53,97,103] Although not shown here, the TiO_2 (A) 270 did not show any spin coupling at room temperature. This because the electrons needed to be immobilized to become paramagnetic. It is not uncommon for Ti^{3+} doped TiO_2 to be EPR inactive at room temperature.[98]

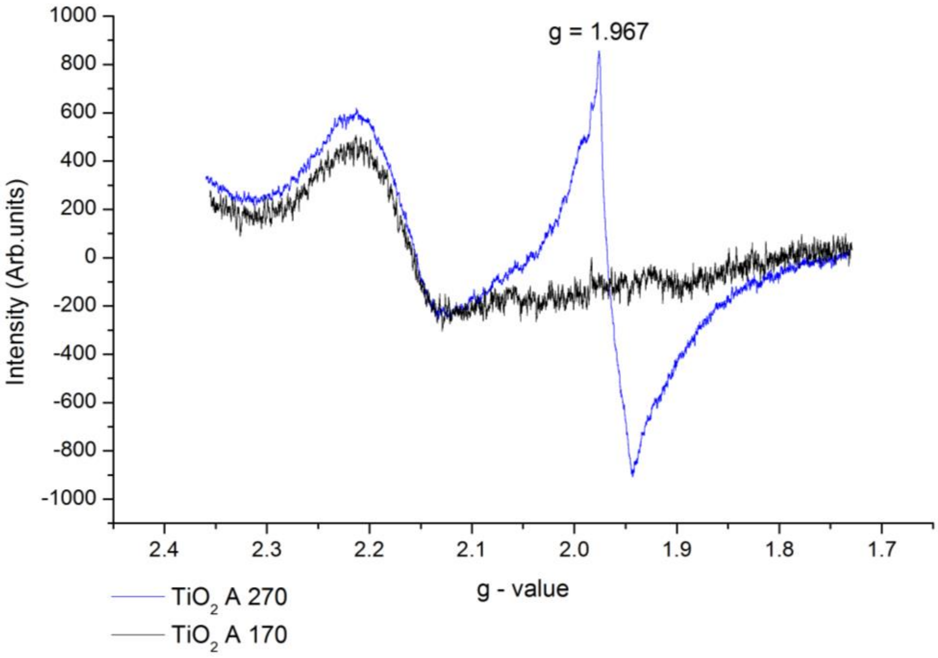

Figure 5.30 EPR spectra of blue TiO_2 sample TiO_2 (A) 270 and white TiO_2 (A) 170.

To complement the EPR, SQUID was used to measure the magnetic properties of the blue TiO_2 synthesised in series (A). The first SQUID experiment performed looked at how the magnetic properties changed with respect to temperature. It was evident that the magnetic properties of the blue TiO_2 changed with temperature, see *Figure 5.31*. The first transition occurs between 100 and 150 K where the zero field cooling (ZFC) and field cooling (FC) measurements begin to diverge. This divergent behaviour indicates a change from diamagnetic to paramagnetic. This initial change from diamagnetic to paramagnetic confirms what was suspected with the EPR measurements above, at room temperature the Ti^{3+} is undetectable due to the lack of order in the crystal.[47] As the temperature is lowered from 65 and 30 K, there is a second and much larger divergence between the ZFC and FC. This indicates a larger shift towards paramagnetism as more ordering occurs. This would also suggest that had the EPR measurements been performed at a lower temperature a sharper Ti^{3+} peak would have been detected giving a more accurate g value. *Figure 5.32* below confirms the change from diamagnetism to paramagnetism *via* loop measurements performed at different temperatures. At 150 K, the slope of the line (M/B) is negative indicating diamagnetism, however, it becomes positive at 30 K and even more positive at 3 K indicating paramagnetic behaviour. The TiO_2 (A) 270 sample shows a small hysteresis (*ca.*0.00025 emu/g) in the measurements; hysteresis (as little as 10^{-5} emu) indicates ferromagnetic behaviour.[101] Ferromagnetic behaviour in TiO_2 has been linked to Ti vacancies, these Ti vacancies make the TiO_2 act as a p-type semiconductor.[101,102] As discussed later in the PXRD section (*Section 5.1.6*), the PXRD data showed that all the hydrothermally synthesised TiO_2 was deficient in Ti. The TiO_2 synthesised at lower temperatures and in the presence of more NH_4F typically showed higher numbers of titanium vacancies according to the PXRD data. Unfortunately, SQUID was only performed on a small number of samples (series (A)) making it hard to conclusively say whether this hysteresis is due to titanium vacancies or not.

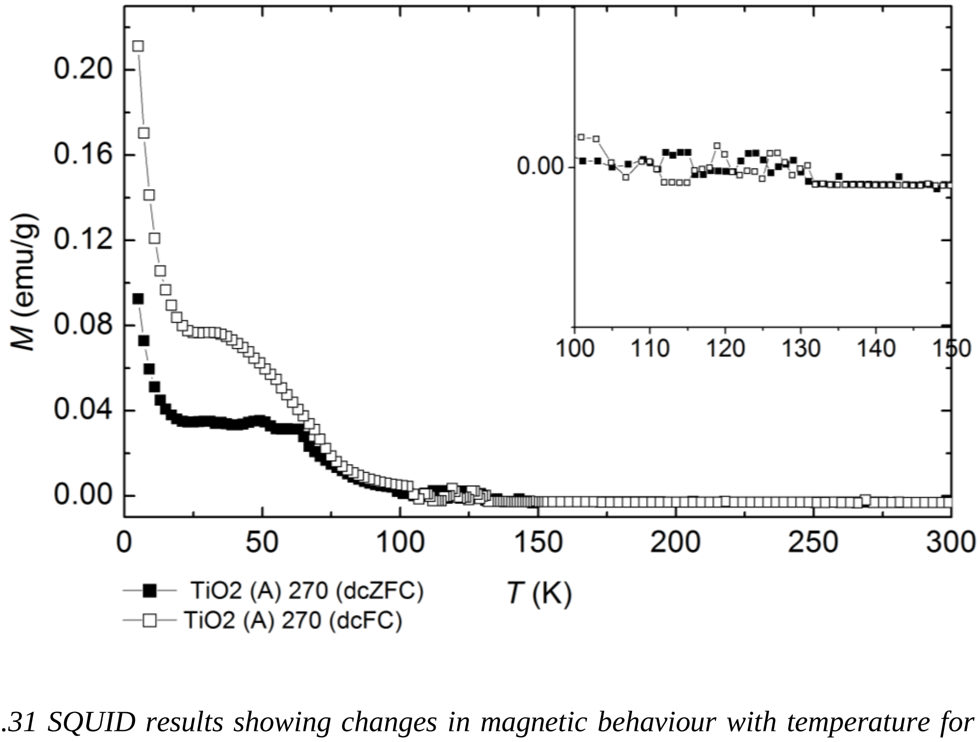

Figure 5.31 SQUID results showing changes in magnetic behaviour with temperature for blue TiO_2 (TiO_2 (A) 270).

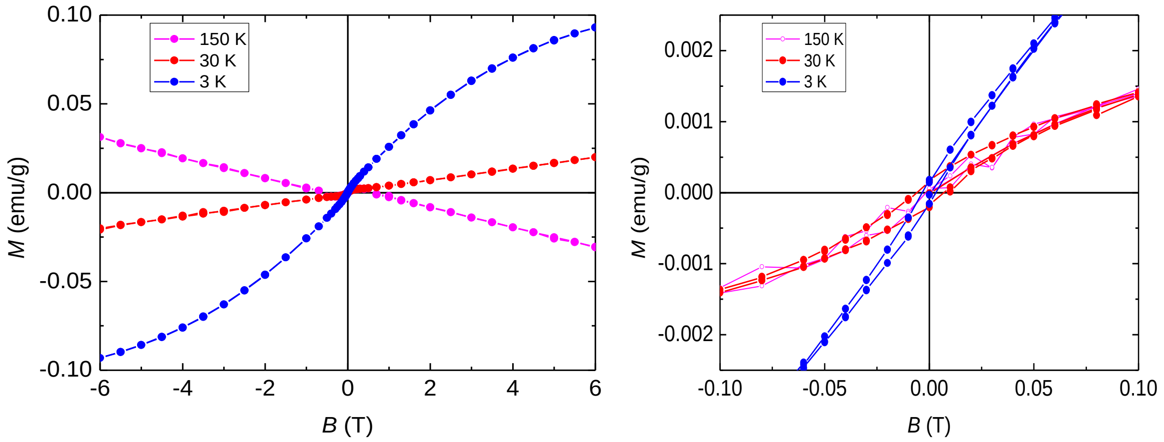

Figure 5.32 SQUID results showing field loop measurements at different temperatures for blue TiO_2 (TiO_2 (A) 270). Right: Overall measurement. Left: Showing close-up of hysteresis.

In order to quantify the number of oxygen vacancies present in series (A), loop measurements were performed at 3 K. It can be seen in *Figure 5.33* that the steepness and positive angle of the loop measurements are increasing with increasing temperature of hydrothermal treatment, thus indicating more paramagnetic behaviour. By fitting the loop measurements with the Brillouin Function, *Equation 4* below, it is possible to calculate the number of oxygen vacancies. Examples of the fits can be seen in *Figure 5.33*. The results of fitting the Brillouin function to samples in series (A) is shown in *Figure 5.34* below. A distinct increase in the number of oxygen vacancies (or paramagnetic centres) with increasing temperature of hydrothermal treatment was observed. The number of oxygen vacancies detected in TiO_2 synthesised at low temperatures (150 °C) was *ca.* 8.8×10^{24} N/m^3 (where N is the number of vacancies), whereas in a blue sample synthesised at 270 °C, the number of vacancies was as high as *ca.* 4.4×10^{25} N/m^3.

$$M(\mathrm{B},T) = \mathrm{N}*\mathrm{g}*\mu_\mathrm{B}*\mathrm{J}*\mathrm{B_J}(x); \qquad (1)$$

$$\text{Where } \mathrm{B_J}(x) = ((2*\mathrm{J}+1)/(2*\mathrm{J}))/(\tanh(x*(2*\mathrm{J}+1)/(2*\mathrm{J}))) - (1/(2*\mathrm{J}))/(\tanh(x/(2*\mathrm{J})));$$

$$x = \mathrm{g}*\mu_\mathrm{B}*\mathrm{J}*\mathrm{B}/(k_\mathrm{B}*T); \qquad (2)$$

μ_B=9.274e-24 J/T; k_B=1.381e-23 J/K; J=1/2; g=2; B=Field; T=measuring temperature (3 °K)

Equation 4 Brillouin Function

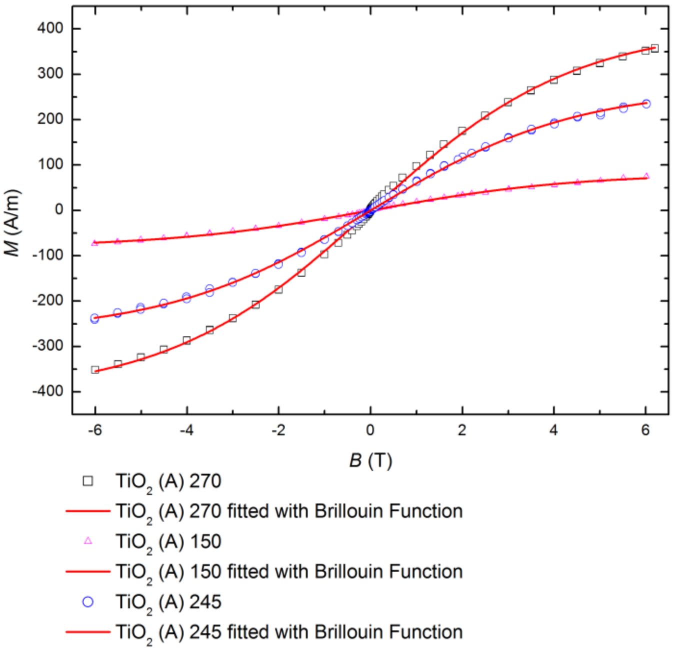

Figure 5.33 SQUID loop measurements of blue TiO_2 series (A) fitted with Brillouin's function. Note: Measurements were performed at 3 K.

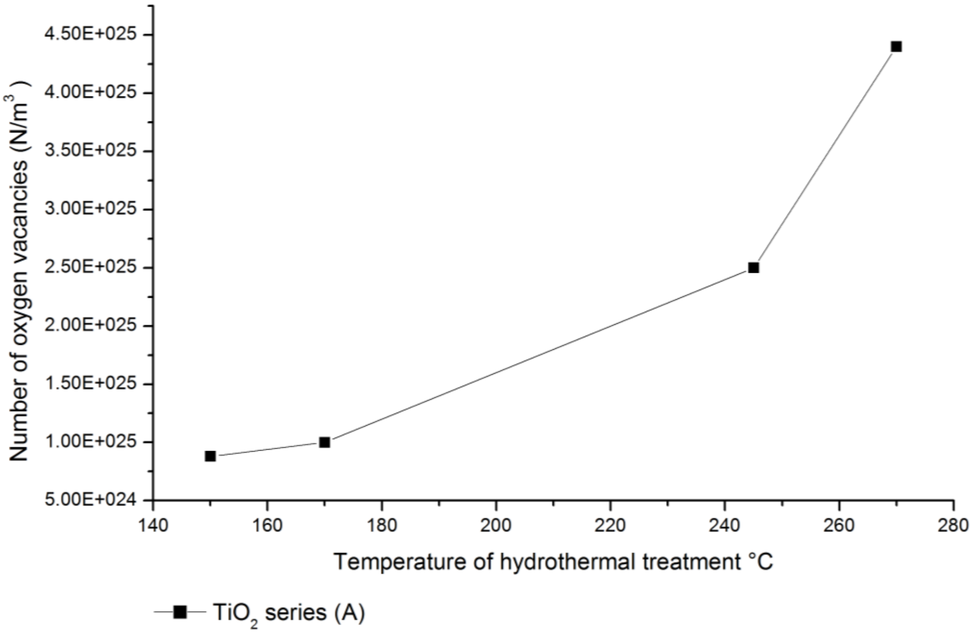

Figure 5.34 Graph showing the number of oxygen vacancies determined in series (A) by fitting the Brillouin Function to loop measurements. Note: Measurements were performed at 3 K.

The fact that a peak was detected using EPR which lined up with the literature value for bulk phase Ti^{3+} and the paramagnetic behaviour measured by SQUID, is a strong indicator that Ti^{3+} is present within the blue TiO_2. Also, the fact that an EPR peak was detected in blue TiO_2 and not in white TiO_2 is a strong indicator that the Ti^{3+} is at least in part responsible for the blue colouration. Blue TiO_2 and Ti^{3+} go hand-in-hand throughout the literature.[47,51,98,100] Unfortunately due to the temperature the EPR was performed at, it is impossible to determine whether the broadness of the peak is due to the range of chemical environments of relevant species or is due to the temperature of the measurement. SQUID measurements suggest the EPR should have been performed at a much lower temperature as the full localisation of the unpaired electrons did not fully occur until the sample was colder than 30 K. However, the peak position is closest to that of bulk Ti^{3+} ($g = 1.96$), which agrees with the chemical stability observed (lack of oxygen sensitivity common for surface Ti^{3+} species).[47,53,97,103] The number of oxygen vacancies was calculated using loop measurements and the Brillouin Function from the SQUID results**.** It was found that, with increasing temperature of hydrothermal treatment and hence coinciding with the deepening of the blue colour, the number of detected vacancies/paramagnetic centres increased. This comprises further evidence supporting the hypothesis that the blue colour is due to Ti^{3+}. Lastly, SQUID study showed that at all temperatures of synthesis, there appears to be a small hysteresis corresponding to some ferromagnetism which could be due to the Ti vacancies.[101,102] This agrees with the PXRD date in *Section 5.1.6*. Furthermore, the presence of ferromagnetism in white samples indicates that such Ti vacancies are unlikely to be causing the blue colour.

5.1.5 Raman Spectroscopy Study of Blue TiO_2

The investigation into the nature of the defect causing the blue colouration was continued using Raman spectroscopy. Raman spectroscopy can be used to identify phase, size, shape and disorder in inorganic materials by looking at the characteristic vibrational modes.[95,107-109]

Raman spectroscopy of TiO_2 synthesised in series (A) showed weaker B_{1g} and A_{1g} modes compared to commercial Aldrich anatase, see *Figure 5.35*. When comparing the whole of series (A) with Aldrich anatase, it is evident that the B_{1g} and A_{1g} peaks were significantly weaker than those present in Aldrich anatase. This applies to all samples synthesised no matter whether blue or white. Previous reports in the literature of hydrogen reduced TiO_2 reported that the reduced intensity of the B_{1g} and A_{1g} peaks relative to the E_g peak is due to oxygen vacancies.[95,109] Between samples in series (A), there does not appear to be any significant changes in the intensity of the B_{1g} and A_{1g} peaks relative to the E_g peaks despite the change in colour observed and EPR/SQUID proof of increasing concentrations of Ti^{3+} with increasing temperature of hydrothermal treatment. This observation was confirmed by fitting the Raman peaks with pseudo-Voigt peaks and determining the area ratio between B_{1g} and A_{1g} with respect to E_g peak. As can be seen in *Figure 5.36*, there was no change in these ratios with increasing temperature of hydrothermal treatment. Furthermore, the same reduced intensity of the B_{1g} and A_{1g} modes can also be seen in white TiO_2 synthesised in series (F), where NH_4OH was substituted for the NH_4F, see *Figure 5.37*. These results would suggest that the hydrothermal synthesis results in the reduced intensity of these peaks relative to the Aldrich anatase sample, most likely due to the shape of crystallites exposing either the {111} or {001} facet rather than oxygen vacancies or the blue colour.[109] Confirmation of this hypothesis comes from the PXRD study discussed in detail below in *Section 5.1.6*, that showed that TiO_2 particles in both series (A) and (F) were elongated in the [001] direction. Thus, there would be greater exposure of the {101} facet relative to more spherical particles of anatase explaining the reduced intensity of the B_{1g} and A_{1g} modes.[109]

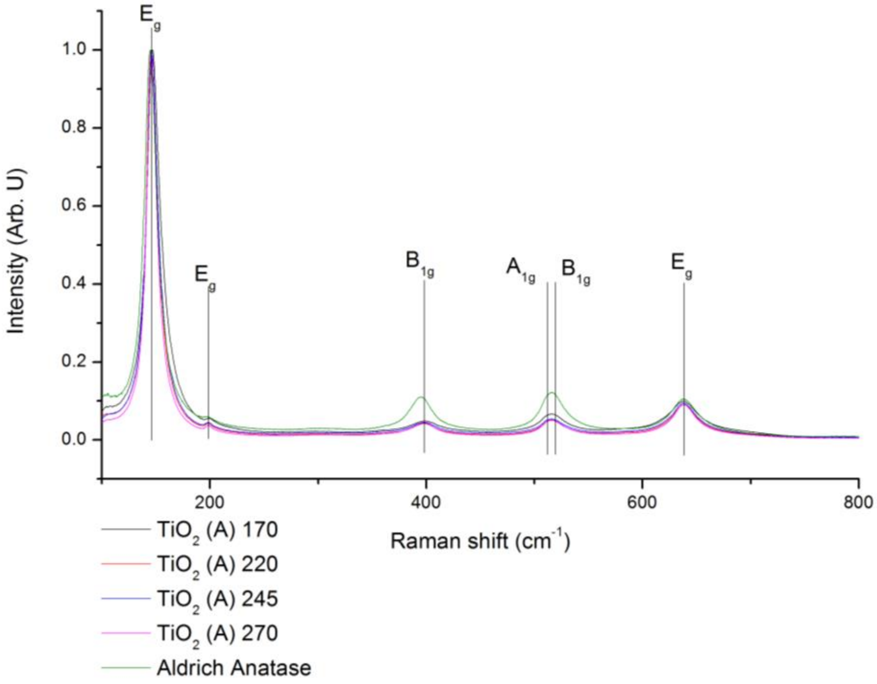

Figure 5.35 Graph displaying the Raman spectra of series (A) vs Aldrich anatase. Note: Samples TiO_2 (A) 150, TiO_2 (A) 200 and TiO_2 (A) 257 are omitted to reduce crowding.

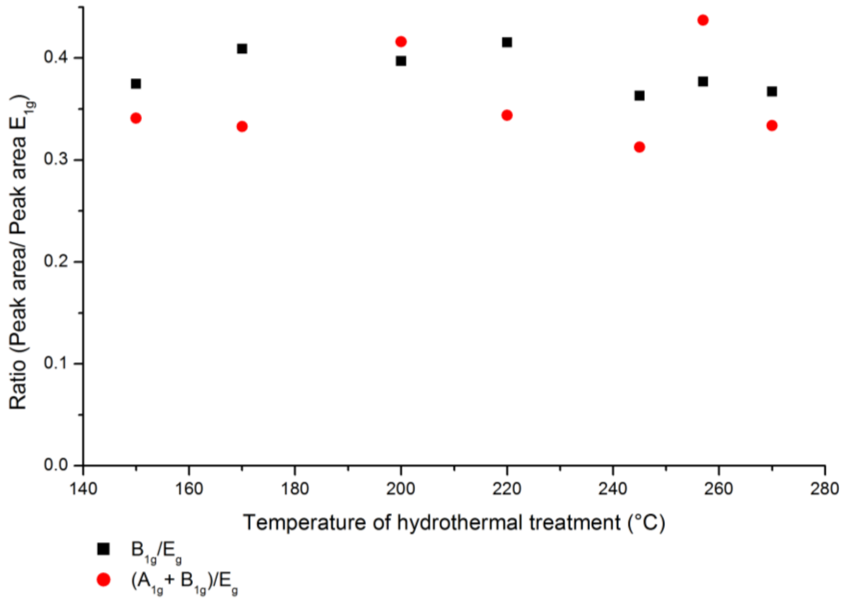

Figure 5.36 Results of fitting pseudo-Voigt functions to the A_{1g}, B_{1g} and E_g peaks, then determining the area ratio of A_{1g} and a sum of A_{1g} and B_{1g} to E_g peak areas.

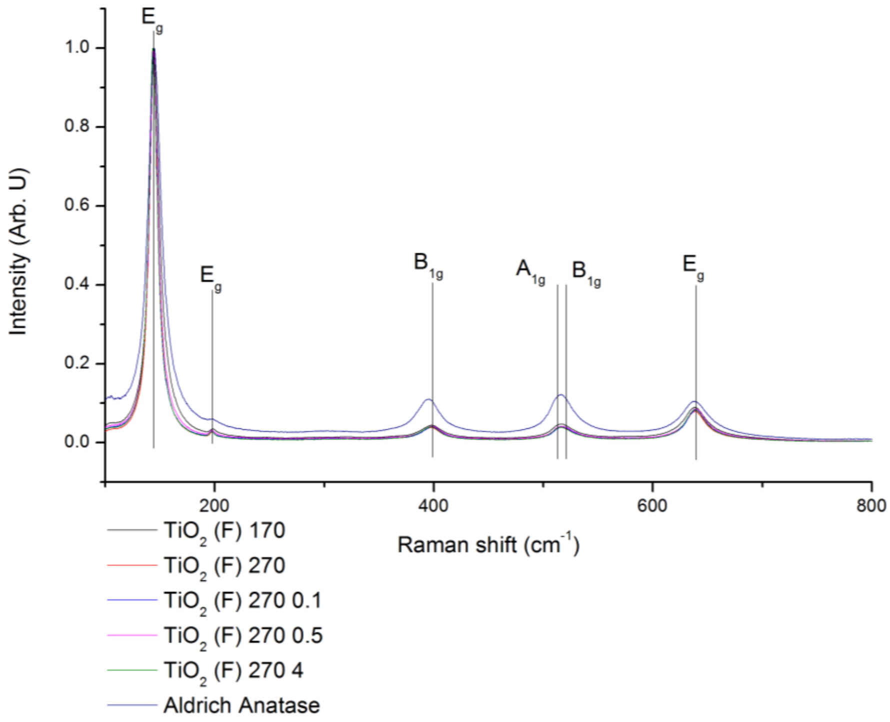

Figure 5.37 Graph displaying the Raman spectra of series (F) vs Aldrich anatase.

Since the size of crystallites has such an impact on the positions and FHWM of Raman peaks, a white and blue sample of similar crystallite size based on PXRD results, were compared to eliminate the size effects. It has been previously reported by Choi *et al.*[108], that small crystallite blue shift and broaden

Raman peaks *e.g.* from 30 nm to 12 nm (as determined by PXRD) will move the third E_g peak 1 cm^{-1} and increase its FHWM by 26 %. Secondly, it has been reported by Wei *et al.*[95], that defects and disorder in blue TiO_2 shifts and broadens the E_g peaks (the shift and broadening were not quantified). Below in *Figure 5.38* a white sample (TiO_2 (F) 270) and blue sample (TiO_2 (A) 245) with a relatively similar crystallite size (*ca.* PXRD size TiO_2 (F) 270 = 28x18 nm and TiO_2 (A) 245 = 28x14 nm) were compared. In the blue sample, the first E_g peak blue shifted from 144 cm^{-1} to 146 cm^{-1} when compared to the white sample, see inset in *Figure 5.38*. Also, the first E_g mode is significantly boarder in the blue TiO_2 when compared to the white TiO_2, see inset in *Figure 5.38*. These results indicate the blue TiO_2 synthesised in the presence of NH_4F is a more disordered crystal with diminished vibrational states related to oxygen.[49,95] As both samples had similar crystallite sizes, these observations must be caused by either the F^- doping, surface F^-, and or oxygen vacancies.

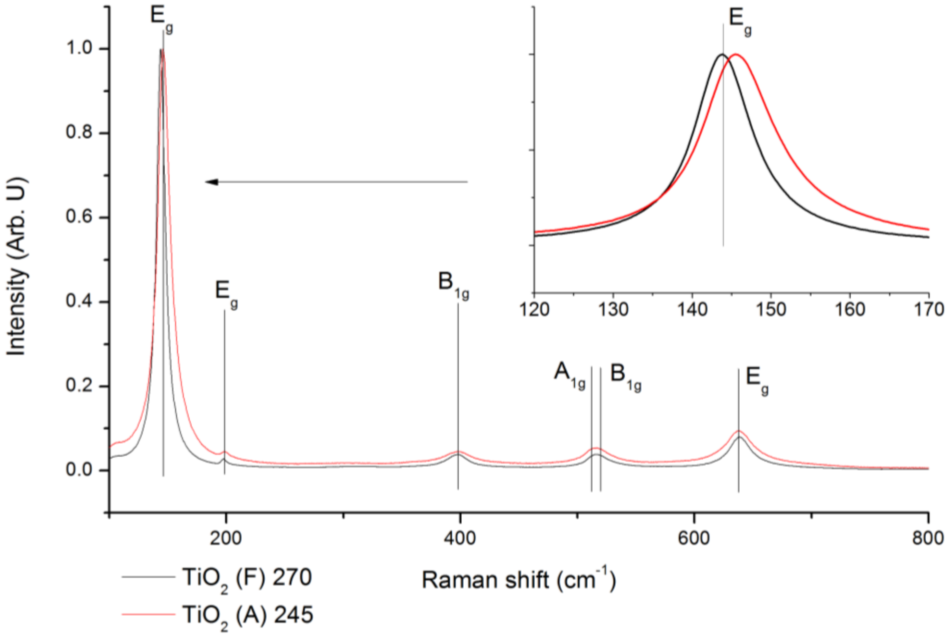

Figure 5.38 Raman spectra of a white (TiO_2 (F) 270) and blue (TiO_2 (A) 245) TiO_2. Inset close up of E_g mode.

The addition of increasing equivalents of NH_4F (series B) had a very large and quantifiable impact on the Raman spectra. First of all, when analysing the first E_g peak in *Figure 5.39*, it can be seen that such peaks for both the F^- free blank (TiO_2 (blank) F) and (TiO_2 (F) 270) samples were significantly shifted towards shorter wavelengths and had much narrower widths. As NH_4F was added to the synthesis media, the first E_g mode shifter towards longer wavelengths and broadened, see *Figure 5.39*. Pseudo Voigt peaks were fitted to the Raman data and revealed there were changes in the position and FHWM of the peaks as NH_4F was added to the synthesis media. It can be seen in *Figure 5.40* (left), the E_g peak blue-shifted to the higher wave numbers as NH_4F was added to the synthesis media, the maximum shift was observed at 0.25 equivalents NH_4F (the sample with the highest absorption at 620 nm *Section 5.1.2*). As the concentration of NH_4F was increased above 0.25 equivalents the E_g peak red-shifted back towards lower wave numbers. The shift pattern observed in *Figure 5.40*, had a remarkable resemblance to the changes in absorption at 620 nm observed through series (B) (UV-VIS DRS results in *Figure 5.21*), thus correlating with the deepening of the blue colour. Furthermore, the shift of the E_g mode through series (B) could be analysed in the light of crystalline domain sizing by PXRD (see *Figure 5.47*), where the maximum crystallite size of *ca*. 151 nm, was observed at 0.1 equivalents NH_4F and the minimum sizes where observed at 0 and 4 equivalents (*ca.* 29 nm and 18 nm, respectively). Also, of note, the second largest crystallites size (*ca.* 56 nm) was observed for the sample made using 0.25 equivalents of NH_4F. Interestingly, the E_g peak began to broaden with the addition of NH_4F reaching a maximum FHWM at 0.75 equivalents NH_4F. As the NH_4F concentration in the synthesis media was increased further to 4 equivalents the peak narrowed down slightly, although the narrowing was relatively insignificant when compared to an NH_4F-free sample, see *Figure 5.40* right. When comparing the *Figure 5.40* and *Figure 5.47,* the size effects and disorder effects can be separated out. Firstly, crystalline domain size alone cannot fully explain the peak shifts in the Raman spectra as the E_g peak of the sample made using 4 equivalents of NH_4F was shifted by a similar amount as the peak of the 0.1 equivalents sample despite having very different crystallite sizes, *ca*. 151 nm and 18 nm, see *Figure 5.40* left and see PXRD *Figure 5.47.* However, the sample made using 4 equivalents of NH_4F was substantially shifted relative to the F^- free blank, despite containing crystallites of similar size (*ca.* 18 nm and 29 nm, respectively). Additionally, the most shifted peak was observed in the case of a sample made using 0.25 equivalents which had the second largest crystalline domain size. This demonstrated the ratio of NH_4F to Ti has a much greater impact on peak position than the crystallite size domain. Furthermore, the broadness of the peaks disagrees with what is stated in the literature, which states that the peaks should be narrower with larger and more crystalline particles.[108] Yet, as shown by the broadness of the peaks in the case of 0.1 equivalents sample, despite having 150 nm crystalline domains *vs* 29 nm for the F^- free blank, the 0.1 equivalents sample has a much broader peak, see *Figure 5.40* right. Continuing to look at *Figure 5.40* (right), the FHWM increases dramatically at 0.25 equivalents and then appears to plateau out to 4 equivalents. Again, the NH_4F is having a much greater impact on the FHWM than the crystallite size domain. Finally, series (F) where NH_4F was substituted for NH_4OH showed no significant changes in the first E_g peak position or FHWM, see *Figure 5.39,* despite the changing synthesis conditions and crystallite size domain (see *Figure 5.48* for PXRD sizing). Clearly, the F^- is doping into the lattice and causing the Raman E_g mode to broaden indicating more disorder in the particles.

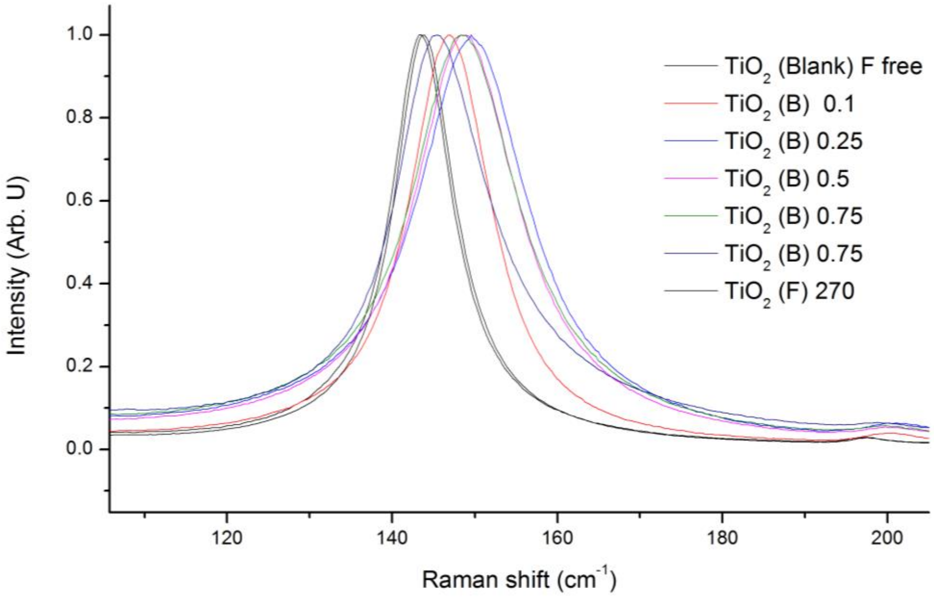

Figure 5.39 Graph displaying the Raman spectra (first E_g mode) of series (B). Note: Samples TiO_2 (Blank) F free and TiO_2 (F) 270 have been included to demonstrate mode broadening.

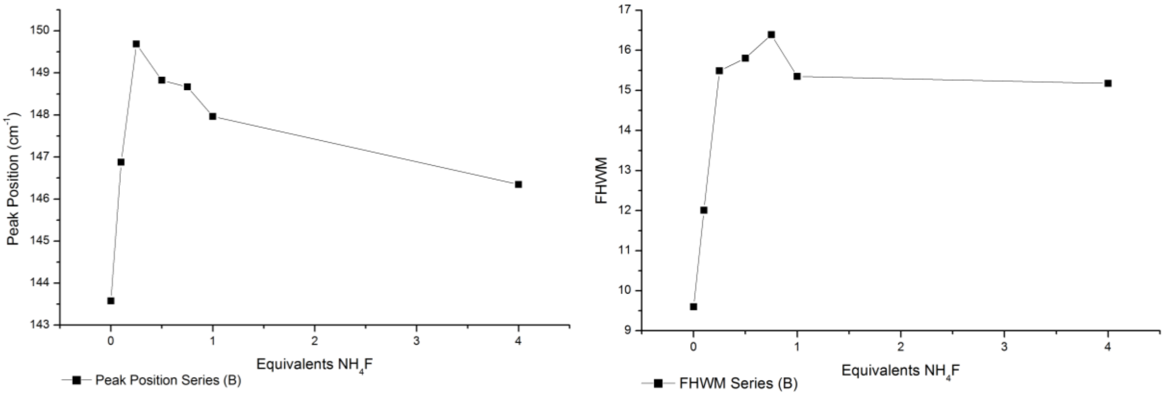

Figure 5.40 Results of fitting pseudo-Voigt peaks to the first E_g mode in series (B). Left: Peak position as a function of synthesis conditions. Right: FHWM as a function of synthesis conditions.

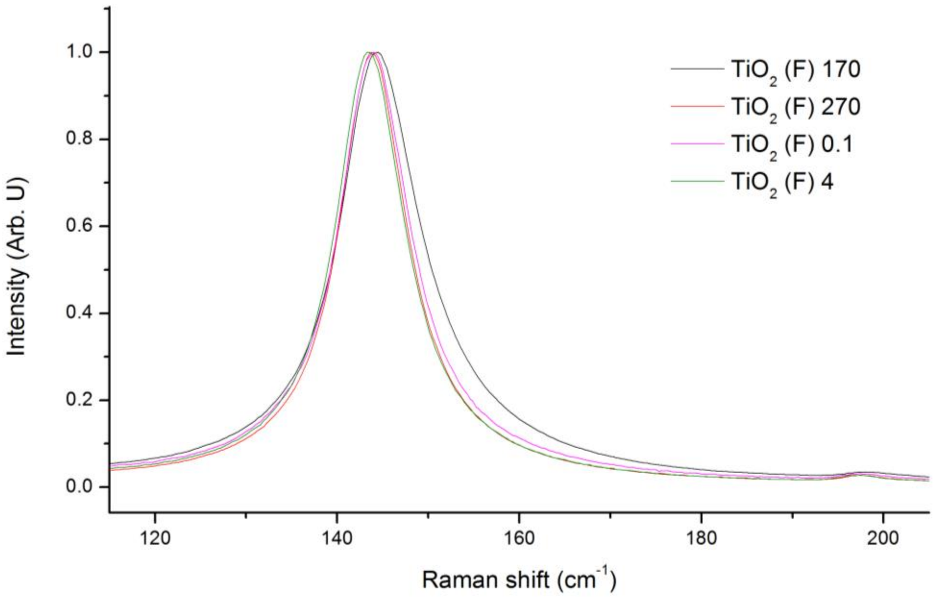

Figure 5.41 Graph displaying the Raman spectra (first E_g peak) of series (F).

Furthermore, substantial changes were observed in the B_{1g} and A_{1g} peaks with changing of the NH_4F to TiO_2 ratio. First, it can be seen in *Figure 5.42*, that the relative intensity of B_{1g}, A_{1g} and E_g to each other changed with the addition of NH_4F. In order to study how the intensity of each mode was changing, pseudo-Voigt functions were fitted to each peak. The area of each peak was compared by taking the area of the peak of interest (*i.e.* B_{1g} or (A_{1g} + B_{1g}) and dividing it by the area of the E_g peak. A similar trend was observed as above in *Figure 5.40*, as the NH_4F was added to the synthesis the area of the B_{1g} peak (relative to the E_g peak) increased rapidly peaking at 0.1 equivalents and then steeply declining as the NH_4F to Ti ratio reached 1:1, see *Figure 5.43* left. Secondly, the ratio of the combined (A_{1g} + B_{1g}) mode (relative to the E_g mode) appeared to just steadily increase with increasing NH_4F concentration. The change in the relative intensity of these modes is explained by changes in the relative concentrations of Ti_{5c}, Ti_{6c}, O_{2c} and O_{3c}; due to the exposure of different facets.[109] The relative concentrations of each of these species could be affected by the shape of the crystallites, the exposed facets or the formation of oxygen vacancies.[95,109] When looking at the B_{1g}/E_g ratio, the peak change occurs at 0.1 equivalents NH_4F to Ti, which happens to coincide with the maximum crystallite size as determined by PXRD, see *Figure 5.43* left and PXRD *Figure 5.47*. This massive change in size must change the exposed facets or the surface to bulk ratio. At 0.1 equivalents, the TiO_2 was very blue, yet the 0.25 equivalents sample had an even higher absorbance at 620 nm (*ca*. 0.17 *vs* 0.25 (*Figure 5.21*)). This observation suggests that the intensity of the B_{1g} is not directly proportional to the colour causing defects. This is also supported by the fact that series (A) showed no consistent change in the B_{1g} mode relative to the E_{1g} mode despite changing from white to blue, see *Figure 5.36* and *Figure 5.18*. The (A_{1g} + B_{1g}) to E_g ratio did not peak between 0-1 equivalents, instead, it showed a relatively consistent change where the (A_{1g}

+ B_{1g}) mode became more intense as the ratio of NH_4F to Ti increased. This increase in intensity seems likely to be independent of the colour or the crystallite size. Again the fact that series (A) showed no change in the (A_{1g} + B_{1g})/E_g ratio with increasing temperature but did show a colour change at increased synthesis temperatures, suggests that this mode is not affected by the colour-causing defects. On the other hand, it could be proportional to the F^- on the surface or as a dopant. XPS survey scans showed that the detected F^- amounts increased monotonically with increasing ratios of NH_4F to Ti, see *Figure 5.60*.

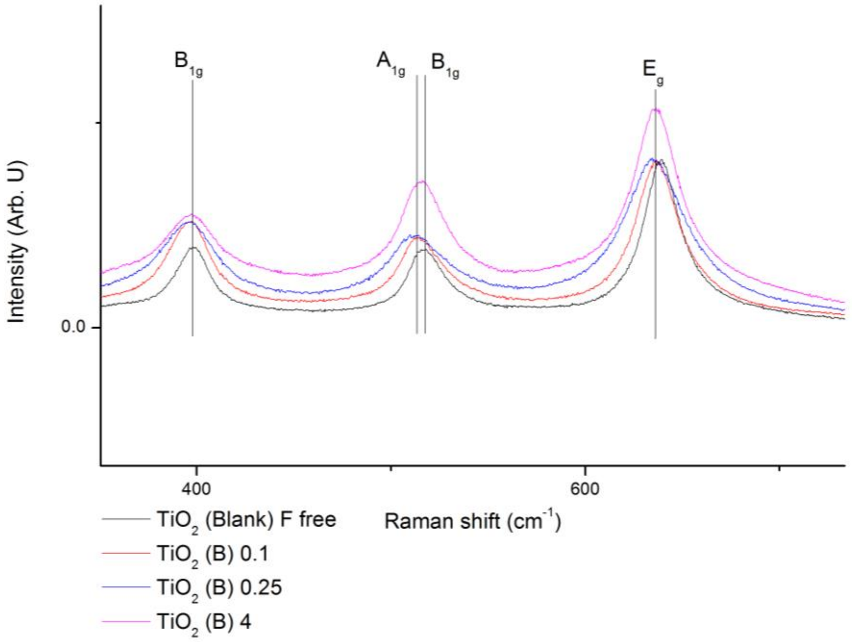

Figure 5.42 Raman spectra of B_{1g} and A_{1g} modes with respect to different equivalents of NH_4F added to the synthesis media (series B). Note: Not all spectra in the series are shown to reduce crowding of the figure.

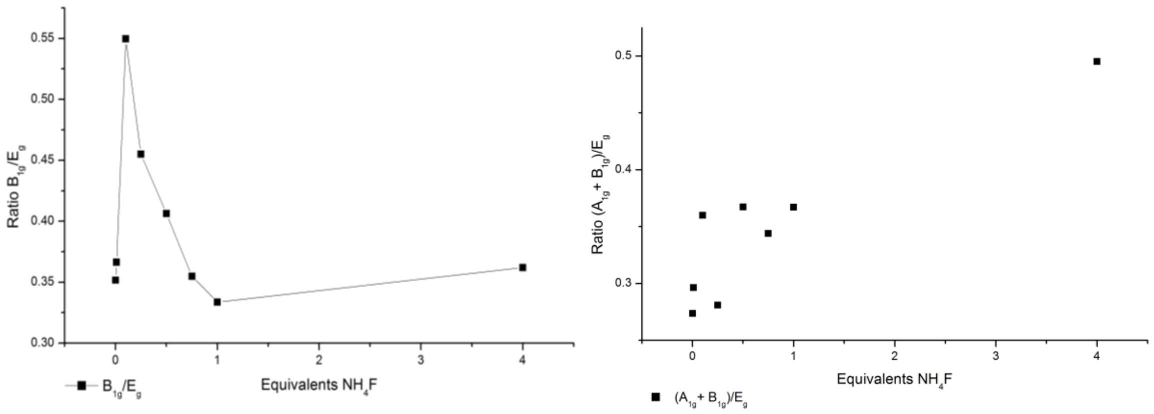

Figure 5.43 Results of fitting pseudo-Voigt functions to the E_g*,* B_{1g} *and* A_{1g} *peaks of Raman spectra throughout series (B). Left: The ratio of the peak area of* B_{1g}/E_g*. Right: The ratio of the peak area of* $(A_{1g}+B_{1g})/E_g$*. Note: Lines have been added to guide the eyes and not link to results.*

5.1.6 Synchrotron Powder X-ray Diffraction study of Blue TiO_2

PXRD results from the Australian Synchrotron were analysed using Rietveld refinement. Variable that were refined include the crystallite shape, size, unit cell dimensions, cell volume and atomic occupancies. All these variables could be refined due to the excellent data quality. It can be seen in *Figure 5.44* that highly crystalline samples gave very high-resolution diffraction patterns. The following section will discuss the results of each parameter that was refined.

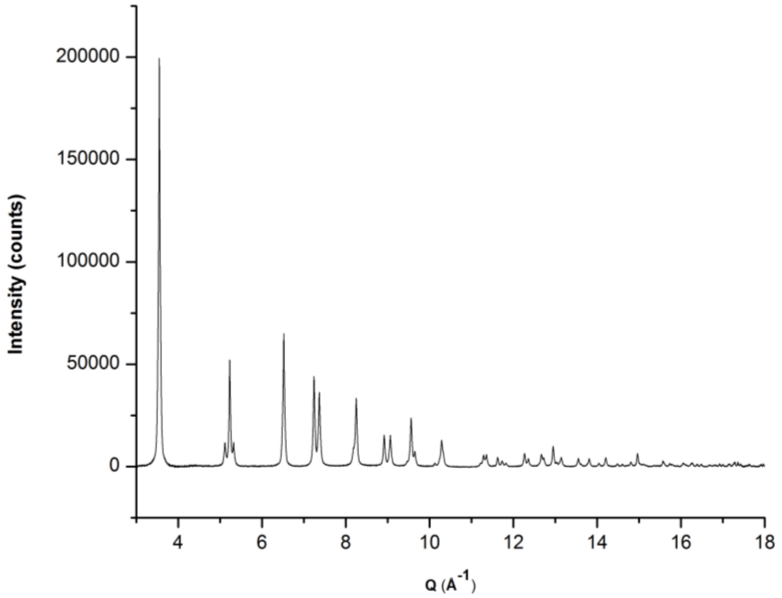

Figure 5.44 The synchrotron radiation PXRD pattern of TiO_2 *(A) 270.*

The shape of crystallites can be determined from line broadening of specific peaks in the diffraction pattern. With the hydrothermal synthesis of blue TiO_2, the crystallites frequently preferentially grew along the [001] direction. When modelling the diffraction patterns, first an isotropic crystallite shape was fitted but, as can be seen in *Figure 5.45*, there was a significant mismatch in the peak area for the {004}, {015} and {022} peaks. This is indicative of crystallites being both anisotropic in shape and orientated. The elongation of the crystallites in a single direction results in the sharpening of specific peaks. Also, the elongated crystallites will preferentially orientate themselves resulting in larger specific peaks areas. To model these anisotropic crystallites, the anatase phase TiO_2 was fitted using two crystallite structures, one to represent the elongated dimension and another to represent the shorter dimensions. Both structural phases are refined at the same time, however, the phases were linked together by as many variables as possible so, the only parameter changing is the size in each direction (see *Section 3.2.1* for more detail).

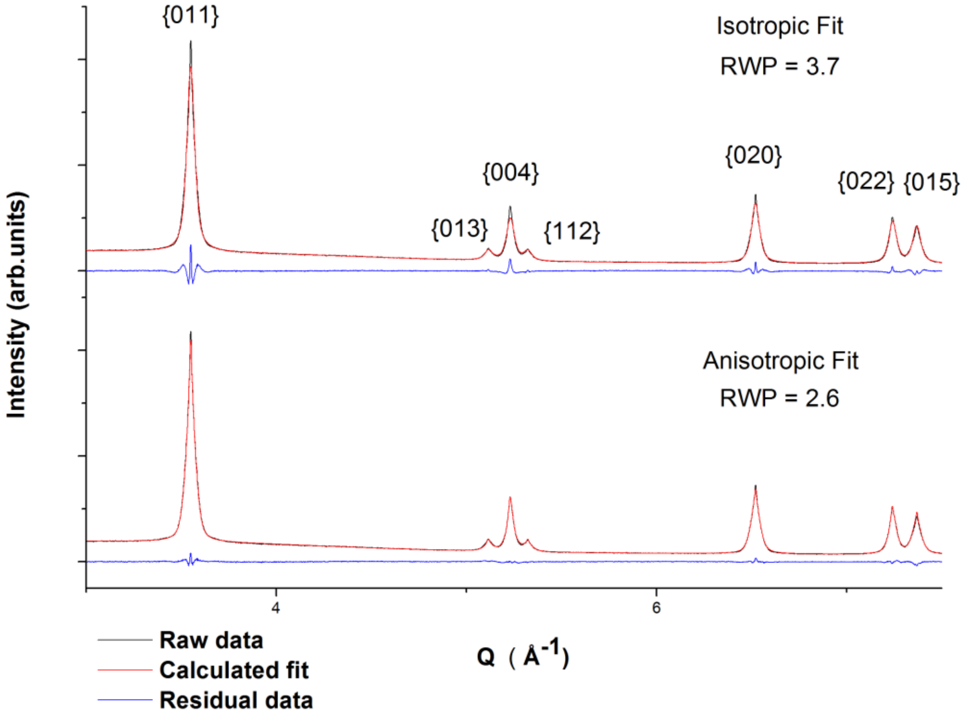

Figure 5.45 PXRD results from the blue TiO_2 sample (TiO_2 (A) 270), showing the difference between modelling isotropic crystallites and anisotropic crystallites.

The shape and size of crystallites in series (A) were examined using the aforementioned Rietveld refinement. It was found that TiO_2 crystallites synthesised hydrothermally using temperatures ranging between 170 and 245 °C have very similar shapes and overall size, see *Figure 5.46*. They are slightly elongated (aspect ratio of *ca.* 2.5) along the [001] direction and isotropic between the [100] and [010] directions, see *Figure 5.46*. When hydrothermally treated at 270 °C the crystallites produced are much larger overall (*ca*. 12x47 nm) and slightly more elongated along the [001] direction (aspect ratio of *ca*.3.9). Blank samples of TiO_2 were also synthesised using the same conditions as TiO_2 (A) 270 but without either the NH_4F or organics (isopropanol) present, *i.e.* samples TiO_2 (C free) and TiO_2 (F free) respectively. When no NH_4F was present, the crystallites were isotropic in shape, whereas when NH_4F was present but no organics were present, particles had similar elongation (aspect ratio of *ca.*2.5) as those synthesised with organics *i.e.* similar to (TiO_2 (A) 270), see *Figure 5.46*. These results point to the NH_4F as the main factor contributing to the elongation along the [001] direction. Thus far, it is not clear as to whether it is the influence of the NH_4^{4+} or F^- ion. The literature states that the F^- ion should bind to the {001} facet and cause growth in the [100] and [010] direction.[28] Clearly, the PXRD results suggest the crystals have grown preferentially in the [001] direction, which is inconsistent with what is stated in the literature. Initially, these results could indicate the NH_4^+ ion maybe more influential in crystallite growth than F^-. NH_4^+ maybe influencing the crystal growth by the *in-situ* formation of ammonium titanate. The ammonium titanate must behave much like sodium titanate which is known to cause elongation along the [001] axis.[132,133]

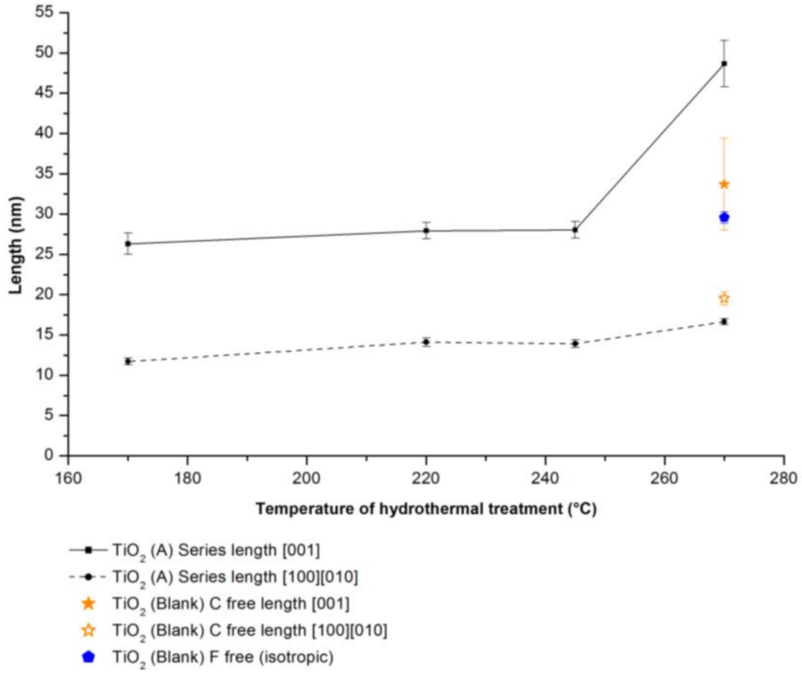

Figure 5.46 Dimensions in nm of crystallites in series (A) as determined by the Rietveld refinement of PXRD data. Note: Lines have been added to guide the eyes and not link to results.

The relationship between crystallite size and NH_4F concentration was examined through series (B). It was found that very low levels of NH_4F (0.01 equivalents), had no significant impact on the size of the crystallites. Yet, as the concentration was increased to 0.1 equivalents there was explosive growth producing a primary crystallite size of greater than *ca.* 300 nm, see *Figure 5.47*. Very quickly as the equivalents of NH_4F exceed 0.1 the crystallites became smaller and eventually, the NH_4F appeared to suppress the growth of the crystals. As crystallites synthesised with 0.5 equivalents or greater are smaller than the F^- free blank, see *Figure 5.47*. The explosive growth was confirmed by TEM, see *Figure 5.78*. It should be noted that the majority of samples through series (B) showed elongation in the [001] direction, however, *Figure 5.47* shows only the isotropic size as the elongation could not be determined for the larger crystals (due to the line broadening being too similar to the instrumental broadening).

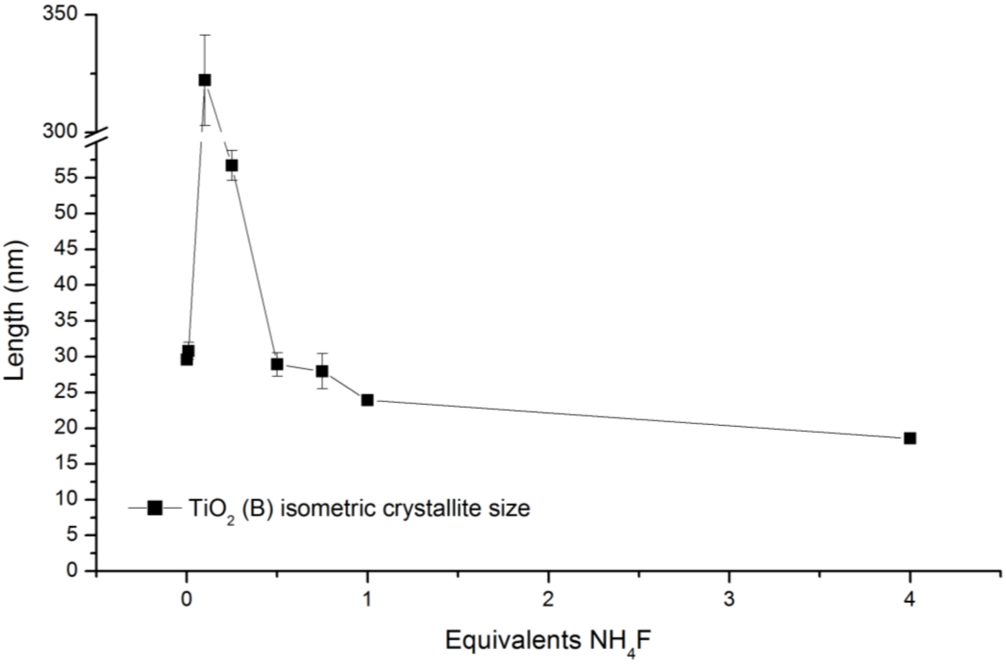

Figure 5.47 Dimensions in nm of crystallites in series (B) as determined by the Rietveld refinement of PXRD. Note: This data was fitted assuming an isometric crystallite shape. Note: Lines have been added to guide the eyes and not link to results.

Series (F) where NH_4F was substituted for NH_4OH, showed a similar degree of elongation in the [001] direction as was observed for series (A). The elongation was greatest at lower, sub-220 °C temperatures of hydrothermal treatment. Increasing the temperature of hydrothermal above 220 °C reduced the elongation. However, the elongation remained relatively constant at higher temperatures of hydrothermal treatment, see *Figure 5.48* left. Furthermore, the number of equivalents of NH_4OH added to the synthesis had a large impact on the size of the crystallites produced and their shape. At 0.25 equivalents NH_4OH the crystals were large and elongated in the [001] direction (*ca. 17x105 nm)* whereas, as more NH_4OH was added the crystals became smaller and less elongated. The explosive growth of the particles at low NH_4OH equivalencies was also seen in series (B) with the addition of 0.1 to 0.25 equivalents of NH_4F. These results confirm that the growth and elongation of crystallites due to the NH_4^+ ion rather than the F^- ion. Thus, confirming that *in-situ* ammonium titanate must control the growth of crystallites in the current hydrothermal synthesis. However, it is not clear as to how NH_4^+ promotes growth at low concentration and then suppresses it at high concentration.

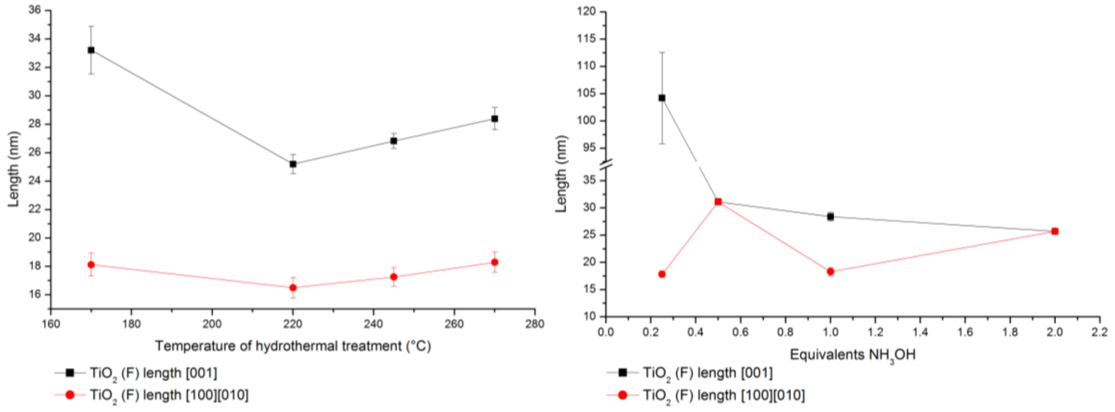

Figure 5.48 Dimensions in nm of crystallites in series (F) as determined by the Rietveld refinement of PXRD data. Left: Temperature dependency. Right: Concentration dependency.

Further evidence pointing towards the NH_4^+ ion playing the main role in enhancing crystal growth is series (C) where NH_4F was substituted for NaF. In series (C), the sample made using 0.1 equivalents of NaF did not show any elongation (*ca.* 30 nm isotropic). Conversely, the 1 equivalent sample showed the [001] axis to be compressed indicating the [100] and [010] axes were actually elongated (*ca.* 7x16 nm). This is the expected effect of F^- ions binding to the surface of the {001} facet preventing growth in the [001] axial direction.[28] Based on the hypothesis that a titanate type mechanism is controlling growth, it would be expected that the elongation should have increased as the ratio of Na^+ to Ti increase. There is literature reports of sodium titanate becoming more elongated along the [001] axis as the ratio of Na to Ti is increased.[132,133] Conversely, this does not appear to be the case here. However, the lack of elongation also supports the theory that the NH_4^+ ion was responsible for the shape and size of crystallites produced in series A, B and F. Clearly, the titanate formation is influenced by the cation. Above, the NH_4^+ ion increased crystal growth up to 0.25 equivalent, then it suppressed crystal growth up to 1 equivalent but still produced elongated crystals. Finally, at 4 equivalents, it suppressed growth and yielded isometric crystallites. Whereas, Na^+ at 0.1 equivalents produced small isometric crystallites, at 1 equivalent the [001] axis was compressed. Finally, at 4 equivalents the Na^+ converted the anatase to brookite (discussed in Chapter 6). It is proposed that the decreased size of the Na^+ ion (116 pm) relative to the NH_4^+ ion (151 pm) increases its activity as a titanate forming agent. That is to say, 0.1 equivalents Na^+ would have the same effect as 4 equivalents of NH_4^+. Hence, NH_4^+ would probably compress the [001] axis and induce a phase change at much higher equivalencies. Thus the Na^+ ion is controlling the growth of crystallites in the same fashion as NH_4^+ was but, it is more effective at doing so. Although it must be said, why NH_4^+ and Na^+ ion suppress growth and reduce elongation at higher concentration is still unclear.

The final observation made in series (C) was that the samples grown with greater than 0.1 equivalents of NaF showed a bi-modal distribution of crystallite sizes. It can be seen in *Figure 5.49*, the PXRD diffractogram shows broad peaks with sharp points at the top of each peak. The broad part of the peaks represents the smaller crystallites determined to be *ca*. 7x16 nm and making up the bulk of the sample. The sharp points represent another population of crystals determined to be *ca*. 160 nm (assumed to be isometric as there was insufficient data to refine the shape). The bi-modal size destitution could also be seen when 4 equivalents of NaF was added to the synthesis media and brookite phase TiO_2 was produced, see Chapter 6.

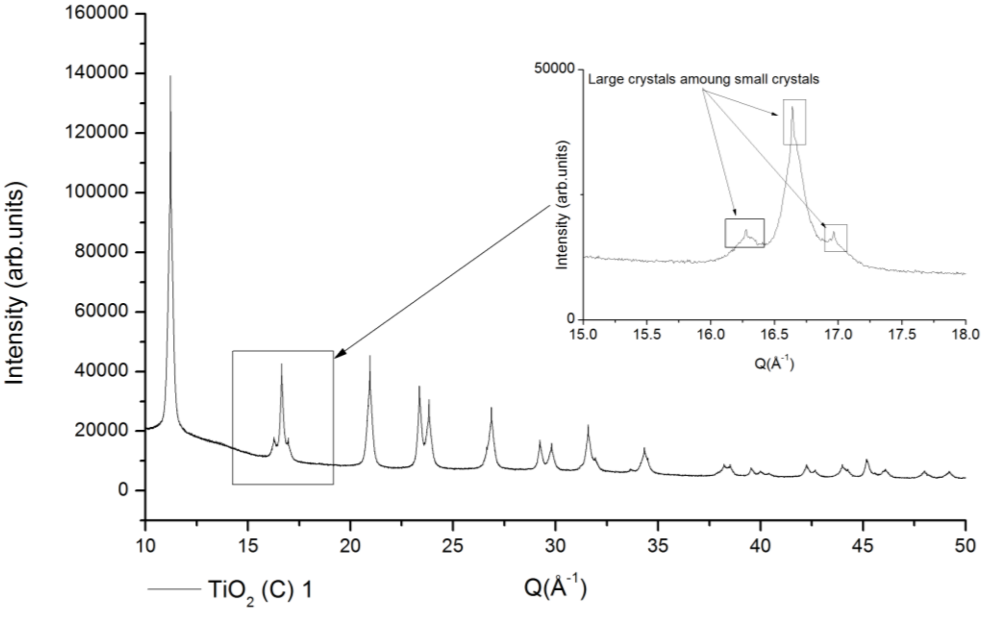

Figure 5.49 PXRD diffractogram of TiO_2 (C) 1 showing the existence of two populations of crystallites of different sizes. One type of crystallites are small producing the broad bulk of the diffractogram. The other crystallites are very large, producing well-defined tips on top of the existing peaks (see inset).

There is clear evidence that the growth and shape of the crystallites produced are affected by the modifying agents added to the synthesis media. The impact of each modifying agent is hard to grasp on its own. Yet, when looking at the facts, NH_4F and NH_4OH both cause the crystals to become anisotropic showing a longer [001] axis. Though, the anisotropic crystals were only produced in a narrow range of modifier concentrations. NaF did not produce anisotropic crystals at any concentrations tested. NH_4F and to a lesser extent NH_4OH, both made the crystallites grow much larger at lower concentrations. Conversely, at higher concentrations, NH_4OH and NH_4F suppressed the growth of crystallites. On the other hand, NaF did not increase the growth at lower concentrations instead, it suppressed growth. Contradictorily to what is stated in the literature, the F^- ion in the NH_4F modified series did not appear to bind to the surface of the {001} facet and force the growth in the [100] and [010] directions.[28,29,33,64] Nor was there any evidence of nano-spheres, hollow spheres or selective facet etching as others have reported when using NH_4F in a hydrothermal synthesis.[32,35,66,67,134] Although, in series (C), it appeared that the NaF suppressed the growth in the [001] axis as is expected from F^- containing modifying agents.[28,29,33,64]

If it is assumed that the F^- is having little impact on the shape and size of crystallites, then that leaves the cation as the shape controlling agent. One possible mechanism influencing the growth of crystallites is the formation of *in-situ* titanates. It is well known that NaOH can react with TiO_2 to produce sodium titanate.[135] Less well known is that NH_4OH can form ammonium titanate.[133] If ammonium titanate is forming in solution, then it may be aiding the transportation of TiO_2 building blocks which enhances the growth of the crystallites. However, at higher concentrations, the growth of crystallites is suppressed (even in NH_4OH-modified systems where F^- was not present) which can not be explained easily. Equally, sodium and ammonium titanate typically form rod-like structures elongated in the [001] direction (the *c* axis).[132,133] If this is occurring in the hydrothermal synthesis, then it would explain the elongation of the anatase phase crystals. The NH_4^+ ions may initially substitute into the TiO_2 structure by acting as the counter-charge between layers of titanate. Subsequently, the NH_4^+ is leached out by the F^- ions creating the pathway for the apparent F^- doping that occurs (see XPS and ion beam analysis *Sections 5.1.7* and *5.1.9* respectively). It is hypothesised that the growth of TiO_2 crystallites is controlled *via* a titanate mechanism. Although there is no conclusive evidence for the following explanation, it may explain some of the observed changes in crystallite size. During the hydrothermal treatment, the solution becomes supersaturated with titanate. At low concentration of modifiers, the saturation level sits in the “metastable zone” causing the growth of existing crystallites. However, as the concentration of the modifier is increased, the supersaturation level crosses over into the “labile zone” causing rapid uncontrolled nucleation. This explains why the crystallites become smaller as the concentration of the modifier increase. It also may explain the bi-modal population observed in the NaF modified sample.

The unit cell dimensions (*a*) and (*c*) were also analysed during PXRD Rietveld refinement. The exact diffraction angle of the peaks can be used to calculate the crystallographic lengths describing the unit cell. The cell volume is the product of the dimensions (*a*) multiplied by (*c*) cubed in both anatase and rutile. The volume of the unit cell is influenced by crystallinity. It is believed that better packing of atoms and fewer defects decreases the unit cell volume.[136] Likewise, the individual lengths (*a*) and *(c)* can be influenced by defects or packing faults independently *i.e.* defects may cause an expansion of (*c*) but not affect the length of (*a*).[111]

In series (A), Rietveld refinement of the unit cell dimensions (*a*) and (*c*) showed that (*a*) and (*c*) were independently influenced by the addition of NH_4F and the temperature of hydrothermal treatment. First, the (*a*) dimension showed a contraction from 3.7917 Å to 3.7887 Å with increasing temperature of hydrothermal treatment, see *Figure 5.50* left. This is quite a significant contraction and is most likely due to an increase in crystallinity with increased temperature of synthesis.[137] Yet, the (*a*) dimension in TiO_2 (A) 270 sample is still significantly longer than (*a*) in P-25 (a highly crystalline commercial TiO_2) at 3.7857 Å. These results suggest that TiO_2 (A) 270 is still lacking in crystallinity compared to P-25.[111,137] The two blanks give more insight into what may be happening. The organic (isopropanol) free blank (TiO_2 (Blank) C free) only shows a slight contraction in (*a*) whereas the NH_4F free sample (TiO_2 (blank) F free) shows a significant contraction in (*a*) at 3.7863 Å. Thus, the F^- free sample's (*a*) is nearly identical to the length of (*a*) in P-25, see *Figure 5.50* left. So, NH_4F expand (*a*) as does lower temperatures of hydrothermal treatment. Higher temperature hydrothermal treatment contracts (*a*). Finally, the presences of organics, and thus the blue colour and O vacancies and Ti^{3+}, has minimal impact on (*a*). On the other hand, the behaviour of (*c*) is more complicated. The effects of temperature are divergent, see *Figure 5.50* right. The dimension (*c*) expands with increasing temperature of hydrothermal treatment from 220 ºC to 270 ºC towards that of P-25. However, at 170 ºC, (*c*) is longer than at 220 ºC, which is unexpected. Furthermore, the blank samples show different behaviours. The F^- free (TiO_2 (blank) F free)) sample showed a contracted (*c*) dimension whereas the organic free (TiO_2 (blank) C free)) sample showed an expanded (*c*) when compared to TiO_2 (A) 270, but it was still shorter than in P-25. The divergent behaviour between samples treated either side of 220 ºC maybe an effect of the decomposing organics or F^- incorporation. It is known that the samples synthesised below 200 ºC do not become blue under any conditions suggesting a lack of Ti^{3+} defects. It is also known that with increasing temperature of hydrothermal treatment the crystallinity of samples should increase expanding (*c*) towards the same length as P-25.[137] Sample TiO_2 (A) 170 displayed a longer (*c*) than TiO_2 (A) 220 may be due to a lack of decomposing organics required to produce the reducing conditions necessary for the formation of Ti^{3+}. This results in the 170 °C sample being more crystalline than the 220 °C and even the 245 °C sample due to very low populations of Ti^{3+}. Whereas sample TiO_2 (A) 270 displaying a longer (*c*) is possibly due to the overall increased crystallinity (caused by the high temperature) outweighing the effects of defects and/or F^- doping. The fact the organic free and low-temperature samples expanded (*c*) towards the length of (*c*) in P-25 is clear evidence the reducing conditions do contract (*c*). Furthermore, the fact the organic free sample expanded (*c*) towards the length of (*c*) in P-25 but, there was only a relatively small change in (*a*) with the organic free sample, is indicative of the colour forming defect existing along the (*c*) lattice direction. Conversely, the fact the F^- free sample contracted (*a*) towards the same length as (*a*) in P-25 but expanded (*c*) away from P-25 is indicative of the F^- doping or NH_4^+ impacting the (*a*) lattice dimension.

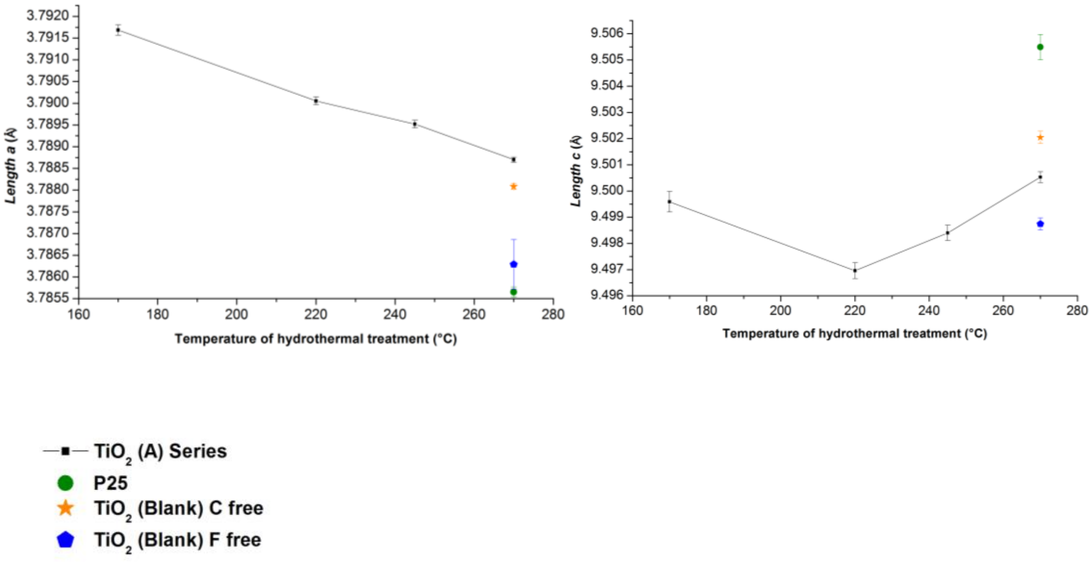

Figure 5.50 Crystallographic lengths (a) and (c) as determined by Rietveld refinement of PXRD data of blue TiO_2 series (A).

PXRD refinement of the lattice dimensions through series (B) showed the ratio of NH_4F dramatically changed the lattice parameters. Firstly, it was found that increasing the ratio of NH_4F to TiO_2 caused the (*a*) dimension of the lattice to expand, see *Figure 5.51* left. Whereas the addition of NH_4F initially increased the length of (*c*), peaking at 0.1 equivalents, then the lattice dimension contracted as the number of equivalences increased to 4, see *Figure 5.51* right. For reference, the length of (*a*) in the sample synthesised with 4 equivalents of NH_4F was 3.7929 Å whereas it is only 3.7857 Å in P-25. Likewise, the length (*c*) was 9.4915 Å *vs* 9.5055 Å for P-25. Interestingly, the sample synthesised with 0.1 equivalents NH_4F, had a (*c*) of 9.5057 Å making it the same length as P-25 when considering errors. Yet, its (*a*) length was 3.7865 Å making it still longer than (*a*) in P-25 (3.7857 Å). The near monotonic increase in (*a*) with increasing NH_4F shows (*a*) is fairly independent of crystal size as it did not show any non-linear behaviour around 0.1-0.5 equivalents where the explosive growth occurred, see *Figure 5.47*. Thus confirming what has been stated above, that NH_4F effects the lattice dimension (*a*). Whereas, the (*c*) dimension showed trends that could be simply explained by the changes in crystallinity related to the crystal size.[137]

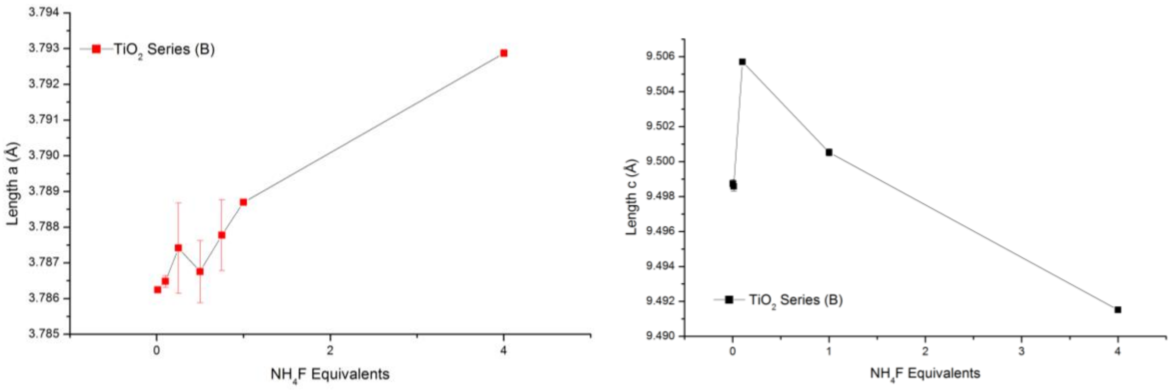

Figure 5.51 Crystallographic lengths (a) and (c) as determined by Rietveld refinement of PXRD data of blue TiO_2 *series (B).*

Series (F) samples were examined in the same fashion. It was found that the temperature of hydrothermal treatment contracted the (*a*) lattice dimension much like series (A) above. However, the length of (*a*) proportionally changed much less and also started much shorter than in series (A) *i.e.* TiO_2 (F) 170 *a* = 3.78861 Å *vs* TiO_2 (A) 170 *a* = 3.791684 Å, see *Figure 5.52* (top left) and *Figure 5.50* (left). The length of (*c*) expanded with increasing temperature of hydrothermal treatment much like in series (A). Yet again, the starting (*c*) length of series (F) was larger and the final length much closer to that of P-25 *i.e.* TiO_2 (A) 270 = 9.5005 Å, TiO_2 (F) 270 = 9.5005 Å and P-25 = 9.5005 Å. Also of note, there was no contraction of (*c*) as the temperature of hydrothermal treatment increased and the organics decomposed *i.e.* TiO_2 (A) 220 above in *Figure 5.50* right. The lengths of (*a*) and (*c*) were much closer to those of P-25 than the samples in series (A), thus indicating the changes in lattice dimensions is due to F^- doping rather than NH_4^+ titanate formation.

Next, the effects of the ratio of NH_4OH to TiO_2 were evaluated. It was found that the lattice dimension (*a*) did not seem affected by the number of equivalents of ammonia added to the synthesis media, see *Figure 5.52* (bottom left), if anything, the (*a*) lattice dimension appeared to contract slightly. This behaviour was very different from what was observed in series (B), where the addition of NH_4F expanded the lattice greatly, compare *Figure 5.52* (bottom left) and *Figure 5.51* (left). On the other hand, the (*c*) lattice dimension was expanding with the addition of more NH_4OH, pushing its length closer to the length observed for P-25. This was the complete opposite behaviour as observed above with series (B), where the addition of NH_4F contracted the length of (*c*), compare *Figure 5.52* (bottom right) and *Figure 5.51* (right). There was no evidence of the crystallite size of affecting (*a*) and (*c*); shown by the linear behaviour around 0.1 equivalents NH_4OH where the crystallites grew quite dramatically, see *Figure 5.48*.

.

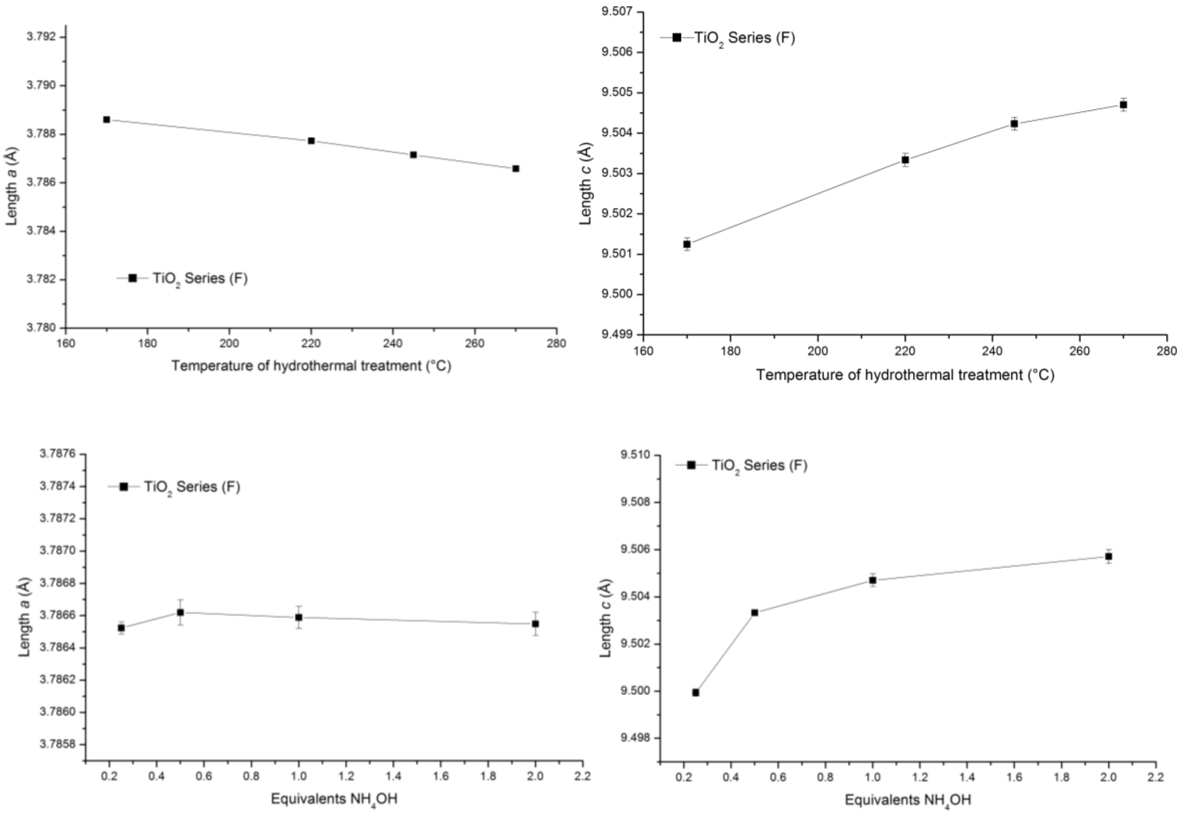

Figure 5.52 Crystallographic lengths (a) and (c) as determined by Rietveld refinement of PXRD data of blue TiO$_2$ series (F). Top: Temperature series. Bottom: Concentration series.

For a final compassion, series (C) was examined in a similar fashion. However, due to the formation of brookite phase TiO$_2$ only 2 samples were available for comparison. Series (C) showed that both the (*a*) and (*c*) lattice dimensions expanded relative to the F$^-$ free blank (TiO$_2$ (blank) F free) with the addition of NaF. The length of (*a*) explained from 3.78629 Å at 0, to 3.78631 Å at 0.1 equivalents of NaF, to 3.78635 Å at 1 equivalent of NaF, respectively. The length of (*c*) expanded from 9.4987 Å at 0, to 9.4991 Å at 0.1, to 9.4995 Å at 1 equivalent NaF respectively. The expansion of (*a*) with the addition of NaF is in agreement with series (B) above, where (*a*) also expanded with the addition of NH$_4$F. However, the expansion was relatively insignificant when compared to the expansion in series (B) *i.e.* a change of 0.000057 Å for series (C) (effectively zero) *vs* 0.002411 Å for series (B). This showed the addition of NaF had a very little impact on the length of (*a*). On the other hand, the length of (*c*) increased with the addition of NaF to the synthesis media, whereas the overall length of (*c*) got shorter with the addition of NH$_4$F in series (B). Unlike the (*a*) dimension, the change in the length of (*c*) through series (C) was of a similar order of magnitude as in series (B) *i.e.* a change of 0.0007 Å for series (C) *vs* 0.0018 Å for series (B). There was no dramatic change in crystallite size (compared with series (B)) observed through series (C), with *ca.* 29.9 nm isotropic to 6.9x15.5 nm anisotropic particles, thus, ruling out any crystallite size effects.[137] Therefore the expansion of (*c*) in series (C) is opposing what was observed in series (B). Finally, an organic free sample was produced and modified with 1 equivalent NaF. This sample showed a large expansion of the (*c*) dimension but, the (*a*) dimension stayed relatively unchanged. This result is very similar to the series (A) organic free sample. This is further evidence towards the reduction caused by the decomposing organics expanding the (*c*) dimension, possibly indicating the reduction aids the F^- doping.

These results suggest the NH_4^+, F^-, Na^+ and reducing conditions all play a role in manipulating the lattice dimensions. Increasing the temperature of hydrothermal treatment shortens (*a*) and lengthens (*c*) as shown by series (A) and (F), see Table 5.4. Shortening (*a*) and lengthening (*c*) pushes the lattice dimensions towards being a well-crystalline, defect-free crystal such as P-25.[137] The addition of NH_4^+ ions in combination with OH^- ions have a negligible effect on the length of (*a*), yet, presence of these species results in longer (*c*) dimensions as shown by series (F). Whereas the combination of NH_4^+ and F^- ions expands (*a*) and shortens (*c*), which is the only reagent tested to contract (*c*). Finally, the combination of Na^+ and F^- ions expands (*a*) and (*c*), but the effects are minimal. Reducing conditions in combination with F^- expands (*c*) as shown by the comparison of series (A) with blank samples. When looking at the scale of change, it becomes evident that the NH_4F has the largest impact on the unit cell (series (B)), followed by temperature as shown by series (A) and (F), followed by NaF (although negligible).

Series	**Variable**	**Change in (*a*) (Å)** (First result in series – last result)	**Change in (*c*) (Å)** (First result in series – last result)
A	Change in Temperature	0.002983 (contraction)	-0.00094 (expansion)
B	Change in NH_4F concentration	-0.00662 (expansion)	0.00707 (contraction)
C	Change in NaF concentration	-0.00006 (expansion)	-0.00075 (expansion)
F	Change in Temperature	0.002021 (contraction)	-0.00346 (expansion)
F	Change in NH_4F concentration	-0.000025 (expansion)	-0.00577(expansion)

Table 5.4. Table showing the total change in length of unit cell dimensions from start to finish of series as calculated by PXRD.

The expansion of (*a*) and the contraction of (*c*) through series (B) with increasing NH_4F:TiO_2 ratio is indicative of the formation of Ti vacancies.[102] Wang *et al.*[102] used DFT calculations (verified experimentally) to calculate the changes in lattice dimensions of small clusters with Ti vacancies and interstitial O. The calculations showed Ti vacancies contracted (*c*) from 9.481 Å (stoichiometric) to 9.372 Å (Ti deficient). Alternatively, interstitial O was shown to expand (*c*) from 9.548 Å (stoichiometric) to 9.511 Å (interstitial O). On the other hand, the length of (*a*) changed very little in the modelled clusters for both interstitial oxygen and Ti vacancies. The total change in (*a*) modelled form intestinal O and Ti vacancy was 3.804 Å (stoichiometric TiO_2) to 3.811 Å for the defect-rich case. Series (B) showed (*a*) expanded from 3.787 Å to 3.793 Å, which means the (*a*) dimension was still significantly shorter than what was theoretically modelled and measured in P-25. However, P-25 also gave a smaller value for (*a*) than reported by Wang *et al.*[102] (*ca.* 3.786 Å). So either the model is wrong or the small cluster shows a large size effect when compared to the 20 nm sized particles in P-25. Either way, these clusters are only used to look at the relative change in the lattice dimensions.[102]

The changes in the unit cell above indicated the possibility of Ti vacancies.[102] Ti occupancy was the last parameter of the refinement reviewed. Ti occupancy is estimated from the relative intensity of peaks associated with diffraction from Ti or O atoms.[110] Again, Ti occupancy is related to crystallinity, substitution and doping.[138]

It can be seen that the hydrothermally synthesised anatase is deficient in Ti atoms, see *Figure 5.53*. As the temperature of hydrothermal treatment was increased (series (A)), the Ti occupancy increased towards 100 %, see *Figure 5.53* left. This is expected as the crystallinity should increase with higher temperature resulting in fewer Ti vacancies.[113,139] However, at one equivalent NH_4F, the Ti occupancy never reaches 100 %, topping out at 97 +/- 0.5 %, see *Figure 5.53* left (Note: errors were based on the fitting of data and an output of the Rietveld Refinement). Bokhimi *et al.*[139] reported Ti vacancies are a result of OH^- inclusions due to incomplete hydrolysis.[139]

When the ratio of NH_4F is altered with respect to TiO_2 (series (B)) the occupancy of Ti behaves very differently. At 0.1 equivalents NH_4F, where the crystallites are very large (see *Figure 5.47*), the Ti occupancy exceeds 100 % relative to oxygen, indicating the TiO_2 is oxygen deficient, see *Figure 5.53* right. Increasing the ratio of NH_4F further decreases the Ti occupancy resulting in only 91 % occupancy at 4 equivalents NH_4F to Ti. The reduced Ti occupancy coincides with the observed decrease in crystallite sizes seen in both TEM and PXRD *Figure 5.80* (bottom) and *Figure 5.47*. Formation of smaller particles at high concentrations of NH_4F also coincides with observation of the longest (*a*) and shortest (*c*) unit cell lengths at the end of series (B), see *Figure 5.51* left, which is another indication of enrichment of TiO_2 with Ti vacancies according to study by Grey *et al*.[113] Furthermore, it was found that the organic (isopropanol) free blank sample was also deficient in Ti (*ca.* 97 %), giving similar occupancy to that observed in TiO_2 (A) 270. The TiO_2 (A) 270 was blue and the TiO_2 (blank) organic free sample was white. This observation demonstrates that Ti vacancies are not the cause of the blue colour. However, the Ti vacancies do explain the ferromagnetic behaviour observed with SQUID, see *Section 5.1.4.*[140]

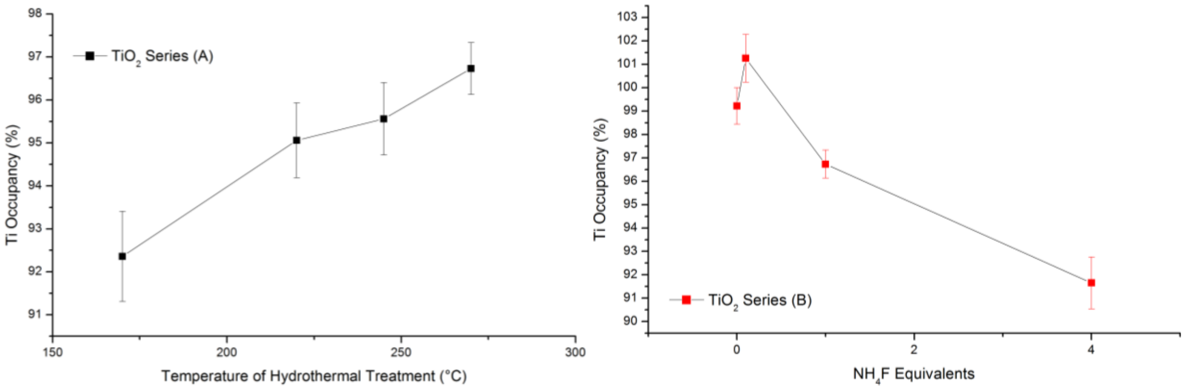

Figure 5.53 Left: Graph showing the Ti occupancy in the lattice for series (A). Right: Graph showing the Ti occupancy in the lattice for series (B). Values of occupancy were determined by detailed analysis of PXRD data as described in Chapter 3, Section 3.3.1.

For a comparison, the Ti occupancy in series (F) was explored. It was found that much like series (A), the Ti occupancy increased with increasing temperature of hydrothermal treatment, see *Figure 5.54* left. Yet, the Ti occupancy for series (F) started much higher (98 +/- 1 %) compared to *ca*. 92 +/- 1.5 % starting point for series (A) and finished at 100 % (within error). Furthermore, the effects of the ratio of Ti to NH_4OH were examined. The NH_4OH appeared to increase the Ti occupancy up to 1 equivalent, then the occupancy started to reduce as more NH_4OH was added, see *Figure 5.54* right. These results continue to demonstrate that NH_4OH has little effect on the TiO_2 lattice when compared to NH_4F. This is despite the NH_4^+ clearly being in control of crystal growth as shown by the shape and size of crystallites earlier in this section. Therefore, it is likely the F^- doping the lattice causing Ti vacancies possibly by hindering hydrolysis leaving OH^- groups trapped within the lattice.[113,139]

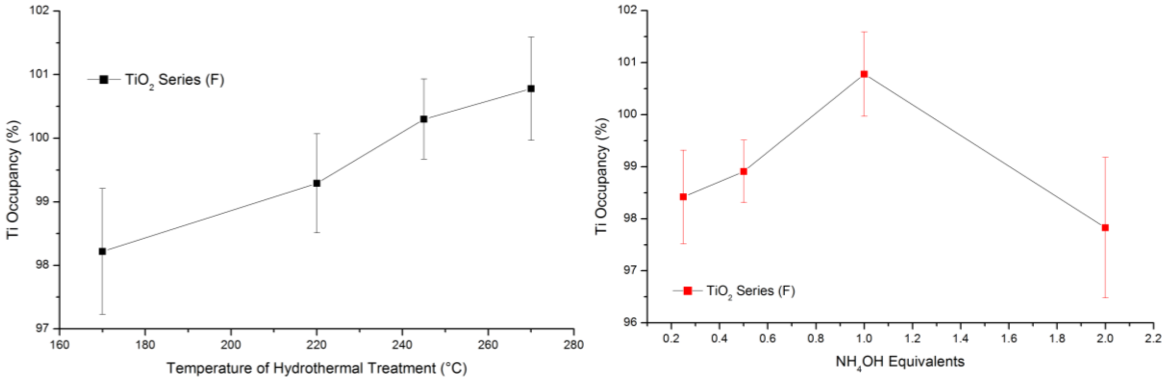

Figure 5.54 Ti occupancy in the lattice for series (F) as determined by PXRD. Left: Graph showing Ti occupancy and temperature of hydrothermal treatment. Right: Graph showing Ti occupancy against increasing equivalents of NH_4OH.

When NaF was used instead of NH_4F in series (C), the Ti occupancy followed a similar trend as series (B). When small amounts of NaF was added to the synthesis (0.01 to 0.1 equivalents), the occupancy increased to 100 % (within error). Yet, in the same fashion as series (B), as more NaF was added the occupancy quickly reduced to only 94 +/- 1.5 % at 1 equivalent. As before, the formation of brookite prevented the evaluation of any greater ratios of NaF to Ti. However, the Ti occupancy at 1 equivalent is low when compared to the equivalent NH_4OH sample, thus once again illustrating that the F^- ion is reducing the Ti occupancy at higher concentrations.

The Ti occupancy is much lower in all samples made in the presence of the high concentrations of F^-. Also, the length of (*a*) is much longer in the presence of the high concentrations of F^-, as consequence of Ti vacancies, which is in line with earlier reports in the literature.[113] The length of (*c*) seems to be the only measured variable that shows a response to the reducing conditions (as shown by organic free blanks and low-temperature syntheses). Although the presence of Ti vacancies should shorten (*c*).[113] However, the sample with the most vivid blue colour studied here and characterised using synchrotron PXRD is one made using 0.1 equivalents of NH_4F in series (B) (as indicated by the absorption at 620 nm) a sample with the highest occupancy, longest (*c*) but a shortish (*a*). It can be hypothesised, that this 0.1 equivalents sample has the highest concentration of bulk Ti^{3+} defects possibly stabilised by F^- giving rise to the darkest sample. As the concentration of NH_4F increases, the number of bulk Ti^{3+} defects decreases possibly due to excessive F^- doping (XPS showed F content increased with the addition of NH_4F (*Section 5.1.7*)). It is hypothesised based of these observations (although no literature states this exactly can be found), as the Ti^{3+} concentration increases with increasing F^- doping, eventually, it becomes more energetically favourable to have one Ti vacancy rather than 4 Ti^{3+} defects to maintain charge neutrality. Thus, the Ti occupancy decreases along with the blue colour as the concentration of NH_4F increases. Additionally, F^- doping is series (A) was constant (XPS and PIGE result *Sections 5.1.7* and *5.1.9*) however, the colour intensified with the increasing temperature of hydrothermal treatment coinciding with a decrease of Ti vacancies. Thus there must be a balance between Ti^{3+}, F^- and Ti vacancies. Further experimentation would be required to confirm this hypothesis.

5.1.7 Synchrotron Soft X-ray Study of Blue TiO_2

The study of the defects present in blue TiO_2 continued with the use of the soft X-ray beamline at the Australian Synchrotron. Where XPS, depth profiling XPS, VB spectroscopy and NEXAFS were used to further understand the electronic properties of the blue TiO_2.

Survey scans of series (A) revealed that the as-synthesised TiO_2 contained only Ti, O, C and F, no N was detected, see *Table 5.5*. The Si detected came from the Si wafer onto which studied here powders were deposited; the X-rays penetrated the deposited layer of TiO_2 in some samples. This compromised some of the high-resolution O_{2s} and VB spectra reported later. The amount of F detected appeared to be approximately 2 % in all samples throughout series (A), except the blanks synthesised without any NH_4F present or organics present. Noteworthy, in the two Si contamination-free samples, the Ti content of the two samples (TiO_2 (A) 270 and TiO_2 (A) 200), the samples synthesised at 270 and 200 °C respectively, shows lower than stoichiometric percentages of Ti relative to O. This would suggest the TiO_2 is Ti deficient. Ti vacancies have been detected using XPS by Wang *et al.*[140] when studying defective p-type TiO_2. The ratio of Ti to O as by measured by XPS changed from just under stoichiometric (*ca.* 0.4 %) in the control to *ca.* 5 % under stoichiometric.

Sample	**Ti (%)**	**O (%)**	**F (%)**	**Si (%)**
TiO_2 (A) 150	14.8	47.1	0.9	37.1
TiO_2 (A) 170	11.0	44.0	0.7	44.3
TiO_2 (A) 200	30.7	67.2	2.0	0
TiO_2 (A) 220	27.8	63.2	2.0	7.1
TiO_2 (A) 245	29.1	67.2	1.8	1.9
TiO_2 (A) 257	23.7	59.8	1.5	15.1
TiO_2 (A) 270	32.1	66.1	1.8	0
TiO_2 (Blank) C Free	26.3	63.8	0	10.0
TiO_2 (Blank) F free	24.8	59.6	0	15.6

Table 5.5 Results of survey scans of series (A) using XPS.

The survey scans of series (B) showed the overall constituents were the same as in series (A). However, the amount of F detected was proportional to the amount of NH_4F added to the hydrothermal synthesis media, see *Figure 5.55* below. All these TiO_2 samples were washed (see *Section 3.1.3*), so it is assumed the F detected must be chemically bound to the surface or present as a dopant in the bulk. It is thought that most of the F detected must be present as a dopant, as the amount detected seems independent of the changes in surface area throughout series (B), *i.e.* the 0.1 sample has only slightly less F than the 0.25 sample, yet there was a large change in surface area, see *Figure 5.89*. Also, the ion beam analysis *Section 5.1.9* suggested that 2/3 of the F^- is present in the bulk phase.

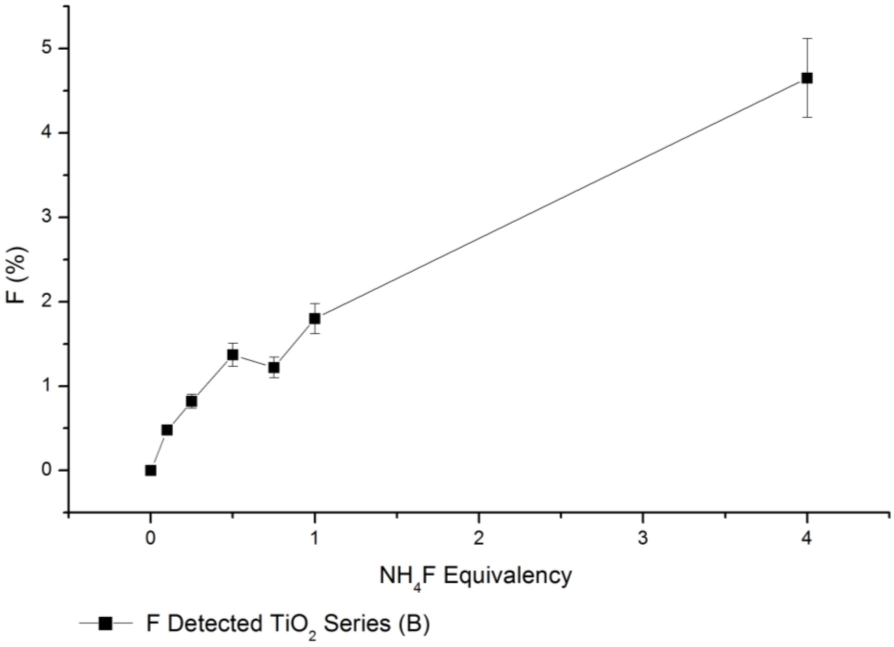

Figure 5.55 Graph showing the amount F detected by the XPS survey scans of TiO$_2$ samples in series (B). Errors are based on sample reproducibility.

High-resolution Ti2p scans were performed on the as-synthesised TiO$_2$. Peak fitting was used to quantify the Ti^{3+} with respect to the Ti^{4+}. First, it can be seen in *Figure 5.56* (top), that the XP spectrum of the NH$_4$F modified TiO$_2$ when compared to an unmodified TiO$_2$ clearly shows a shoulder on the $Ti^{4+}2p_{3/2}$ peak. This shoulder is generally reported to be the $Ti^{3+}2p_{3/2}$ peak.[47,51,52,95,111,125] The $Ti^{4+}2p_{3/2}$ peak was centred at 458.6 eV binding energy agreeing with literature values for unmodified Ti^{4+}.[47,51,52,95,111,125] The Ti^{3+} peak appears to be centred at 457.3 eV binding energy, see *Figure 5.56* (top). This is a reasonably common position reported for Ti^{3+}.[47,51,52,95,111,125] Assuming that the shoulder is Ti^{3+}, a Shirley background and mixed Gaussian/Lorentzian functions were fitted to the data as seen in *Figure 5.56* bottom. The Shirley background had fixed start and end points (452 to 468 eV). The peak positions were fixed at 457.8 eV for $Ti^{4+}2p_{3/2}$ and 457.0 eV for $Ti^{3+}2p_{3/2}$. The 2/3 to 1/3 relationship between the peak areas (as a measure of peak intensity) of the $2p_{3/2}$ and $2p_{1/3}$ peaks were fixed for both Ti^{4+} and Ti^{3+}. Then FWHM and intensity of the peaks were refined until the best fit was achieved. The relative Ti^{3+} concentration was calculated by comparing the intensity of the $Ti^{3+}2p_{2/3}$ to the $Ti^{4+}2p_{2/3}$ peaks.

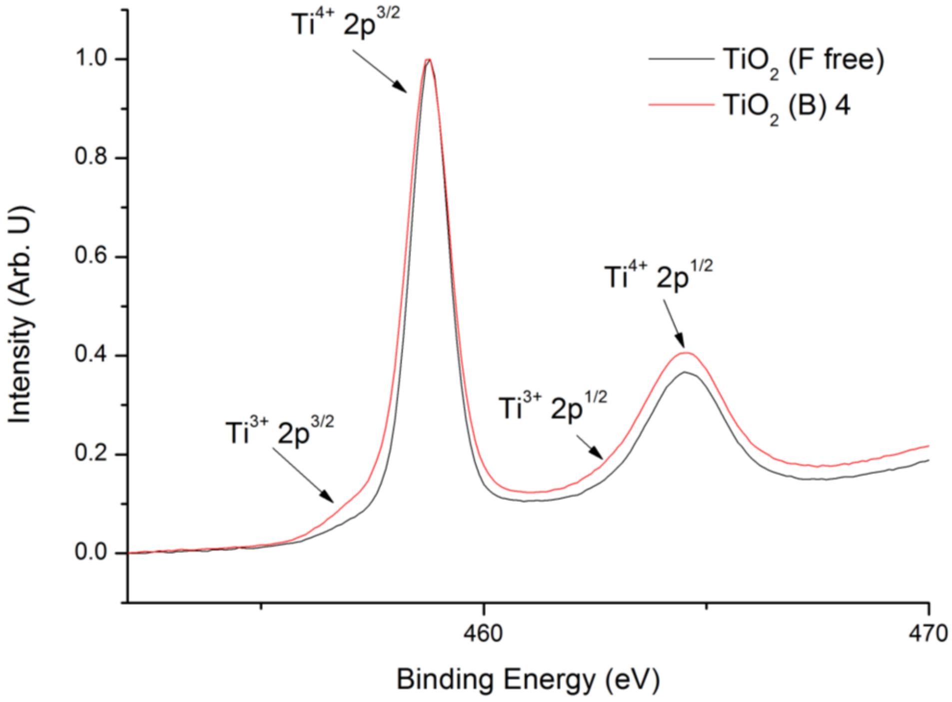

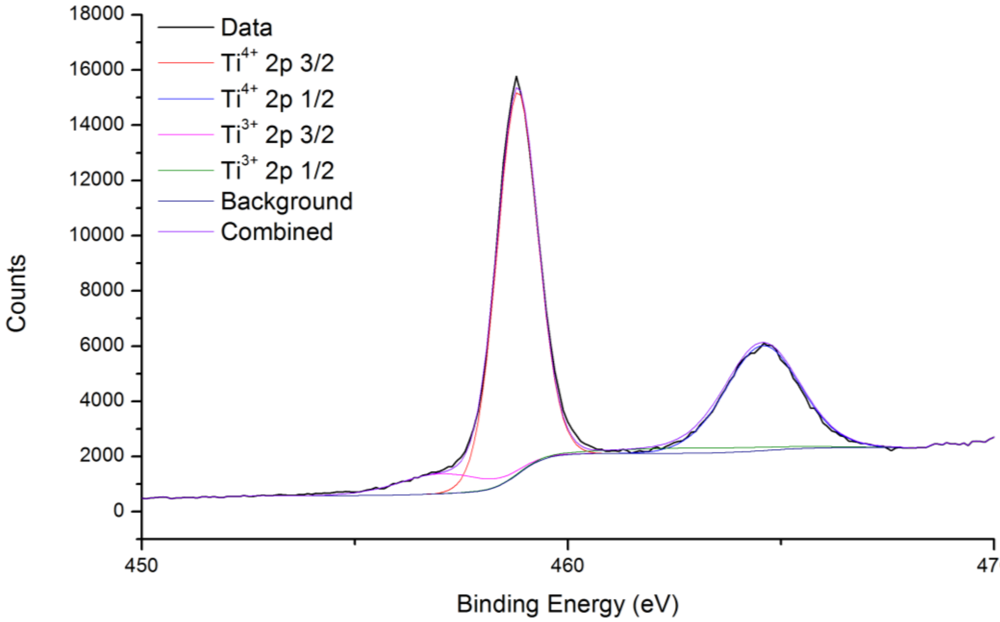

Figure 5.56 Top: XPS spectra of a white F^- free TiO_2 sample (TiO_2 (F free)) and a light blue TiO_2 sample synthesized with 4 equivalents of F^- (TiO_2 (B) 4). Bottom: Fitting of a spectrum showing Ti^{4+} and Ti^{3+} peaks and Shirley background fit.

When the Ti2p peaks of series (A) were fitted, several features became notable. First, throughout the series, the average amount of Ti^{3+} detected was between 6 % and 9 % depending on the incident X-ray energy, see *Figure 5.57*. Yet, there was no significant increase in the amount of Ti^{3+} detected between samples synthesised at 170 °C and those synthesized at 270 °C, despite a very large difference in colour *i.e.* 0.005 *vs* 0.125 absorbances at 620 nm, see *Figure 5.19*. Secondly, 5.6 to 8.9 % (depending on X-ray energy) Ti^{3+} was detected in the carbon-free blank sample (TiO_2 (F) C free). This confirms that the Ti^{3+} being detected by XPS is independent of the observed colour of the TiO_2 samples. However, it cannot be purely surface bound either, as there was no change in Ti^{3+} despite the decreasing surface area from *ca.* 96 to 42 m^2/g (see N_2 adsorption *Section 5.1.10*) with increasing temperature of hydrothermal treatment.

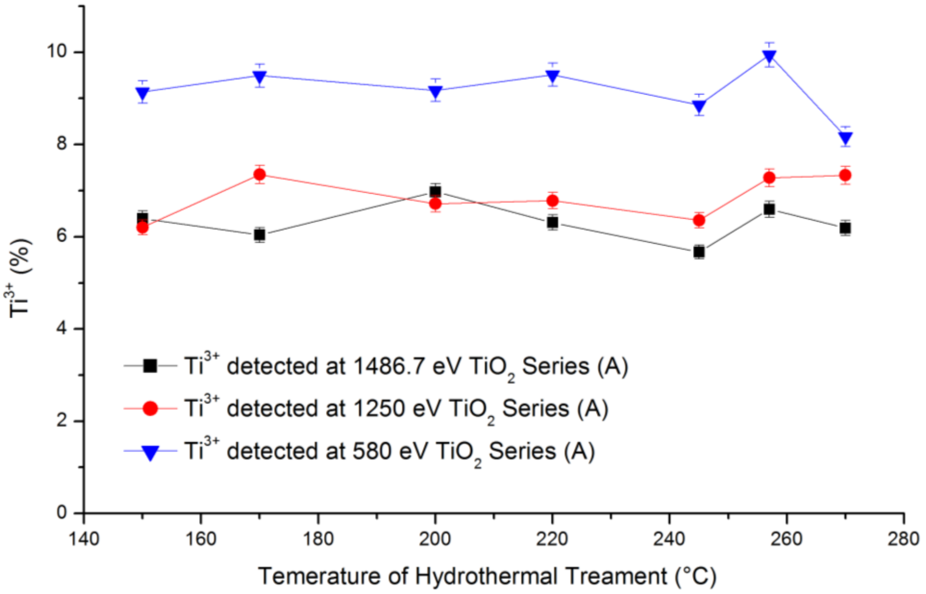

Figure 5.57 Graph of the percentage of Ti^{3+} detected in series (A) for different incident energy X-rays. Note: Lines have been added to guide the eyes and not link to results

Whereas, when examining the amount of Ti^{3+} detected in series (B), there was distinctly more Ti^{3+} detected in the sample synthesised with 4 equivalents of NH_4F. This was true for all incident X-ray energies, see *Figure 5.58*. However, the amount of Ti^{3+} detected below one equivalent NH_4F was consistently around 9 % to 5.5 % (depending on the incident X-ray energy) and showed no clear relationship to the NH_4F to Ti ratio, see *Figure 5.58*. Interestingly, the amount of Ti^{3+} detected seems independent of the F^- detected in the survey scans (see *Figure 5.55*) and the concentration of F^- in the synthesis media. As it is suspected that most of the F^- detected in the survey scans is present as a dopant, it seems that there is no correlation between F^- doping and Ti^{3+} detected when the NH_4F present in the synthesis media is less than 1 equivalent. At 4 equivalents there is some correlation but this is only one sample. Also, this means there is no correlation between Ti^{3+} (detected in the Ti2p region) with lattice changes *i.e.* Ti vacancies and the lengths (*a*) determined by PXRD or the changes in peak ratios and positions as observed in the Raman spectroscopy study. Overall no relationship between colour and Ti^{3+} detected could be found in the Ti2p region.

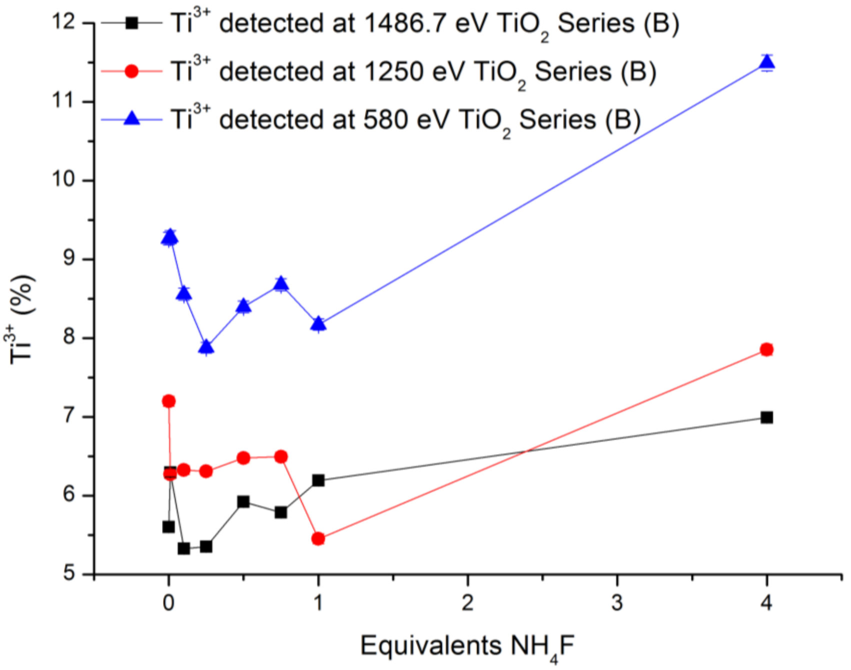

Figure 5.58 Graph of the percentage Ti^{3+} detected through series (B) for different incident energy X-rays. Note: Lines have been added to guide the eyes and not link to results.

Conversely, it was found that in series (C) the amount of Ti^{3+} detected decreased with increasing amounts of NaF added to the synthesis media, see *Figure 5.59*. Interestingly, even a small amount of NaF decreased the amount of Ti^{3+} detected when compared to the F free blank (TiO_2 (F free)). The decrease in Ti^{3+} with increased concentration of NaF used is evident throughout the series. However, the decrease is quite dramatically as brookite phase TiO_2 formed. There was also quite a narrowing of the amount of Ti^{3+} detected at different incident X-ray energies. The Ti^{3+} detected at 1486.7 eV (mean free path 1.4 nm) stayed relatively constant from 0.01 equivalent to 4 equivalents NaF added to the synthesis media. Moreover, the amount of Ti^{3+} detected at 580 eV (mean free path 0.85 nm) dropped from 8.5 % to 6.0 % at 4 equivalents NaF added to the synthesis media. This would suggest that the Ti^{3+} detected was more bulk than surface.[114] Although, as per Chapter 6, when 4 equivalents of NaF is added to the synthesis media, brookite phase TiO_2 is produced. It is not known how this would affect the concentration of Ti^{3+} (surface or bulk).

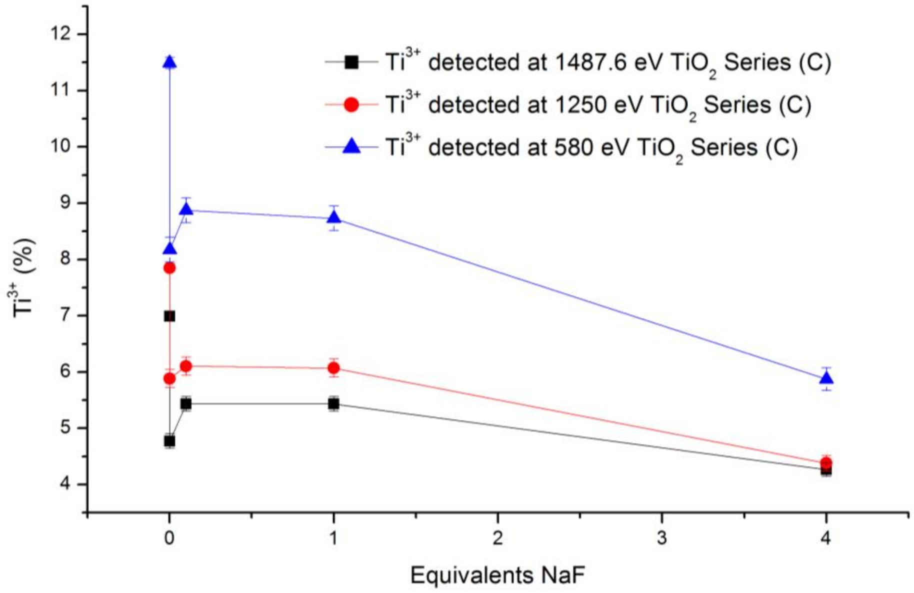

Figure 5.59 Graph of the percentage of the Ti^{3+} detected in series (C) and F-free blank (data for latter is shown at 0 equivalents of NaF) for different incident energy X-rays. Note: Lines have been added to guide the eyes and not link to results.

Since the sample synthesised with 4 equivalents NH_4F showed the largest amount of detectable Ti^{3+}, it was used as a case study to determine the location of the Ti^{3+} species. When performing depth profiling, the incident X-ray energy is varied and hence the probability of the photo-ejected electrons escaping changes due to the mean free path changes with depth.[114] It was found that the amount of Ti^{3+} detected by XPS dramatically increased with decreasing incident X-ray energy, see *Figure 5.60* left. These results would suggest that the Ti^{3+} being detected by XPS was mostly surface bound. This is also true for all the as-synthesised TiO_2 samples examined above (see *Figure 5.57, Figure 5.58* and *Figure 5.59*), were the Ti^{3+} detected at 580 eV was always greater than the amount detected at 1487.6 eV. Series (C) was the only series to show the amount of Ti^{3+} being detected at 580 eV was getting closer to the amount detected at 1486.7 eV, see *Figure 5.59*. Thus, suggesting more bulk Ti^{3+} relative to surface Ti^{3+} in the case of series (C).[114] However, to look at the position of the Ti^{3+} in more detail, the Ti^{3+} concentration was replotted (see *Figure 5.60* right) against the mean free path at various incident X-ray energies (using calculations reported by Fuentes *et al.*[114]) and the corresponding number of monolayers of TiO_2 (assumed to be 0.38 nm as reported by Ruzicka *et al.*[115]). As it can be seen, the bulk of the Ti^{3+} is in the first monolayer of TiO_2. By 4 monolayers deep the total average concentration of those layers (including the first monolayer) has dropped to *ca.* 7 %. As the crystallite is *ca.* 18 nm (as determined by PXRD) and after 1.5 nm the Ti^{3+} has decreased considerably, it is though most of the Ti^{3+} in the outer shell of the crystallite. [114,115]

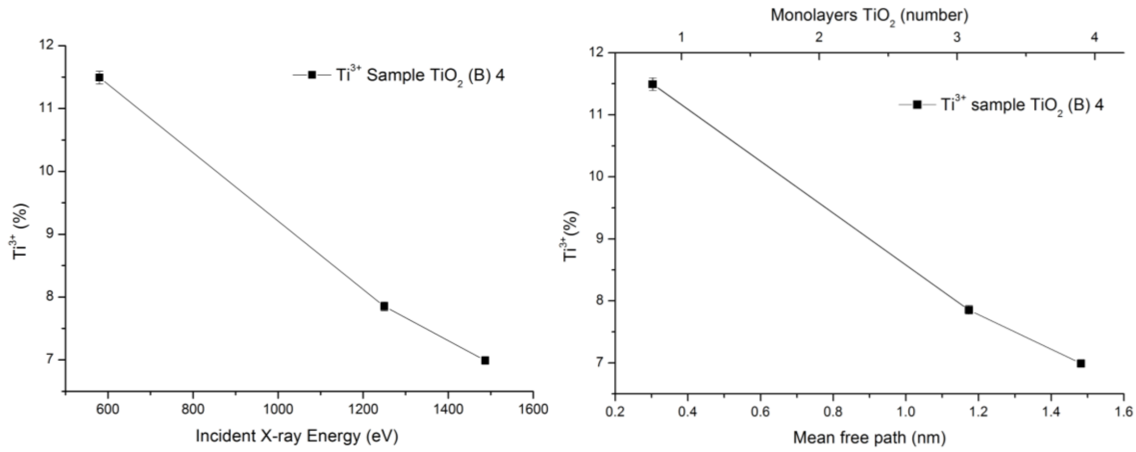

Figure 5.60 Left: Percentage Ti^{3+} *detected (with respect to* Ti^{4+}*) and its relationship to incident energy of X-rays for sample* TiO_2 *(B) 4. Right: Percentage* Ti^{3+} *detected (with respect to* Ti^{4+}*) and its relationship to the photo-ejected electron mean free path and the number of* TiO_2 *monolayers. Note: Errors calculated by the fitting algorithm.*

Valence band (VB) spectroscopy was used to examine the electronic structure of the NH_4F-modified TiO_2. VB spectroscopy shows the binding energies of the outer shell electrons; which provides information on the density of states (DOS).[116,117] VB does not give any information on the conduction band as there are no electrons occupying it in the non-photoexcited TiO_2. *Figure 5.61* shows the VB spectra of series (B) as an example. The most interesting feature of the VB spectra was the strong peak at *ca.* 1.5 eV, *Figure 5.61*. The literature states the peak at 1.5 eV is Ti3d photoelectric emissions from localized states associated with Ti^{3+}.[117,141] Also of interest is the band bending effect observed by looking at the angle of the O2p π leading edge and the intercept with the x-axis.[117] This band bending effect shows the narrowing of the band gap and is commonly reported in black TiO_2.[99,116] To interpret changes in the VB spectra with respect to synthesis conditions, the intensity of the 1.5 eV peak was measured and the intercept of the O2p π leading edge with x-axis was measured. Due to SiO_2 being detected in some samples, there was no attempt to look at the relative intensity of the non-bonding and bonding O2p π electrons.

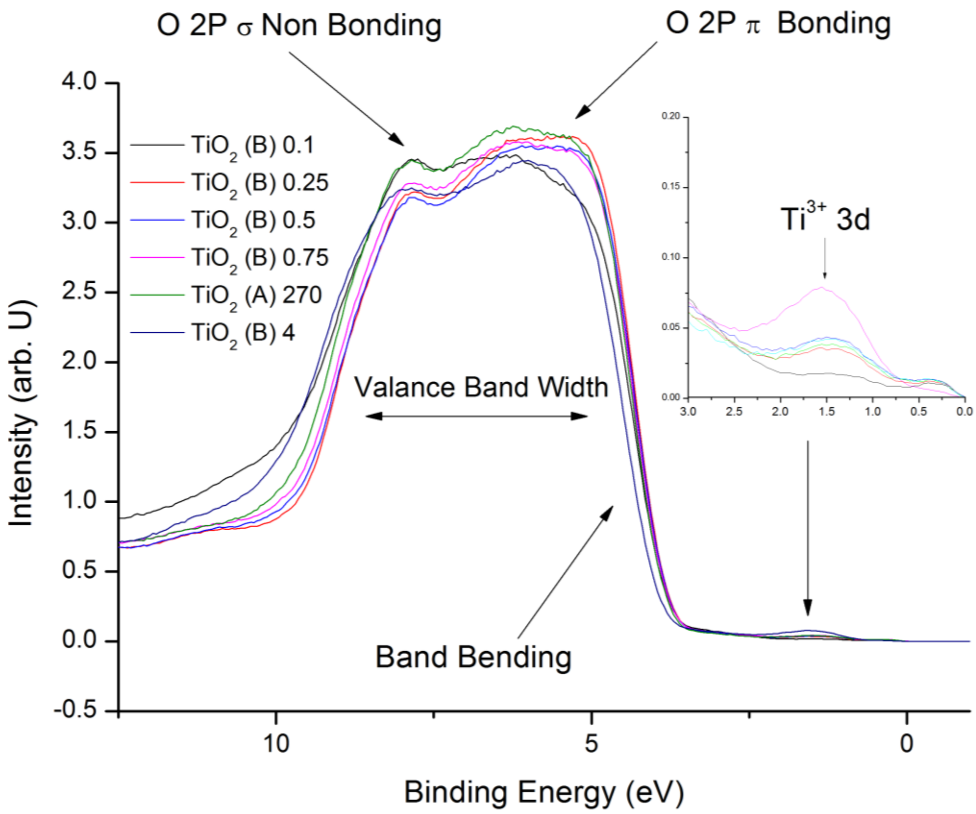

Figure 5.61 Valance band spectra of TiO_2 Series (B). The inset shows close up of the Ti^{3+}3d region.

First of all, the VB spectra of series (A) were visually analysed (not shown) and were found to remain very constant despite the changing temperature of hydrothermal treatment. Analysis of the spectra showed both the O2p π leading edge x-intercept values and the Ti^{3+}3d peak intensity remained constant over the whole series, see *Figure 5.62* top graphs. On the other hand, the analysis of series (B) showed there were distinct changes in the VB spectra with respect to the changing Ti to NH_4F ratio, see *Figure 5.61*. The intensity of the Ti^{3+}3d peak (found at 1.5 eV) increased monotonically with increasing ratios of NH_4F to Ti, see *Figure 5.62* bottom left. Also, the x-intercept of a line fitted to the leading edge of the O2p π bonding peak, *i.e.* band bending, also increased monotonically with increasing ratios of NH_4F to Ti, see *Figure 5.62* bottom right.

Analysis of the VB spectra of series (F) showed no significant peaks associated with the Ti^{3+}3d electrons or any shift in the O2p π leading edge. However, series (C) showed a similar in intensity features at *ca*. 1.5 eV assigned to the Ti^{3+}3d electrons and a shifted O2p π leading edge as was observed in series (A).

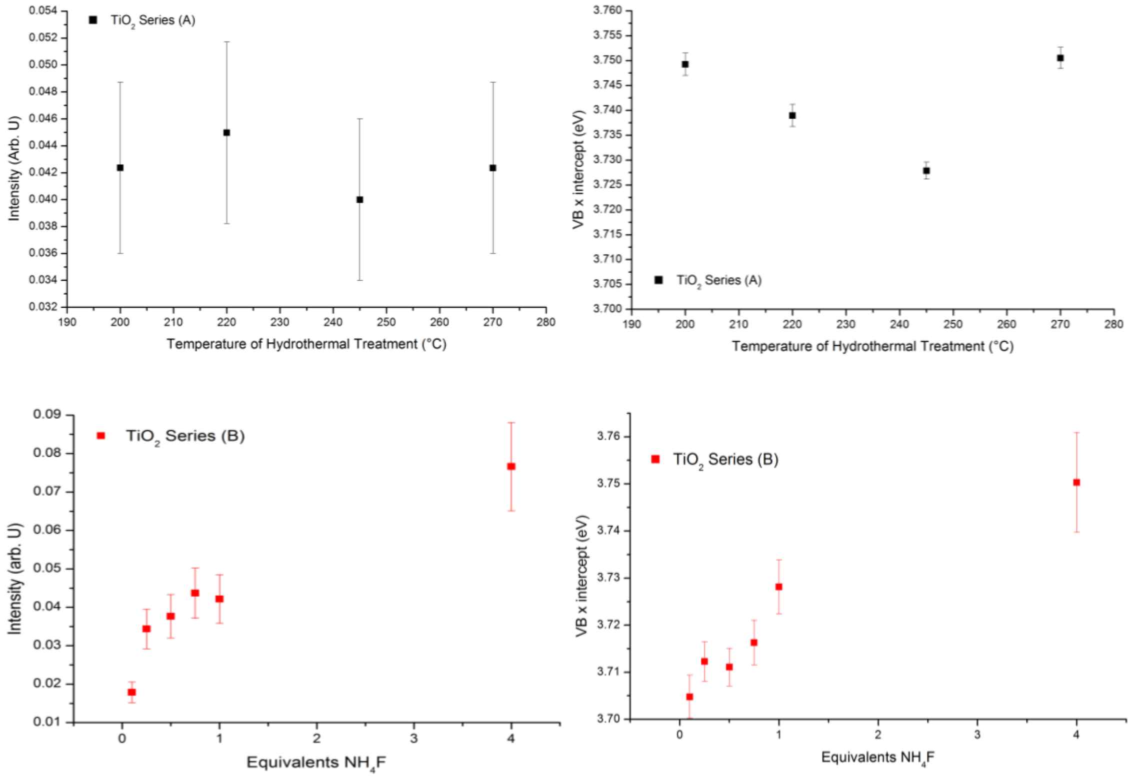

Figure 5.62 Valance band spectra summary. Top left: Intensity of Ti3d peak in series (A). Top right: X-intercept of the leading edge of O2p π bonding region series (A). Bottom left: Intensity of Ti3d peak in series (B). Bottom right: X-intercept of the leading edge of O2p π bonding region series (B).

The increased intensity of the Ti^{3+}3d peak with higher NH_4F ratios indicates that the concentration of Ti^{3+} present in the surface of the crystal must be increasing with higher F^- content in the synthesis media. Thus, agreeing with the observations in the Ti2p XPS above (*Figure 5.58*). The fact that series (C) also contained a Ti^{3+}3d peak and series (F) did not, confirms the Ti^{3+} is proportional to the F^- added to the synthesis. However, as the spectra were measured using 100 eV incident X-rays, the Ti^{3+} species detected are likely to be at the surface of the particles due to the very short mean free path (*ca.* 0.27 nm which less than a single monolayer of TiO_2). [114,115] As the penetration is less than a monolayer of TiO_2, the measurement of Ti^{3+} becomes insensitive to the surface area of the sample being measure as it does not see the bulk material. The O2p π leading edge moving to higher binding energies indicates the valence band was moving further away from the vacuum level. This suggests either the direct band gap has increased or the Fermi level has increased. The optical band gap measured using the Tauc plot above (see *Figure 5.20*) indicated the band gap remained unchanged. Therefore it seems more likely that the presence of notable quantities of Ti^{3+} has increased the n-type nature of the TiO_2 and shifted the Fermi level to a higher energy relative to the vacuum level.[117,142]

Using the VB data above and the optical band gap (determined to be 3.20 eV (*Figure 5.20*)) an electronic structure was constructed, see *Figure 5.63*. Using the position of the valence band and optical band gap in the sample (TiO_2 (A) 270), the edge of the conduction band was found to be located at -0.55 eV. The Ti^{3+}3d defect is centred at -1.5 eV with approximately a 1 eV spread in observed binding energies. As per the diagram, this would result in the absorption of light from 576 to 730 nm (2.15 to 1.7 eV) and 1301 to 2254 nm (0.95 to 0.45 eV), which explains the red light adsorption observed in the UV-Vis DR spectra (*Figure 5.20*).

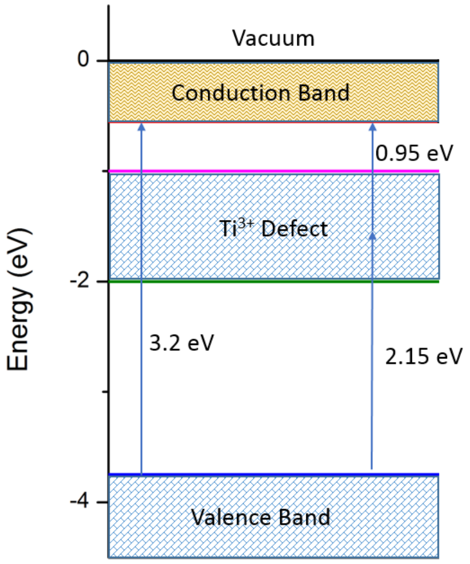

Figure 5.63 Electronic structure of blue TiO_2 *as determined by VB spectroscopy and UV-VIS DRS.*

Near edge X-ray absorption fine structure spectroscopy (NEXAFS) was used to study the bonding peculiarities in the coloured TiO_2. There were three different spectra collected per sample: total electron yield (TEY), fluorescence yield (FY) and partial electron yield (PEY). The total electron yield was measured by the sample ground current. Total fluorescence is measured by a scintillation counter. PEY was measured using an electron multiplier with a bias voltage that excluded all secondary electrons. All three spectra were collected at the same time while exposing the sample to the gradually changing incident X-ray beam (hence, the technique is available only at the synchrotron). An example of typical spectra can be seen below in *Figure 5.64*. It can be seen that the relative signal intensity is in the order of TEY, PEY and FY. The photoelectron based measurements are more sensitive to the surface features *i.e.* 5 nm depth sampling (due to a shorter mean free path). Whereas the fluorescence is more bulk sensitive *i.e.* 100 nm.[143] The PEY measurement displays narrower peaks than the TEY spectrum. This is because the PEY signal is mainly Auger electrons as the bias voltage excludes secondary electrons. Thus, the PEY is even more surface sensitive. The assignment of peaks was in accordance with those reported in the literature.[144]

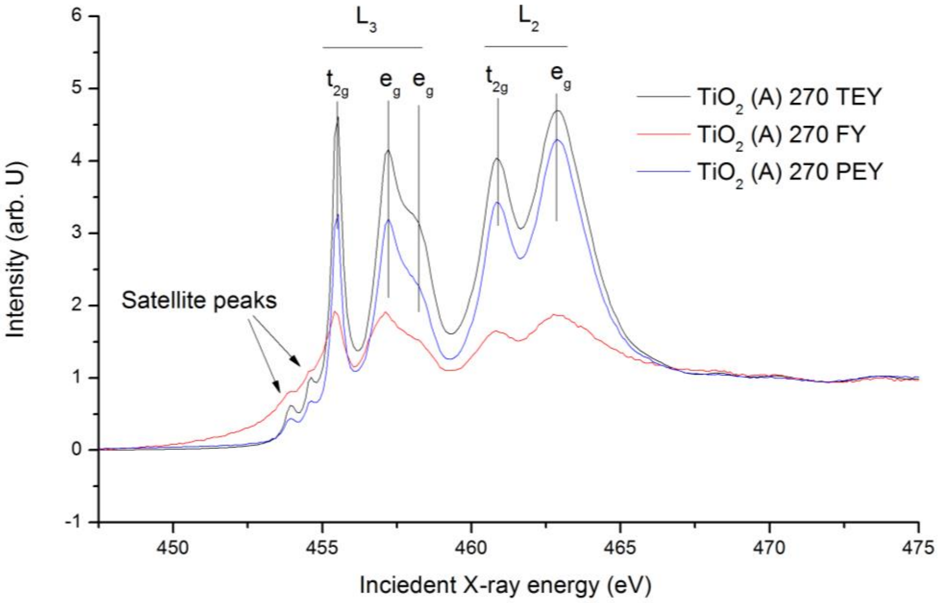

Figure 5.64 The NEXAF spectrum of sample TiO_2 (A) 270.

To analyse the spectra, the relative intensity of the L_3 t_{2g}, L_3 $e_{g\ \text{(left-hand side peak)}}$, L_2 t_{2g} and L_2 e_g peaks were evaluated. It has been reported that presence of pentacoordinate Ti^{3+} defects reduces the relative ratios of L_3 t_{2g}/L_3 $e_{g\ \text{(left-hand side peak)}}$ and L_2 t_{2g} /L_2 e_g.[115] Phase can also alter the L_3 t_{2g}/L_3 e_g ratio, however, all samples studied by NEXAFS in this chapter are phase pure anatase.[115]

NEXAFS analysis of series (A) showed that the temperature of hydrothermal treatment had little impact on the relative peak intensity. The relative ratio of L_2 t_{2g}/L_2 e_g did not appear to significantly change with increasing temperature of hydrothermal treatment as indicated by the horizontal lines fitted, see *Figure 5.65* left. The relative ratio of L_3 t_{2g}/L_3 e_g did appear to have a slight downwards trend when fitted, see *Figure 5.65* right. This would indicate there was no significant increase in detectable pentacoordinate Ti^{3+} with increasing temperature of hydrothermal temperature despite the colour change. Conversely, the carbon-free blank did show greater L_2 t_{2g}/L_3 e_g and L_3 t_{2g}/L_3 e_g ratios than the reduced samples. This would indicate that on average there was less pentacoordinate Ti^{3+} present in the blank sample.[115,145] Thus, the lack of change across series (A) when analysing the NEXAFS, agrees with the VBS and Ti2P XPS above, there is no evidence (based on soft X-ray techniques) of Ti^{3+} increasing with the temperature of hydrothermal treatment.

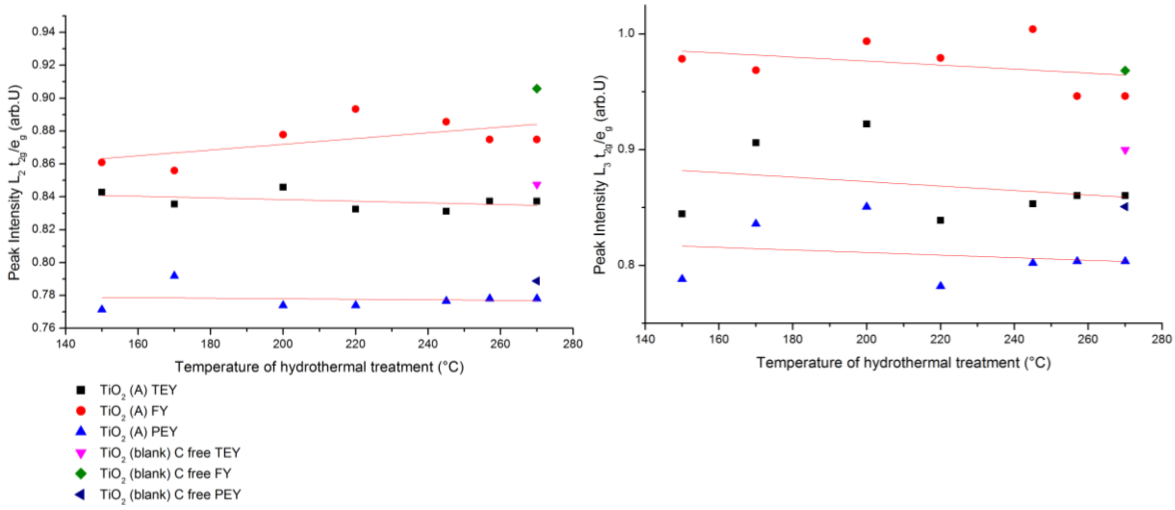

Figure 5.65 Graph showing the relative ratios of NEXAFS peaks in series (A): Left: L_2 t_{2g}/L_3 e_g Right: L_3 t_{2g} /L_2 e_g.

NEXAFS analysis of series (B) showed that the ratio of NH_4F to TiO_2 had an impact on the relative peak intensity. In both the L_3 t_{2g}/L_3 e_g and L_2 t_{2g} /L_2 e_g there was a trend towards lower t_{2g} / e_g ratios, see *Figure 5.66*. The evidence for pentacoordinate Ti^{3+} was most prominent in the PEY suggesting the Ti^{3+} was surface bound.[115,143,145] However, the L_3 t_{2g}/L_3 e_g FY was increasing with the addition of more NH_4F to the synthesis media, indicating the bulk pentacoordinate Ti^{3+} may be reducing.[115,145] This could explain the reduce red light absorption in the TiO_2 (B) 4 and is evidence towards the hypothesis of Ti^{3+} being replaced by Ti vacancies.

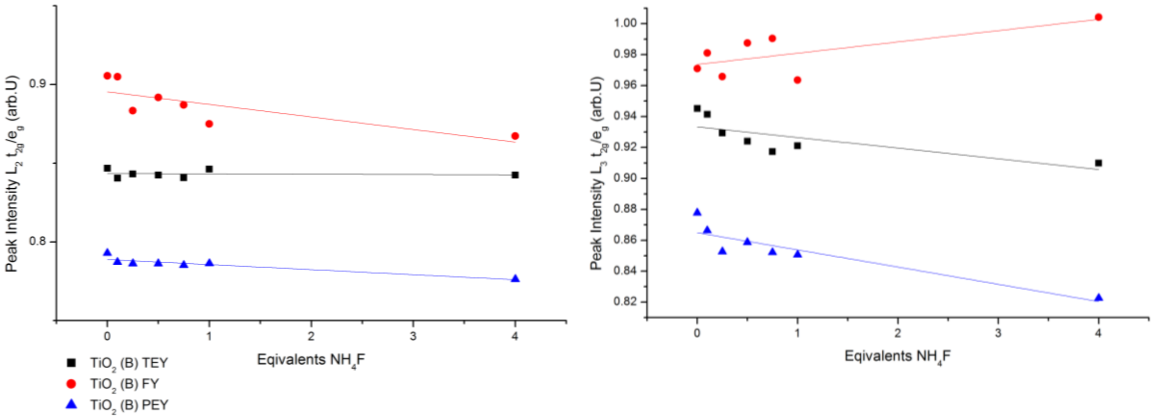

Figure 5.66 Graph showing the relative ratios of NEXAFS peaks in series (B): Left: L_2 t_{2g}/L_2 e_g Right: L_3 t_{2g} /L_3 e_g.

NEXAFS analysis of series (F) showed that the temperature of hydrothermal treatment had some impact on the relative peak intensity. The L_2 t_{2g} /L_2 e_g ratios stayed constant throughout the range of processing conditions tested, see *Figure 5.67* left. Whereas the ratio of L_3 t_{2g} /L_3 e_g in the TEY and PEY showed a decrease in ratio with increasing temperature of hydrothermal treatment, see *Figure 5.67* right. As there was little change in the FY spectrum, the effect is clearly surface bound. This may indicate that not only the Ti^{3+} defects are found both on the surface and in the bulk, but also that there may be some pentacoordinate Ti^{3+} due to the exposure of specific facets being detected.[109]

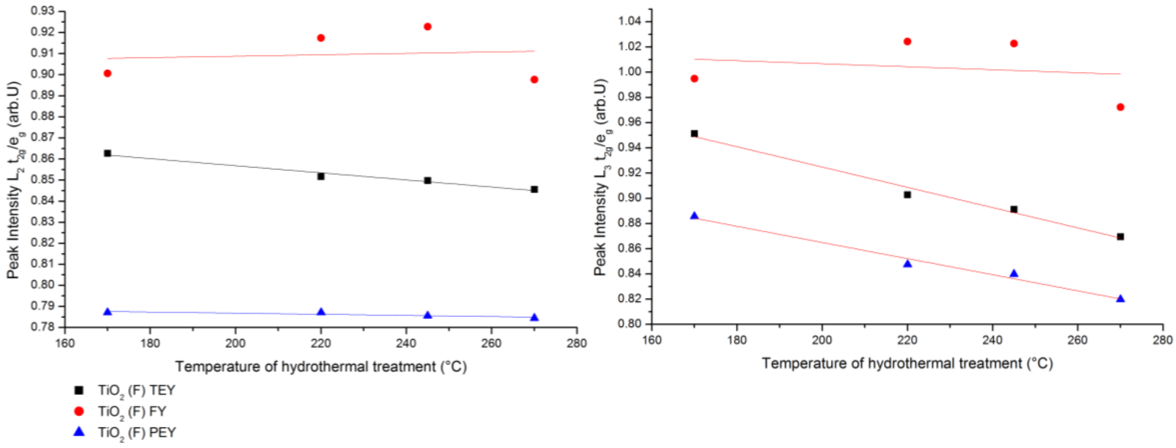

Figure 5.67 Graph showing the relative ratios of NEXAFS peaks in series (F): Left: L_2 t_{2g}/L_2 e_g Right: L_3 t_{2g} /L_3 e_g.

As a final point, when NaF was used instead of NH_4F in series (C) it was found that the L_3 t_{2g}/ L_3 e_g and L_2 t_{2g} / L_2 e_g ratios were near identical to TiO_2 (A) 270 for the TEY and PEY. However, the ratios were greater in the FY suggesting there was less bulk pentacoordinate Ti^{3+}.[114,140,142]

Overall, the NEXAFS shows there is pentacoordinate Ti^{3+} present in most of the as-synthesised TiO_2. The temperature of hydrothermal treatment does not show any signs of generating more bulk Ti^{3+}. However, series (B) showed the surface pentacoordinate Ti^{3+} was increasing with the addition of NH_4F (in both L_2 t_{2g} / L_2 e_g and L_3 t_{2g} / L_3 e_g PEY) however, the bulk pentacoordinate Ti^{3+} may have been decreasing (L_2 t_{2g} / L_2 e_g FY). On the other hand, the decreasing L_2 t_{2g} / L_2 e_g ratios in the FY with respect to the ratio of NH_4F to TiO_2 would suggest that there is some additional formation of bulk Ti^{3+} with the addition of greater concentrations of F^- ions. As the FY spectrum was significantly more noisy than the PEY spectrum, it is hard to say conclusively if the bulk pentacoordinate Ti^{3+} was decreasing.

5.1.8 Electron Microscopy Study of Blue TiO_2

Scanning secondary electron microscopy (SEM) was used to investigate the blue TiO_2 particle shape and general morphology. SEM and sample preparation is detailed in *Section 3.3.4*. The results from the SEM study of series (A) were not as expected. First, there was no consistent increase in the overall particle size with increasing temperature of hydrothermal treatment, as was expected from the PXRD results focused on the crystalline domain size estimates, see *Figure 5.68* (SEM) and *Figure 5.46* (PXRD). The particles synthesised at 170 ºC and 270 ºC appear to be the smallest, whereas particles synthesised 220 ºC and 245 ºC appear larger, see *Figure 5.68*. Also, all the particles are larger than what is predicted by the PXRD results by an order of magnitude. They also have no well-defined shape and there does not appear to be any elongation as predicted by PXRD. Most of these observations are explained by the limitations of SEM and the differences between overall particles and crystallites within such particles. PXRD determines crystallite sizes. Whereas SEM is taking a relatively low-resolution image of the electrons interacting within a pocket near (the interaction volume is proportional to the accelerating voltage) the surface of the particle, observing the small aggregated crystals as on large particle.[120] Therefore, a particle observed in SEM could be made of multiple crystallites that have aggregated or agglomerated tightly to form a larger particle, observed by SEM. This explains why the particles observed with SEM are larger and not elongated as predicted by PXRD. Finally, the sample synthesised as a carbon-free blank showed no significant differences in morphology compared to samples synthesised with organics present in series (A), see *Figure 5.68*.

By pushing SEM to the limit, the primary particles can are observable. *Figure 5.69* below, shows the maximum magnification possible for TiO_2 (A) 170 and TiO_2 (A) 270 (*Note:* Not always possible with SEM). The high magnification images show individual particles coated with gold (the gold is visible as the 10 nm bumps, deposited onto the sample to make the particles conduction to avoid charging). These particles may still consist of multiple crystals aggregated or agglomerated together. However, they do show a difference in size between TiO_2 hydrothermally synthesised at 170 and 270 °C. Neither sample shows well-defined crystals or elongated crystals. However, the size of the individual particles is much closer to that predicted by PXRD. It can be seen in the sample TiO_2 (A) 270, *Figure 5.69* bottom, that there is one much larger crystal. These were occasionally seen in the samples synthesised at 270 °C. They are also seen in the PXRD diffractogram of TiO_2 (A) 270 as shaper small peaks on the broader peaks, see *Figure 5.49* (PXRD). They were also observed when using TEM, see *Figure 5.77*.

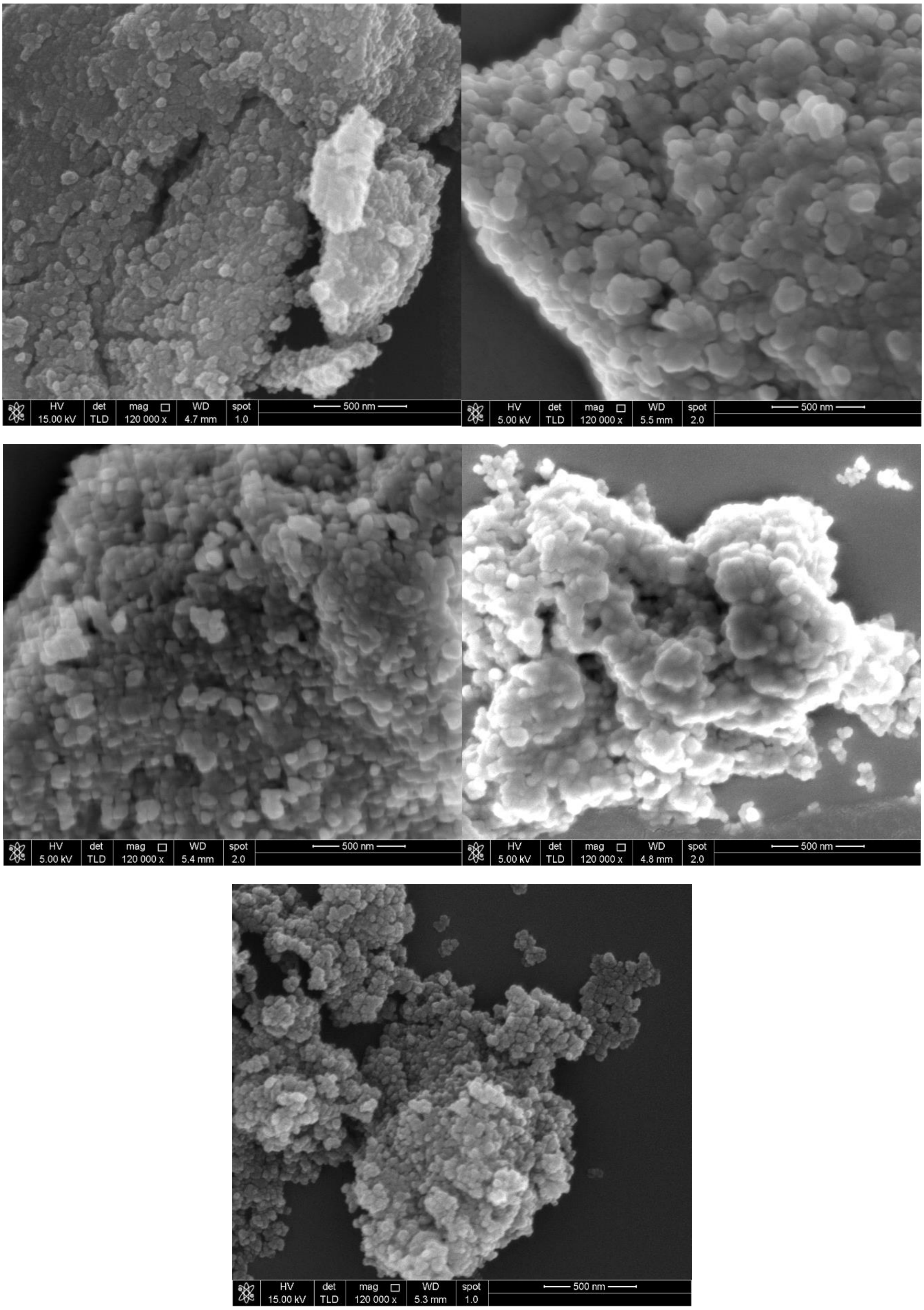

Figure 5.68 SEM images of the as-synthesised TiO_2 samples: Top left: TiO_2 (A) 170. Top right: TiO_2 (A) 220. Middle Left: TiO_2 (A) 245. Middle right: TiO_2 (A) 270. Bottom centre: TiO_2 (C free) blank.

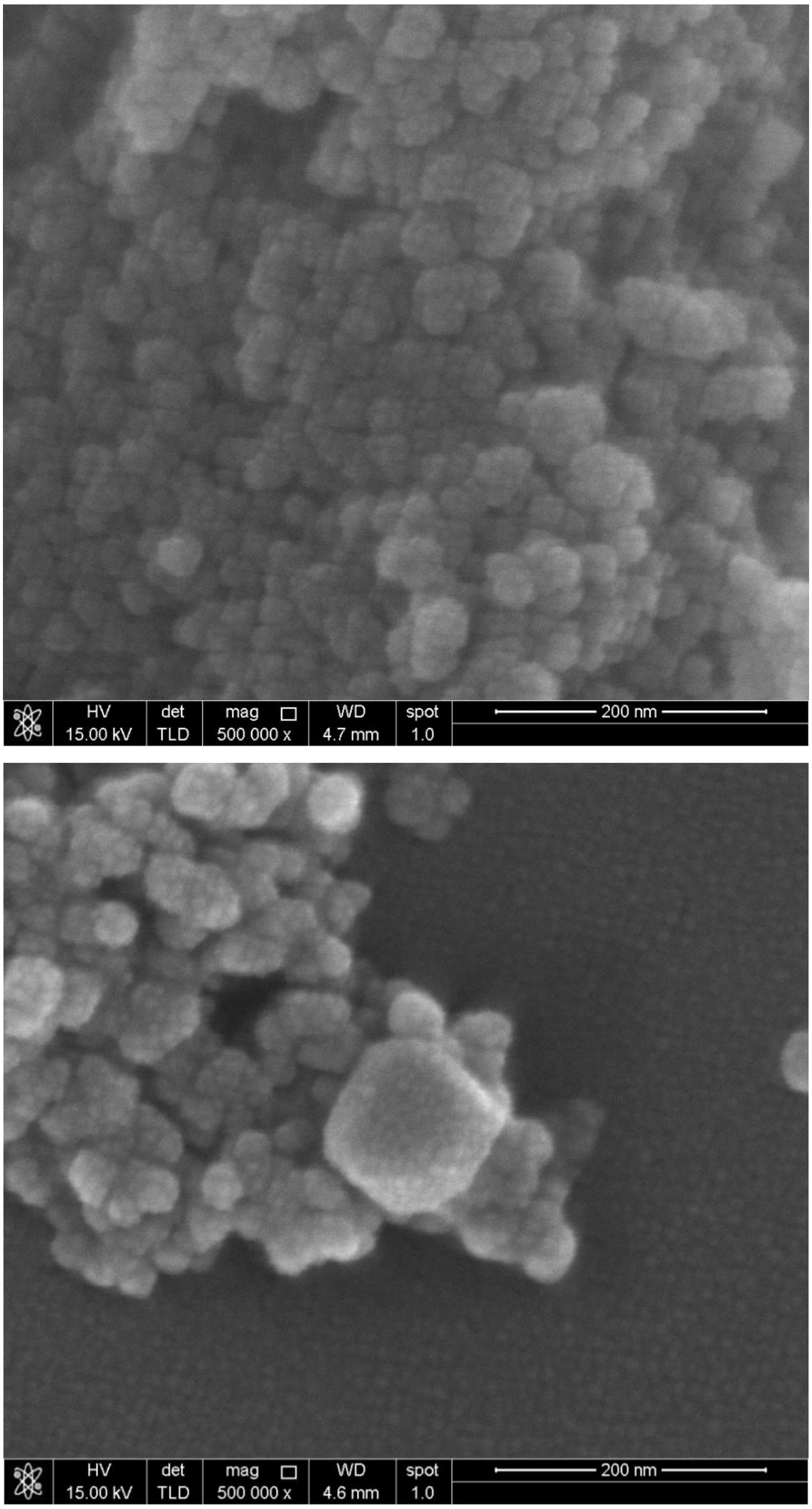

Figure 5.69 High magnification images. Top: TiO_2 (A) 170. Bottom: TiO_2 (A) 270.

The SEM study of series (B) revealed changes in particle size that agreed with the predictions of the PXRD study above. It can be seen in *Figure 5.70* (top), that the F^- free blank sample consisted of small particles lightly agglomerated with no discernible shape. Also, it can be seen in *Figure 5.70* (bottom), that the sample synthesised by adding 4 equivalents of NH_4F to the synthesis media, consisted of particles of a similar nature. Conversely, it can be seen in *Figure 5.70* (middle), the sample synthesised using 0.1 equivalents of NH_4F consisted of highly agglomerated, large but well-defined particles. The sample itself is very polydispersed with some small round particles, some very large round particles and some classic bipyramidal anatase shaped particles. Most particles are larger than 100 nm and some are microns in size. Thus, these results agree with what was determined using PXRD. The particles in the sample synthesised with 0.1 equivalents NH_4F are so large that their visible light scattering mechanism will be described by Mie theory rather than Rayleigh scattering. Thus, the deepness of the blue may be in part explained by the particle size.[146,147] That is, the scattering cross-section for blue light is greater than that of red light, which means red light would pass through more crystallites than blue light before being reflected. Thus, there is a higher probability of the red light being absorbed by the defect making the sample appear bluer.

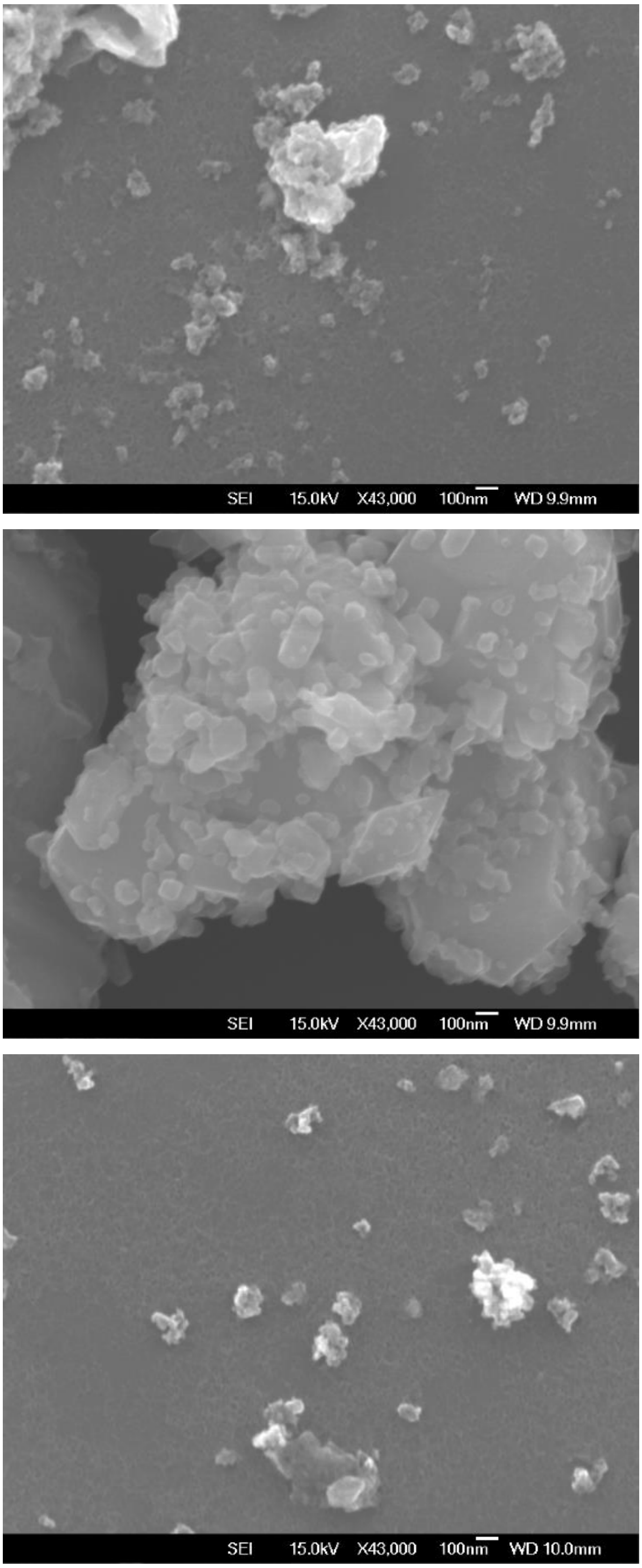

Figure 5.70 SEM images. Top: TiO$_2$ (B) B1. Middle: TiO$_2$ (B) 0.1. Bottom: TiO$_2$ (B) 4

Series (F) was also studied using SEM. SEM images of series (F) revealed the particles looked near identical to those synthesised in the presence of NH_4F (series (A) and (B)), compare *Figure 5.69* (bottom) and *Figure 5.71*. This observation is illustrating the fact that the F^- ion has no dramatic impact on overall particle morphology which can be observed using SEM. It would appear that neither NH_4F nor NH_4OH in this reaction mixture produces complicated hierarchical morphologies observed by others.[32,143] This is in contrast to what has been reported in the literature, where NH_4F has been used in hydrothermal synthesises to produce hierarchical self-assembled microspheres.[32,148]

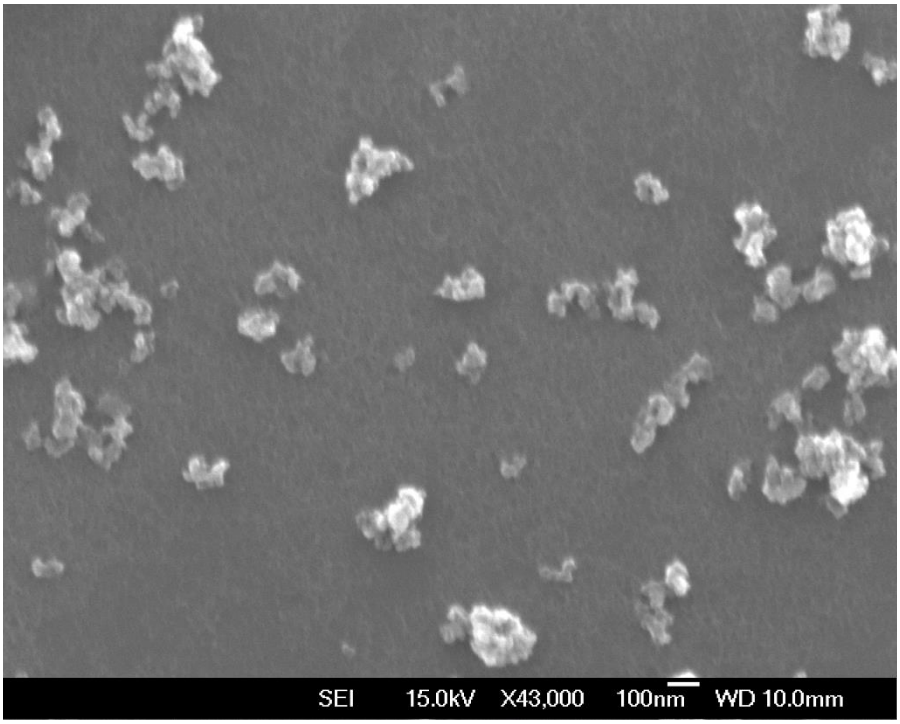

Figure 5.71 SEM image of sample TiO_2 (F) 270.

SEM revealed that it had insufficient resolution to truly to study the morphology of the crystallites which had been produced in the current hydrothermal synthesis. So, TEM was used in the next section to investigate the morphology of individual crystals at an atomic level. The TEM used by me in collaboration with Prof Richard Tilly (Victoria University) and sample preparation is detailed in *Section 3.3.5*.

TEM images of the TiO_2 synthesised in series (A) showed a regular crystallite size and shape. TiO_2 synthesised at a lower temperature (170 °C) showed small regular cubic crystallites with an average size of 11.5 nm, see *Figure 5.73* (top). As the temperature of hydrothermal treatment was increased to 220 and 245 °C the average crystallite size increased to 21 nm, see *Figure 5.73* (bottom) and *Figure 5.74* (top). However, it can be seen the shape stayed relatively constant. Finally, when the temperature of hydrothermal treatment was increased to 270 °C, the average size increased marginally to 22 nm yet, the shape became more bipyramidal see *Figure 5.73* (bottom). The organic free blank was also examined using TEM. It was found to have marginally smaller crystals and a more cubic shape when compared to TiO_2 (A) 270, see *Figure 5.75*. Overall TEM showed a gradual increase in crystallite size with temperature as expected from PXRD results. There was also a borderline shift towards more by bipyramidal shaped crystals as the temperature increased. The polydispersity of sizes did not appear to change dramatically between 220 and 270 °C. However, there was a narrowing of the distribution at 170°, see *Figure 5.72*. Overall, the size of crystallites was smaller and there was less elongation than estimated by PXRD (see *Figure 5.46*). However, sizes reported here are based on the crystallites being isometric in shape as there was insufficient fringing to determine the orientation of every crystallite while measuring their size.

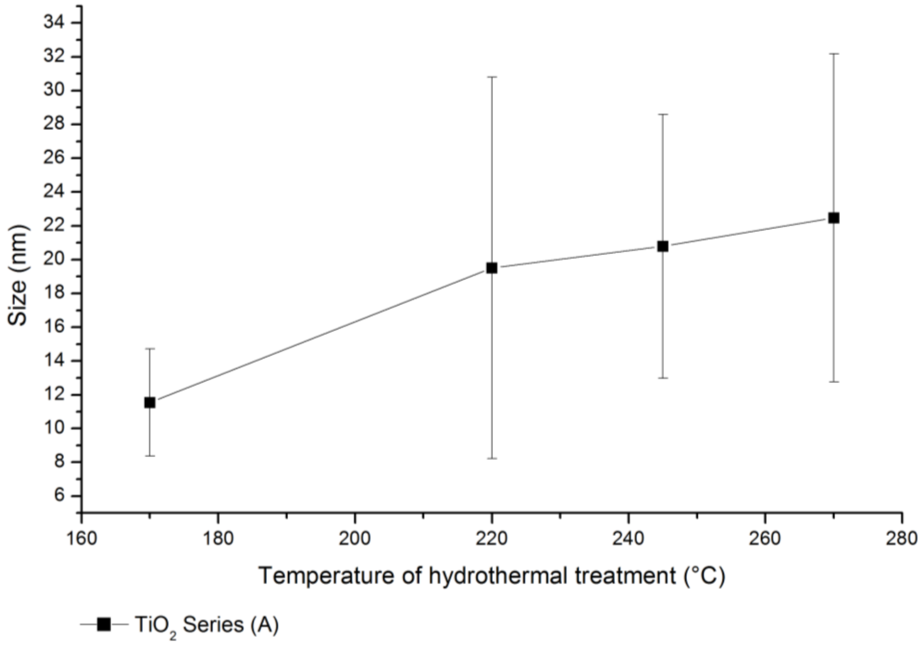

Figure 5.72 Graph of mean size as measured using TEM. Error bars represent one standard deviation of sizes distribution.

Looking at the TEM images closely and particularly focusing at the edges of crystallites, there did not appear to be any significant signs of the edge becoming progressively more distorted due to higher concentration of defects with increasing temperature of hydrothermal treatment. If anything, there appeared to be a movement to towards more well-defined fringing patterns right up to the very edge, see *Figure 5.73* and *Figure 5.74*. The organic free sample did not appear to have a sharper edge than any of the particles synthesised in the presence of organics, compare *Figure 5.74* and *Figure 5.75*. Depth profiling Ti2P XPS (*Section 5.1.7*) estimated most of the Ti^{3+} resides in a monolayer on the outside of the crystallite, there may be Ti^{3+} present in the bulk, although it is at a much lower concentration. Therefore, it is thought that it is beyond the resolution of the TEM to resolve the disordered monolayer. In the black TiO_2 reported by Chen *et al.*,[116] the H_2 reduction had penetrated several layers and the TEM was much higher resolution making the distortion much more obvious.

Through series (A) the electron diffraction patterns were consistent with PXRD results, showing only anatase particles present. Furthermore, within a reason, there did not appear to be any noticeable change in the haze around the diffraction rings which would indicate the surface is highly distorted due to the defect-rich layer at the surface.[49,122] As above, the highest concentration of Ti^{3+} resides in a monolayer around the particle with a lower concentration relatively evenly dispersed through the bulk (*Section 5.1.7*). The defect concentration and hence disorder may not have been concentrated enough to cause haze.

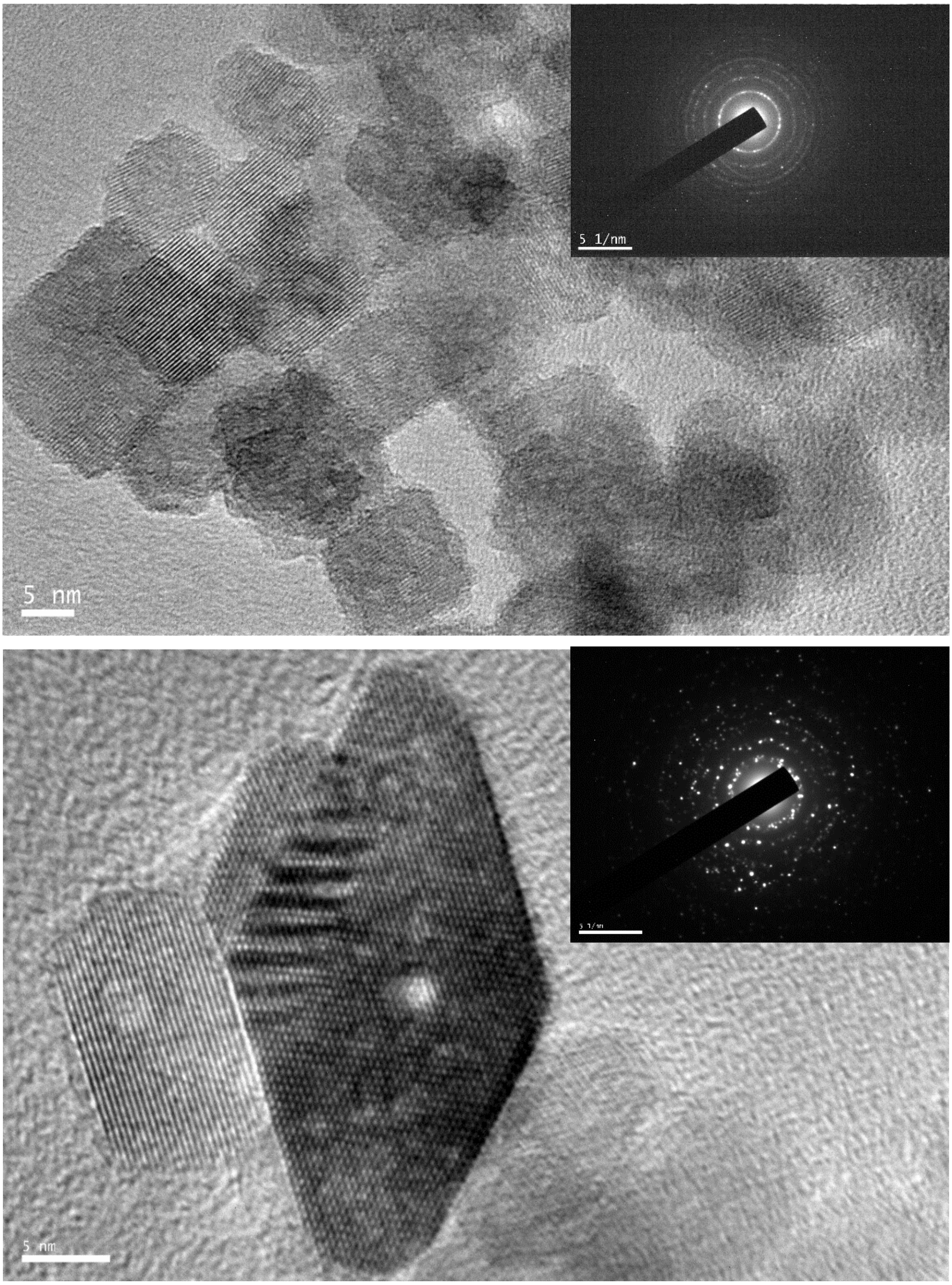

Figure 5.73 TEM images. Top: TiO_2 (A) 170. Bottom: TiO_2 (A) 220. Inset electron diffraction patterns.

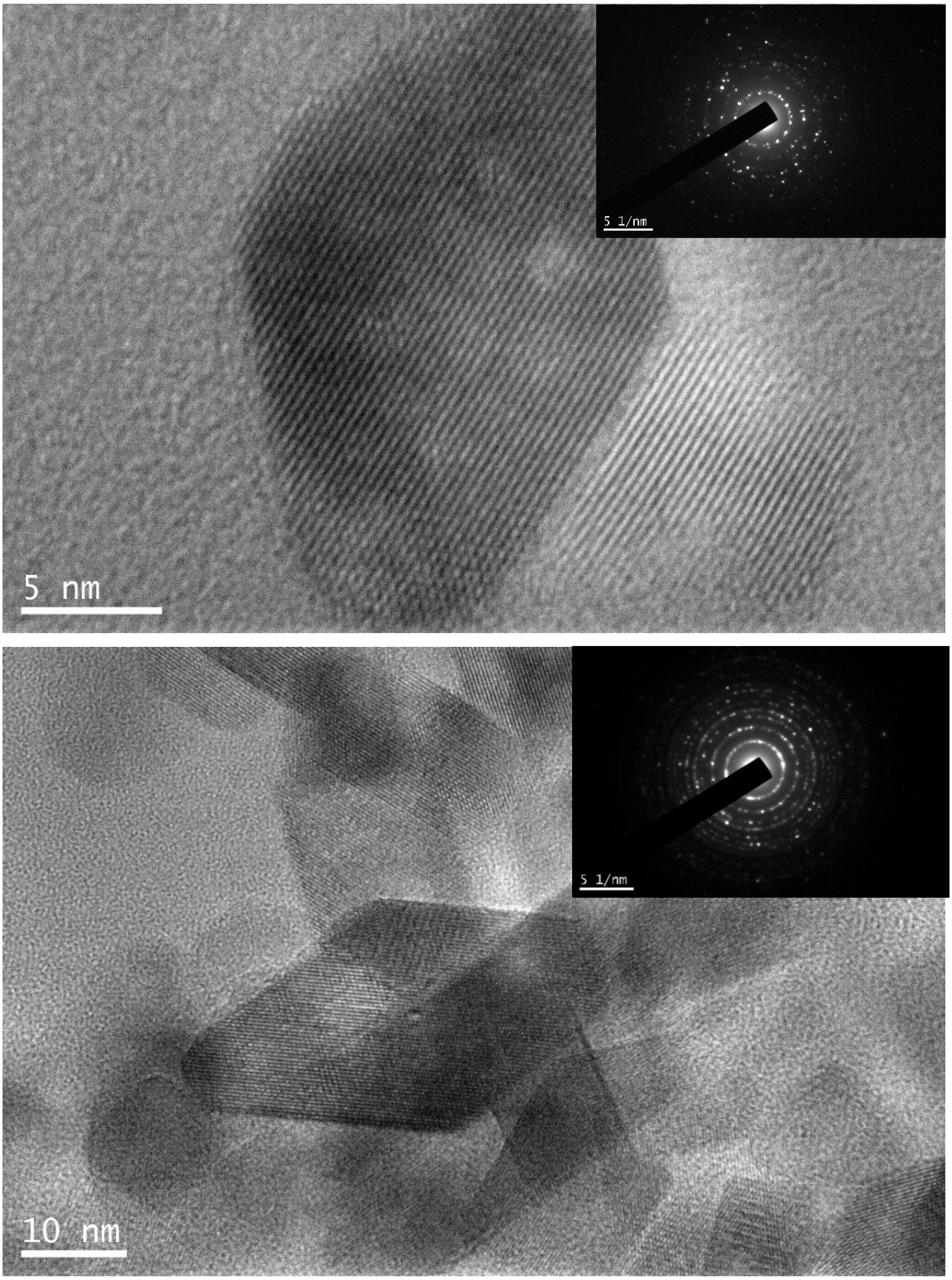

Figure 5.74. TEM images. Top: TiO_2 (A) 245. Bottom: TiO_2 (A) 270. Inset electron diffraction patterns.

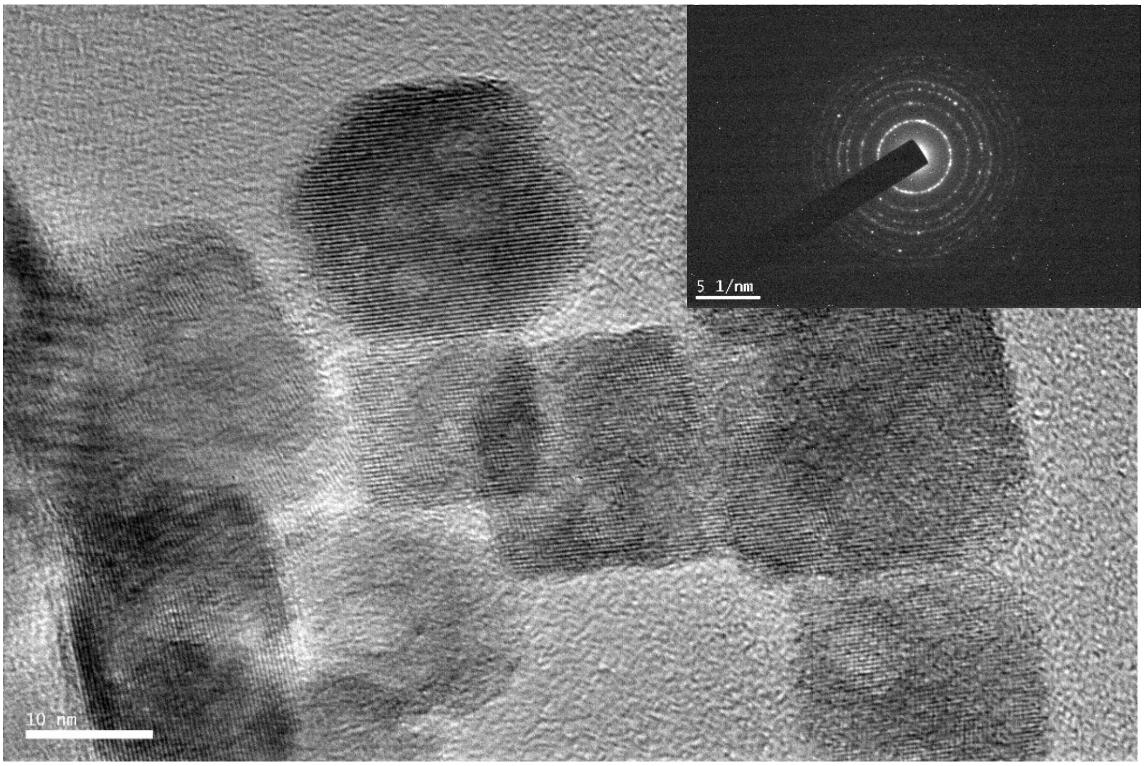

Figure 5.75 TEM image of TiO_2 *(A) carbon-free blank. Inset electron diffraction pattern.*

The electron diffraction patterns through series (A) were analysed, see *Figure 5.76*. The diffraction rings representing the {011} lattice spacing gradually lengthened with increasing temperature of hydrothermal treatment. Secondly, the diffraction rings representing the {013}, {004} and {112} lattice dimensions linearly lengthened with increasing temperature of hydrothermal treatment. The ring representing the {002} lattice dimension did not seem to change position with increasing temperature of hydrothermal treatment. Thus, these results would show (*a*) shortening and (*c*) lengthening agreeing with the PXRD results, see *Figure 5.50*.

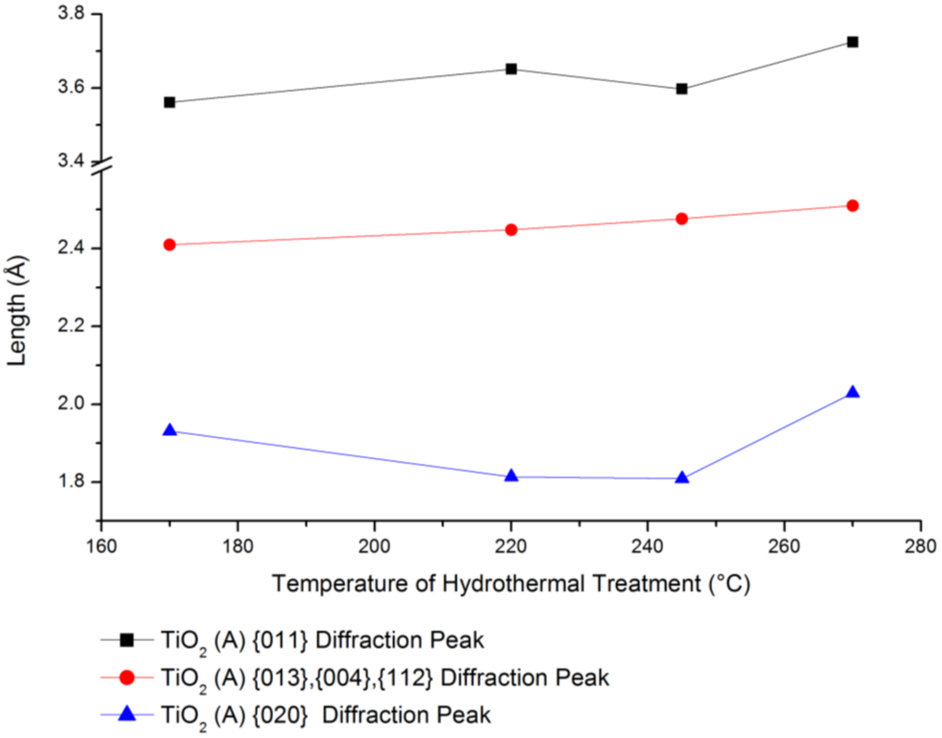

Figure 5.76 Graph of diffraction peak spacing in series (A) as determined by electron diffraction in TEM.

The sample (TiO_2 (A) 270) synthesised at the highest temperature contained a small population of enormous crystals. It can be seen in *Figure 5.77* that there is a very large crystal in the sample TiO_2 (A) 270 sitting amongst the smaller crystals. These large crystals were present throughout the sample. Although they made up a very small proportion of the total crystallites, they were certainly consistently present, even in repeat synthesises. The crystallite seen in *Figure 5.77* itself measures over 400 nm in size. As can be seen in the inset, the electron diffraction pattern showed these giants crystals are anatase. These large crystals were observed only in samples synthesised at temperatures greater than 200 °C with NH_4F present. At processing temperatures lower than 270 °C, there appeared to be a smaller fraction of these large crystals. Proof of the existence of these crystals was not only limited to TEM and SEM but also, as small sharp points on top of some of the broader peaks in PXRD diffractograms thus proving their existence within the bulk of the samples, see *Figure 5.49*.

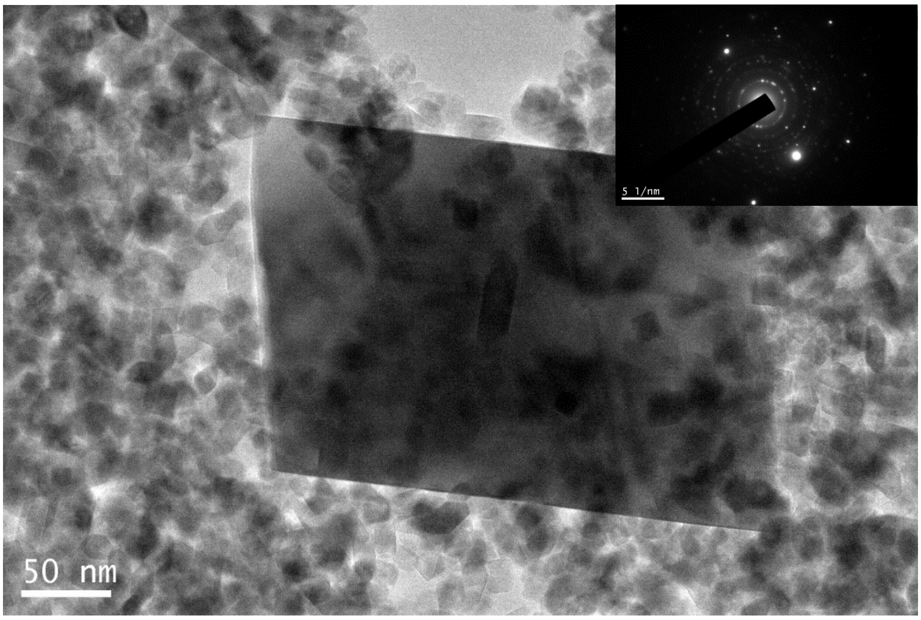

Figure 5.77 TEM image of large crystal in sample TiO_2 (A) 270. Inset diffraction pattern.

Series (B) was analysed using TEM revealing there was a great change in crystallite size with changing concentration of NH_4F in synthesis media. First of all, the fluorine-free blank produced reasonably large crystals that appeared to have a slight rod-like structure, see *Figure 5.78* top. When 0.1 equivalents of NH_4F was added to the synthesis media, the crystals became much larger with very soft and rounded edges, tending towards spherically shaped particles, *Figure 5.78* bottom. As the concentration of NH_4F was increased to 0.25 equivalents, the particles became more block-like, the crystallite size reduced and the polydispersity increased. As the NH_4F increased to 4 equivalents, the particles became much smaller, cubic and the polydispersity narrowed dramatically, see *Figure 5.80*. Throughout series (B) the electron diffraction patterns only indicated anatase phase TiO_2. The size and distribution of sizes throughout series (B) were also measured. It was found that the size of particles measured matched closely with the size determined by PXRD, compare *Figure 5.81* and *Figure 5.47*. However, PXRD does not estimate the distribution of sizes. The fluoride-free blank and 0.1 equivalent samples had the larger mean particle sizes but were very polydisperse. As the concentration of NH_4F increased, the mean size reduced and the particles became more monodisperse, with the 4 equivalents sample having the narrowest particle size distribution, see *Figure 5.81*.

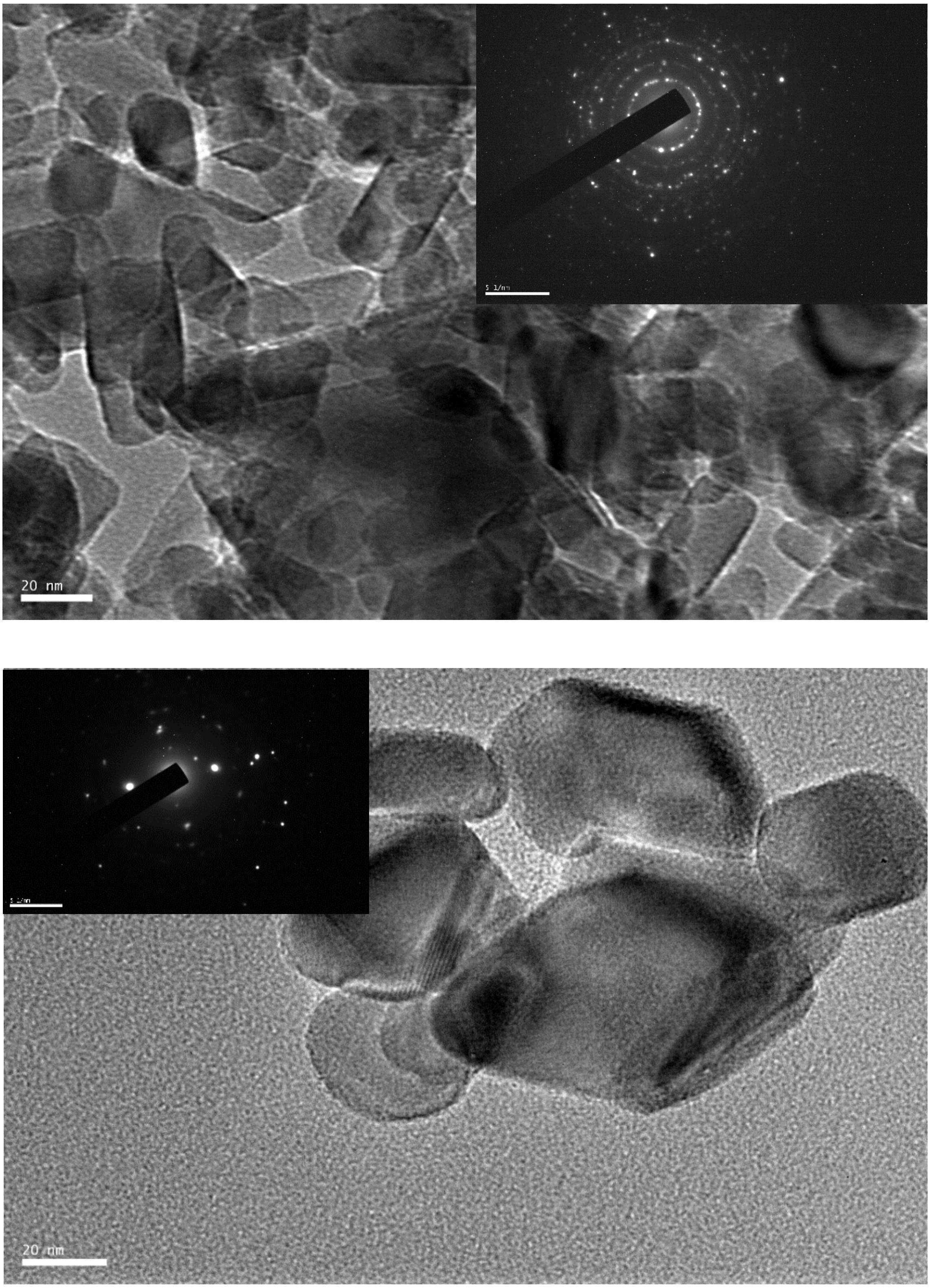

Figure 5.78 TEM images. Top: TiO_2 (F free) blank. Bottom: TiO_2 (B) 0.1. Inset electron diffraction patterns.

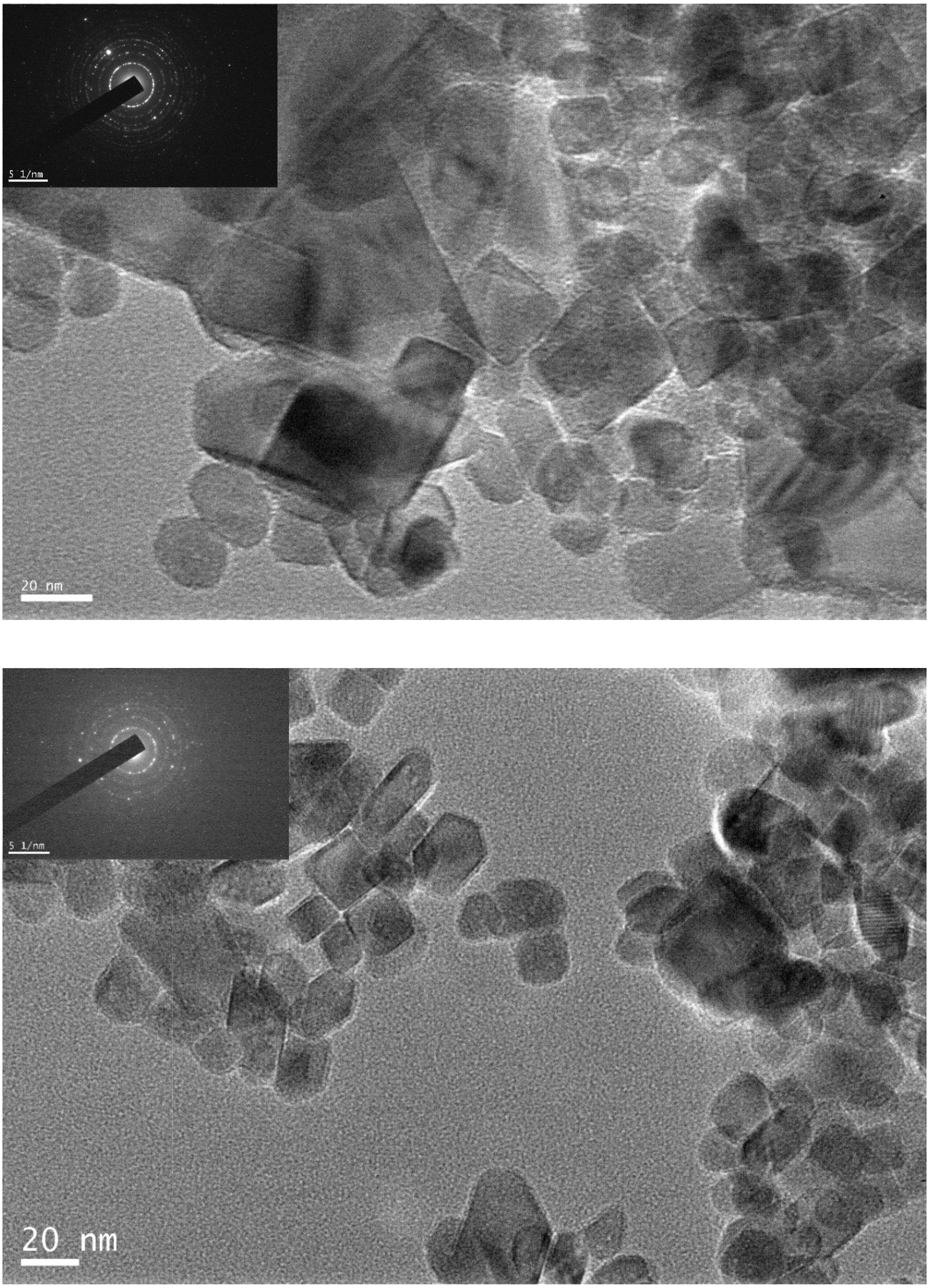

Figure 5.79 TEM images. Top: TiO_2 (B) 0.25 blank. Bottom: TiO_2 (B) 0.5. Inset electron diffraction patterns.

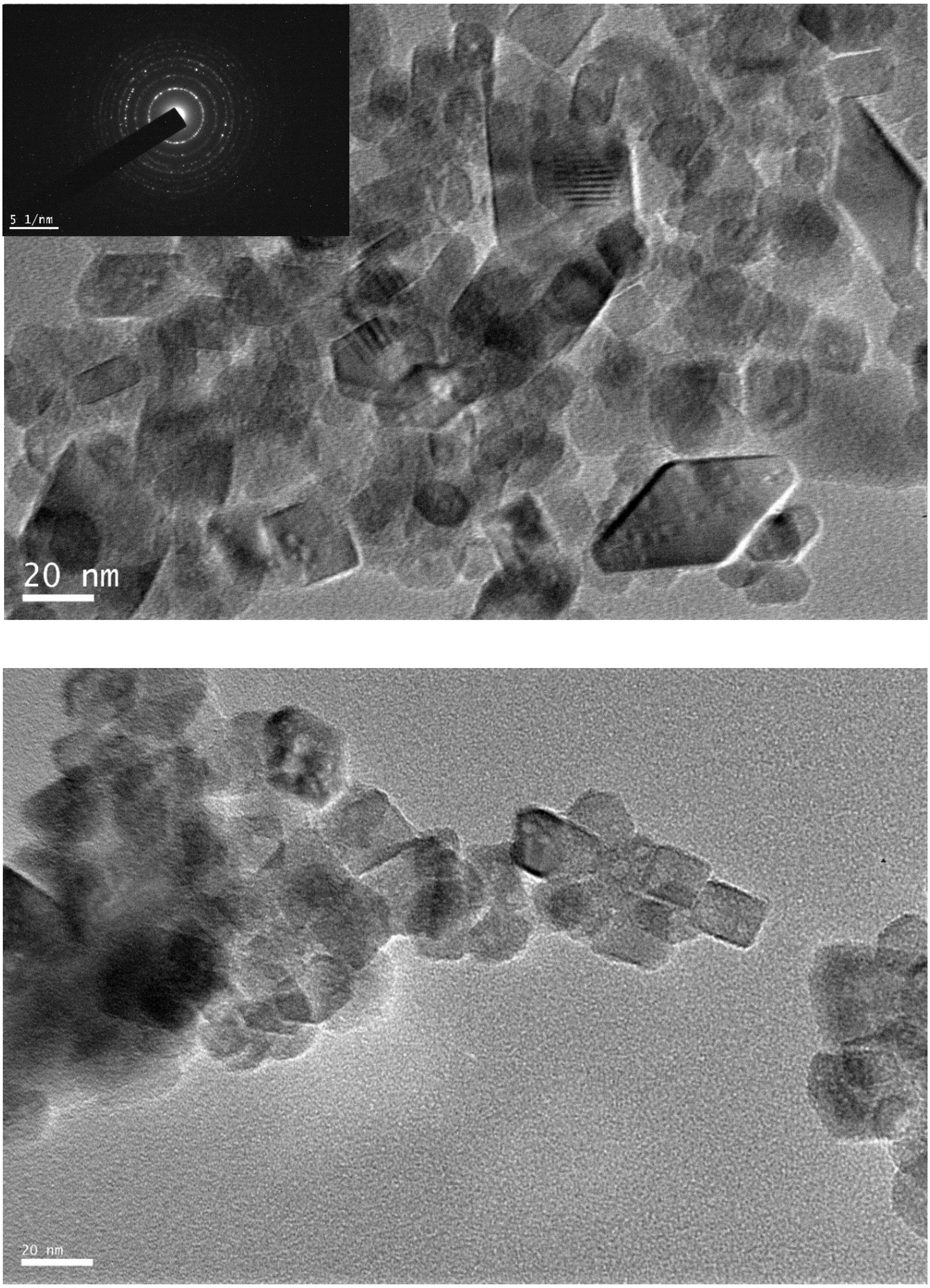

Figure 5.80 TEM images. Top: TiO_2 *(B) 0.75 blank. Bottom:* TiO_2 *(B) 4. Inset electron diffraction patterns. Note: No electron diffraction pattern was collected for* TiO_2 *(B) 4.*

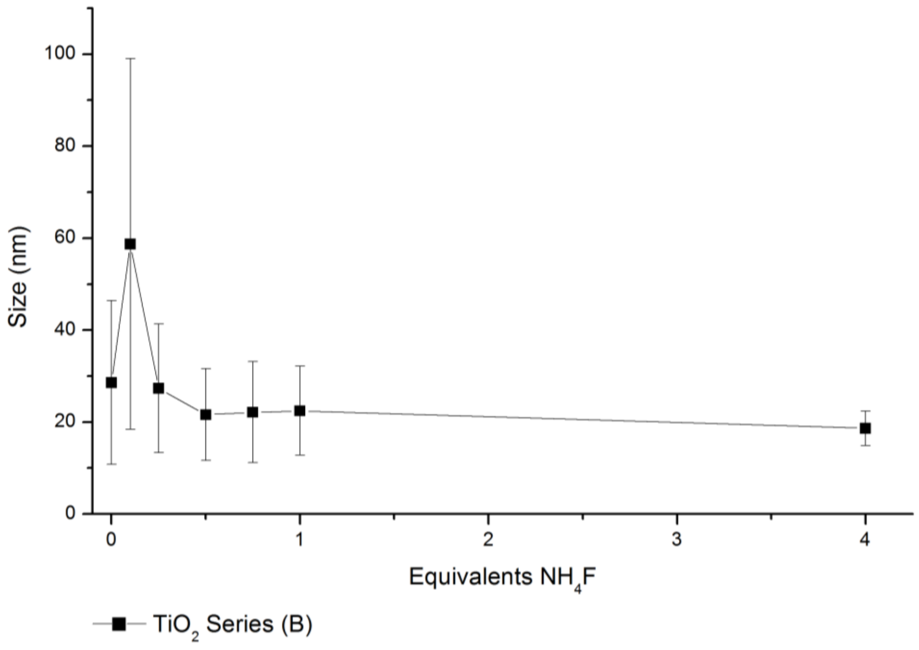

Figure 5.81 Mean particle size and distribution of particle sizes as measured by TEM through series (B). Note: Error bars indicate one standard deviation.

High-resolution TEM (HRTEM) images were used to study the disorder in the outer surface of the crystals through series (B). High-resolution TEM images of the fluoride-free blank, TiO_2 (B) 0.1 and TiO_2 (B) 4 samples can be seen below in *Figure 5.82*. The F-free blank and the sample synthesised with 4 equivalents of NH_4F show a similar crystal edge. Where the crystal lattice ends, there is a dark and distorted 2.5 nm boundary before moving to the carbon background. Whereas, the 0.1 equivalents sample shows well-defined fringing patterns right up to the edge of the crystal, followed by a light area of low density and then the amorphous carbon background. Overall, even at the maximum magnification possible on this particular TEM, it is very hard to say whether a disordered layer on the outside of the crystals is present or not, as the distortion observed could just be an artefact of focus. Because both the 4 equivalents sample and the F-free sample show the same structure at the crystallite edge, it seems far more likely it is just an artefact of focus. Thus, as above, the monolayer of high concentrations of Ti^{3+} (determined by depth profiling Ti2P XPS (*Section 5.1.7*)) does not appear observable with the current TEM.

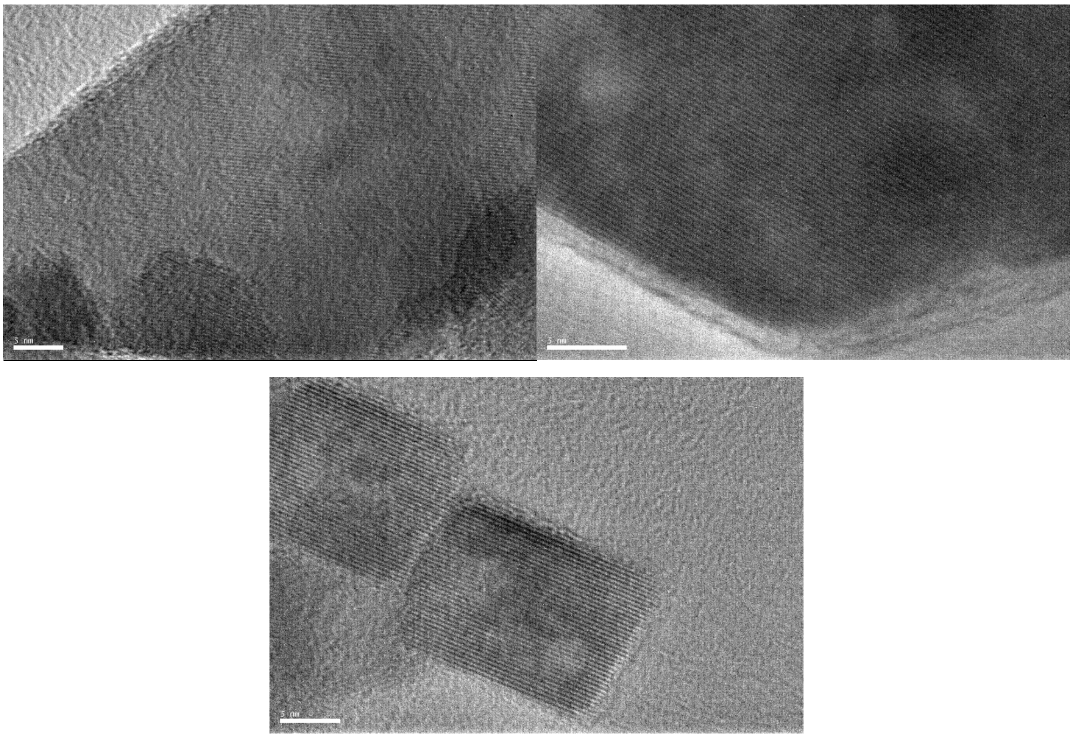

Figure 5.82 High-resolution TEM images. Top left: TiO_2 (F free) blank. Top right: TiO_2 (B) 0.1. Bottom: TiO_2 (B) 4.

The electron diffraction patterns produced by particles in series (B) were analysed, see *Figure 5.83*. Much like series (A), the {001} peak move towards greater inter planner distances. The {013}, {004} and {112} peaks also moved to greater into planner distances. However, there was a slight dip for the sample synthesised with 0.1 equivalents of NH_4F. Lastly, like series (A) the {020} peak showed little change throughout the series. Unfortunately, no electron diffraction was collected on the 4 equivalents sample. Thus, the results appear to agree with the PXRD findings, see *Figure 5.51*.

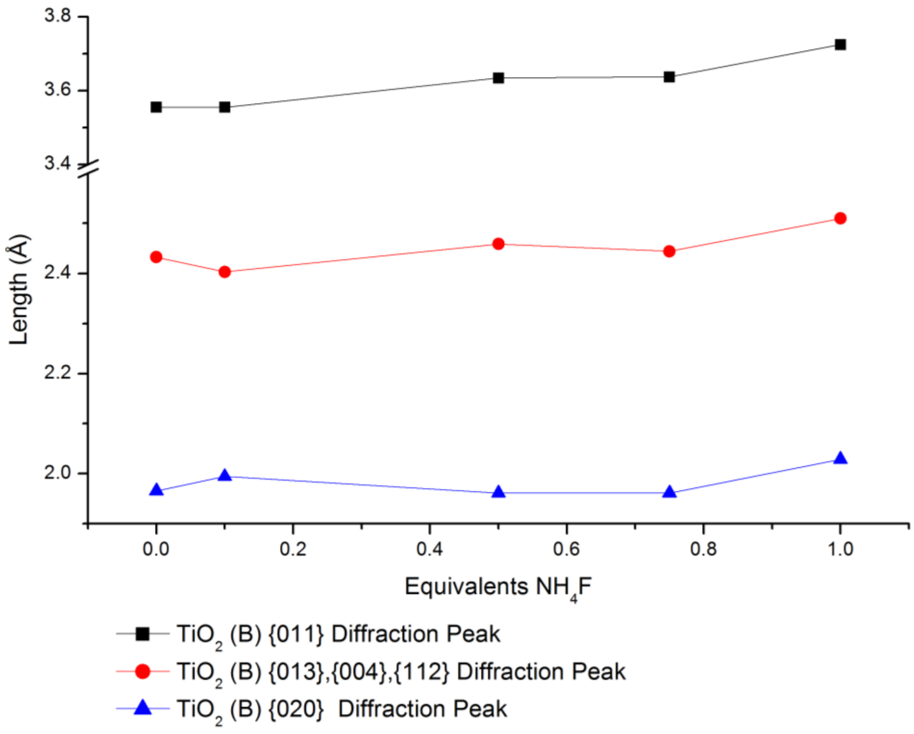

Figure 5.83 Graph of diffraction plane spacing series (B) as determined by electron diffraction in TEM.

Series (C) where NH_4F was substituted for NaF was examined using TEM. It was found that the particles produced in series (C) had a very similar shape to those seen in both series (A) and (B), see *Figure 5.84*. The size was determined to only be 10 nm making these crystals much smaller than those observed in the NH_4F series (agreeing with PXRD predictions). Also, the standard deviation was determined to be 6 nm making these quite polydisperse compared to the NH_4F series. When the electron diffraction pattern of TiO_2 (C) 1 was analysed, it was found that the {010} and ({013}, {004} and {112}) inter planner distances were shorter than those of the NH_4F series, *ca.* 3.59 and 2.44 Å respectively. This makes the bonds shorter than a sample synthesised at 170 °C in the presence of NH_4F, *ca.* 3.56 and 2.41 Å respectively. On the other hand, the {020} showed the same inter planner distance as the equivalent NH_4F sample, *ca.* 1.93 *vs* 1.93 Å respectively (TiO_2 (A) 270).

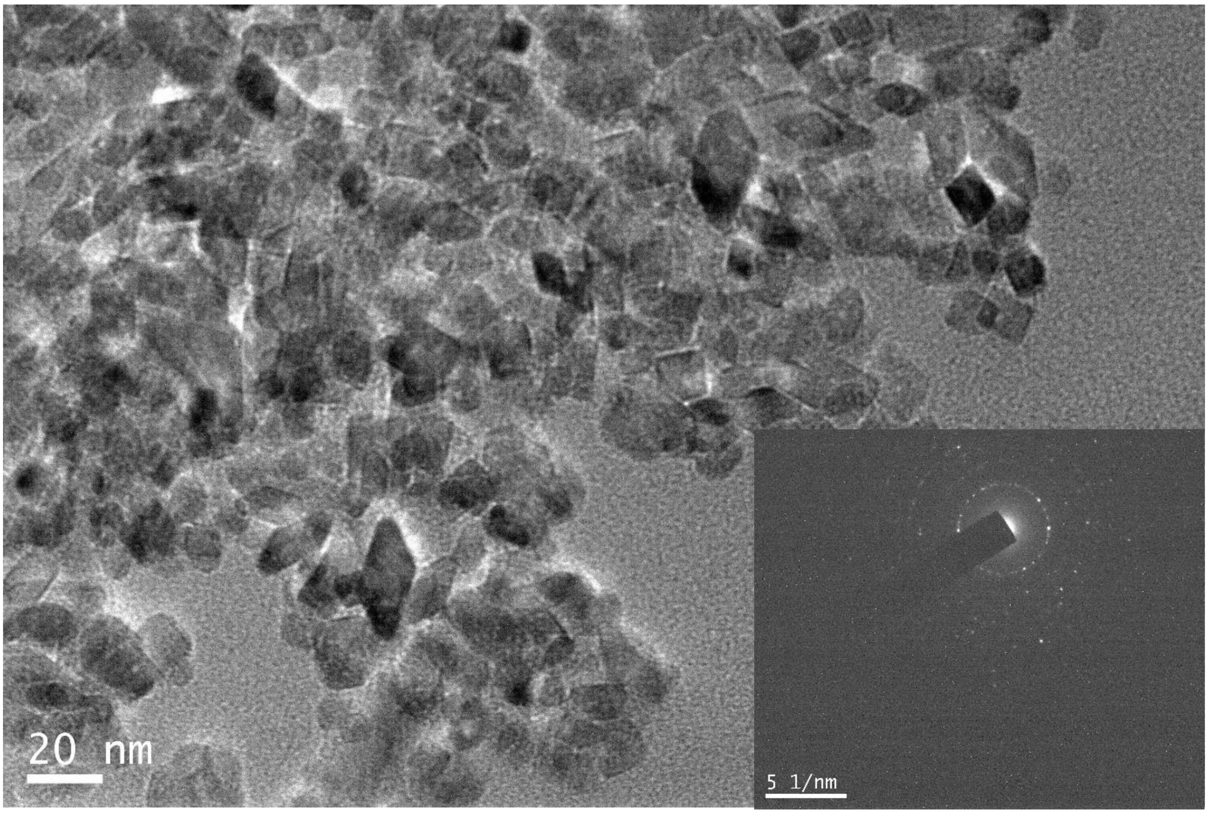

Figure 5.84 TEM image of sample TiO_2 (C) 1. Inset electron diffraction pattern.

Series (F) was also studied using TEM to see if there were any changes in morphology observed by substituting NH_4F for NH_4OH. *Figure 5.85* (top), shows the particles synthesised at 170 °C in the presence of one equivalent of NH_4OH. It can be seen that the particles produced were much larger than the equivalent NH_4F sample, compare with *Figure 5.73* bottom. The particles were determined to have a mean size of 20 nm and a standard deviation of 8 nm, making them larger than the particles in TiO_2 (A) 170 (agreeing with PXRD predictions). Interestingly, the polydispersity was much greater for in the NH_4OH sample when compared to the NH_4F sample *i.e.* 8 nm *vs* 3 nm for TiO_2 (A) 170. As for the shape, the particles synthesised using NH_4OH appeared to be more rounded than those synthesised using NH_4F. PXRD fitting (*Section 5.1.6*) estimated the crystallites synthesised in the presence of NH_4OH to be elongated but to a lesser extent compared to those synthesised with NH_4F (*cf.* 18x28 nm *vs* 47x12 nm for crystallites synthesised at 270 °C in the presence of NH_4OH and NH_4F respectfully). When the temperature was increased to 270 °C, the particles became only marginally larger, see *Figure 5.85* bottom. The particles were measured to have a mean size of 22 nm with the standard deviation of 6 nm, making them only 2 nm larger but with a much narrower distribution. The particles synthesised with NH_4OH maintained their rounded edges when compared to the equivalent NH_4F sample (TiO_2 (A) 270). When the electron diffraction patterns were analysed, it was found that much like series (A), the diffraction peaks responsible for the {010} and ({013}, {004} and {112}) were lengthening with increasing temperature of hydrothermal treatment. The NH_4OH series showed slightly longer inter planner distances than the equivalent NH_4F samples *i.e.* TiO_2 (A) 170 3.56 and 2.41 Å *vs* TiO_2 (F) 170 3.64 and 2.43 Å, also TiO_2 (A) 270 3.72 and 2.51 Å *vs* TiO_2 (F) 270 3.78 and 2.55 Å.

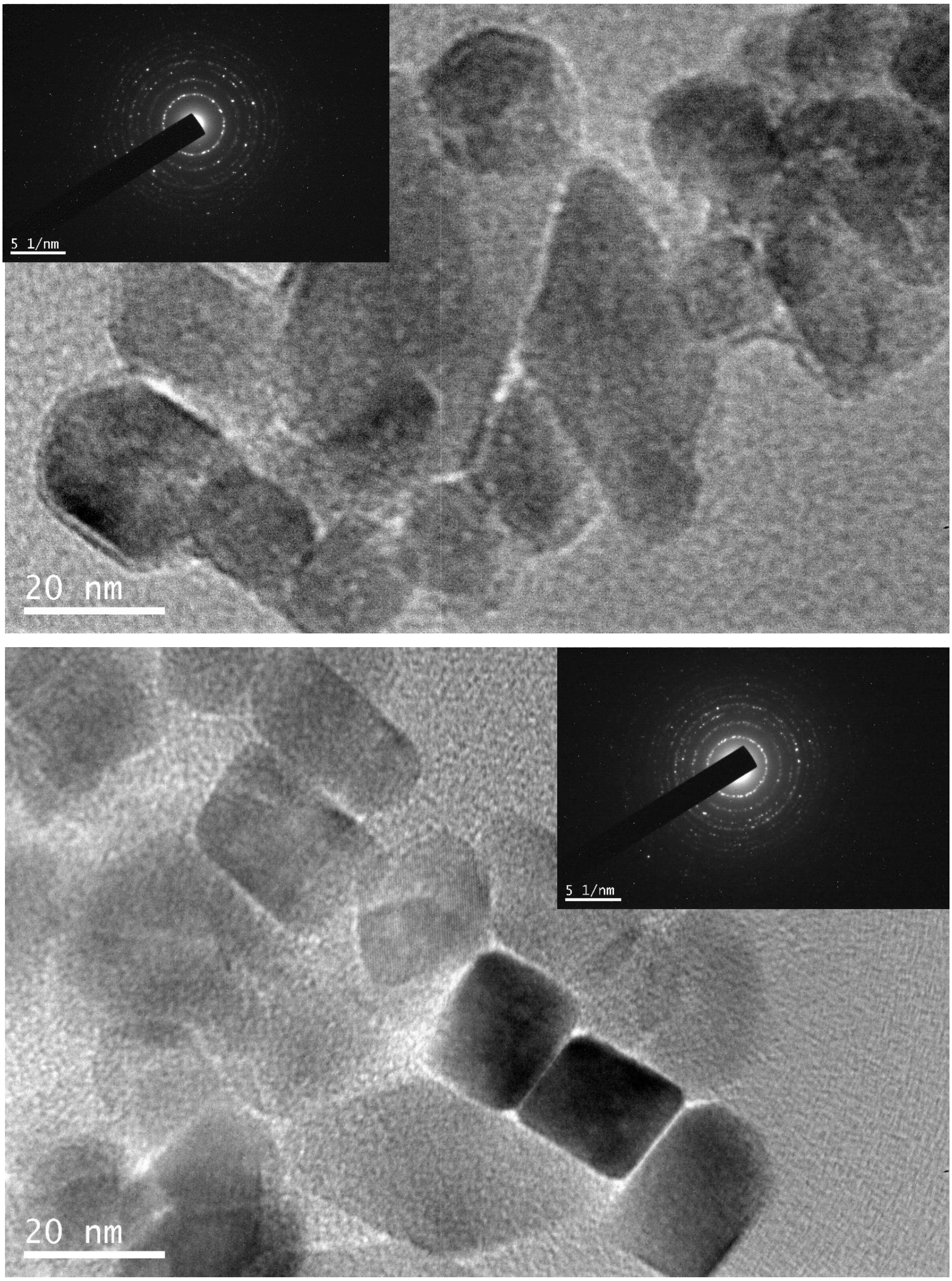

Figure 5.85 TEM images of. Top: TiO_2 (F) 175. Bottom: TiO_2 (F) 170. Inset electron diffraction patterns.

To study possible surface abnormalities caused by NH_4OH, HRTEM images of the sample TiO_2 (F) 270 were analysed. When looking at *Figure 5.86*, it can be seen that the TiO_2 synthesised in series (F) had very clean edges on the outside of the crystals. There were no obvious signs of any distorted layer, unlike the possible distortion in series (A) and (B) above, see *Figure 5.82*.

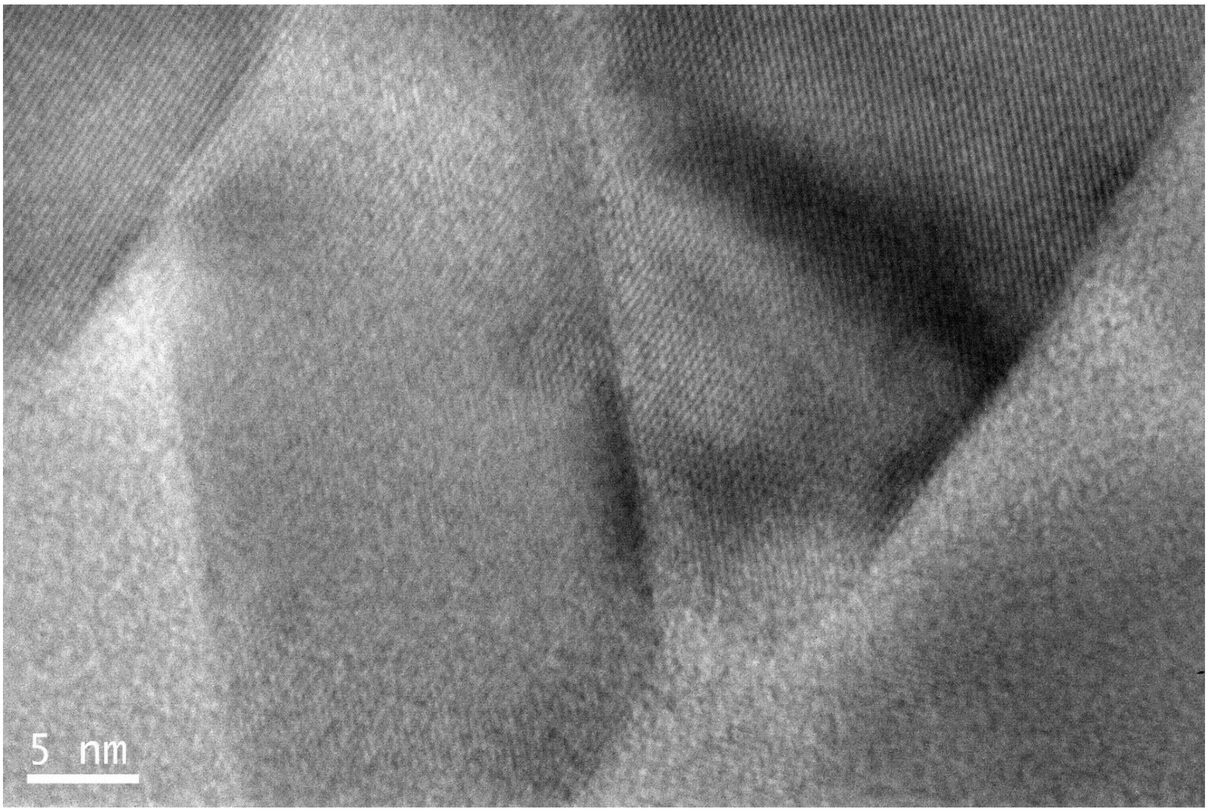

Figure 5.86 High-resolution TEM image of TiO_2 (F) 270.

The electron microscopy study of blue TiO_2 showed many interesting morphological features. However, clues as to the nature of the defects were limited. The SEM study showed highly agglomerated particles that were difficult to distinguish from the individual crystallites within such larger particles. The degree of agglomeration seemed independent of the conditions used. Through in series (B), the 0.1 equivalent sample showed very large crystals with a bipyramid shape that could be seen with SEM. High-resolution SEM images did show a size difference of the individual crystallites between samples synthesised at 170 and 270 °C, unfortunately, this experiment was not possible for every sample. Yet, this did show that in general SEM had insufficient resolution to show the morphology of individual crystallites. Hence, what was observed in SEM initially did not appear to agree with the PXRD analysis as there was no gradual increase in size or elongation. SEM images of samples synthesised in the presence of NaF or NH_4OH did not show any significant differences to those synthesised in the presence of NH_4F. No hierarchical structures were observed unlike what has been reported in the literature.[32,66,67] Either the conditions did not induce self-assembled structures *e.g.* NH_4F concentrations were too low for the selective etching to occur, or the post-processing of samples before imaging *i.e.* washing with water and ultrasonic dispersion when preparing SEM samples destroyed the hierarchical structures (see *Section 3.3.5*).

TEM made it possible to study the morphology of individual crystallites. First of all, it was seen that as per the PXRD results, the size increased with increasing temperature of hydrothermal treatment. Additionally, it was found that the polydispersity of the samples increased quite dramatically at processing temperatures above 170 °C. The fact that the carbon-free blank sample showed similar morphology and polydispersity to the rest of series (A) indicates that the decomposing organics had little impact on the morphology of crystallites. Also, in line with the PXRD analysis, the crystallites showed more elongation in the [001] direction as the temperature of hydrothermal increased. The elongation in the [001] direction was observed as a change from cubic crystals at lower processing temperatures to more bipyramidal crystals at higher processing temperatures (assignment of direction based on shape). It has been shown that the natural shape of anatase is bipyramidal. This bipyramidal shape comes from minimising the exposure of the {001} facet.[28] As a result, the [001] axis of the crystal becomes elongated.[149] Thus, nether titanate formation nor the F^- ion really impacted the observed crystallite shape.

The crystallite sizes observed in series (B) also agreed with the sizes predicted by PXRD. The 0.1 equivalents sample was very large and the 4 equivalents sample was very small. Interestingly, the polydispersity was greatest in the sample made using 0.1 equivalent of NH_4F and smallest in the "4 equivalents" sample. Also, the crystallites observed in the F-free sample were large (*ca.* 28 nm). The addition of NH_4F caused the crystallites to grow larger with rounder corners at concentrations less than 1 equivalent. Yet, as the NH_4F concentration increased to 4 equivalents, the crystallites became cubic and more isometric, agreeing with PXRD analysis. This change from large crystals to smaller square crystals could be due to the *in-situ* formation of ammonium titanate or the effects of the F^- ion.

As above in the PXRD results, it appeared that Na^+ ion was a stronger morphology directing agent than the NH_4^+ ion having a greater effect at lower concentrations. This is shown by the fact that the crystallites in TiO_2 (C) 1 look like the crystallites in the sample TiO_2 (B) 4, indicating that 1 equivalent of Na ions had the same effects of 4 equivalents of NH_4^+ ions. On the other hand, this would also rule out F^- as the main morphological director as the F^- concentration is 4 times greater in the sample TiO_2 (B) 4 *cf.* TiO_2 (C) 1. Similarly, the sample TiO_2 (A) 270 shows bipyramidal crystals with shapes more consistent with the F-free blank than the "4 equivalents" sample. This indicates the F^- ions activity in morphology control is limited. Then again, the NH_4OH produced more cubic crystals at higher temperatures than the equivalent NH_4F sample. This could mean that the F^- ion still does have some impact on the morphology, while there were no obvious signs of the {001} facet being enhanced. The contraction of the (*c*) axis and the less bipyramidal shaped crystallites found in TiO_2 (B) 4, could indicate the presence of a greater {001}/{101} facet ratio.[149] More detailed analysis of the fringing patterns is required to determine facet ratios.

At the higher end of processing temperatures in series (A), a small population of very large crystallites were observed. Also, very large crystals were observed in series (B) at 0.1 equivalents of NH_4F. These larger crystals appear in some of the darkest blue samples. As the crystallites become larger and their size approaches half the wavelength of the visible light, their light scattering cross-section becomes wavelength dependent (Mie theory).[146147] This means blue light will be reflected by passing through fewer particles than red light, thus red light ends up having a higher probability of being absorbed by Ti^{3+} defects. This could result in samples containing larger particles appearing bluer while containing the same concentration of defects. This would also explain the experimental observation that the bottom part of a centrifuged sample would appear darker. This is because the larger crystallites settle faster due to Stokes' law.[150]

The electron diffraction patterns taken using TEM agreed with the findings in PXRD. All of the samples examined were anatase phase, including the minority populations of very larger crystallites. There was no evidence of titanates, titanium oxyfluorides or titanium nitrides. Importantly, there were distinct shifts in the electron diffraction pattern indicating the lengthening and shortening of inter-planar distances.

First of all, there was a distinct lengthening of both the {011} and {004} inter-planer distances with increasing temperature of hydrothermal treatment. Series (B) showed the same lengthening of both the {011} and {004} inter-planer distances as the ratio of NH_4F to TiO_2 increased. Series (F) showed longer inter-planar distances than the equivalent NH_4F sample at both 170 and 270 °C. On the contrary, the NaF modified sample showed much shorter distances indicating NaF was having a greater effect on crystal growth than NH_4F. In all series analysed, the {020} peak hardly moved, this may be due to limitations in the measurement method. These results agree with what was observed with PXRD. That is, the ammonium/sodium titanate formation is the main director of morphology. Also, the sodium titanate is much effective at lower concentrations.

A final point of discussion is the surface distortion and haze present in the electron diffraction patterns. Crystals in both series (A) and series (B) were analysed at 800,000+ times magnification. At this magnification, lattice fringing could be seen and there did appear to be an area of distortion near the outer edge of the crystals. What was not clear was whether this distortion was a focus effect or actual distortion present in the crystal. Either way, there was no conclusive evidence that more or less NH_4F or higher temperatures of hydrothermal treatment produced a more distorted surface. Also, the haze in the electron diffraction patterns did not seem consistent with any other experimental results (*e.g.* Ti^{3+} or F^- doping detected by XPS, see *Section 5.1.7*). Therefore, the haze was likely just to do with the sample preparation or focusing of the TEM instrument. With the limitations of the instrument, it cannot be concluded whether there was any surface distortion present as per the findings of Chen *et al.*[122] and Naldoni *et al.*[49]

5.1.9 Ion Beam Analysis

The survey scans in the XPS section quantified the F^- present in the samples; however, as the survey scans were performed using a single incident energy (1487.6 eV) it did not indicate whether it was surface or bulk. In the following section, particle-induced gamma-ray emission spectroscopy (PIGE) was used to measure the relative concentrations of F^- in as-synthesised and NaOH washed samples. As the proton beam has an energy of a few MeV, penetration into the sample is in the order of 10s of µm (atomic number dependent). Also, the emitted gamma rays have an energy of greater than 100 eV; thus there is little self-absorption.[151] So, the particles analysed here were less than 100 nm, therefore, PIGE would measure the total F in the samples with no consideration as to whether it was bulk or surface (As opposed to XPS which is only sensitive to the out shell of the particles *cf.* less than 2.8 nm mean free path at 1487.6 eV).[114]

In order to determine if the F^- ions being detected were indeed associated with bulk or surface, PIGE was used to quantify the F present in samples before and after washing with 10 M NaOH. Washing nanoparticulate TiO_2 with 10 M NaOH has been reported to remove surface-bound F^-.[98,152] Therefore, the F^- detected after the wash must belong to the bulk phase. As can be seen in *Figure 5.87*, all the samples maintained roughly ¾ of their F after washing with 10 M NaOH. Thus, a large amount of the F is present as a bulk phase dopant.

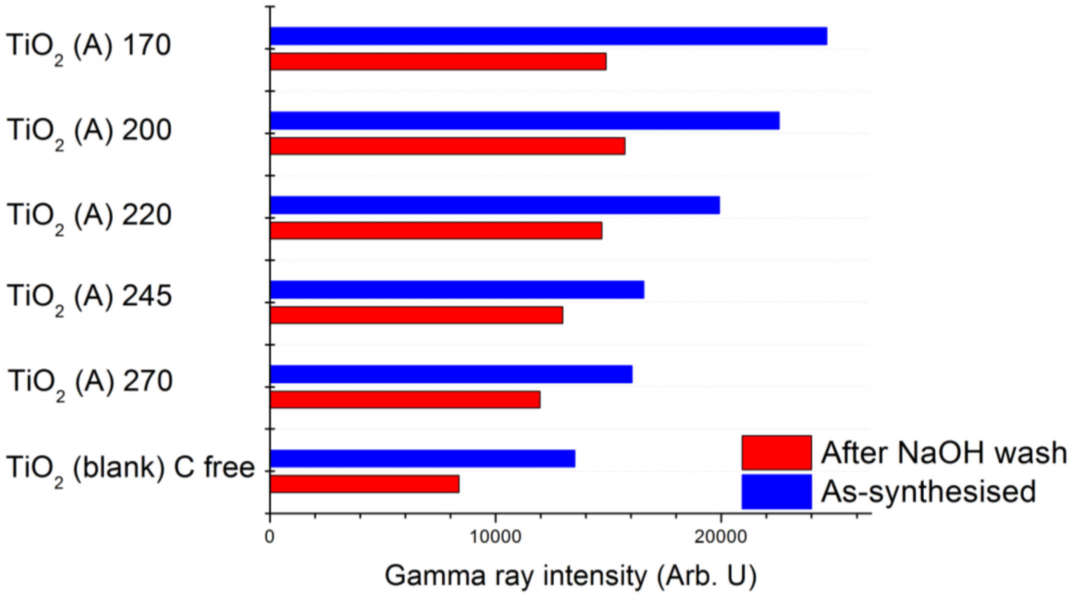

Figure 5.87 PIGE results of F gamma emission intensity before and after being washed with 10 M NaOH.

There appeared to be F^- doping occurring in all samples independently of whether these were blue or were produced under reducing conditions. This confirms that the presence of bulk phase F^- doping alone does not cause the blue colouration. The doping with F^- must be accompanied by reducing conditions to produce blue TiO_2. Furthermore, it is known that without F^-, reducing conditions alone do not produce blue TiO_2 (as indicated by the white (F free) blank sample. Therefore, the F^- must be involved in the defect, possibly stabilising the Ti^{3+}.

5.1.10 Nitrogen Adsorption Analysis

The surface area of the particles synthesised in series (A) was evaluated using nitrogen adsorption isotherms and Brunauer-Emmett-Teller (BET) theory. The surface area of series (A) was found to decrease with increasing temperature of hydrothermal treatment, see *Figure 5.88*. The decreasing surface area agrees with the PXRD and TEM results discussed above as both these methods showed the average crystallite size was decreasing as the temperature of hydrothermal treatment increased.

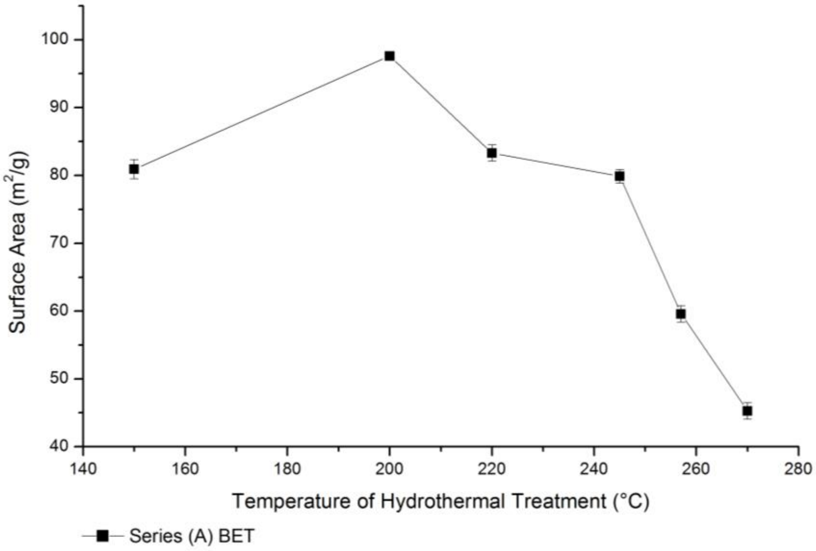

Figure 5.88 Surface area results of series (A) using BET analysis of nitrogen adsorption isotherms.

Likewise, the surface area of the particles synthesised in series (B) was evaluated using nitrogen adsorption isotherms and BET theory. It was found that the surface area decreased rapidly when 0.1 equivalents of NH_4F were used in synthesis, see *Figure 5.89*. These results are in good agreement with the significantly larger particle/crystallite sizes (*cf*. the rest of the series) observed in TEM and calculated using PXRD above. The surface area of the samples synthesised with more than 0.25 equivalents of NH_4F exceeds the surface area of the F-free blank sample although the crystallite size was still larger when looking at the PXRD results above, see *Figure 5.47*. The surface area in the NH_4F modified samples was greater as the anisotropic crystal shape increased the exposure of facets relative to the bulk *i.e.* rods have a greater surface area than the equivalent weight of spheres.

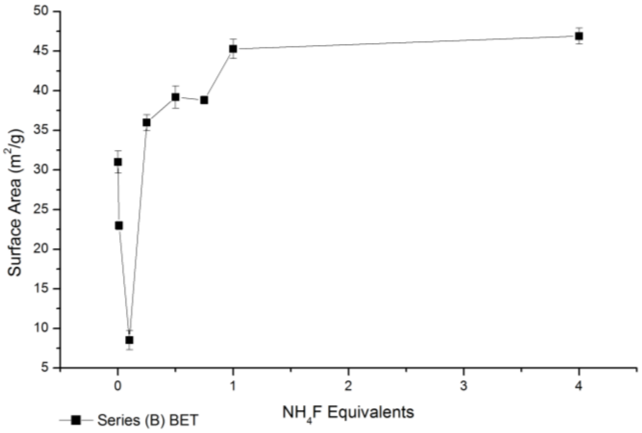

Figure 5.89 Surface area results of series (B) using BET analysis of nitrogen adsorption isotherms.

The surface area of a few selected samples in series (F) was evaluated. It was found that the surface area of samples synthesised in series (F) was very similar to the equivalent sample in series (A) *e.g.* 45 *vs* 43 m_2/g for TiO_2 (A) 270 and TiO_2 (F) 270 respectively. Which agrees with the PXRD results estimating the crystallite domain sizes were not significantly different *e.g.* 12x47 *vs* 18x28 nm for TiO_2 (A) 270 and TiO_2 (F) 270 respectively. Thus, the F^- ion was having little effect on the surface area of the particles.

5.3 Conclusions:

In conclusion, it would appear that the temperature of hydrothermal treatment, the presence of organics (isopropanol as a by-product of TIPP hydrolysis) and the presence/concentration of the F^- ion are very important in the formation of the blue coloured TiO_2. It was found by mass spectrometry and FT-IR spectroscopy that the *in-situ* decomposition of isopropanol into non-saturated hydrocarbons results in the formation of H_2 gas. Under the intense autogenic pressures and temperatures, *i.e.* 270 °C and 200 atm, the H_2 dissolves into the liquid phase and reduces Ti^{4+} to Ti^{3+} in growing particles. EPR results showed that the blue TiO_2 contained paramagnetic centres as indicated by a signature at g= 1.96, which are most likely bulk Ti^{3+} defects.[47,53,97,103] This bulk phase Ti^{3+} was incorporated into the crystallites as they were growing, hence, producing chemically stable defects (*cf.* surface only Ti^{3+}). Further confirmation of the bulk Ti^{3+} was observed using SQUID where the blue TiO_2 changed from diamagnetic to paramagnetic with a hint of ferromagnetism once cooled to 3 K. The paramagnetism was due to the Ti^{3+} and was quantified using the Brillouin Function and the concentration of these Ti^{3+} centres was found to be in the order of $4.4\text{x}10^{25}$ N/m^3. The ferromagnetism was due to the Ti vacancies as a result of the hydrothermal synthesis.[102] The presence of Ti vacancies was confirmed during a Rietveld refinement of the PXRD data while refining Ti occupancy. It was found that at greater than 0.1 equivalents, the F^- ions reduced the Ti occupancy whereas, up to 0.1 equivalents the Ti occupancy increased. This was thought to be due to the number of defects. As the Ti^{3+} concentration increases, eventually, it comes more energetically favourable to have one Ti vacancy rather than 4 Ti^{3+} defects. This change from bulk Ti^{3+} to bulk Ti vacancies is believed to explain the colour results. UV-VIS DRS study of series (B) focused on changing the ratio of TiO_2 to NH_4F demonstrated that the colour intensity as estimated by absorbance at 620 nm responded non-linearly to the ratio of TiO_2 to NH_4F. The TiO_2 produced was the bluest at 0.25 equivalents of NH_4F, more or less NH_4F resulted in a whiter TiO_2. Surprisingly, at 4 equivalents of NH_4F, a near white TiO_2 was produced. Finally, PXRD analysis of the lattice dimensions showed that the (*a*) dimension expanded and (*c*) dimension contracted with increasing ratios of NH_4F. Through analysis of the changes in lattice parameters, it was found that the changes in (*a*) were caused by the F^- doping whereas the changes in (*c*) were caused by the reducing conditions. Therefore, it is believed the Ti^{3+} defect must lie along the (*c*) axis of the crystallites.

The existence of surface Ti^{3+} was also found in the blue TiO_2. However, the concentration of the surface Ti^{3+} did not seem to be proportional to the intensity of the colour, but would instead originate as a consequence of the increasing F^- concentration in synthesis solution. High-resolution XPS of the Ti2p region showed the concentration of detectable Ti^{3+} increased with the ratio of NH_4F to TiO_2 added to the synthesis mixture. Upon synchrotron-based XPS depth profiling, it was found the Ti^{3+} detected by XPS was mostly surface bound residing in a monolayer at the surface of the particle. Furthermore, VB spectroscopy found evidence of the states associated with Ti3d electrons and the presence/magnitude of the band bending, which were related to the concentration of F^- rather than any other parameter of synthesis.

NEXAFS was one of the only techniques to show the presence of both surface and bulk Ti^{3+}. Analysis of the TEY, PEY and FY showed that the increasing ratio of NH_4F to TiO_2 increased the presence of pentacoordinate Ti^{3+} both in the bulk and at the surface. This was determined by looking at the relative intensity of the signal associated with E_g and t_{2g} states. Raman spectroscopy study also indicated that the pentacoordinate Ti^{3+} populations were proportional to the amounts of NH_4F added to the synthesis media. The position of the first E_g peak in Raman spectra appeared to shift with the changing NH_4F concentrations; the magnitude of the redshifts correlated with the intensity of the blue colour (as determined by absorption at 620 nm). By comparing the shift in the E_g peak and the crystallite size determined using PXRD, it was determined that this shift was independent of the changes in crystallite size. Secondly, the same E_g mode appeared to broaden with the addition of NH_4F. The broadening was also found to be independent of crystallite size. Therefore it is believed the broadening is related to F^- doping (matching with XPS F results).

With respect to the band structure of obtained materials, the UV-VIS DRS study found that the blue anatase phase TiO_2 synthesised in series (A) to (C) showed no shift in the absorption edge, indicating the bandgap had not been affected by the defects. VB spectroscopy also confirmed the valance band’s top edge had not shifted to higher energies; in fact, it moved slightly to more negative energies further away from the vacuum level. However, the Ti^{3+}3d electrons appeared between the valence band and conduction band. The defect state explained the absorption of 576 to 730 nm (2.15 to 1.7 eV) and 1301 to 2254 nm (0.95 to 0.45 eV) nm light giving the TiO_2 its blue colour.

The general morphology of the crystallites and overall particles was analysed using PXRD, TEM, SEM and Raman spectroscopy. Electron diffraction, PXRD and Raman spectroscopy showed that in the vast majority of cases the only phase produced by the hydrothermal synthesis was anatase, with brookite observed as minority phase in just a few samples (the follow-up study on the latter samples is reported in Chapter 6). It was found by PXRD, TEM, SEM and Raman that it was the NH_4^+ ions which influenced the growth of TiO_2 crystallites rather than the F^- ions. At low concentrations (up to 0.1-0.25 equivalents), NH_4^+ ions accelerated growth producing large (*ca*. 150+ nm) crystallites. At medium concentrations (approximately 1 equivalent) its presence resulted in crystallites elongated in the [001] direction. Finally, at high concentrations (4 equivalents) it suppressed growth. It is believed the growth was regulated by producing ammonium titanate as an intermediate, which could have different roles (facilitator or moderator) depending on the relative ratio to TiO_x-building blocks.

Chapter 6 : Blue Rutile and Brookite Phase TiO_2

6.1 Introduction:

Blue rutile and brookite phase TiO_2 where synthesised using the methods developed in Chapters 4 and 5. It was known from Chapter 4 that introducing oxalic acid into the sol-less synthesis at low concentrations could result in blue rutile being produced. On the other hand, when NH_4F was substituted for NaF during the synthesis of blue anatase, it was found that brookite formed at high concentrations. This accidental discovery was explored further and it was found that blue brookite could be reproducibly synthesised. In the following chapter, blue rutile and blue brookite are characterised using similar techniques as in Chapter 5. The following introduction summaries relevant literature on the synthesis and characterisation of blue rutile and brookite.

6.1.1 Blue Rutile

Blue rutile has previously been synthesised by reductive combustion methods.[48,55] However, it has mostly been synthesised to study fundamental properties of this material or by an accident as it is not generally synthesised for use as a visible light photocatalyst as it is believed to be photocatalytically inferior to anatase.[6]

6.1.2 Ultra-Violet Diffuse Reflectance Spectroscopy studies of Blue Rutile

Blue rutile has been characterised using UV-VIS DRS by Zuo *et al.*[48], Zhao *et al.*[153] and Hamdy *et al.*[55]. Zuo *et al.*[48] did not report the optical bandgap to change for blue rutile although it was not compared to a non-reduced rutile but did report the blue rutile absorbed red light starting at approximately 500 nm. On the other hand, Hamdy *et al.*[55] synthesised blue rutile using the same methods as Zuo *et al.*[48] but did report that the bandgap narrowed to 2.93 eV.

6.1.3 Raman spectroscopy studies of Blue Rutile

Hamdy *et al.*[55] characterised blue rutile using Raman spectroscopy. No peak shifts were mentioned; as the sample was not completely pure rutile peak shifts would have been masked anyway.

6.1.4 Soft X-ray Characterisation of Blue Rutile

Hamdy *et al.*[55] characterised the blue rutile using XPS. In the Ti2p region, a Ti^{3+} peak (shoulder) centred at 457.7 eV was reported. However, the Ti^{3+} was reported to be unstable and photocatalytically oxidised when the rutile was used as a photocatalyst to oxidise methylcyclohexene. Zuo *et al.*[48] also characterised blue rutile using XPS but did not detect any Ti^{3+}.

Zhao *et al.*[153] synthesised blue rutile using Zn as a reducing agent. The blue rutile was characterised by XPS and the Ti2$p_{3/2}$ peak position was found to be dependent to the amount of Zn added to the synthesis mixture, see *Figure 6.1*. It was reported that the shift in the Ti2$p_{3/2}$ peak was due to the Ti^{3+} concentration (the total Ti^{3+} concentration was not reported).[153]

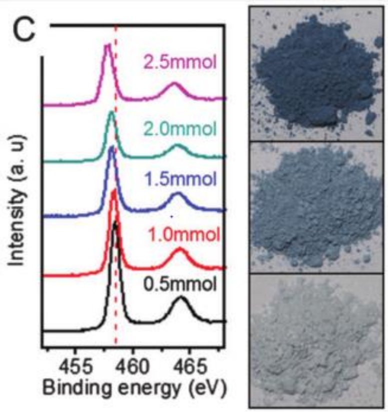

Figure 6.1 XPS results showing the shift of the Ti2$p_{3/2}$ peak relative to the molar amount of Zn metal added to the synthesis media. Reproduced from Zhao et al.[153]

Thus far, to the best of the author's knowledge, there are no NEXAFS or VB characterisation studies of blue rutile reports in the literature.

6.1.5 Powder X-ray Diffraction Characterisation of Blue Rutile

In all the previously published work this author was able to identify where blue rutile has been synthesised, PXRD has only been used to estimate phase purity. No other information on the unit cell or Ti occupancy was ever reported.[48,55,153] However, single crystal rutile that contains oxygen vacancies as a result of O bombardment (2 meV) was used to show that the strain in the crystal can increase to 0.5 % before the point defects (Ti^{3+}) rearrange into a dislocation defect.[101]

6.1.5 Electron Microscopy Characterisation of Blue Rutile

The use of electron microscopy to characterise blue rutile is limited to the general morphology (shape and size) of the particles. Zhao *et al.*[153] reported the blue rutile synthesised to be elongated rods, exposing a large percentage of the [110] facet (relative facet coverage was not reported), see *Figure 6.2*.

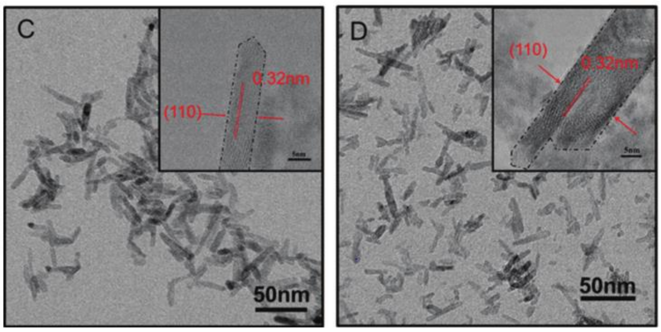

Figure 6.2 TEM images of blue rutile rods synthesised by Zhao et al.[153]

Of relevance to the following chapter (even though the rutile was not reported to be blue), the aspect ratio of rutile crystallites has been shown to be affected by the presence of F^-. Wu *et al.*[86] synthesised rutile hydrothermally in the presence of HF, see *Figure 6.3*. The binding of the F^- ion to the {001} facet resulted in “nano-hills” between the {001} and {111} facets giving the rutile crystallites rounded edges. Also, the aspect ratio could be controlled by altering the ratio of F^- to TiO_2.

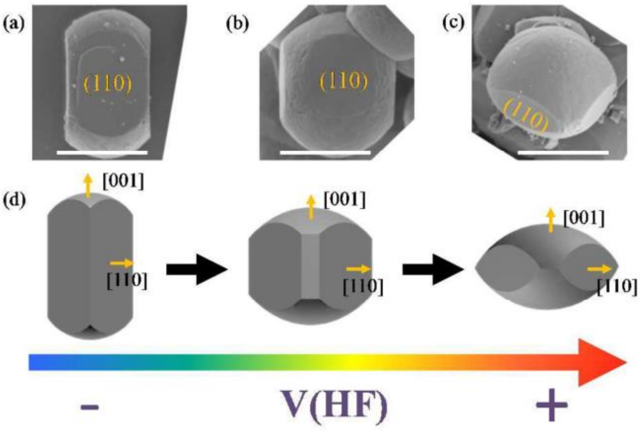

Figure 6.3 SEM images of rutile synthesised with HF showing a compressed [001] axis. Reproduced from Wu et al.[86]

6.1.6 Characterisation of Blue Brookite

Only one report of black brookite has been found; there have been no reports of blue brookite.[147] Brookite is notoriously difficult to synthesise in a phase pure form.[21] Also, due to a belief of inferior photocatalytic activity, brookite is rarely studied.[21,154]

6.1.7 Ultra-Violet Diffuse Reflectance Spectroscopy Studies of Blue Brookite

Thus far no UV-DR spectra for blue brookite can be found in the literature. However, black brookite has been synthesised by Zhu *et al.*[154] and the UV-VIS DRS study of this black brookite showed no shift of the intrinsic absorption edge. Nevertheless, the black brookite absorbed all visible wavelengths extending out into the inferred region.[154]

6.1.8 Raman Spectroscopy Studies of Blue Brookite

Brookite phase TiO_2 displays a complicated Raman spectrum consisting of 16 modes.[154] Thus far, there have been no reports of Raman peaks shifting with respect to the presence of Ti^{3+} defects.

6.1.9 Soft X-ray Characterisation of Blue Brookite

Black brookite was studied using XPS and VB spectroscopy. Zhu *et al.*[154] showed that the $Ti2p_{3/2}$ and $Ti2p_{1/2}$ peaks shifted to lower binding energies in black brookite due to surface Ti^{3+}, see *Figure 6.4* left. Also, VB spectroscopy showed that the O2p π bonding edge shifted by 0.33 eV to lower in binding energy, which was attributed to surface disorder and localized defects.[154]

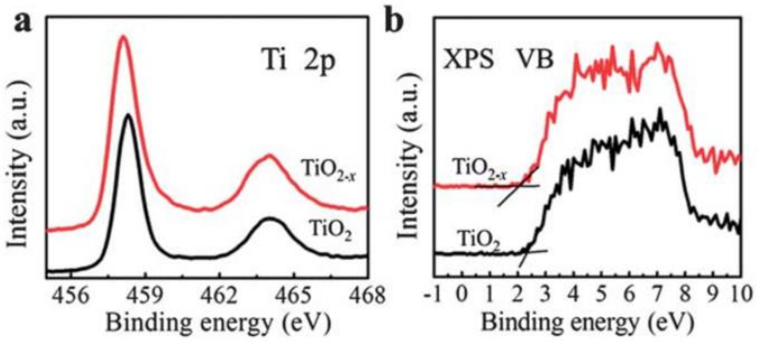

Figure 6.4 XPS and VB spectra of black brookite reproduced from Zhu et al.[154]

6.1.10 Powder X-ray diffraction Studies of Blue Brookite

Thus far there has been no in-depth characterization of blue or black brookite using PXRD beyond phase identity. Although, determining phase purity of brookite can be challenging due to the peak overlaps with anatase.[21] According to Hu *et al.*[155], the only true way to determine phase purity is to look for a characteristic peak of anatase at 62.57 ° (Cu radiation) that has no overlaps with brookite. On the other hand, a Rietveld refinement has been reported to work as well.[21]

6.2 Results and Discussion:

For the following discussion, the naming scheme used for brookite sample is as follows: TiO_2 (Brk) “XXX” “Y” where “XXX” is the temperature of hydrothermal treatment and “Y” is the number of molar equivalents of NaF with respect to Ti added to the synthesis media. For the rutile samples often observed in series (G), the naming scheme is as follows: TiO_2 (G) “XXX”ox“Y” where the “XXX” is the number of molar equivalents of oxalic acid to Ti and “Y” is the number of molar equivalents NH_4F to Ti.

6.2.1 UV-VIS DRS Blue Brookite and Rutile Phase TiO_2

UV-VISDRS was used to study the light absorbing properties of the blue brookite with respect to the temperature of its hydrothermal treatment. As with the blue anatase (Chapter 5), the blue brookite can be seen absorbing red light, see *Figure 6.5*. Also, like series (A) (Chapter 5), the absorption of red light increased as the temperature of hydrothermal treatment increased, making the samples appear bluer. When compared to the equivalent blue anatase sample (TiO_2 (A) 270), the blue brookite absorbs more red light, see *Figure 6.5*. In fact, the bluest anatase phase sample within series (A) absorbed less light than the brookite synthesised at 220 °C, see *Figure 6.5*. All the brookite samples can be seen absorbing near-infrared light with no signs of the intensity dropping off. This could suggest the main absorption maxima is in fact located in the infrared region. If true, the blue brookite shows similar IR properties as the material reported by Gordon *et al.*,[98] who speculated that the blue colour was due to a localized surface plasmon or conduction band to conduction band transitions. Although, as with blue anatase in Chapter 5, VBS (*Section 6.2.5*) confirmed Ti3d electrons were present in the blue brookite. Also, the absorption tail in the UV-DR spectra closely resembles those predicted by Guo *et al.*[127] who used DFT calculation for F^- dopped TiO_2 (anatase phase) to predict the UV-VIS DRS observed. Although as stated before, the transitions described by Guo *et al.*[127] are hard to comprehend making the conclusions drawn questionable. Nevertheless, it seems likely the Ti3d electrons transition to the conduction band is responsible for the absorption of red light (600 and 700 nm) and hence the blue colour.[127]

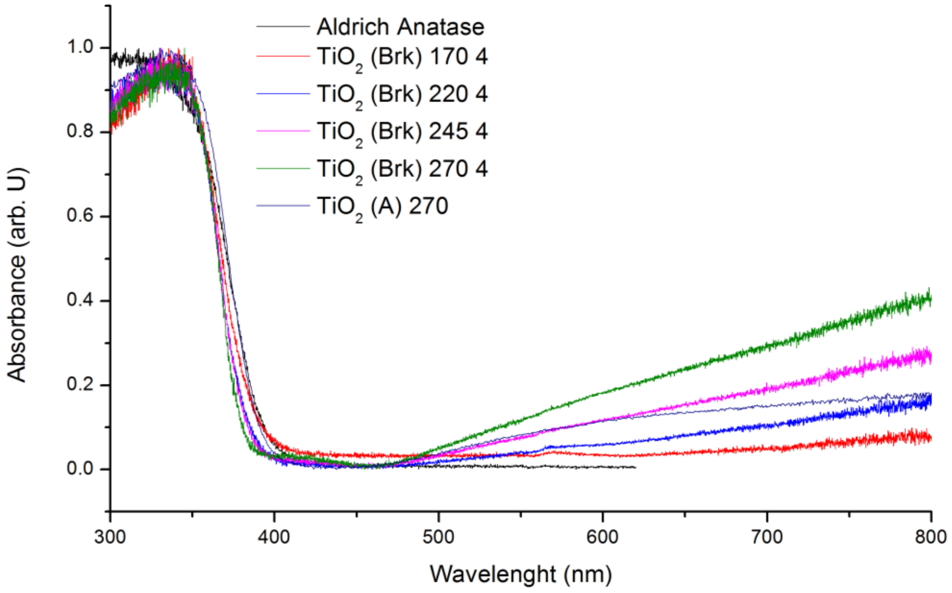

Figure 6.5 UV-DR spectra of brookite phase TiO_2 synthesised at different hydrothermal temperatures with 4 equivalents of NaF. Note: Aldrich Anatase measure with measurement ending at 620 nm.

In a similar study, UV-VIS DRS was used to examine the effects of hydrothermal treatment temperature but the molar ratio of NaF to TiO_2 was increased from 4:1 to 8:1. The brookite produced at the higher molar ratio was still blue, see *Figure 6.6*. However, it was not as blue as the samples made using 4 equivalents, compare *Figure 6.5* and *Figure 6.6*. Furthermore, the effects of temperature were minimal. Once the temperature of hydrothermal treatment was above 220 °C, there was no further increase in red light absorption. Both samples (4 and 8 equivalents) show a blue-shifted absorption edge when compared to the anatase sample (TiO_2 (A) 270), see *Figure 6.5* and *Figure 6.6*. This indicates the band gap has increased relative to anatase as expected for brookite phase TiO_2; literature values range from 3.1 to 3.4 eV with the latter being more common.[21]

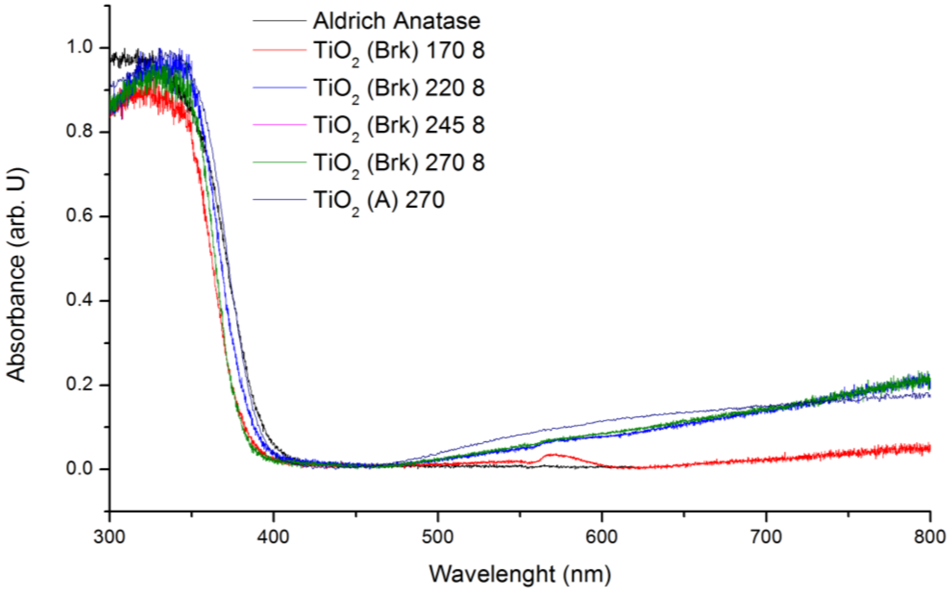

Figure 6.6 UV-DR spectra results of brookite phase TiO_2 *synthesised at different hydrothermal temperatures with 8 equivalents of NaF.*

The absorption at 620 nm was used to compare the intensity of the blue colour in the as-synthesised brookite with respect to the synthesis conditions. *Figure 6.7* shows the absorption at 620 nm increasing almost monotonically with increasing temperature of hydrothermal treatment for both the 4 and 8 equivalents series. However, in the case of the 4 equivalents series absorption increases much more steeply than the 8 equivalents series. When compared to the anatase phase TiO_2 of series (A) and (B), the absorption at 620 nm is much greater *ca.* 0.131 for TiO_2 (A) 270, 0.247 for TiO_2 (B) 0.25 and 0.273 for TiO_2 (Brk) 270 4. The decrease in red-light absorption between the 4 at 8 equivalents brookite samples is not indifferent to series (B), where increasing the ratio of NH_4F to TiO_2 decreased the red light absorption above a critical point. This was theorised to be due to a decrease in the Ti^{3+} defect concentration due to an increase in Ti vacancies. The same effect may be observed here; although, without synchrotron PXRD data it cannot be said for certain.

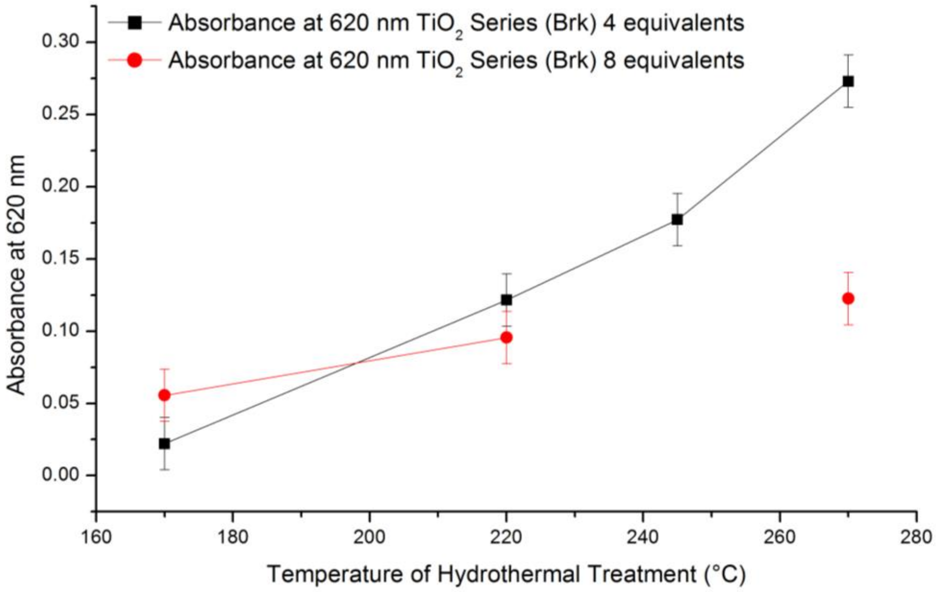

Figure 6.7 Graph showing the absorption at 620 nm as measured by UV-VIS DRS for brookite samples synthesised at 4 and 8 equivalents NaF through a range of hydrothermal temperatures. Note: Lines have been added to guide the eyes and not link to results.

A Talc plot of the UV-DR spectra (TiO_2 (Brk) 270 4) showed a blue shift in the absorption edge indicating the change in the band gap value compared to anatase due to the formation of brookite. *Figure 6.8* shows the Talc plot of brookite synthesised at 270 °C with 4 equivalents NaF *vs* Aldrich anatase. By extending lines down from the steepest part of the graph to where it intercepts the X-axis gives the value of the optical bandgap.[117,124]Aldrich anatase was determined to have a bandgap of 3.25 eV matching closely to the literature value of 3.20 eV.[21] Whereas a band gap of 3.34 eV was found for the blue brookite sample. This result falls within the literature values reported for brookite ranging from 3.1 to 3.4 eV.[21] Thus, showing the blue colouration has not changed the intrinsic bandgap of the brookite phase TiO_2 (within the reason given the large range of reported values in the literature), much like the blue colour did not change the intrinsic bandgap of the blue anatase phase TiO_2 above (Chapter 5).[21]

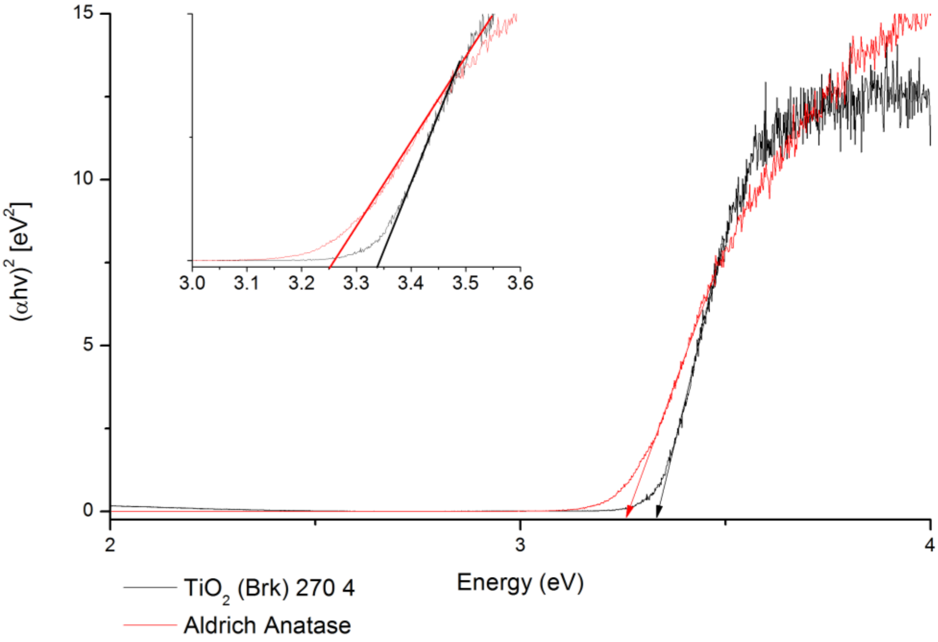

Figure 6.8 Tauc plot of Aldrich anatase verse blue brookite TiO_2 *sample* TiO_2 *(Brk) 270 4. Inset showing a close-up of the point of inflexion and where* $(\alpha h\nu)^2$ *equals zero corresponding to the bandgap.*

Furthermore, a Talc plot of a brookite sample synthesised with 8 equivalents versus 4 equivalents of NaF showed there were subtle differences between the respective optical bandgaps. *Figure 6.9* shows that the 4 equivalents sample has a bandgap of 3.34 eV, whereas the sample synthesised with 8 equivalents of NaF had a band gap of 3.36 eV. The blue-shift in the bandgap could be explained by the size effect as TEM results below (*Section 6.2.3*) showed the crystallites produced were much smaller at higher equivalents of NaF.[6]

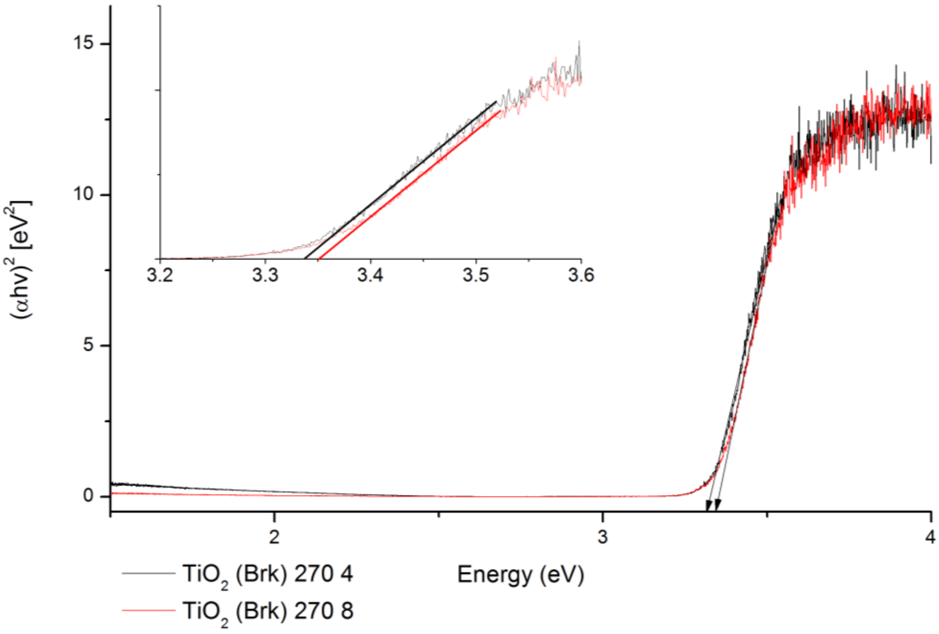

Figure 6.9 Tauc plot of blue brookite TiO_2 sample TiO_2 (Brk) 270 4 verse TiO_2 (Brk) 270 8. Inset showing close-up of the point of inflexion and where $(\alpha h\nu)^2$ equals zero corresponding to the bandgap.

Next, blue rutile phase TiO_2 was examined using UV-Vis DRS. Much like with the blue anatase, the rutile phase TiO_2 showed considerable absorption of red light extending into the near-IR region, see *Figure 6.10*. Secondly, when compared to anatase, the band-edge was considerably red-shifted to longer wavelengths at lower equivalents of NH_4F. At higher NH_4F concentrations in the synthesis media, PXRD showed that the anatase phase became the dominating phase, see *Figure 6.20*. Therefore, the blue-shift in the band-edge under these conditions is due to the formation of anatase phase and its' larger bandgap of 3.2 eV.[6]

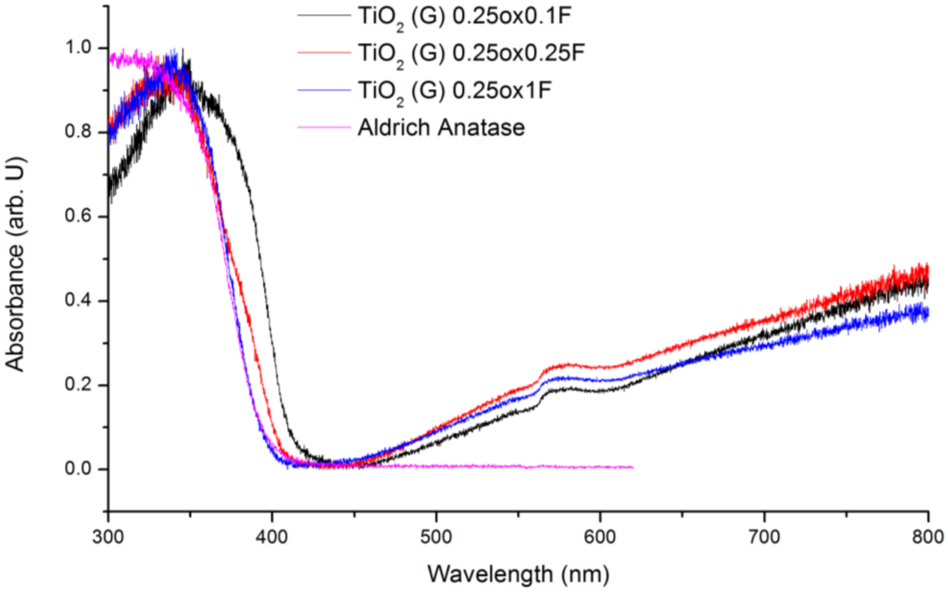

Figure 6.10 UV–DR spectra of series (G) showing samples hydrothermally synthesised with 0.25 equivalents oxalic acid and 0.1 to 1 equivalents of NH_4F*.*

As with the blue anatase, the absorption at 620 nm was used to measure the depth of the blue colouration. Unlike series (B), where the absorption of red light peaked at 0.25 equivalents of NH_4F, see *Figure 5.21*, series (G) showed decreasing absorption from 0.1 equivalents to 1 equivalent NH_4F, see *Figure 6.11*. Overall, the 0.1 equivalent sample was significantly bluer than the bluest anatase sample, *i.e.* TiO_2 (B) 0.25 *ca.* 0.24 *vs* TiO_2 (G) 0.25ox0.1F *ca.* 0.36. Interestingly, even the phase pure anatase sample TiO_2 (G) 0.25ox1F (see *Figure 6.20*) had much higher absorption than anatase synthesised in series (A) without the OX added to the synthesis media *i.e.* TiO_2 (G) 0.25ox1F *ca.*0.30 *vs* TiO_2 (A) 270 at *ca.* 0.247. This could indicate that the greater concentration of organics, due to the addition of oxalic acid along with the isopropanol (from the TIPP), increased the total amount of Ti^{4+} reduced to Ti^{3+}. The decrease in absorption with increasing NH_4F ratios does not appear linearly related to the anatase content, contrast *Figure 6.11* and *Figure 6.20*. However, it may be explained by the decreasing Ti^{3+} content (as confirmed using XPS, see *Figure 6.31*), possibly due to the formation of Ti vacancies, although, no synchrotron PXRD data is available to confirm the increasing concentration of Ti vacancies.

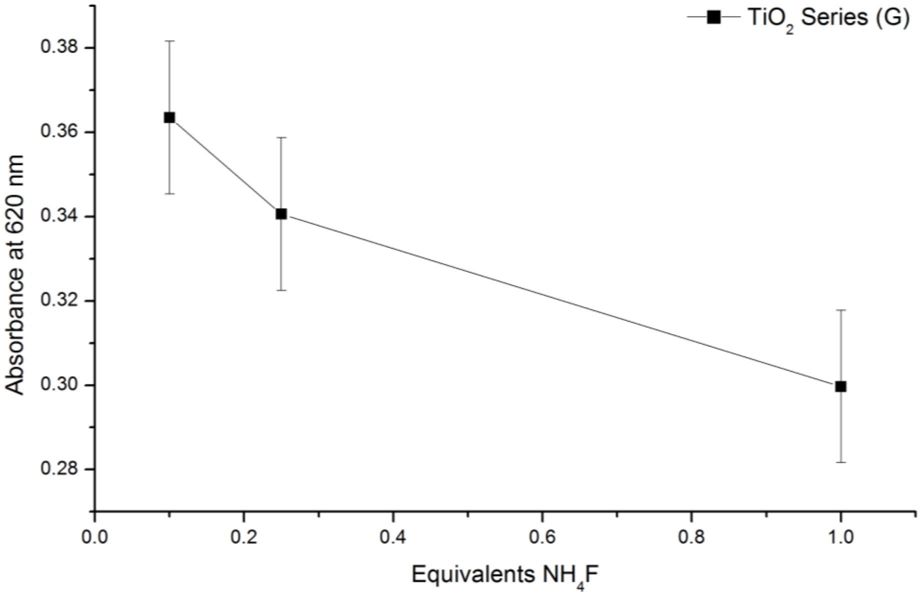

Figure 6.11 Graph showing the absorption at 620 nm as measured by UV-VIS DRS for the rutile samples in series (G).

A Talc plot was used to assess the bandgap of the blue rutile samples in series (G). It was found that only the “0.1 equivalents” sample possessed a bandgap close to 3.0 eV (*ca.* 3.07 eV), the literature reported value for rutile, see *Figure 6.12*.[6] However, it was seen that the bandgap increased throughout the series to that of anatase 3.2 eV.[6] This was due to anatase phase TiO_2 forming and becoming the dominating phase as the NH_4F concentrations increased, see PXRD *Figure 6.20*. The bandgap in the phase-pure rutile sample did not seem to be shifted to lower energies by the Ti^{3+} defects; thus, the intrinsic bandgap of rutile remained unchanged and agreeing with the values of 3.0 eV reported in the literature.[6,48,153]

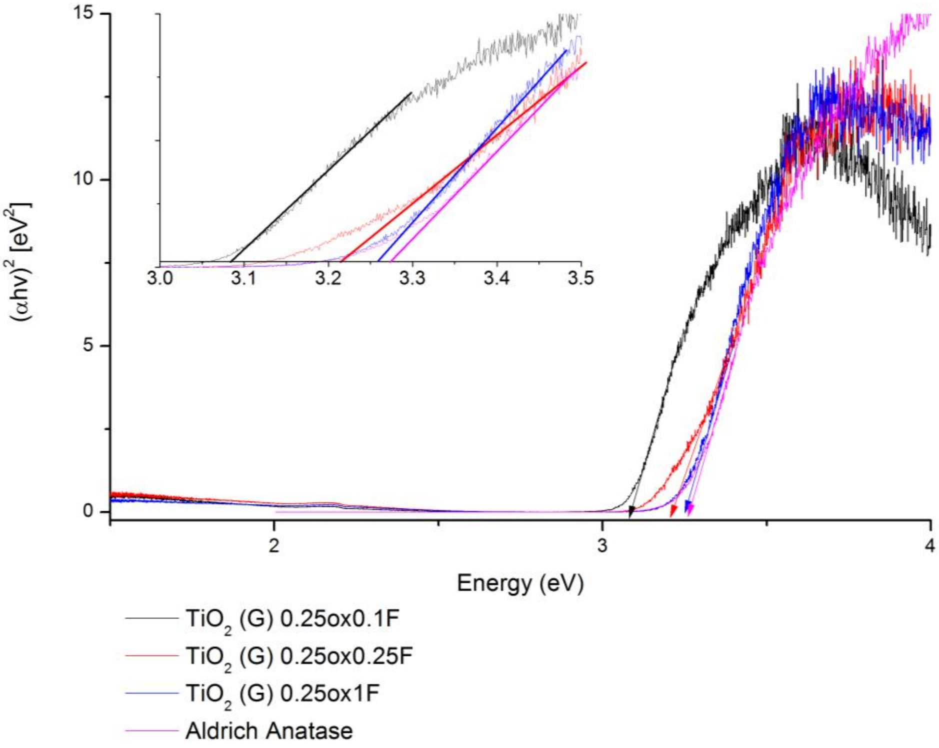

Figure 6.12 Tauc plot of blue rutile series (G). Inset showing close-up of the point of inflexion and where $(\alpha h\nu)^2$ *equals zero corresponding to the bandgap.*

6.2.2 Raman Spectroscopy on Rutile and Brookite Phase TiO$_2$

Raman spectroscopy was used to analyse the blue brookite synthesised at 270 °C. First of all, it can be seen in *Figure 6.13*, that brookite shares many of the same modes as anatase. However, there are many extra modes (peaks) present in the brookite Raman spectra, 16 in total.[21] Unfortunately, no phase pure commercial standard of brookite was available for studies in parallel with the synthesised blue brookite. Therefore, it is difficult to establish if the peaks have shifted relative to the standard, unmodified brookite. On the other hand, Raman spectroscopy does offer a good check as to whether anatase is present in the brookite. The peak at 516 cm^{-1} is unique to anatase and does not overlap with any brookite peaks. Therefore, the 516 cm^{-1} peak is a good way to check for the presence of anatase as nearly all brookite PXRD peaks have an overlap with anatase peaks.[21] It can be seen in *Figure 6.13*, that the brookite sample TiO$_2$ (Brk) 270 4 is anatase free.

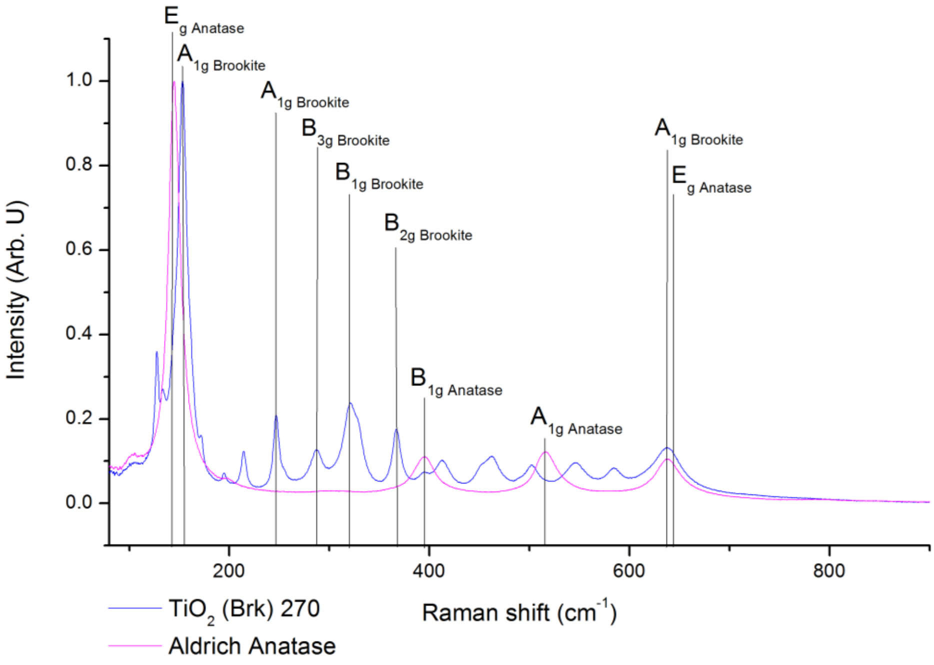

Figure 6.13 Raman spectra of Brookite TiO_2 sample (TiO_2 (Brk) 270 4) compared to Aldrich anatase.

The change of the brookite with time at 170 °C was evaluated. It was found that over the 24 hour time period of hydrothermal treatment, the Raman peaks narrowed and red-shifted, see *Figure 6.14*. Interestingly, a weak anatase peak at 516 cm^{-1}, was only observed in the 2 and 4 hour samples, see *Figure 6.14*. No other signs of anatase were observed in any of the spectra of the materials which underwent longer hydrothermal treatment.[21] Therefore, it would appear that the brookite is formed through the transformation of anatase to brookite. This is evidence of the NaF assists in redissolving the anatase, possibly through a sodium titanate mechanism, then reprecipitating it as brookite phase TiO_2. Strong alkaline solutions have been reported to dissolve small anatase particle and form sodium titanate.[156]

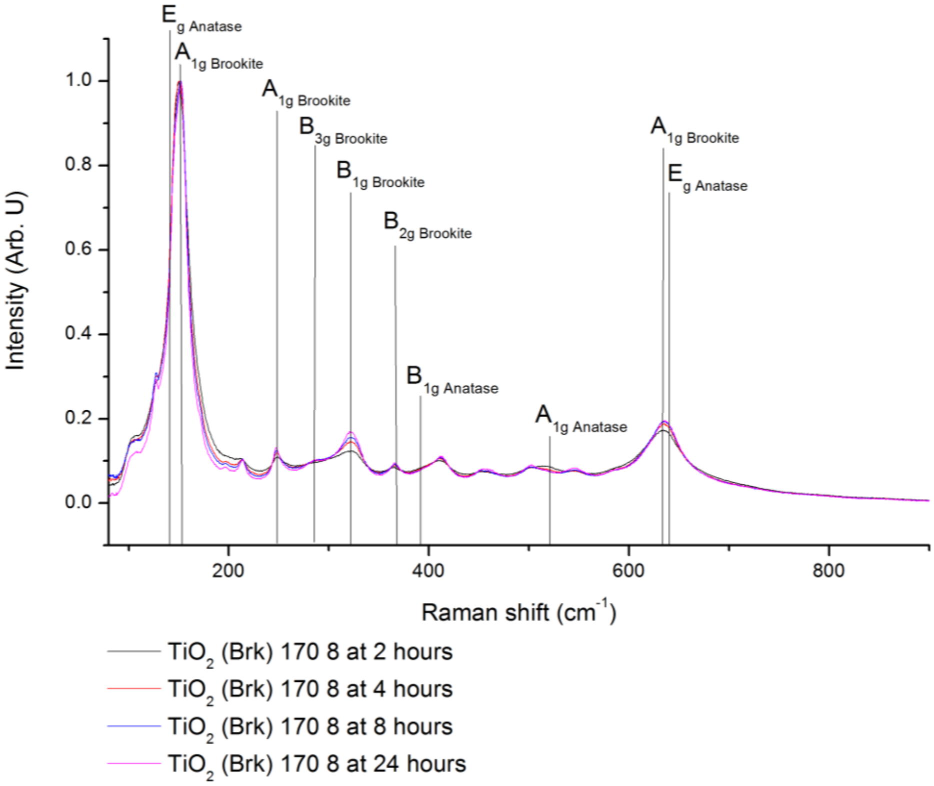

Figure 6.14 Raman spectra of brookite TiO_2 hydrothermally treated for 2, 4, 8 and 24 hours at 170 °C with 8 equivalents NaF.

The effects of the hydrothermal temperature in the brookite series were evaluated using Raman spectroscopy. *Figure 6.15* shows the Raman spectra of brookite synthesised at 170 to 270 °C with 8 equivalents of NaF added. It can be seen that the peaks representing each mode of brookite sharpen and increase in intensity with increasing temperature of hydrothermal treatment. Interestingly, anatase peaks were only observed in the 170 °C sample, despite there only being *ca.* a 5 % increase in brookite phase content (from 170 to 270 °C) according to the PXRD results below (*Figure 6.19*). Furthermore, there is a significant decrease in the intensity of the A_{1g} 650 cm^{-1} peak and a great increase in the intensity of all other brookite peaks between 180 cm^{-1} and 650 cm^{-1}, this indicates changes in shape.[109] TEM below showed the aspect ratio of the particles increased with increasing temperature of hydrothermal treatment. The increasing aspect ratio minimised the exposure of the {212} and {001} facets. The 650 cm^{-1} peak must represent a vibrational state present on one or both of the aforementioned facets.

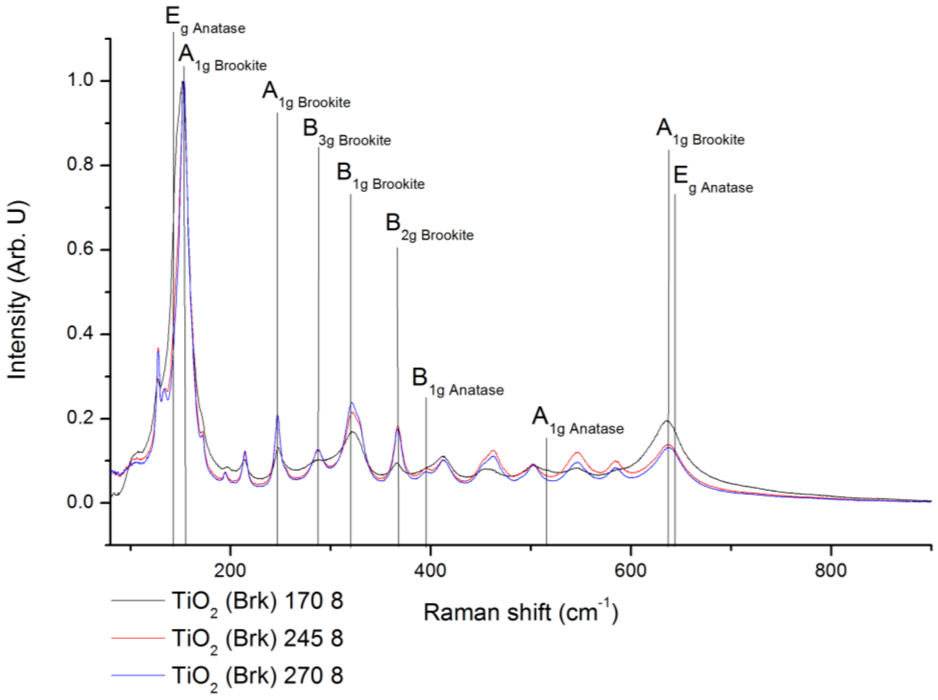

Figure 6.15 Raman spectra of brookite phase TiO_2 synthesised in the presence of 8 equivalents NaF and hydrothermally treated at 170 to 270 °C for 24 hours.

Lastly, the Raman spectrum of the blue rutile was examined. *Figure 6.16* below shows the Raman spectrum of phase pure blue rutile synthesised in series (G) (sample TiO_2 (G) 0.25ox0.1F) *vs* commercial Aldrich (white) rutile. First of all, it can be seen that compared to the commercial white rutile, the E_{1g} mode is significantly shifted to smaller wavenumbers. However, the A_{1g}, B_{1g} and B_{2g} peaks do not appear shifted. The peaks are considerably broader in the as-synthesized blue rutile sample compared to the commercial rutile. The broadening of the peaks indicates disorder or small crystallite sizes due to phonon confinement.[108] The Aldrich rutile is a pigmentary grade rutile, which means it would have a crystallite size of approximately 200 nm, thus, making it relatively large and highly crystalline. Therefore, it should not show any size or disorder effects.[108] On the other hand, the blue rutile sample consisted of very large particles when observed by TEM (*Section 6.2.3* below) and should not express any size effects.[108] Therefore it is likely the broader peaks are due to disorder, caused by doping of the crystal either Ti^{3+} or F^-. The large shift in the E_{1g} peak compared to the other peaks may be due to a specific facet being exposed or surface chemistry. The changes in shape observed in both the fluorine-modified sols (Chapter 4) and in series (G) (see TEM *Section 6.2.3* below), indicate that the NH_4F modifies the surface and controls the shape of the rutile crystals synthesised.[86] Rather than elongated rutile rods being formed, isometric crystals are formed.[86] The crystallites clearly expose more of the {001} facets due to the F^- ion binding to the {001} facet. Currently, it is not clear as to whether it is the binding of F^- to the crystal facets or the exposure of particular facets shifting the Raman E_g peak.

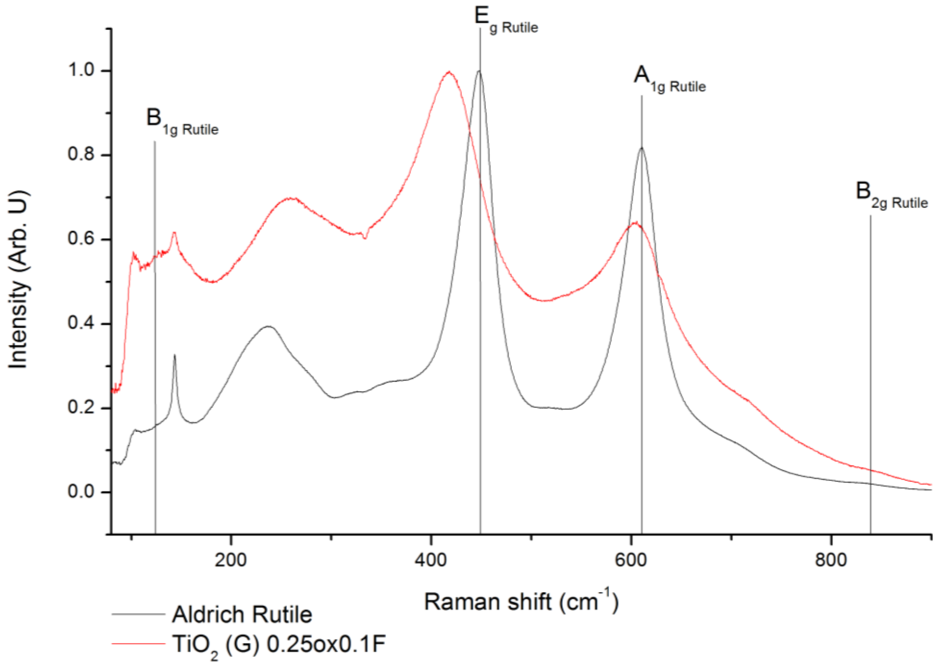

Figure 6.16 Raman spectra of blue rutile TiO_2 (TiO_2 (G) 0.25ox0.1F) vs Aldrich rutile TiO_2.

6.2.3 PXRD study of Rutile and Brookite Phase TiO_2

One sample of the as-synthesised blue brookite was analysed by synchrotron PXRD. Brookite was initially synthesized by accident, so only the accidental blue brookite sample was analysed using the synchrotron radiation. *Figure 6.17* shows the diffractogram of sample TiO_2 (C) 4 (later called TiO_2 (Brk) 270 4) which formed blue brookite rather than anatase as was originally intended. When this particular sample was analysed using Topas and a Rietveld refinement, it came out to be 100 % brookite. Yet, it was only possible to accurately fit the data by including 2 populations of brookite. The first population of brookite consisted of very large (>200 nm) and highly preferentially orientated crystallites making up 32 % of the sample. The other population of brookite was made up of *ca*. 22 nm isometric crystallites and made up the remaining 68 % of the sample. *Figure 6.17* inset shows the small particles as the wide base of a very tall and narrow peak. Later in the TEM section, it can be seen that the as-synthesised brookite was indeed made of elongated crystals and smaller isometric crystals. Much like the blue anatase above, the larger blue brookite crystals appeared deficient in titanium having an occupancy of 0.98 +/- 0.02. On the contrary, the smaller crystallites were deficient in oxygen have an occupancy of only 0.94 +/- 0.01. These results would indicate that only the smaller crystallites contain

Ti^{3+} defects causing the colour change. However, Topas was fitting two populations in a single pattern, it would be wise to not put too much emphasis on this result.

Of note, all the rest of the brookite analysed in this chapter by PXRD was done on a lab-based instrument. The resolution and sample preparation meant the orientation and relative ratios of larger and smaller crystals could not be analysed. In fact, it was very hard to get enough resolution to define accurately the ratio of anatase to brookite. Hence, there may appear to be some discrepancies between the Raman data and PXRD.

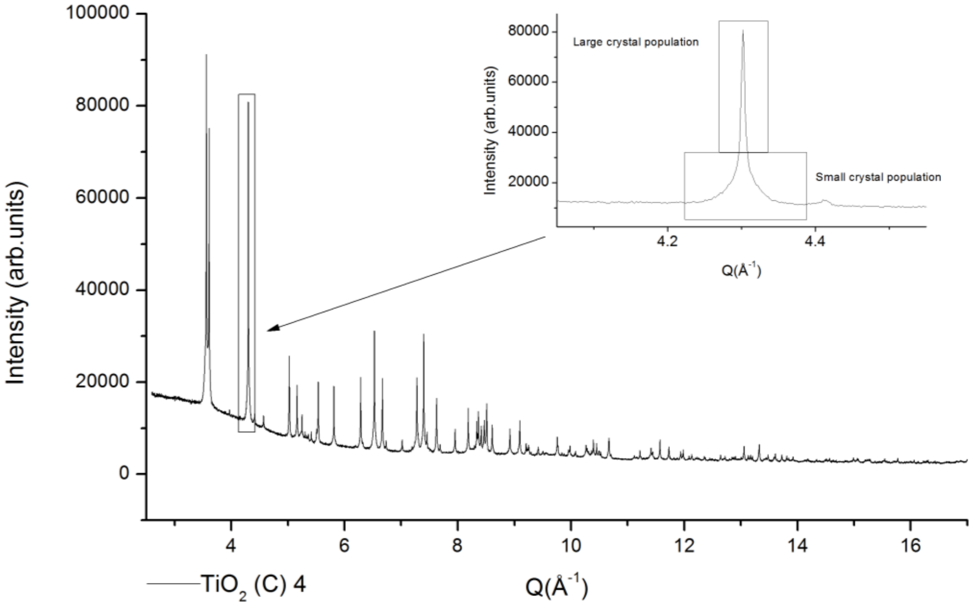

Figure 6.17 Synchrotron PXRD diffractogram of sample TiO_2 (C) 4 showing the multiple populations of brookite. Inset: Shows close up of a typical brookite peak showing a broad base and shape top due to two different sized populations of brookite crystallites.

Lab PXRD and Rietveld refinement were used to study the formation of the brookite phase relative to the number of equivalents of NaF added to the synthesis media (*Figure 6.18*). It can be seen that the greater the NaF concentration, the greater the brookite phase content, dominating over anatase phase. Although, it does appear that there is a critical concentration of NaF required to start the transformation of anatase to brookite. The critical concentration is between 1 and 2 equivalents NaF. This is shown by the lack of brookite formed from 0 to 1 equivalents of NaF. Raman results above showed anatase converts to brookite with time during the hydrothermal treatment. This critical NaF ratio may indicate that the phase transition from anatase to brookite goes by titanate mechanism which requires an excess of NaF. The synthesis of brookite using NaOH has been reported to proceed by the formation of sodium titanate and then leaching of the Na^+ ions from between the layers resulting in brookite phase TiO_2.[157-159]

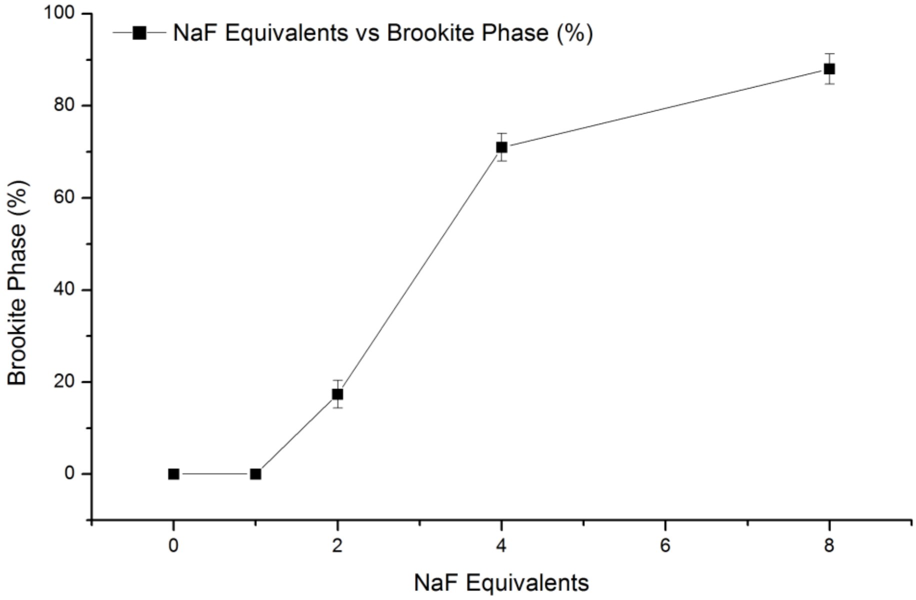

Figure 6.18 PXRD results showing the relative percentage of brookite to other phases in samples synthesised with different equivalencies NaF. Note: Lines have been added to guide the eyes and not link to results.

The brookite phase domination over anatase with respect to the temperature of the hydrothermal treatment was investigated by PXRD. *Figure 6.19* shows the brookite phase content at different temperatures of hydrothermal treatment at two different Ti:NaF ratios. It can be seen that throughout the “4 equivalents” series, the percentage of brookite ranges from 65 % to 84 %. Whereas, the “8 equivalent” series showed only a small trend towards greater brookite phase dominance ranging from 85 % and 90 %. The lack of a significant change in the phase distribution between anatase and brookite with temperature indicates that the formation of brookite is highly dependent on the number of equivalents of NaF added rather than the temperature of hydrothermal synthesis. The formation of sodium titanate does not require a great deal of activation energy. Industrially, this process is done at 110 °C when digesting colloidal anatase to produce sodium titanate.[156] Therefore activation energy is not the limiting factor to form 100 % brookite.

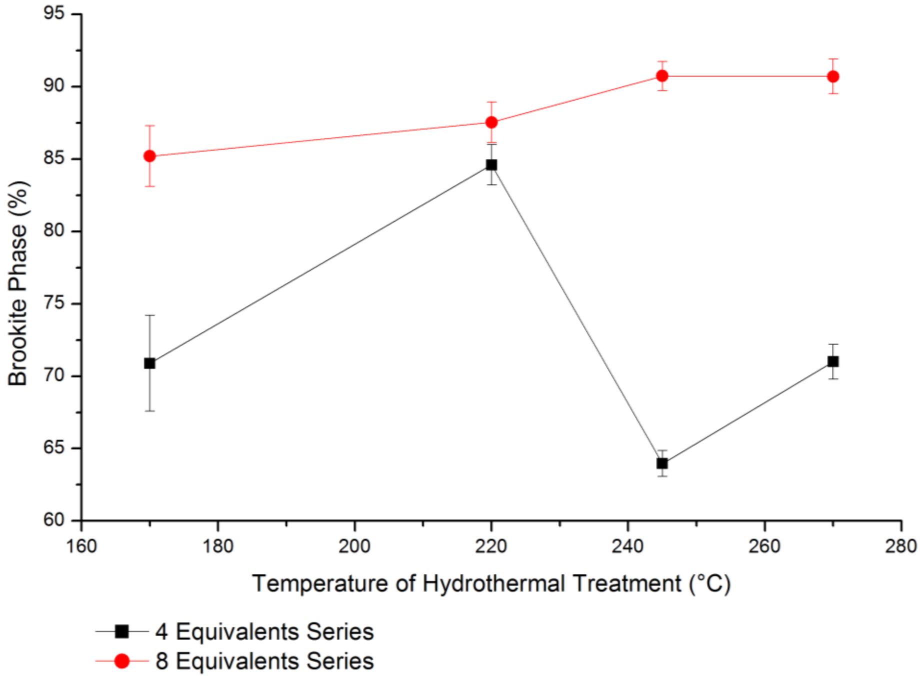

Figure 6.19 PXRD results showing the relative percentage of brookite to other phases in samples. Samples were synthesised at hydrothermal temperatures ranging from 170 to 270 °C with either 4 or 8 equivalents of NaF. Note: Lines have been added to guide the eyes and not link to results.

Lab PXRD and Rietveld refinement were used to evaluate the phase composition of the rutile series (G) relative to the NH_4F added to the synthesis media. *Figure 6.20* shows that rutile phase content drops off quickly with the addition of NH_4F to the synthesis media. Relative to the oxalic acid sols (Chapter 4), rutile phase TiO_2 is only produced in a narrower range of conditions during the sol-less synthesis. In Chapter 4, it was theorised that rutile and anatase nuclei were formed during the peptization reaction forming the oxalic acid stabilized sols. During the hydrothermal treatment, the rutile nuclei grew and hence the product was a mixture of anatase and rutile; only the addition of strong acids could dissolve the rutile nuclei to produce phase pure anatase. Here, amorphous TiO_2 is formed by the addition of the TIPP to cold water, the amorphous TiO_2 is then hydrothermally treated to induce crystallinity. The formation of rutile nuclei due to the oxalic acid added to the amorphous TiO_2 must occur during the heat-up time as the oxalic acid decomposes before the autoclave reaches 270 °C. Therefore, when 1 equivalent of NH_4F is added to the synthesis, it must suppress the formation of rutile nuclei during the heat-up time period. Thus, even though oxalic acid is present during the hydrothermal synthesis, no rutile grows as it never nucleates.

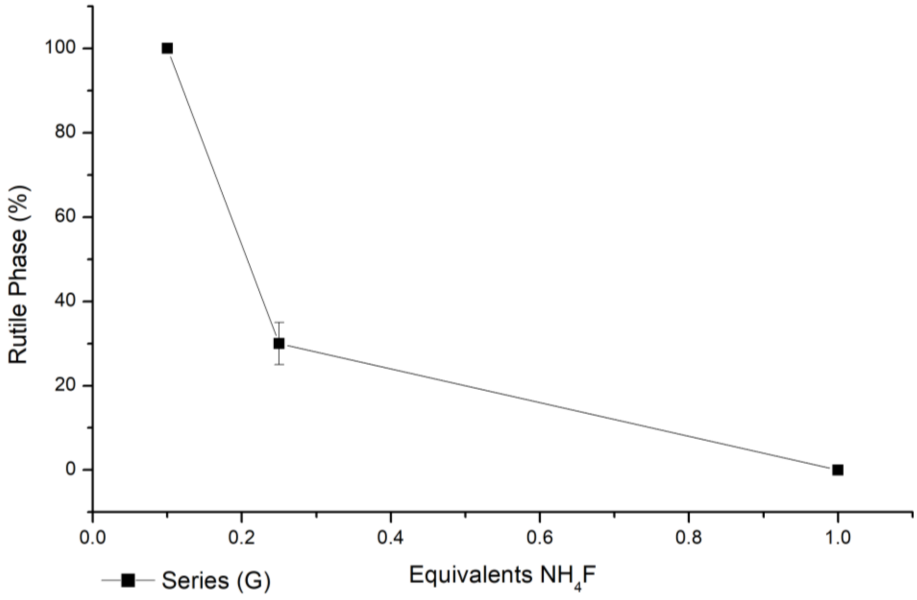

Figure 6.20 PXRD results showing the relative percentage of rutile in series (G). Note: Lines have been added to guide the eyes and not link to results.

6.2.3 Electron Microscopy Study of Rutile and Brookite Phase TiO_2

SEM was used to examine the morphology of the blue brookite synthesised. *Figure 6.21* shows the difference between brookite synthesised at 170 and 220 °C. When looking at the images, it becomes apparent that there are far fewer rods amongst the roundish-looking particles processed at 170° compared to 220 °C. *Figure 6.22* shows the difference between brookite synthesised at 245 and 270 °C. Much much like the previous comparison, the proportion of sample in the shape of the rods appears to increase with the increasing temperature of hydrothermal treatment, although, no attempts were made to quantify the average aspect ratio. The particles also appear to get slightly larger with increasing temperature as expected. These observations agree with the observations made using Raman spectroscopy above (*Figure 6.15*). There is a large change in morphology from the sample synthesized at 170°C to the one made at 220 °C. However, the change between samples synthesized at 245 and 270 °C was minimal. The change from spherical particles at 170 °C to rod-like particles at temperatures greater than 170 °C coincides with the changes in the relative intensity of Raman peaks *i.e.* the peak at 650 cm^{-1} *vs* the rest, see *Figure 6.15*. This change from spherical particles to rod-like particles is probably due to the titanate intermediate. It has been reported that sodium titanate becomes elongated and rod-like when synthesised at increasing hydrothermal temperatures.[160] Oddly, very large crystals appear amongst the small rods and spherical particles, see *Figure 6.22* bottom. Much like the blue anatase (see *Figure 5.77*), these seemingly random large crystallites were present in all brookite samples synthesised at higher processing temperatures. The origin of these crystals is still very elusive, however, they seem to only be found when higher processing temperatures were used *i.e.* 245 °C and above.

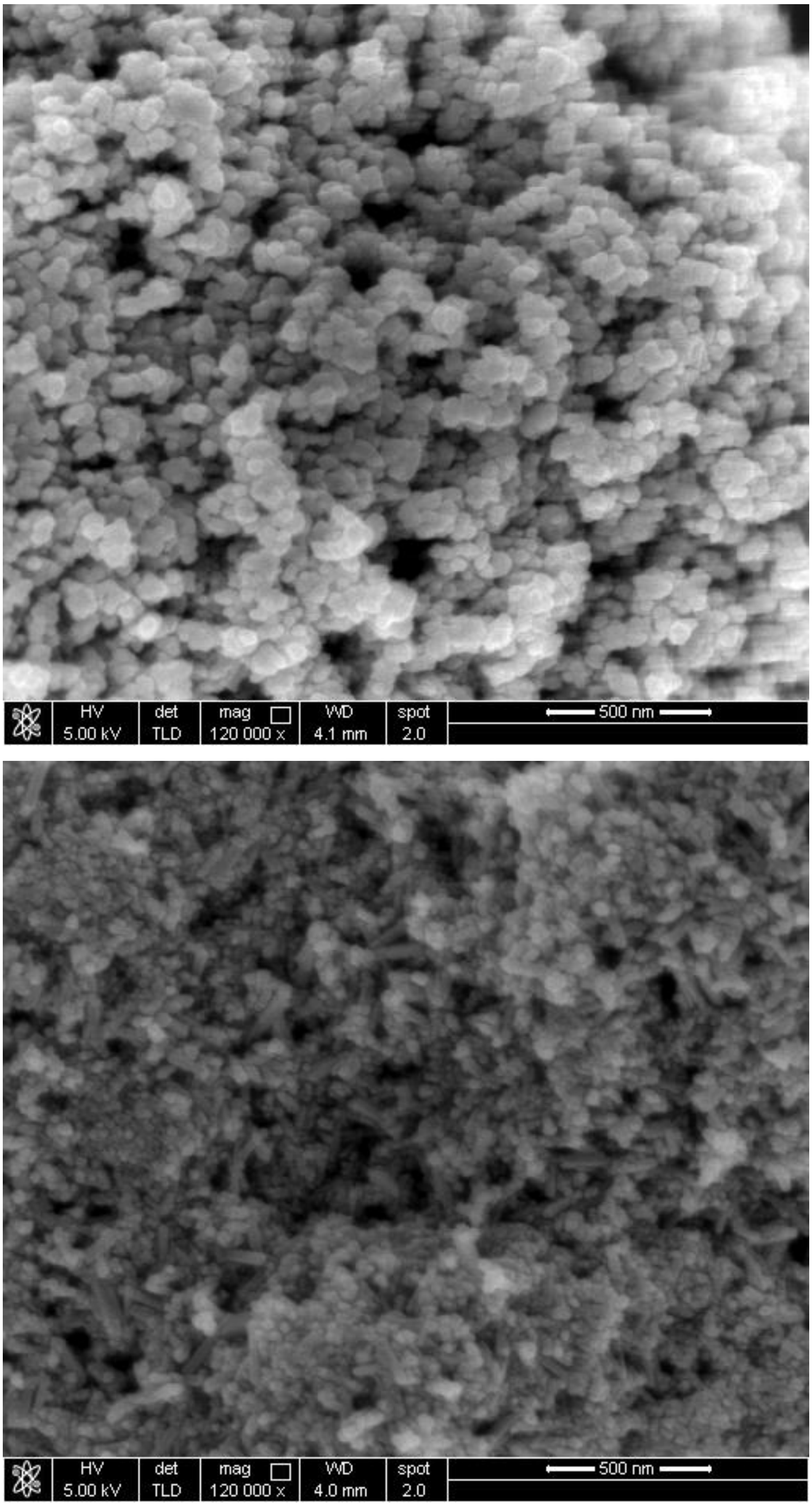

Figure 6.21 SEM images of brookite synthesised at: Top 170 °C. Bottom 220 °C.

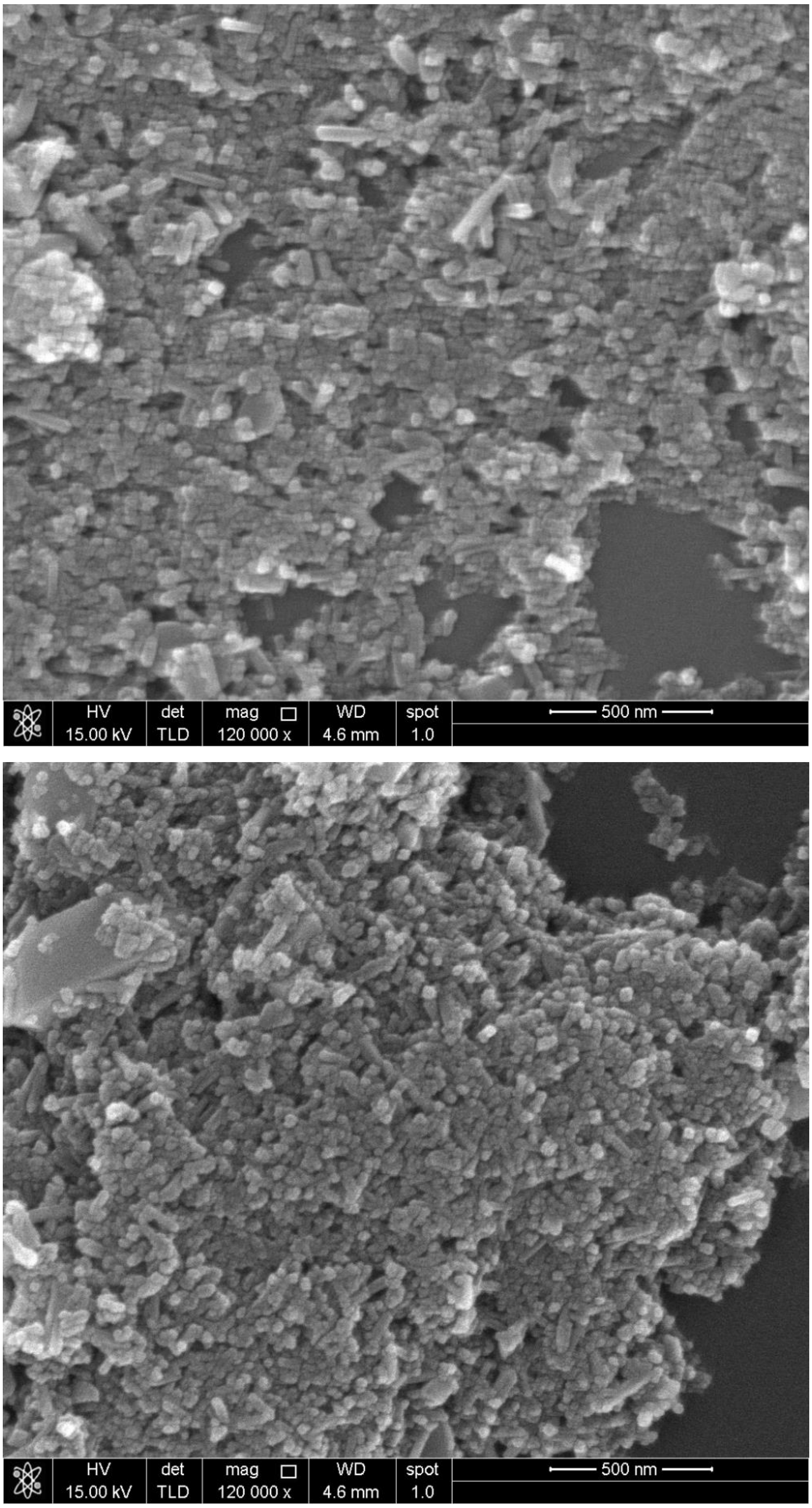

Figure 6.22 SEM images of brookite synthesised at: Top 245 °C. Bottom 270 °C.

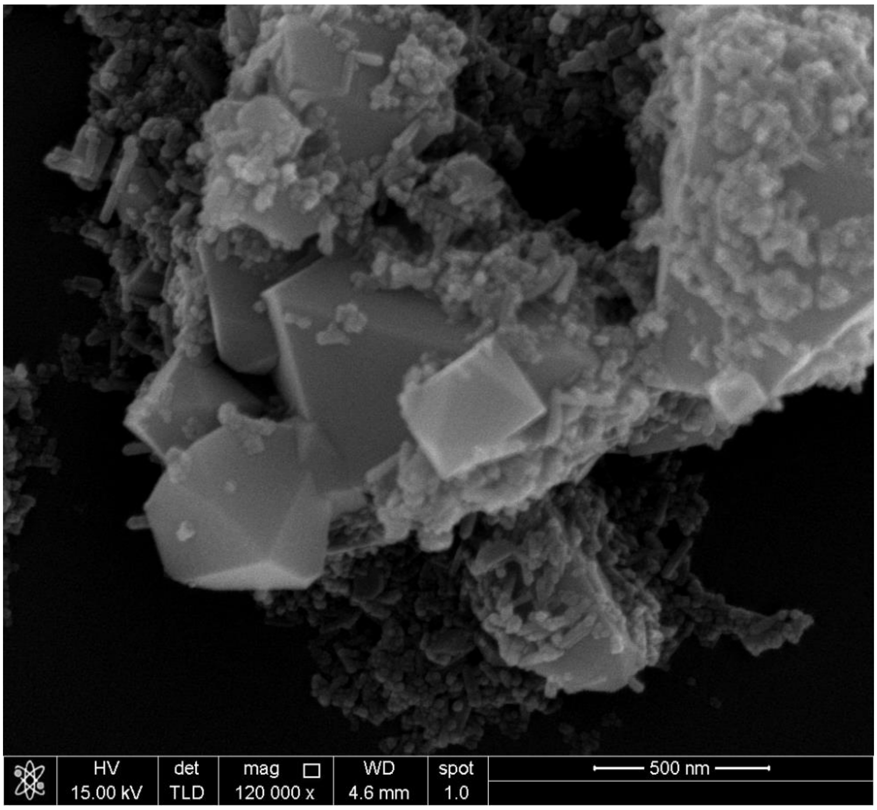

Figure 6.23 SEM image of TiO$_2$ (Brk) 270 4 showing the presence of the large crystals in the sample.

Transmission electron microscopy (TEM) was used to evaluate the morphology of brookite synthesised at different hydrothermal temperatures and NaF:Ti ratios. At 170 °C, TEM showed the brookite particles synthesised at both 4 and 8 equivalents were a mixture of rod-like particles and smaller spherical particles, see *Figure 6.24*. However, the ratio of rod-like particles to spherical particles was influenced by the ratio of NaF to Ti. The higher NaF to Ti ratio, the greater the relative ratio of the rod-like particles to the spherical particles. TEM images showed that the particles made at 270 °C had a similar morphology to those synthesised at 170 °C, but the particles were larger and there appeared to be fewer spherical particles, see *Figure 6.25*. The impact of the NaF to Ti ratio was not as clear at the effect of the higher processing temperatures.

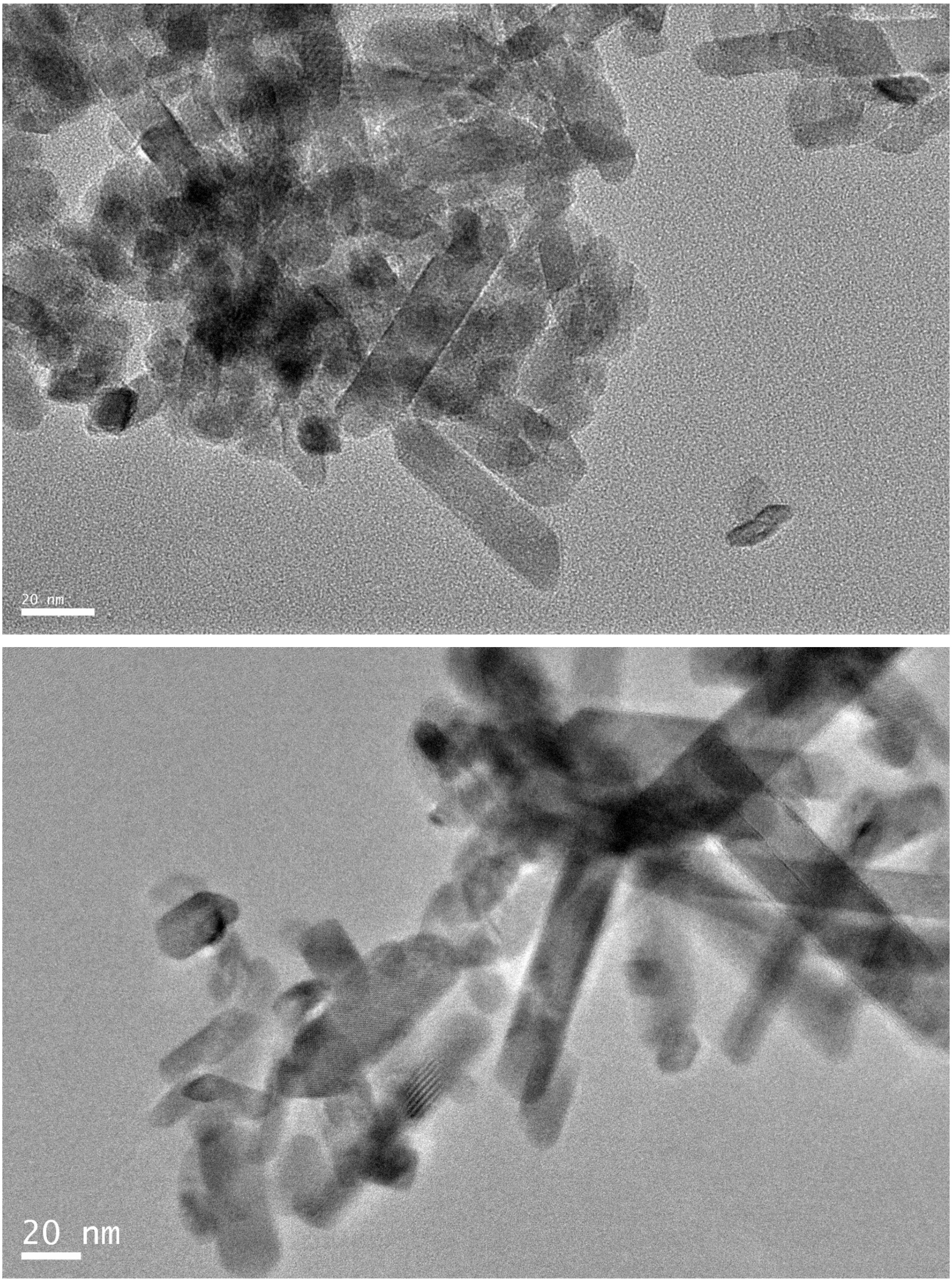

Figure 6.24 TEM of brookite samples synthesised at 170 °C with different NaF to Ti ratios: Top: 4 equivalents of NaF. Bottom 8 equivalents of NaF.

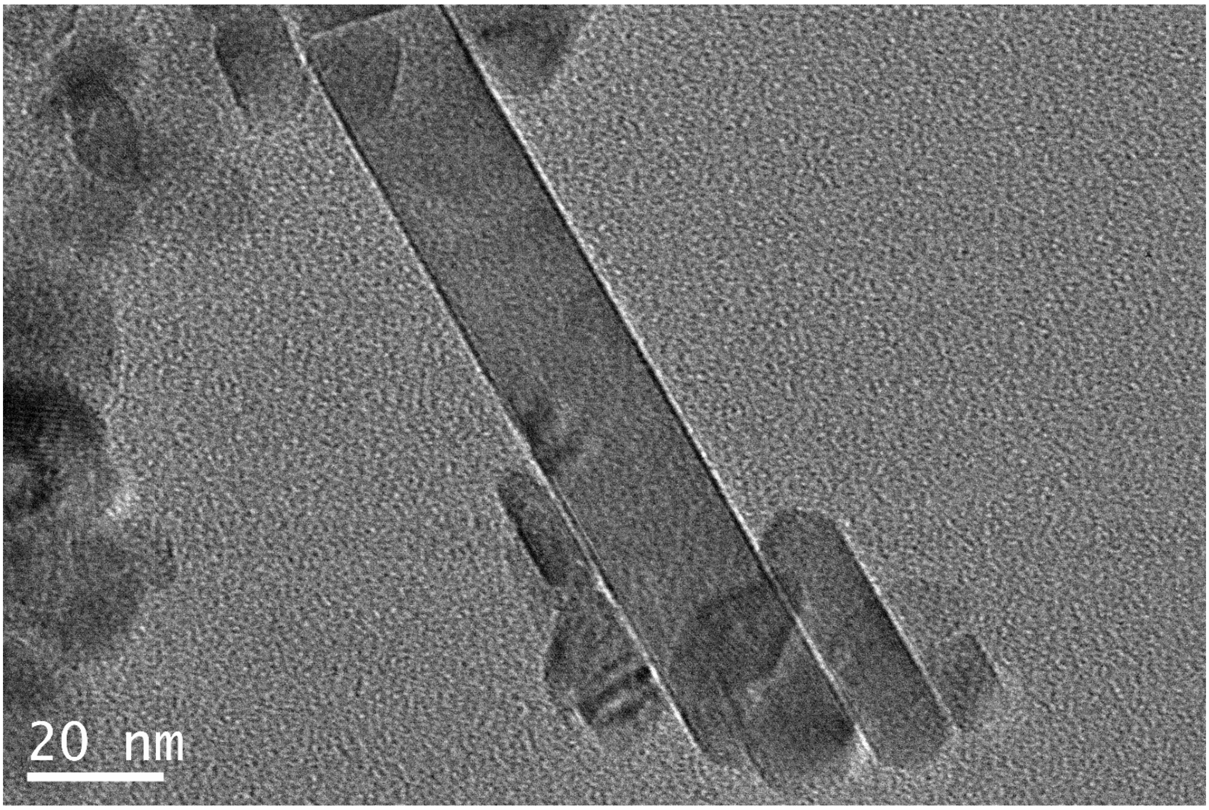

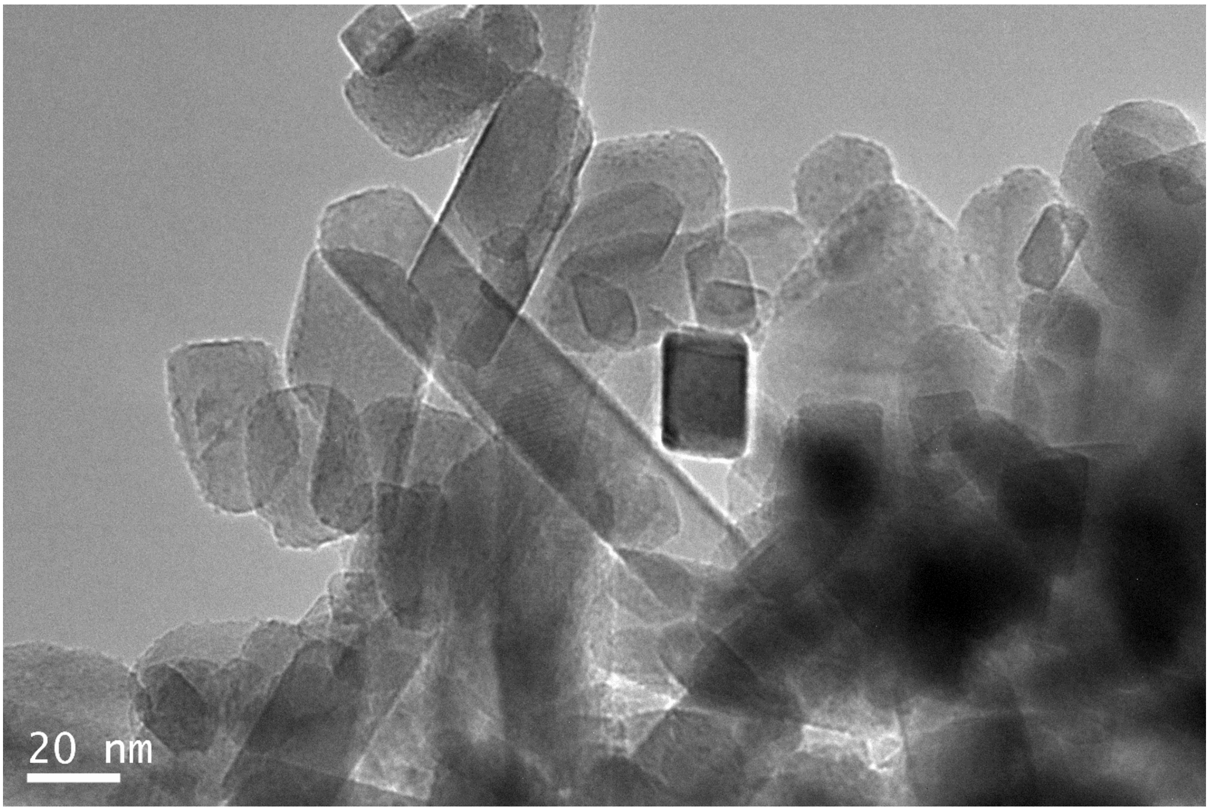

Figure 6.25 TEM of brookite samples synthesised at 270 °C with different NaF to Ti ratios: Top: 4 equivalents of NaF. Bottom 8 equivalents of NaF.

High-resolution TEM was used to determine the direction of elongation and the exposed facets of the brookite crystallites. *Figure 6.26* shows a high-resolution TEM image of brookite synthesised with 4 equivalents of NaF at 270 °C. It can be seen that the lattice fringing indicates a 3.45 Å spacing for both the rod and the cubic crystallites, which could be assigned to the {120} plane.[161] Therefore, the nanorod to the left-hand side of the image was determined to be elongated along the [001] direction, exposing a large ratio of the {210} facet and a smaller proportion of the {212} and {001} facets.[21,161,162] On the other hand, the cubic crystallites were also aligned in the same direction giving a much smaller ratio of the {210} facet and a larger ratio of the {212} and {001} facets. Unfortunately, it is beyond the capability of the TEM used to do area selective diffraction to truly determine the coordination of the crystallites. The elongation in the [001] direction and increased exposure of the {210} facet have great implications when it comes to photocatalysis. A few authors have reported increased exposure of the {210} facet of brookite increases photocatalytic activity much like the increased exposure of the {001} facet of anatase increases its photocatalytic activity.[27,161,162]

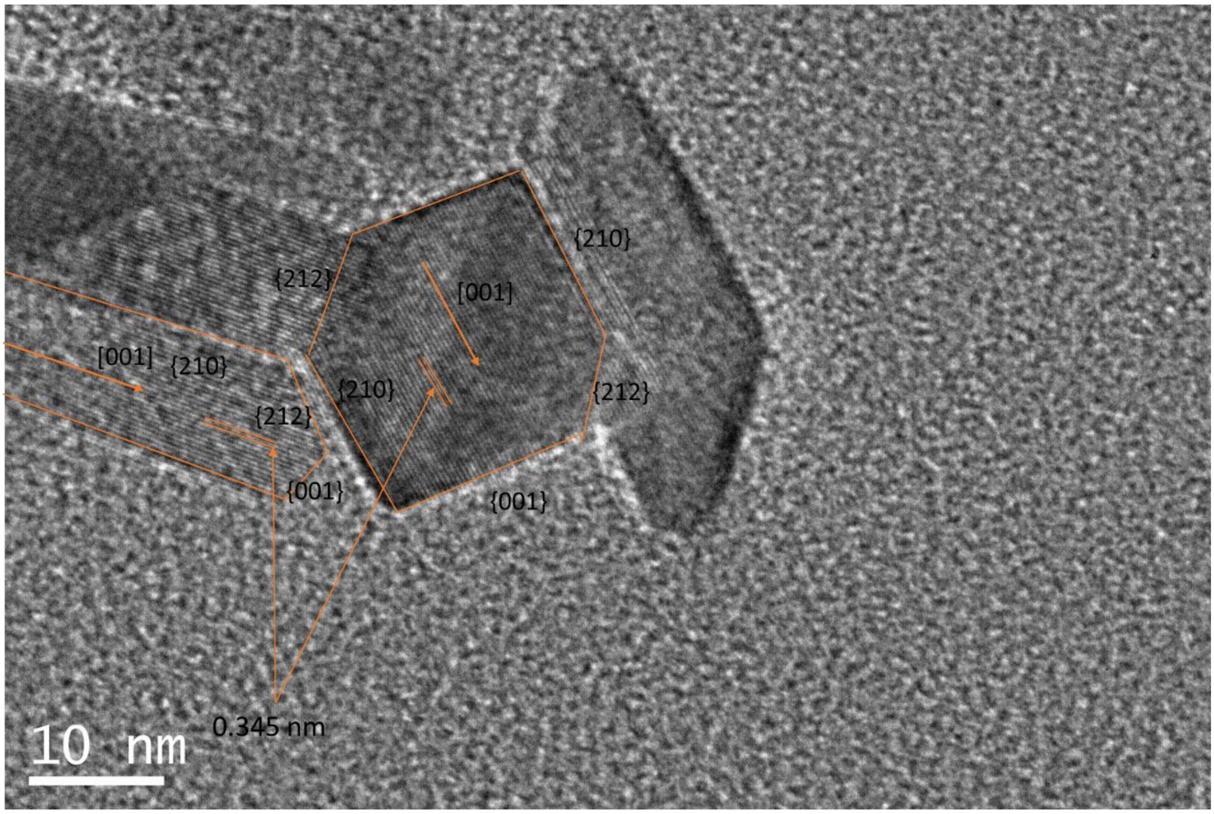

Figure 6.26 Hi-resolution TEM image of brookite synthesised at 270 °C with 4 equivalents of NaF showing the orientation of the crystallites.

TEM was used to study the morphology of the blue rutile synthesised in series (G). *Figure 6.27* shows a low magnification image of the rutile synthesised with 0.1 equivalents of NH_4F and 0.25 equivalents of oxalic acid. Clearly, the crystallites produced are very large. Although, the sample of rutile does appear to be very polydisperse with some crystallites in the size range of microns and others with sub-50 nm size present in the same image. With regards to morphology, the rutile crystallites do not appear to be elongated. In fact, they appear to be the relatively cubic in shape. The shape is much closer to the fluorine-modified oxalic acid sols rather than the unmodified oxalic acid sol (Chapter 4, see *Figure 4.15*). The rounded particle shape is consistent with F^- modified rutile with enhanced {110} facet exposure and "nano-hills" at the edges reported by Wu *et al.*[86] The inset shows selected area electron diffraction pattern of rutile. The electron diffraction pattern is made up of several bright dots indicating highly crystalline large crystallites. Unfortunately, fringing patterns could not be determined due to the size of the crystals (see *Figure 6.28*). Therefore, the exposed facets could only be hypothesised based on the literature.[86] It is suspected the main facets exposed are the {001} and {110}.

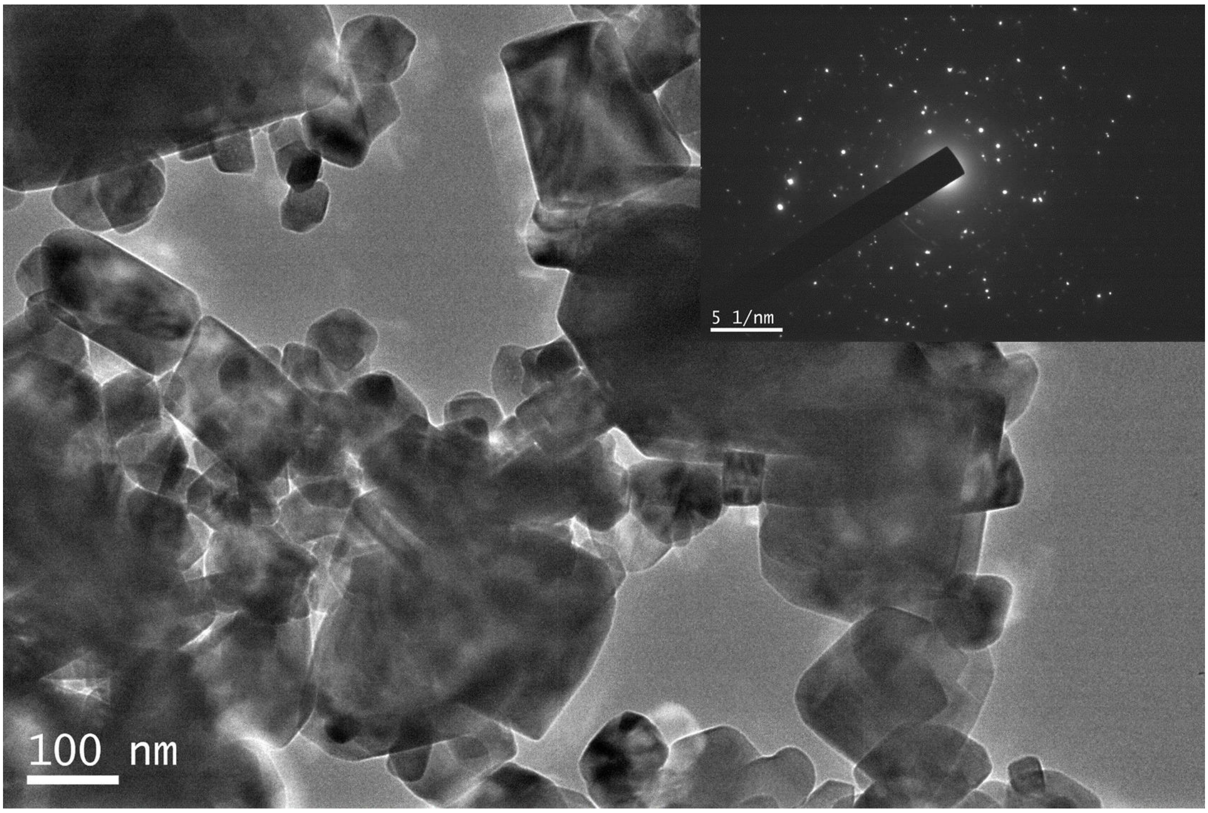

Figure 6.27 TEM image of rutile in the sample TiO_2 (G) 0.25ox0.1F. Inset is the electron diffraction pattern of the imaged area.

Although lattice fringing could not really be determined, it was noticed when attempting to image the lattice fringing there was a distinct disordered layer on the outer edge of the rutile crystals. *Figure 6.28* shows a high-resolution image of the edge of a blue rutile crystal (sample TiO_2 (G) 0.25ox0.1F). Some lattice fringing can be seen going towards the edge but then it quickly becomes disordered in a shell of approximately 7 nm. This disordered layer is believed to be caused by surface reduction.[116]

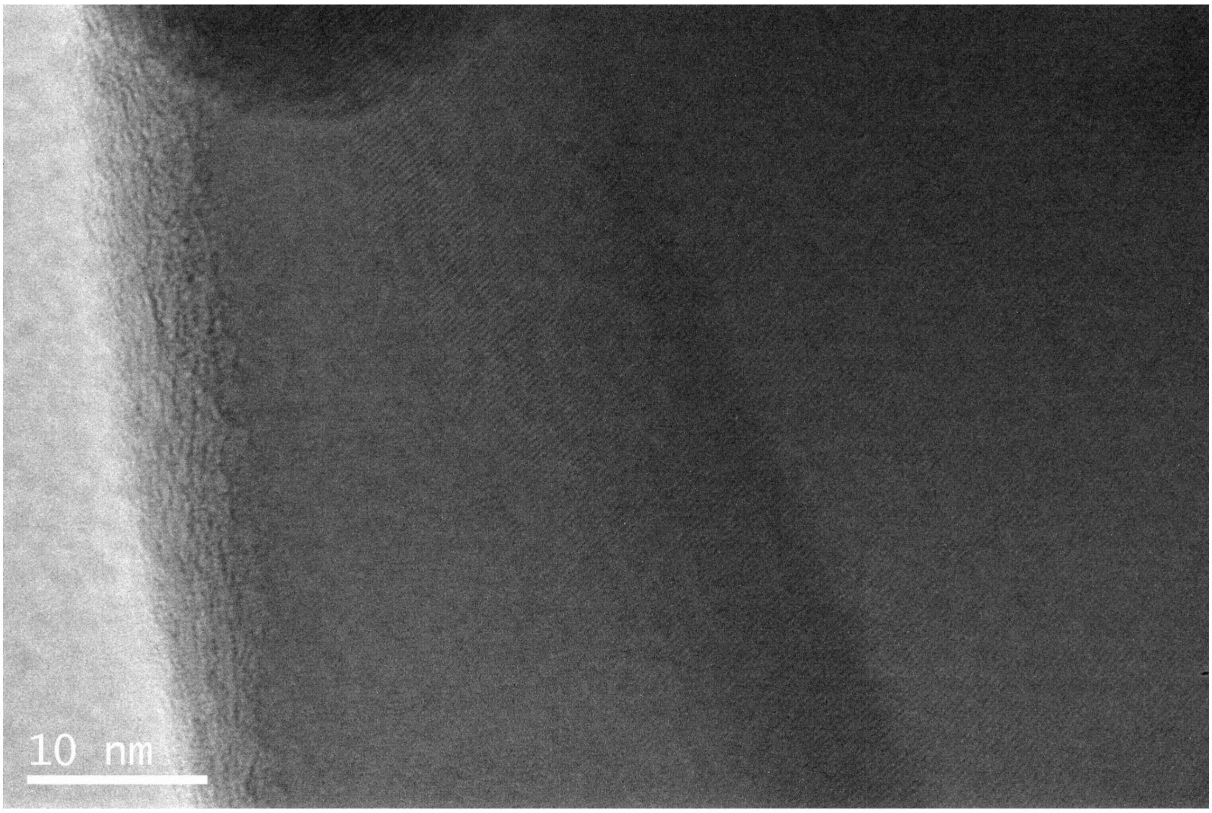

Figure 6.28 High-resolution TEM image of rutile sample (TiO_2 (G) 0.25ox0.1F) showing the disordered edge of the crystal.

6.2.4 Nitrogen adsorption study of Rutile and Brookite Phase TiO_2

The surface area of the as-synthesised brookite (4 equivalents series) was evaluated using nitrogen adsorption isotherms and BET theory. It was found that the surface area decreased as the temperature of hydrothermal treatment was increased, see *Figure 6.29*. This result would be expected as the increasing temperature of hydrothermal treatment will increase the mean crystallite size decreasing the surface area. Despite the large aspect ratio of the crystallites, the surface area was very similar to the anatase series (A) in Chapter 5 *ca.* 80 to 30 m^2/g depending on processing conditions.

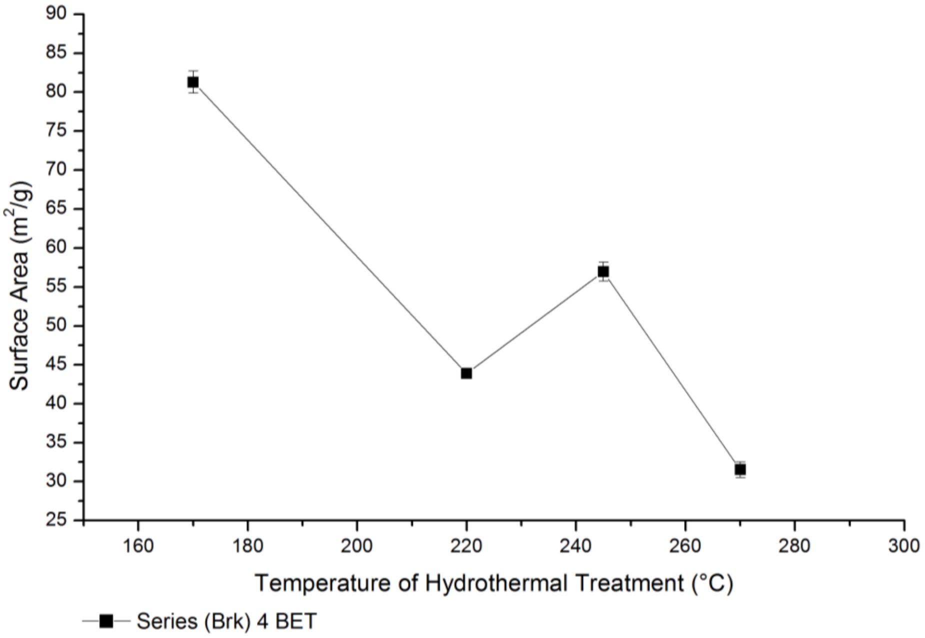

Figure 6.29 Surface area values for series (B) samples estimated using BET analysis of nitrogen adsorption isotherms.

The surface area of the as-synthesised pure rutile sample (TiO2 (G) 0.25ox0.1F) was evaluated using a nitrogen adsorption isotherm and (BET) theory. It was found that the surface area was 18.5 m_2/g. The crystallites were very large when observed using TEM, therefore, the low surface area is expected.

6.2.5 Soft X-ray study of Rutile and Brookite Phase TiO_2

Elemental survey scans were performed on both the brookite and rutile series using XPS. The results, *Table 6.1*, show that both the brookite and rutile still had detectable F either adsorbed to the surface or as a bulk dopant. Although, it is more likely that the F^- detected is surface bound, as the depth sampling is only *ca.* 2.8 nm for 1487.6 eV X-rays due to the limited electron mean free path.[114] Interestingly, the F detected can be seen increasing with increasing temperature of hydrothermal treatment through the brookite series. Contrary, there was no increase in F detected throughout series (A) with respect to the temperature of hydrothermal treatment. Potentially this is caused by the aspect ratio changing exposing a particular facet for the F^- to adsorb to. It must be related to the exposure of a particular facet as the overall surface area was decreasing, see *Figure 6.29*. Note: there were only minor changes to the crystallite shape through series (A) explaining the constant amount of F detected.

Likewise, the amount of F detected can also be seen increasing with respect to the number of equivalents of NH_4F added to the rutile synthesis media. This result is expected as it was seen in series (B) too, where the amount of F detected increased with increasing ratios of NH_4F to Ti (Chapter 5).

Si due to the Si wafer onto which samples were deposited for measurements was only detected in the phase pure rutile sample (TiO_2 (G) 0.25ox0.1F). Unfortunately, this makes interpretation of some results (particularly VB spectroscopy) later impossible.

Sample	**Ti (%)**	**O (%)**	**F (%)**	**Si (%)**
TiO_2 (Brk) 170 4	32.0	57.3	0.8	0
TiO_2 (Brk) 220 4	25.1	52.7	1.1	0
TiO_2 (Brk) 245 4	30.9	57.2	2.0	0
TiO_2 (Brk) 270 4	29.5	53.7	5.0	1.8
G0.25ox0.1F	18.0	55.2	1.1	25.7
G0.25ox0.25F	33.0	65.4	1.6	0
G0.25ox1F	31.1	66.1	2.7	0

Table 6.1 Results of survey scans of series (A) using XPS.

Hi-resolution XPS of the Ti2p region was used to determine the amount of Ti^{3+} (with respect to total Ti) present in the as-synthesised blue brookite samples. It was found that the blue brookite contained a relatively low amount of Ti^{3+} when compared to the blue rutile and anatase *i.e.* 4.2 % for TiO_2 (Brk) 270 4 the bluest sample compared to 6.1 % for the rutile sample and 6.9 % TiO_2 (B) 0.1 at 1486.7 eV. The amount of Ti^{3+} appeared to peak at 220 °C and then decline as the temperature of hydrothermal treatment increased, see *Figure 6.30*. Much like the blue anatase and rutile, the Ti^{3+} detected increased at low incident X-ray energies indicating it was mostly surface bound, see *Figure 6.30*.[114,115] However, the difference in the Ti^{3+} detected at different depths decreased with increasing temperature of hydrothermal treatment. This could be an effect of the crystallite aspect ratio increasing with increasing temperature of hydrothermal treatment. Thus the surface Ti^{3+} may be isolated to a specific facet. Of note, the surface and bulk Ti^{3+} decreased with increasing temperature of hydrothermal treatment yet, the F detected in the survey scans increased. Therefore, F cannot be proportional to the Ti^{3+} defect concentration.

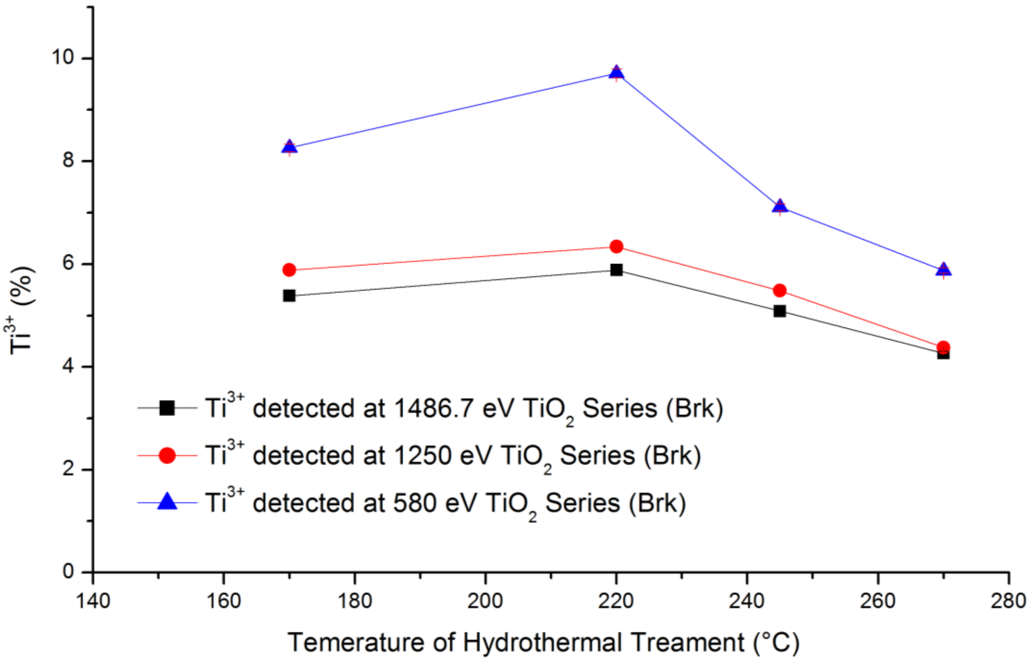

Figure 6.30 Graph of the percentage Ti^{3+} *detected through series (Brk) synthesised with 4 equivalents of NaF for different incident energy X-rays. Note Lines have been added to guide the eyes and not link to results.*

Hi-resolution XPS of the Ti2p region was used to verify the presence of Ti^{3+} in the blue rutile. It was found that the sample synthesised with 0.1 equivalents NH_4F contained 6.1 % Ti^{3+} as determined at 1487.5 eV, see *Figure 6.31*. The amount of Ti^{3+} present was greater than the equivalent blue anatase sample in series (B) *ca.* 5.32 % for TiO_2 (B) 0.1. As more NH_4F was added to the synthesis, the amount of Ti^{3+} detected appeared to decline as anatase became the dominant phase. As with the anatase, the amount of Ti^{3+} increased with decreasing incident X-ray energy. Thus, like in the case of blue anatase, most of the Ti^{3+} being detected is surface bound.[114,115]

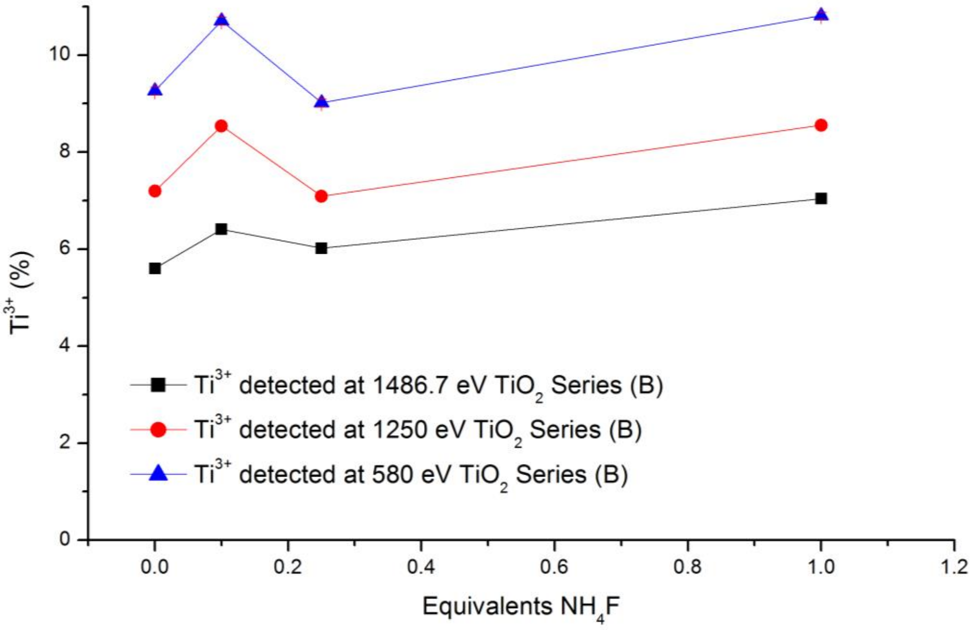

Figure 6.31 Graph of the percentage Ti^{3+} detected through series (G) for different incident energy X-rays. Note: Lines have been added to guide the eyes and not link to results.

VB spectroscopy was used to look at the electron band structure of the blue brookite. Firstly, the O2p π bonding edge remains constant throughout the series, see *Figure 6.32*. The x-intercept was found to be at 3.76 eV, slightly higher than those determined for the blue anatase *ca.* 3.72 eV for TiO_2 (B) 0.1. Brookite should have a slightly larger band gap than anatase *i.e.* 3.2 *vs* 3.3 eV.[21] Thus, within error, the conduction band has not moved relative to vacuum. Secondly, peaks due to the Ti^{3+}3d electrons were detected, see *Figure 6.32* inset. The relative intensity of the Ti^{3+}3d peak was decreasing with the increasing temperature of hydrothermal treatment. Overall, the area of the Ti^{3+}3d peak detected was lower than in the equivalent blue anatase samples *ca.* 0.074 TiO_2 (B) 4 *vs* 0.02 for TiO_2 (Brk) 270 4. This result agrees with the Ti2p XPS analysis above. The blue brookite contains less bulk and surface Ti^{3+} than the equivalent blue anatase samples. This may be due to the NaF used in the synthesis or to do with the difference in the stabilization of Ti^{3+} in each phase.

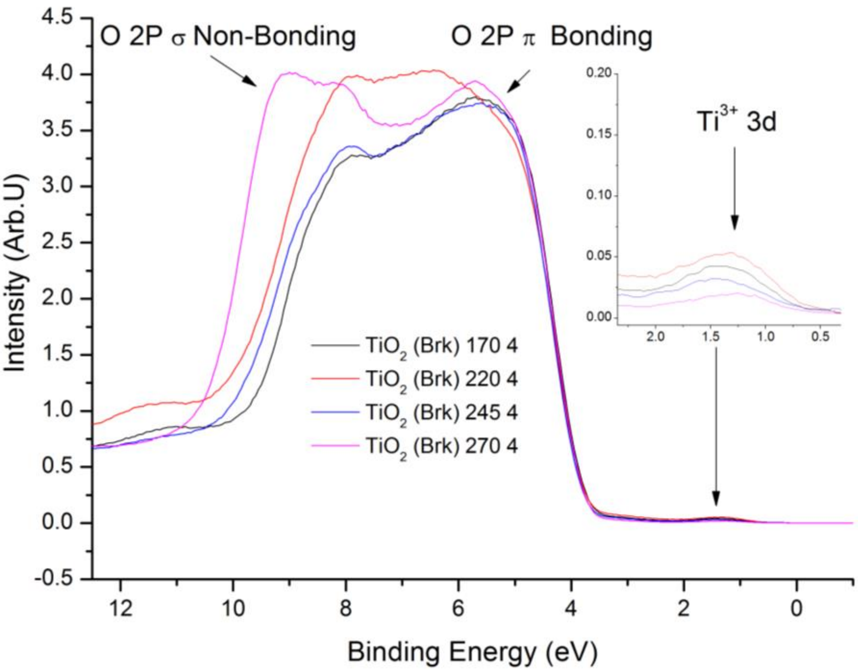

Figure 6.32 Valance band spectra of TiO_2 Series (Brk). The inset shows close up of the Ti^3 3d region.

VB spectroscopy was used to look at the electron band structure of the blue rutile. The rutile showed a much more intense O2p σ non-bonding peak relative to anatase, see *Figure 6.33*. This is probably due to the overlap with the signal originating due to the Si wafer (based on the XPS survey scans above), *Table 6.1*. Also, the leading edge of the O2p π bonding can be seen moving towards lower binding energies. The x-intercept was found to be at 3.50 eV, ~0.2 eV lower than the x-intercept of the equivalent anatase sample *ca.* 3.72 eV for TiO_2 (B) 0.1. The change in the intercept agrees well with the change in optical bandgap due to the rutile phase *i.e.* 3.0 *vs* 3.2 eV.[6] Thus, the conduction band must be at the same energy level relative to the vacuum level. Finally, a Ti^{3+}3d peak can be seen in the inset (*Figure 6.33*).[141] The relative intensity of this peak was *ca.* 0.04, similarly to the equivalent anatase sample TiO_2 (B) 0.1 at *ca.* 0.04. As the ratio of NH_4F added to the synthesis increased, the intensity of the Ti^{3+}3d peak increased. The fact that the intensity of the Ti^{3+}3d peak was greater in the sample synthesised with 1 equivalent of NH_4F, whereas the Ti^{3+} detected in the Ti2p region was greatest at 0.1 equivalents suggest the rutile synthesised at 0.1 equivalents contained more bulk Ti^{3+} as VB spectroscopy is very surface sensitive due to the low incident X-ray energy (mean free path 0.2 nm).[114] The greater bulk Ti^{3+} would also explain why the rutile samples absorbed more red light than a typical blue anatase sample; compare *Figure 6.5* and *Figure 6.10*.

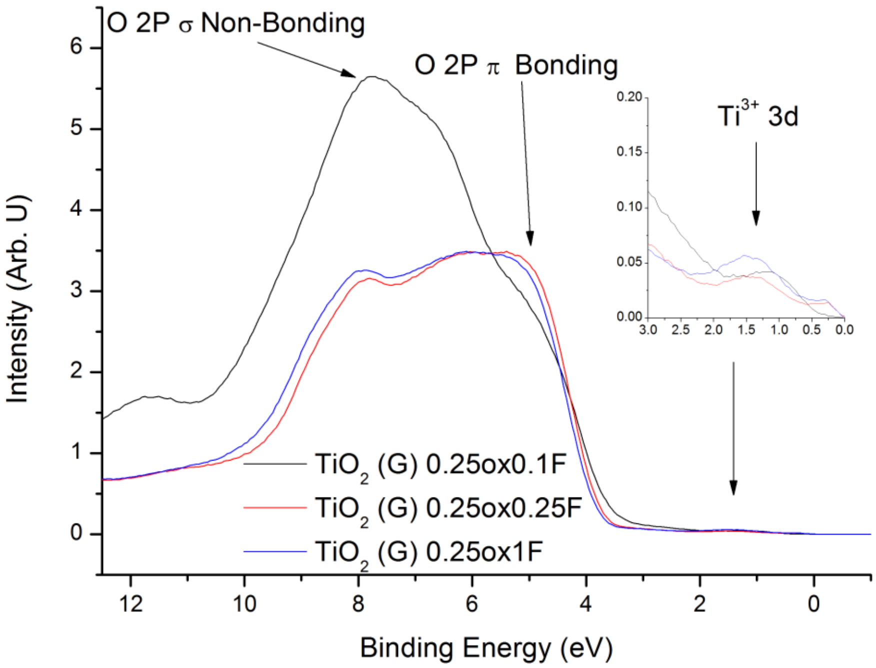

Figure 6.33 Valance band spectra of TiO_2 Series (G). The inset shows close up of the Ti^{3+}3d region.

NEXAFS was used to further evaluate the electron structure of the blue brookite. *Figure 6.34* shows the NEXAFS spectrum of a blue brookite sample compared to the F free blank sample. It can be seen that the peak intensities have significantly diminished relative to the blue rutile below. Also, the ratios of the L_3 e_g peaks are quite different in the brookite relative to the anatase.[143]

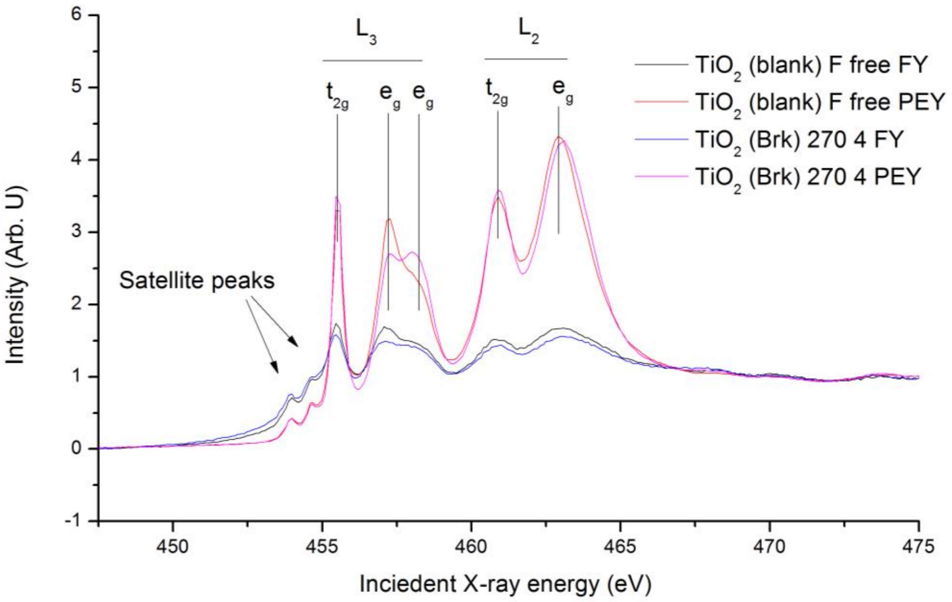

Figure 6.34 The NEXAFS spectra of sample TiO_2 (Brk) 270 4 vs TiO_2 (blank) F free.

When looking at the NEXAFS spectra of the brookite series it can be seen that the ratios of the L_2 t_{2g} to L_2 e_g changed throughout the series, see *Figure 6.35* top. *Figure 6.35* bottom shows the analysis of the L_2 t_{2g}/L_2 e_g. It can be seen in the PEY and to a lesser extent the TEY, the ratio of L_2 t_{2g}/L_2 e_g is increasing with increasing temperature of hydrothermal treatment. This would indicate the Ti^{3+} concentration is indeed decreasing as the temperature of hydrothermal treatment increases.[115,145] These results agree with the Ti2p XPS and VB measurements above. However, the same trend is not observed in FY, therefore the bulk Ti^{3+} is not changing with temperature; FY signal is more representative of the bulk whereas PEY is more surface sensitive.[115] Yet, the brookite was absorbing more red-light and becoming bluer with the increasing temperature of hydrothermal treatment.

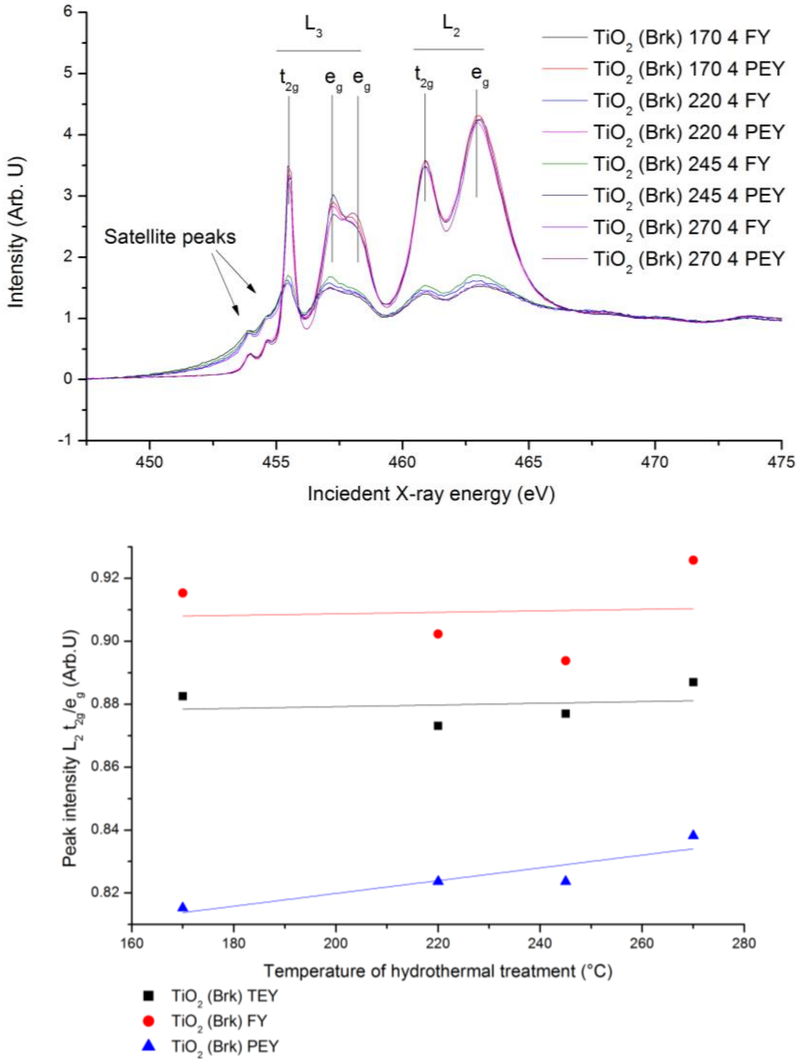

Figure 6.35 Top: The NEXAFS spectra of series (Brk) 4.Bottom: The relative ratios of L_2 t_{2g}/L_2 e_g for the series (Brk).

NEXAFS was used to further evaluate the electron structure of the blue rutile. *Figure 6.36* shows the NEXAFS spectrum of the blue rutile compared to the F free blank anatase sample. It can be seen that the phase change has shifted most of the peak positions. It has also dramatically changed the peak ratios, particularly the L_3 e_g peaks.[145] Due to the phase change though series (G), evaluating the ratios of specific peaks to look for Ti^{3+} is relatively pointless, particularly as no blank rutile sample was measured.

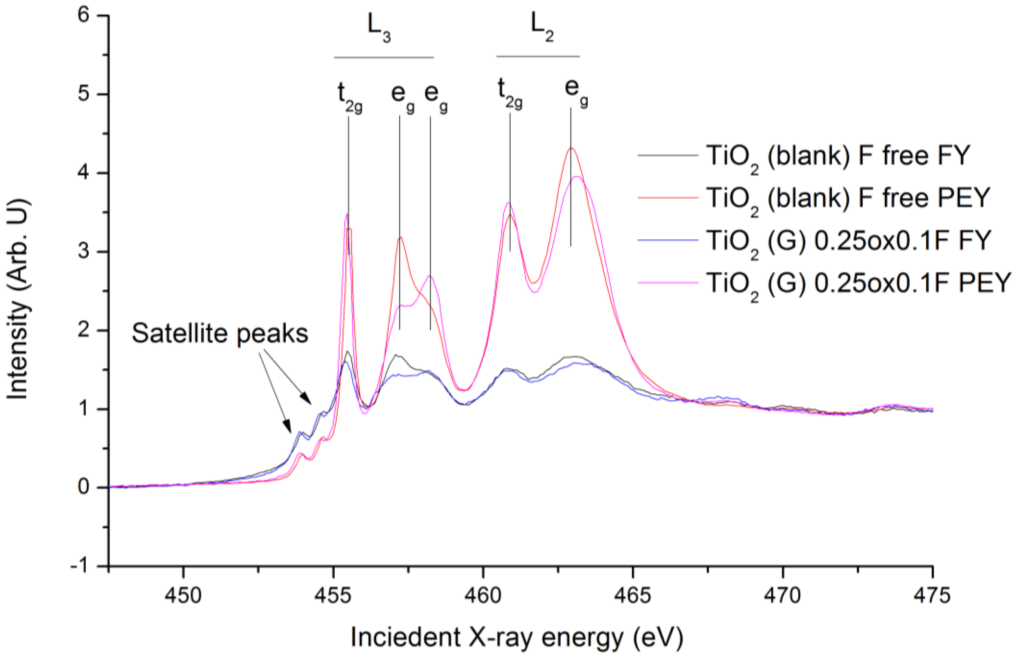

Figure 6.36 The NEXAFS spectra of sample TiO_2 (G) 0.25ox0.1F vs TiO_2 (blank) F free.

6.3 Conclusions:

In conclusion, phase pure blue rutile and brookite were synthesised by modifying the synthetic conditions used to make samples discussed in Chapter 5.

Brookite was synthesised by adding NaF to the sol-less synthesis in a large excess. It was found by PXRD that there was a critical ratio of NaF to TiO_2 which was required to trigger the phase conversion of anatase to brookite. This level was between 1-2 equivalents of NaF to TiO_2. Increasing this ratio further resulted in greater phase percentage by brookite. Also, it was found by PXRD that the temperature of hydrothermal treatment had some effect on the phase percentage of brookite: the higher temperatures tended to favour formation of brookite. Furthermore, Raman spectroscopy showed that the brookite formed at the expense of anatase. It is hypothesised that the Na^+ ion results in the *in-situ* digestion of anatase and amorphous material to form a titanate intermediate. The titanate intermediate transforms into brookite phase TiO_2 as the Na^+ ions are removed from the layered structure.[21,83,157,158]

The general morphology of the brookite was analysed by TEM, SEM, nitrogen adsorption and Raman spectroscopy. It was found that as the temperature of hydrothermal treatment increased, the brookite changed from smaller spherical particles to elongated rods. This change in shape increased the exposure of the {210} facet. The shape change could also be observed in the Raman spectra as a significant decrease in the A_{1g} 650 cm^{-1} peak intensity as well as an increase in the intensity of all other brookite peaks between 180 cm^{-1} and 650 cm^{-1}. The shape change was believed to be a result of the titanate intermediates as sodium titanate favours rod formation at greater temperatures of hydrothermal treatment.[160]

Finally, the trend in the intensity of the colour of the blue brookite was near identical to the blue anatase in Chapter 5. The colour increased in intensity as the temperature of hydrothermal treatment increased. Though, XPS showed the Ti^{3+} was decreasing with the increasing temperature. However, depth profiling XPS, VB spectroscopy and NEXAFs demonstrated that the decrease in Ti^{3+} was mostly surface bound and the bulk Ti^{3+} remained constant. Thus, the colour is probably due to the bulk Ti^{3+}. Furthermore, the surface Ti^{3+} appeared to be related to the aspect ratio of the crystallites and possibly located on a specific facet.

Blue rutile was synthesised using the sol-less approach by modifying the synthesis media with oxalic acid. It was found by PXRD that rutile was only formed in a narrow range of NH_4F concentrations. Out of this range, anatase took over very quickly. The range was narrower than with the oxalic acid sols discussed in Chapter 4. It was hypothesised that the sol-less synthesis did not start with any rutile nuclei so they had to be formed during the heat-up period before the oxalic acid thermally decomposed during the hydrothermal treatment.

Electron microscopy showed the blue rutile particles were large and near spherical. It is believed the F^- ions bound to the {001} facet and prevented the rutile from forming rods.[86] High-resolution TEM showed a disordered shell around the outside of the crystallites that may be a result of surface reduction.[116]

Finally, the rutile was very blue and absorbed the same wavelengths of red-light as the blue anatase but to a greater extent. VB spectroscopy and Ti2p XPS both showed that there was Ti^{3+} present in the blue rutile. In fact, the blue rutile had a greater proportion of Ti^{3+} than the equivalent blue anatase sample.

Chapter 7 : Photocatalysis

7.0 Introduction:

The photocatalytic activity of TiO_2 will be evaluated in this chapter. The photocatalytic activity of TiO_2 has become a hot topic in the literature after the publication from Fujishima and Honda, showing TiO_2 can photocatalytically split water into hydrogen and oxygen.[11] There are many research groups investigating the photocatalytic activity of TiO_2 and its ability to break down chemical waste, produce self-cleaning materials, splitting water, reduce carbon dioxide, remove air pollutants (such as NO_x) and oxidise plant hormones, such as ethylene.[6,42,163,164]

Quantifying the photocatalytic performance of TiO_2, depending on the reaction, can often be challenging. For instance, monitoring the splitting of water into H_2 and O_2 is relatively straightforward if the equipment is available *i.e*. a gas chromatography mass spectrometry. On the other hand, using the degradation of organic pollutants, such as phenol, as a model system to study the performance of the TiO_2 can be difficult, because the breakdown products and reaction scheme to those products is relatively unknown.[7] In order to test the photocatalytic activity of TiO_2 using relatively simple equipment, dyes are often used because the decolouration can be easily measured by UV-Vis spectroscopy. The problem with this approach is that some dyes may discolour from just one bond being oxidised or reduced in the conjugated system of the chromophore while other dyes will require many bonds to oxidised or reduced before discolouring. Methylene blue (MB) for instance, requires reduction by 4 electrons to discolour.[165] Also, a molecule of the dye may be discoloured but its remnants can be bound the photocatalyst and continue receiving excited electrons and holes until it is eventually oxidised to carbon dioxide gas.[7,165] When trying to determine the activity of a photocatalyst, knowing the actual electron/hole yield is the only true way to determine how active it is. In the following chapter, the photocatalytic activity of as-synthesised blue and white TiO_2 was evaluated using two dyes:

- The first dye used was reactive blue (RB-19). RB-19 is a blue dye used in the textile industry for staining clothing items, such as jeans. It is a very stable dye capable of keeping its colour in both acidic and basic conditions. It is only very slowly broken down by exposure to sunlight; its half-life is approximately 40 years under ambient conditions.[166,167] The use of RB-19 was also due to collaboration with Dr Faridah Abu Bakar who established extremely robust testing protocols and had already published papers using the results from P-25.[167]
- The second dye used was MB. MB was chosen as it is a very commonly used dye for evaluating the photocatalytic activity of TiO_2.[37,168,169] It is a relatively unstable dye which can be easily

decoloured by mild oxidants. However, it is also the dye of choice by the ISO Standards Committee who have used it for testing the activity of photocatalytic films (ISO10678:2010).[59]

The industry standard for benchmarking photocatalytic activity is a commercially available photocatalyst P-25 originally produced by Degussa. P-25 is a mixture of anatase and rutile, approximately 3 parts anatase to 1 part rutile (WT/WT) with an overall surface area of 49 m^2/g.[167,170] The mixture of anatase and rutile has been shown to make P-25 more photoactive.[170] It is believed that the combination of rutile and anatase has synergetic effects, resulting in an enhanced electron-hole separation reducing the recombination rate.[171]

There are 2 elements to photocatalytic activity: one is the performance of the photocatalyst under broad-spectrum illumination, which includes UV light, ideally mimicking levels of ambient sunlight reaching surface of the Earth; the other is broad-spectrum illumination but with the UV proportion of the light filtered out *i.e.* visible light with photon energy of less than 3.0 eV. In the last two decades, there has been a push to extend the photocatalytic activity of TiO_2 into the visible light portion of the solar spectrum. This is because less than 10 % of the available energy in solar radiation has photon energy of above 3.0 eV *i.e.* UV.[22] Visible light photocatalytic activity has been achieved through doping, coupling and dye sensitisation for TiO_2.[7,163] However, all these methods have drawbacks. Generally, the visible light photocatalytic activity can come at a cost of the overall performance of the photocatalyst under broad-spectrum illumination. This is because crystal defects often encourage electron-hole recombination, lowering the photocatalytic activity.[42]

There have been a number of studies into the visible light photocatalytic activity of blue TiO_2. Currently, there does not appear to be any concise agreement on whether blue TiO_2 is visible light photoactive or not. It would appear that different synthetic approaches to synthesising blue TiO_2 can alter whether it is visible light active or not. For example, Wang *et al.*[95], who synthesised blue TiO_2 hydrothermally with obtained in the presence of HF material having an increased exposure of the {001} facets, reported visible light activity for the degradation of Rhodamine B (red dye). Whereas, Gordon *et al.*[98], who prepared blue TiO_2 solvothermally in the presence of HF and surfactants, found obtained TiO_2 to be visible light inactive for water splitting.

In the following chapter, two different dyes, broad-spectrum light, filtered broad-spectrum light, UV LEDs and red LEDs, were used to determine whether the hydrothermally synthesised blue TiO_2 (anatase, rutile and brookite phases) is photocatalytically active. Also, the performance was benchmarked against an industry standard P-25.

7.1 Results and Discussion:

7.1.1 Photocatalytic activity of oxalic acid sols tested with RB-19

The photocatalytic activity of the hydrothermally treated oxalic acid sols was tested by looking at the degradation of RB-19. The activity of the hydrothermally treated sols was evaluated under broad-spectrum light (Xe lamp). Overall, the activity of the hydrothermally treated sols was lower than that of P-25 (a commercial TiO_2 photocatalyst), see *Figure 7.1*. Between the samples synthesised with different ratios of NH_4F modifying the sols, the sample modified with 0.5 equivalents was the most active, almost the same activity as P-25, see *Figure 7.1*. The next most active sample was the 1 equivalent sample (TiO_2 (1F)). Both the 0.5 and 1 equivalent samples contained anatase, the more photocatalytic active phase of TiO_2 due to better transportation of excited electrons and holes to the surface from the bulk.[6,39] The samples synthesised with less than 0.5 equivalents were phase pure rutile, see *Figure 4.9*. Interestingly, both these samples were photoactive, albeit possessing around half the activity of their anatase counterparts. In fact, when normalised for surface area, the activity of the 0.25 equivalents sample is much higher than all other samples tested, see *Figure 7.1* (blue bars). This is in part due to the way testing was performed using the same mass across the series and normalizing obtained results by surface area. It could be that the particularly high activity, in this case, is related to the exposure of different facets, due to the shape change induced by the NH_4F, see *Figure 4.15*. The shape change is believed to have exposed more of the rutile {101} facet, which has been reported to be the more active facet of rutile.[172] This facet has been shown to be particularly active for oxidation, which would be effective for dye decolouration.[38,165,172]

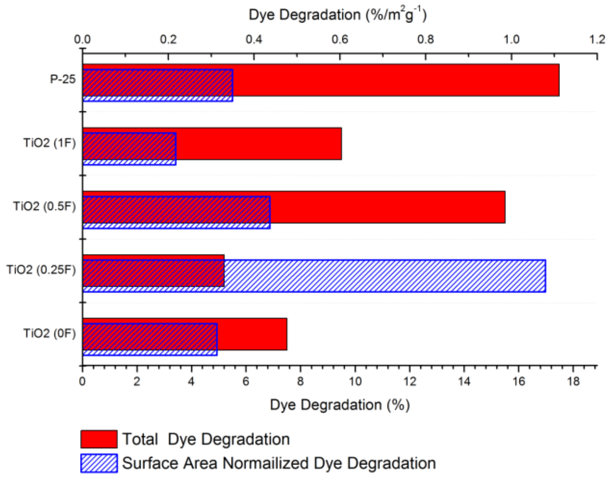

Figure 7.1 Graph showing the total degradation of RB-19 dye under a Xe lamp catalysed by TiO_2 synthesised by modifying TiO_2 oxalic acid sols with different ratios of NH_4F.

7.1.2 Photocatalytic activity of Blue Anatase tested with RB-19

Initially, the photocatalytic activity of series (A) was examined using RB-19 under Xe light. It was found that the as-synthesised samples were less photoactive than P-25, see *Figure 7.2*. Also of note, the activity of the TiO_2 synthesised without using an oxalic acid sol was lower, compare *Figure 7.1* and *Figure 7.2*. The sol-based TiO_2 above may have benefited from the synergetic effects of mixing anatase and rutile.[170] The activity of the as-synthesised TiO_2 declined through the series with increasing temperature of the hydrothermal treatment. This was expected, as there was a decline in surface area, see *Figure 5.88* (Chapter 5). Also, the optimum crystal size as determined by PXRD for the photocatalytic activity of anatase is between 10 and 15 nm, with TiO_2 (A) 170 having closest to such optimum size, see *Figure 5.46*.[6] The carbon-free white sample showed very similar activity as its blue counterpart TiO_2 (A) 270. Despite the colour change from white to blue through the series, the activity did not appear to increase; in fact, it decreased. These two results suggest the blue colour certainly did not improve the photocatalytic performance under broad-spectrum illumination instead the decreased the activity was observed most likely due to the diminished surface area. When evaluating the activity per unit of surface area, the sample synthesised at 170 °C was still the most active by a long shot, see *Figure 7.2* (blue bars). The TiO_2 170 was actually slightly more active than P-25 when normalised for surface area. The high activity of the white TiO_2 (A) 170 in the cases of both mass-based and surface area normalised activity, indicated that the crystallite size is the main factor influencing photocatalytic activity.

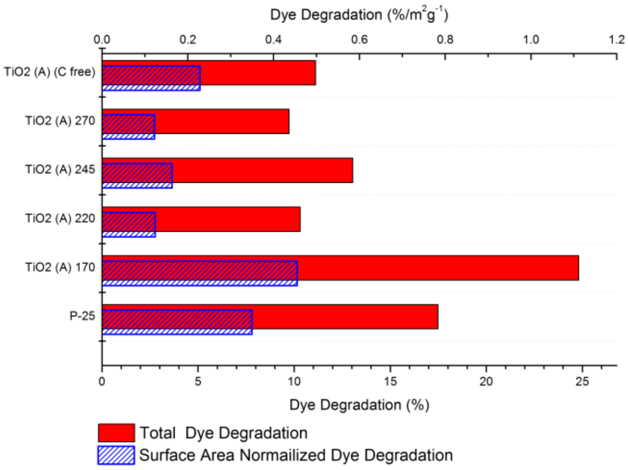

Figure 7.2 Graph showing the total degradation of RB-19 dye under a Xe bulb catalysed by TiO_2 in blue TiO_2 series (A) experiments.

Of course, the defects introduced by the NH_4F to generate the blue colour are likely to make the photocatalysts overall lower in activity compared to P-25 due to their possible behaviour as the electron/hole traps. However, the colour of the TiO_2 should affect the visible light activity. So, the photocatalytic activity of P-25, TiO_2 (A) 270 and TiO_2 (A) 170 was evaluated under filtered "visibly light only" Xe light (400 nm cut off). *Figure 7.3* shows the gradual degradation of the RB-19 under visible light. It can be seen that overall the photocatalytic activity was much lower compared to the non-filtered light (3 % *vs* 18 % for P-25). However, all the TiO_2 catalysts tested did discolour some dye. Interestingly, the TiO_2 (A) 270 outperformed the P-25 by almost 100 % overall. In fact, the blue TiO_2 (A) 270 retained 50 % of its activity under the non-filtered light. Also, the TiO_2 (A) 170 performed very poorly, contrary to the case of the broad spectrum illumination above where TiO_2 (A) 170 outperformed all the blue samples. The visible light photocatalytic activity of P-25 can in part be explained by the rutile content of the P-25 and the 400 nm cut off filter. On the other hand, the visible light activity of the blue phase pure anatase (TiO_2 (A) 270) is a clear indicator of the improved visible light photocatalytic activity. One thing to note, if the red light is absorbed by the blue TiO_2 to generate electron-hole pairs, then the blue TiO_2 would be competing with the RB-19 to absorb red light.[173] This means the full potential of the blue TiO_2 as a visible light photocatalyst may not be realised by such tests.

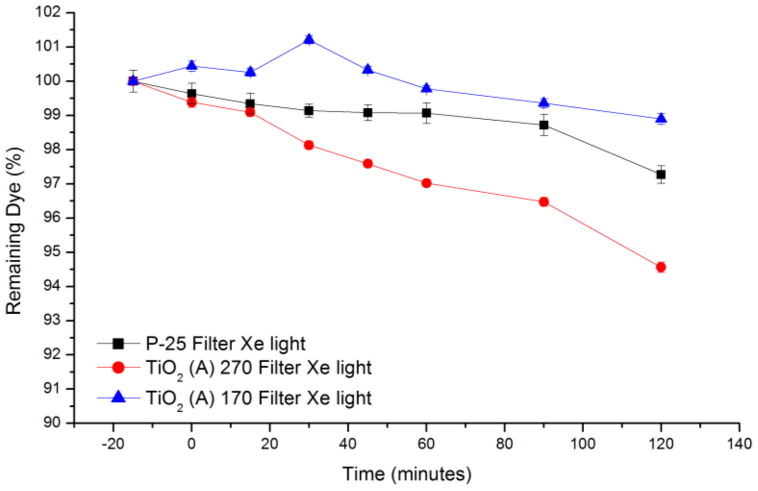

Figure 7.3 Graph showing P-25 vs TiO_2 (A) 270 for visible light RB-19 degradation under filtered Xe light.

7.1.3 Photocatalytic activity of Blue Anatase tested with MB

RB-19 is a very robust dye that can be hard to degrade. Whereas MB is easily degraded and commonly used for testing the photocatalytic activity of particles and surfaces.[59] The actual ISO10678:2010 standard is a standard test for evaluating the photocatalytic activity of surfaces.[59] However, there is no ISO standard for testing the photocatalytic activity of powders, so the ISO10678:2010 standard was modified to use powders in the forthcoming work.

First of all, the activity of series (A) and (F) in the degradation of MB was evaluated under Xe light (not filtered). P-25 was used as a reference; the obtained results are presented in *Figure 7.4*. The photocatalytic degradation of MB showed the increase in activity through series (A) with increasing temperature of hydrothermal treatment, see *Figure 7.4* This result was unexpected based on the RB-19 dye results above, where the activity decreased with increasing temperature of hydrothermal treatment. On the other hand, series (F) also showed increasing photocatalytic activity with increasing temperature of hydrothermal treatment. However, the activity of series (F) was overall substantially lower compared to the fluoride-modified blue series (A). The crystallite sizes of TiO_2 in both series were determined to be relatively similar by PXRD, therefore this increased activity of the blue TiO_2 may be attributed to the better utilization of the visible light. The activity of both series was greater than that of P-25; however, series (F) was also white so the origins of the increased photocatalytic activity are not yet understood in this case.

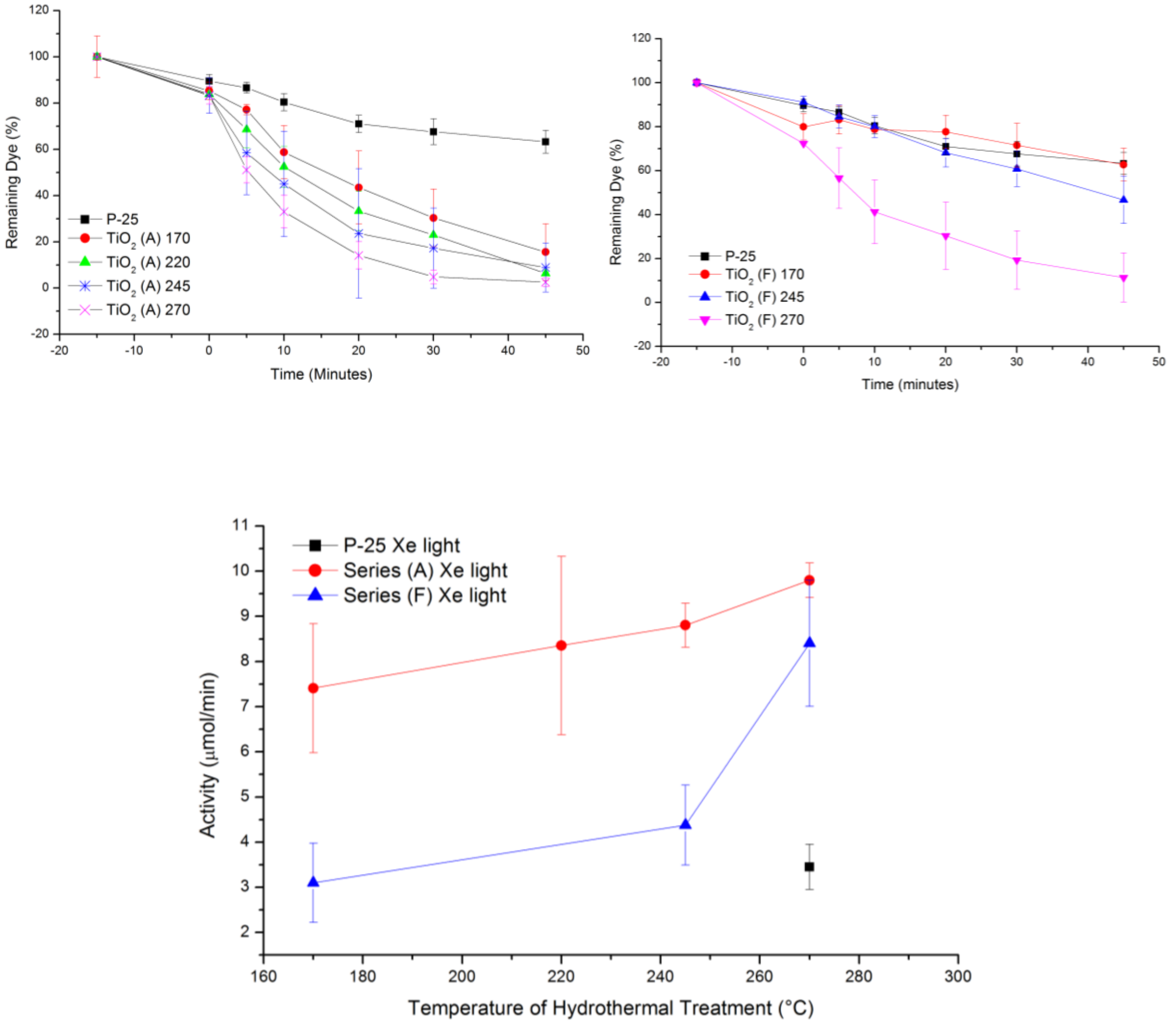

Figure 7.4 Graphs showing the degradation of MB under a Xe light. Top left: Series (A). Top Right: Series (F) temperature. Bottom: Graph shows the overall degradation.

To look at the difference between potential visible light photocatalytic activity and UV light photocatalytic activity, under otherwise the same conditions, experiments on the photocatalytic degradation of MB dye were repeated using UV LEDs (50 W). As can be seen below in *Figure 7.5*, the MB was decoloured quickly by the P-25 under UV illumination. The overall performance of the P-25 was higher under the UV LEDs: *ca.* 3.45 µmol/hr for Xe lamp *vs* 7.21 µmol/hr for UV LED illumination. Yet, series (A) still showed on average higher activity than P-25. However, there was a change in the trends of activity versus temperature of hydrothermal treatment. From 170 to 245 °C the activity of TiO_2 synthesised in series (A) increased. Then the activity suddenly decreased to the same level as P-25 for the sample synthesised at 270 °C. In contrast, the activity through series (F) increased to greater than P-25 for the 270 °C sample. The activity difference between samples modified with NH_4F and NH_4OH (synthesised at 270 °C) was very large when examined using UV light as opposed to when examined with broad-spectrum light. The variations in photocatalytic activity under the different lights could, therefore, be related to the blue colour. The blue fluoride-modified samples benefited from the visible light activity overcoming the detrimental effects of the induced defects and potential electron-hole trapping. Whereas the samples of white NH_4OH-modified TiO_2 did not benefit from the enhanced broad-spectrum performance, however, they did benefit from the reduced number of defects under UV light. It must be said, that although the photocatalytic experiments were run in duplicates, the reproducibility of the experiments under UV LEDs was poor. This may be attributed to the light intensity fluctuating. Inside the photocatalytic reactor, it was very warm and the LEDs were brand new. This may have resulted in premature ageing and a reduction in flux.[174]

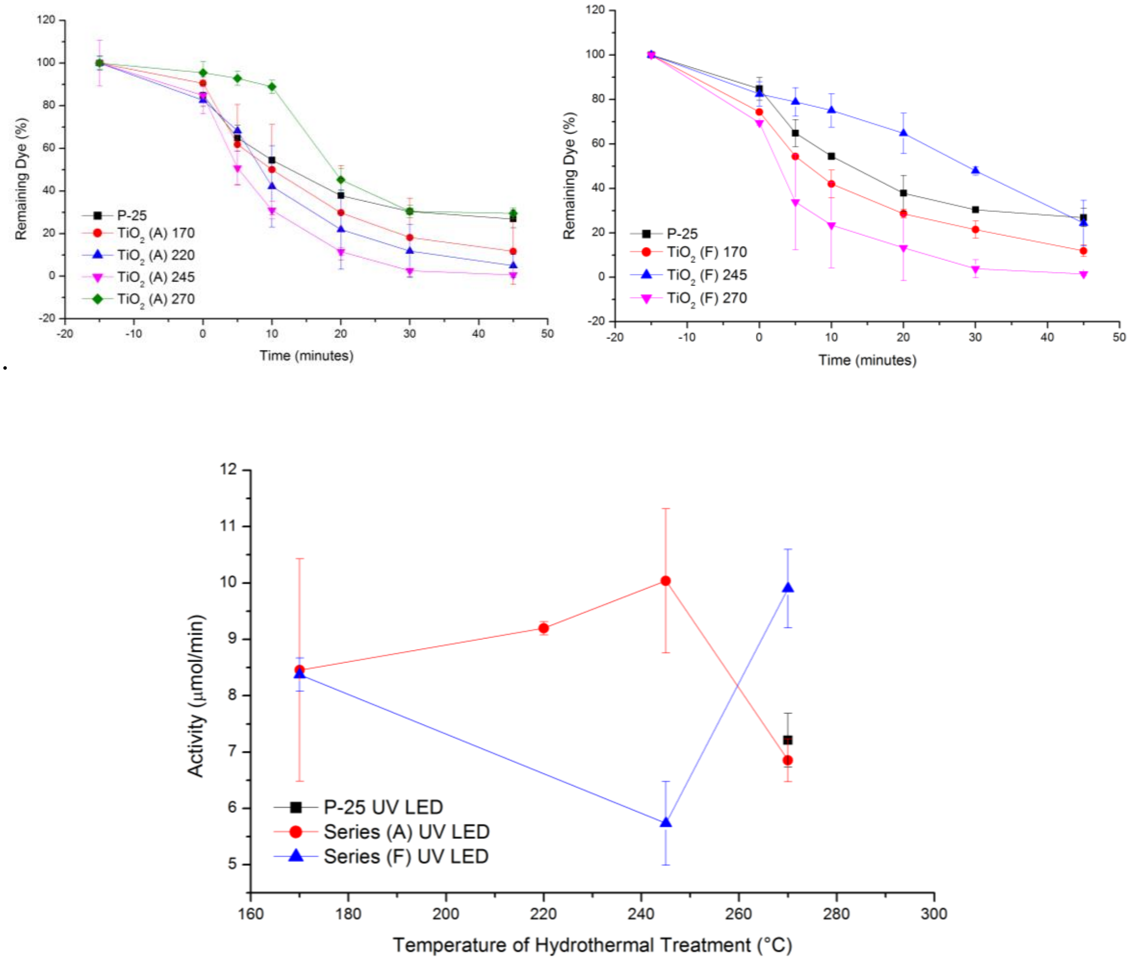

Figure 7.5 Graphs showing the degradation of MB under UV LEDs. Top left: Series (A). Top right: Series (F) temperature. Bottom: Graph shows the overall degradation.

Next, the photocatalytic activity of series (B) was examined under broad Xe light. For comparison, the equivalent part of series (F) (the NH_4OH-modified series) was run in parallel. Much like above, the activity of the NH_4F and NH_4OH modified TiO_2 was much higher than P-25, see *Figure 7.6*. However, the activity of the studied materials varied throughout the series. From 0 to 0.1 equivalents the activity declined. It then increased at one equivalent before steeply declined again at 4 equivalents of NH_4F, see *Figure 7.6*. Whereas the activity of the equivalent NH_4OH sample did not substantially change throughout the series, even at 4 equivalents there was only a marginal decline in activity, see *Figure 7.6*. The changes in activity through series (B) could be explained by the changes in surface area and reducing crystallinity. At 0.1 equivalents the surface area steeply declined from approximately 35 m^2/g to less than 6 m^2/g (as the crystallites produced grew to over 150 nm), see *Figure 5.89*. On the other hand, the 4 equivalents NH_4F sample had the highest surface area out of all the samples tested *ca.* 45 m^2/g but, it is known from the PXRD and TEM in Chapter 5, that the sample had significantly reduced crystallinity from excessive F^- doping and very low Ti occupancy. Ti vacancies are known to act as electron acceptors and have been reported to enhance charge carrier mobility and the photocatalytic performance.[140] Surface Ti vacancies have been reported to enhance water splitting due to enhanced chemical adsorption.[45] On the other hand, foreign electron acceptors, such are Cr and Mo, have been reported to have detrimental effects on photocatalytic performance.[45] Noteworthy, the 4 equivalents sample had the greatest quantity of Ti^{3+} (as determined by XPS), but it is believed to be mostly surface bound Ti^{3+} (See Ti2P XPS depth profiling *Figure 5.60*), yet the poorest photocatalytic activity. Thus, it is unclear why the 4 equivalents sample shows poor photocatalytic activity.

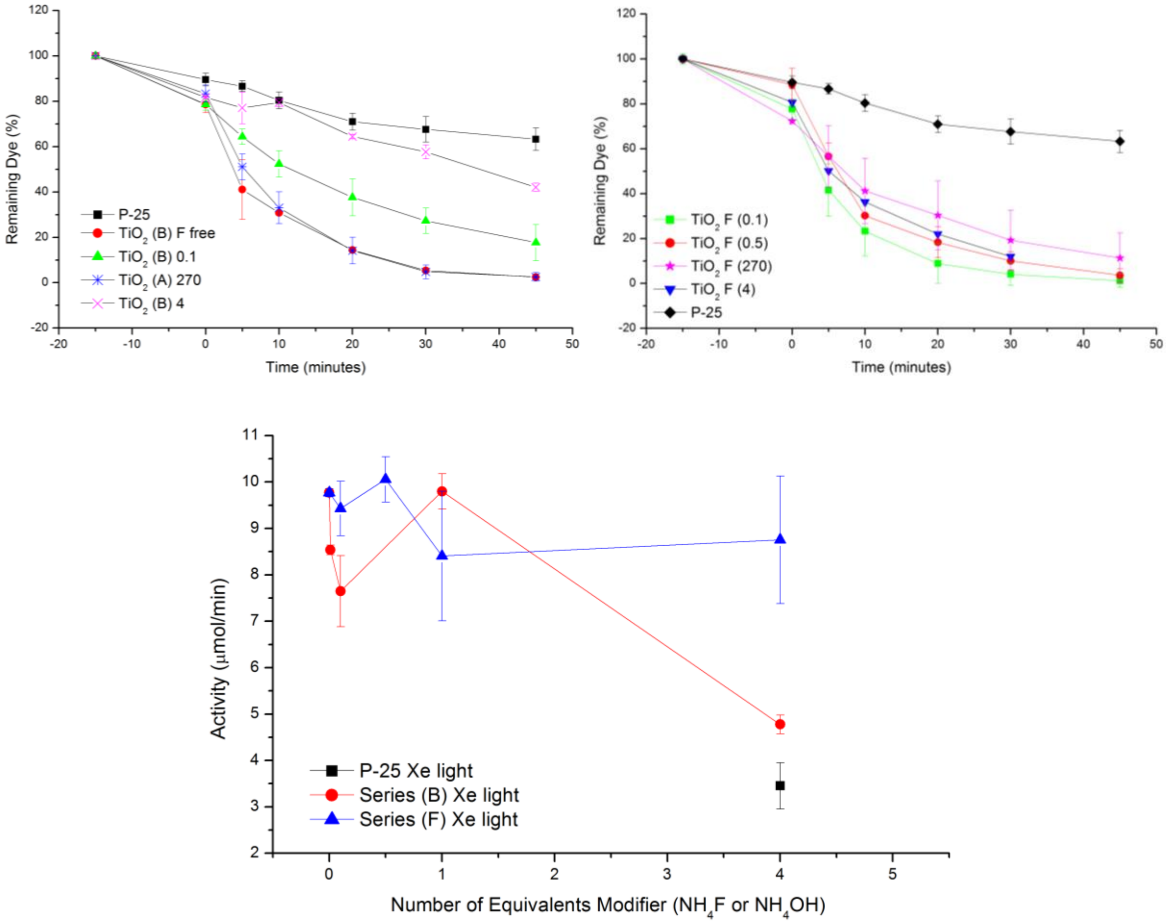

Figure 7.6 Graphs showing the degradation of MB under a Xe light. Top left: Series (B). Top right: Series (F) concentration. Bottom: Graph shows the overall degradation.

For comparison, the photocatalytic activity of the above samples (series (B) and (F)) were examined under UV light. Interestingly, under UV illumination from 0 to 0.1 equivalents of NH_4F there was an increase in activity, see *Figure 7.7*. However, as the equivalents of NH_4F increased, the activity dropped off quickly until it was less than that of P-25 at 4 equivalents. On the other hand, the activity of the NH_4OH modified series increased initially at 0.1 equivalents and then plateaued all the way up to 4 equivalents. These results confirm that the poor crystallinity of the “4 equivalents” sample must have an impact on photocatalytic activity that is not related to colour. Instead, it will be related to electron/hole trapping. Furthermore, the activity of the “0.1 equivalents” sample demonstrates that under UV illumination, large crystallite size (*ca.*61 nm isometric determined by PXRD) and hence low surface area, does not significantly impact photocatalytic activity; crystallinity and electron-hole migration appears more important.

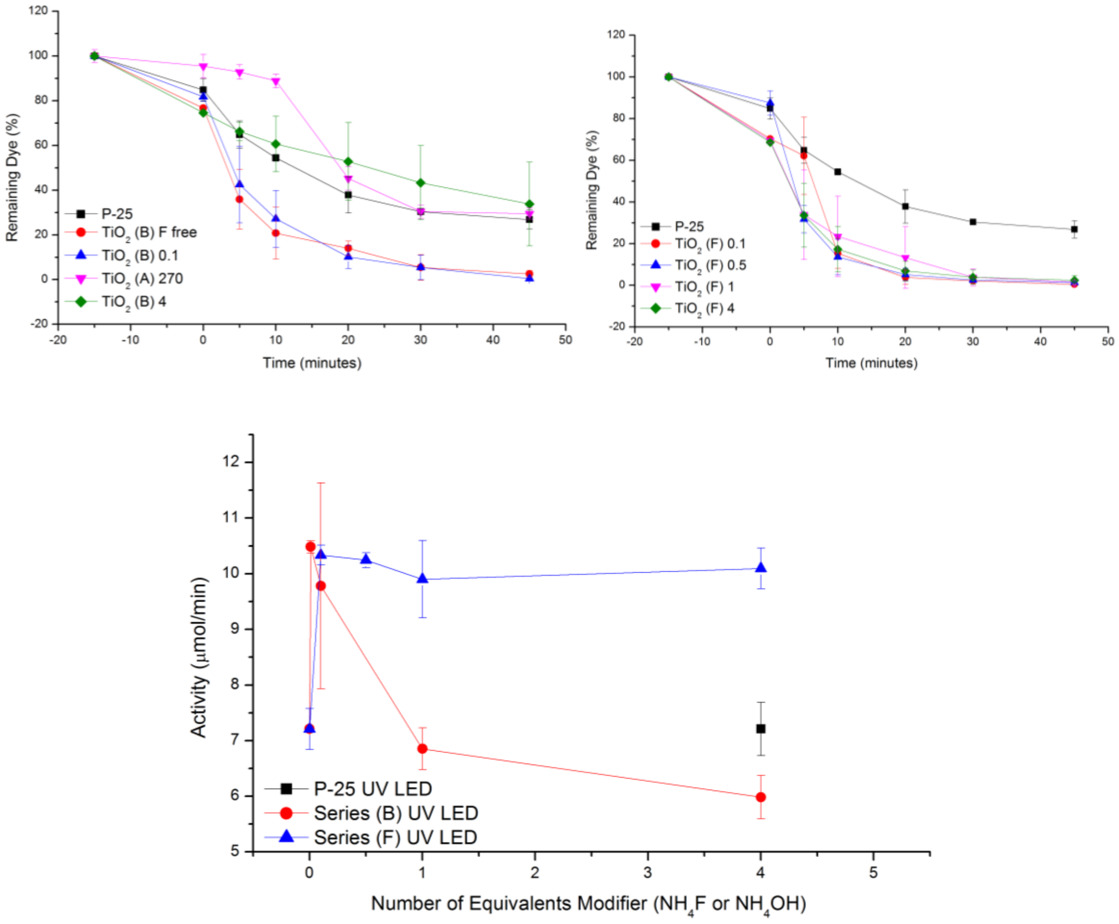

Figure 7.7 Graphs showing the degradation of MB under UV LEDs. Top left: Series (B). Top right: Series (F) concentration. Bottom: Graph shows the overall degradation.

The negligible changes in photocatalytic activity under both Xe and UV LED light for the NH_4OH-modified TiO_2 series confirms, that the NH_4OH had little impact on the crystal lattice or elements of morphology that affect photocatalysis. In contrast, changing the NH_4F to TiO_2 ratio had a substantial impact on the photocatalytic activity under both Xe and UV light. In particular, there were some differences noticed in the trends between the photocatalytic activity under UV LEDs and broad-spectrum Xe light. These changes indicated that the performance under broad-spectrum light can offset some of the negative impacts NH_4F has on the crystal structure, such as probable diminution in the electron-hole migration due to trapping on the F-induced defects. Finally, the 4 equivalents sample demonstrated visible light activity and its performance relative to P-25 was much greater under broad-spectrum illumination than under UV light.

For a final comparison, the activity of series (C) was evaluated under both broad-spectrum Xe and UV light. This was then compared to P-25 and the related NH_4F modified sample (TiO_2 (A) 270). It was found that under broad-spectrum light the NaF sample (TiO_2 (C) 1) was active, showing greater activity than P-25 but less than the related NH_4F sample, see *Figure 7.8*. However, under UV light only, the NaF modified sample was the least active. Much like with the NH_4F modified blue TiO_2, the NaF-modified TiO_2 was very active under broad-spectrum light, however, relative to P-25 the activity decreased under UV light only. This is most likely due to the absorption of the visible light (mainly red) increasing the photocatalytic activity despite the increased number of defects caused by the F^- doping (estimated by XPS) and low Ti occupancy (estimated by PXRD). Interestingly, the NaF modified sample showed lower activity under UV than the equivalent NH_4F sample. The NaF modified sample was not as blue as the NH_4F sample (according to UV-Vis DRS), suggesting there were fewer defects. However, PXRD showed that the NaF changed the crystal structure *via* a titanate mechanism to a greater extent than the NH_4F, which lead to very low Ti occupancy. So it could be said, that the Ti vacancies reduce the photocatalytic activity for the photocatalytic oxidation of MB in this system, despite literature reports of Ti vacancies increasing photocatalytic activity.[45,140]

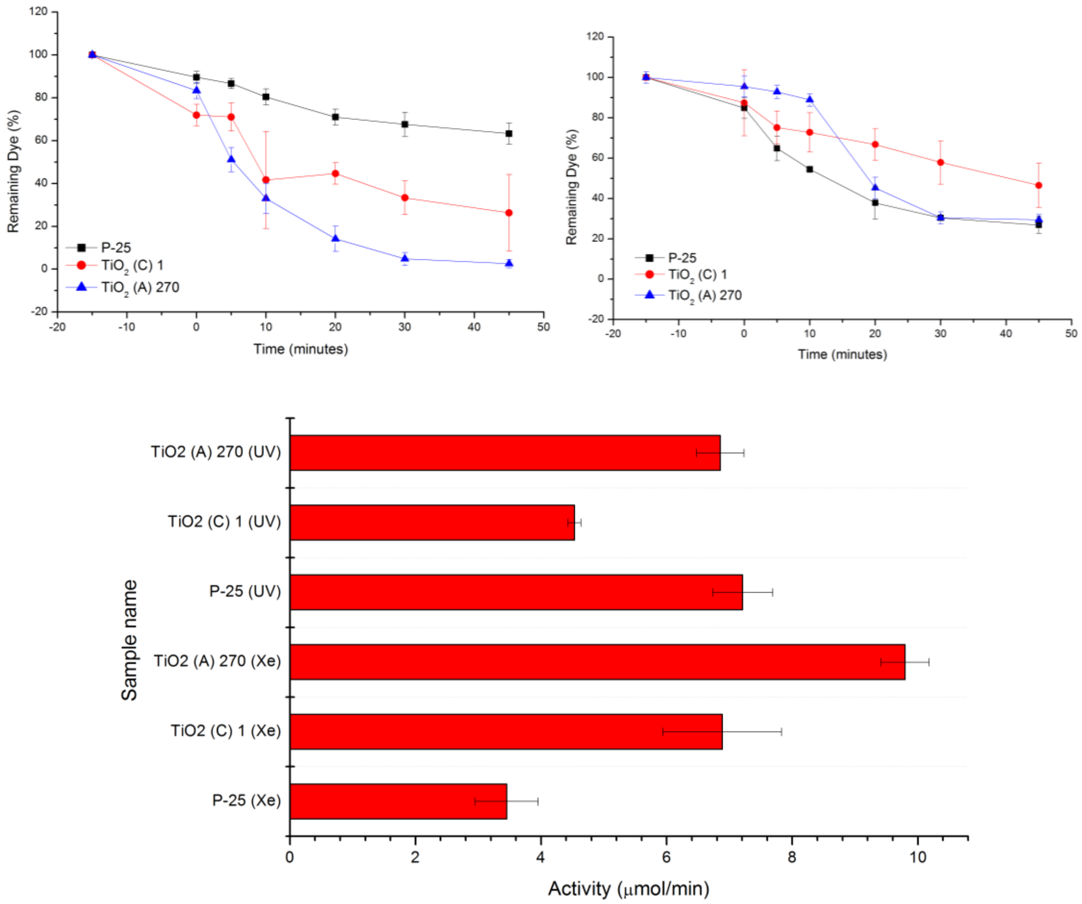

Figure 7.8 Graphs showing the degradation of MB with samples from series (C). Top left: Xe light. Top right: UV LEDs. Bottom: Graph shows the overall rate of degradation.

7.1.4 Photocatalytic activity of Blue Brookite tested with MB

The activity of the brookite synthesised in the presence of NaF was evaluated under both UV and broad-spectrum Xe light using MB. This study yielded some very exciting results, as the hydrothermal samples we prepared showed very good photocatalytic activity, *Figure 7.9*, despite many previous reports of brookite being photocatalytically inactive (although a few recent papers have reinvestigated and found brookite to be active).[21,162] Under broad-spectrum light the brookite was more active than P-25. However, throughout the series, the activity of the brookite was declining with the increasing temperature of hydrothermal treatment. Note: the "4 equivalents" sample was not analysed for photocatalytic activity due to the sample being lost. On the other hand, under UV light the activity of the brookite was similar to that of P-25. As in the case of series (A) discussed above for the MB degradation under the broad-spectrum light, the activity appeared to decline with increasing temperature of hydrothermal treatment, yet it peaked again at 270 °C. The difference in performance between broad-spectrum and UV light when compared to P-25, suggests that the brookite was also benefiting from visible light photocatalytic activity as was the case with the blue anatase. The changes in photocatalytic performance with respect to the temperatures of hydrothermal treatment could relate to the changes in the ratio of particular facets exposed. As seen in the TEM images, see *Figure 6.24* and *Figure 6.25* (Chapter 6), the aspect ratio of the brookite was increasing along the [001] direction with the increasing temperature of hydrothermal treatment. This decreased the exposure of the {212} facet and increased the exposure of the {210} facet. The increased activity at lower temperatures came from the greater exposure of the {212} facet agreeing with the findings of Ohno *et al.*[162]

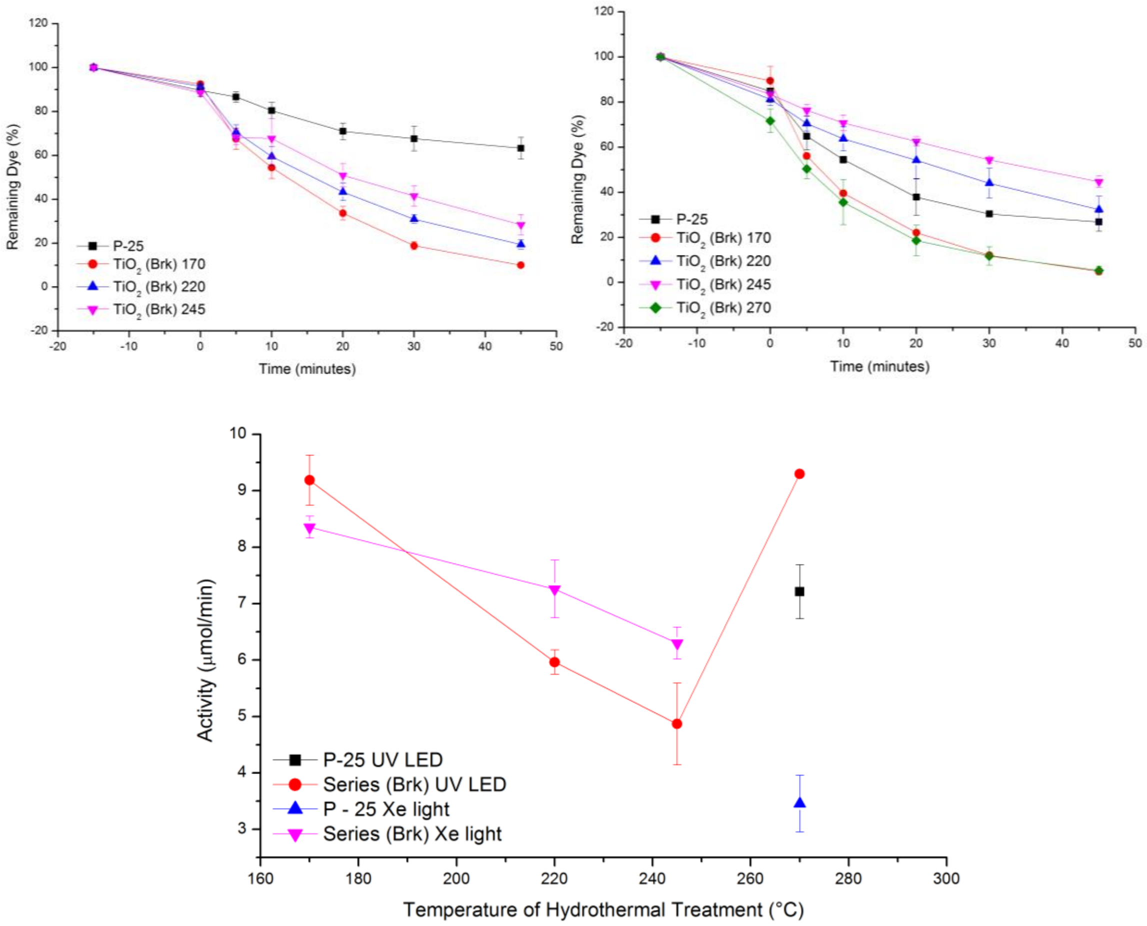

Figure 7.9 Graphs showing the degradation of MB with samples from series (Brk). Top left: Xe light. Top right: UV LEDs. Bottom: Graph shows the overall degradation.

7.2 Conclusion:

The photocatalytic activity of sols hydrothermally treated in the presence of NH_4F was evaluated using RB-19 dye degradation experiments. It was found that the rutile phase was very active when normalised for surface area. On the other hand, the most active blue samples contained the largest amount of anatase, yet it was not as active as P-25.

The photocatalytic activity of series (A) was also evaluated using RB-19 degradation under both broad-spectrum Xe light and a filtered Xe light (400 nm cut-off). It was found that samples synthesised at lower temperatures had greater photocatalytic activity under the broad-spectrum light. All samples tested with broad-spectrum light had inferior activity compared to P-25. Yet, when the UV part of the broad-spectrum light was filtered out, the blue NH_4F-modified sample showed almost double the activity P-25 and quadruple the activity of its white counterpart synthesised at a lower temperature. Overall, these experiments demonstrated that the blue TiO_2 was photocatalytically active for RB-19 degradation under visible light.

MB was used to evaluate the activity of series (A), (B) and (F) under UV LEDs and broad-spectrum light. It was found that the photocatalytic activity increased with increasing temperature of hydrothermal treatment under the broad-spectrum light. However, when using UV LEDs, the increasing temperature of hydrothermal treatment only increased the activity of white TiO_2 in series (F). When evaluating the effects of the ratio of NH_4F/NH_4OH to TiO_2 used during the synthesis, it became clear that the addition of more than one equivalent NH_4F had negative effects on the photocatalytic activity under both types of light. This is believed to be due to high levels of Ti vacancies increasing electron-hole recombination or impairing their migration. On the other hand, the addition of NH_4OH had almost no impact on photocatalytic activity throughout the range tested. The "0.1 equivalents of NH_4F to TiO_2" sample (which has the smallest 6 m^2/g surface area) demonstrated that surface area has little impact on the rate of reaction, indicating the observed performance is more to do with electron-hole creation and migration rather than dye adsorption. Finally, the NaF modified anatase sample showed poorer performance than the equivalent NH_4F sample, probably due to decreased Ti occupancy.

Lastly, the photocatalytic activity of the blue brookite was evaluated. The activity of the blue brookite was greater than that of P-25 under the broad-spectrum light. It was also within the same range of photocatalytic activity as that of the blue anatase. Under UV light, the activity was less than P-25, as well as blue and white anatase. This is highly novel findings as there are no few reports of the photocatalytic activity of brookite.

Chapter 8 : Conclusions and Future Work

8.0 Final Conclusions

In conclusion, oxalic acid (OX) passivated TiO_2 sols were synthesised while varying the Ti:OX ratio. It was found that increasing the Ti:OX ratio decreased the particle size from *ca.* 7 to 5 nm and decreased the percentage of anatase phase from *ca.* 30 to 5 %. These oxalic acid sols were hydrothermally treated at temperatures ranging from 90 to 270 °C. It was found that at low Ti:OX acid ratios (0.25 molar equivalents), rutile rods elongated in the [001] direction were formed. At higher Ti:OX acid ratios (greater than 0.25 equivalents), phase pure rutile was produced at lower temperatures (below 170 °C), however, at higher temperatures (above 170 °C) anatase phase reappears. It was found that the oxalic acid was decomposing, producing CO_2 and H_2O. It is hypothesised the CO_2 was responsible for the reappearance of anatase phase at higher processing temperatures. It was found that the anatase crystallites produced at high Ti:OX ratios were very small and had no discernible shape (according to the SEM study).

The oxalic acid sols were modified with NH_4F to try to retain the anatase phase during hydrothermal treatment. It was found that at 0.25 equivalents of NH_4F to Ti, rutile phase was still formed and the crystallites were found to be bipyramidal exposing the {101} facet; possibly due to the binding of the F^- ion to the {001} facet. As more NH_4F was added the hydrothermal synthesis media, anatase phase was retained becoming the major phase. Peak of the anatase phase content occurred at 0.5 equivalents. Increasing the NH_4F further did not result in more anatase phase. It was hypothesised that the change in pH with the addition of NH_4F was causing the phase change. However, the addition of mineral acids (HCl and H_2SO_4) to the hydrothermal synthesis did not confirm this. In fact, the experiments demonstrated that the acids were effective as modifying agents. However, it was found that the nuclei of each phase present in the oxalic acid sols influenced the phases produced during hydrothermal treatment. Thus, by removing the oxalic acid sol from the synthesis and directly hydrothermally treating titanium isopropoxide in the presence of NH_4F, NaF and oxalic acid, phase pure anatase, brookite and rutile could be produced.

While hydrothermally treating the oxalic acid sols in the presence of NH_4F, it was observed that blue TiO_2 was produced at temperatures above 220 °C. Blue TiO_2 is rare and interesting, so the focus of the thesis changed from morphology control to characterising and understanding the blue TiO_2. Thus, using the phase pure synthesis, blue anatase, brookite and rutile were synthesised and studied using PXRD, XPS, VBS, NEXAF, TEM, SEM, EPR, SQUID, Raman spectroscopy, PIGE, FT-IR spectroscopy, MS, UV-vis DRS and nitrogen adsorption isotherms.

Blue phase pure anatase was synthesised by directly hydrothermally treating titanium isopropoxide in an NH_4F solution. It was found using FT-IR spectroscopy and mass spectrometry that the decomposing isopropanol (liberated during the hydrolysis of the titanium isopropoxide) produced H_2 gas. At the high pressures and temperature inside the autoclave, the H_2 reduced Ti^{4+} to Ti^{3+}. The existence of bulk Ti^{3+} in the TiO_2 was proven by EPR and SQUID. It was hypothesised that the bulk Ti^{3+} was stabilized by F^- which substituted lattice oxygen and was responsible for the blue colour observed. Based on synchrotron VBS, the Ti^{3+} defect lay 0.95 eV below the conduction band and the promotion of a Ti3d electron to the conduction band was responsible for the red light absorption and hence blue colour observed.

During the characterisation of the blue anatase, it was found that many other features of the TiO_2 changed as the synthesis conditions changed. Using synchrotron PXRD it was found that the growth of crystallites was occurring *via* a titanate mechanism and therefore the size and shape of the crystallites was controlled by the NH_4^+ ion. The titanate mechanism resulted in crystallites that were elongated in the [001] direction at a ratio of 1:1 Ti:NH_4F. Whereas at lower ratios, very large (*ca.* greater than 150 nm) isometric crystallites were produced. Conversely, at the high ratio Ti:NH_4F of 1:4, the growth of crystallites was suppressed and very small (15 nm) isometric crystallites were produced. It was also found that there was a substantial amount of F^- doping occurring. PIGE showed that 2/3 of the fluorine detected *via* XPS was bulk phase doping (*i.e.* about 0.5 wt/wt % TiO_2). The amount of fluorine detected was proportional to the concentration of NH_4F present in the synthesis media. The concentration of fluorine present in the synthesis was also directly proportional to the amount of Ti^{3+} detected *via* Ti2p XPS and VBS, however, depth profiling TI2P XPS showed that the majority of Ti^{3+} detected *via* XPS and VBS was surface Ti^{3+}. Interestingly, it was clear from the measured red light absorption (UV-VIS DRS) and the amount of surface Ti^{3+} detected that surface Ti^{3+} had no impact on colour of obtained materials. Furthermore, it was found *via* PXRD that the concentration of NH_4F added to the synthesis media and most likely the fluorine doping that ensued, reduced the titanium occupancy. The reduced titanium occupancy gave the blue TiO_2 ferromagnetic properties detected using SQUID. Finally, PXRD analysis of the lattice dimensions showed that the (a) dimension expanded and (c) dimension contracted with increasing ratios of Ti:NH_4F. Through analysis of the changes in lattice parameters, it was found that the changes in (a) were caused by the F^- doping whereas the changes in (c) were caused by the reducing conditions. Therefore, it is believed the Ti^{3+} defects must lie along the (c) axis of the crystallites.

By directly hydrothermally treating titanium isopropoxide in presence of 4 or greater equivalents NaF, phase pure blue brookite could be produced. It was found that as with the blue anatase, the brookite was blue due to the bulk Ti^{3+} defects stabilised by F doping. It was also found that the brookite formed *via* a sodium titanate mechanism resulting in rod-like crystals elongated in the [001] direction exposing the

{210} facet (*Note:* The aspect ratio was much greater than that observed for the blue anatase). Furthermore, it was found that the aspect ratio of the brookite crystallites was proportional to the Ti:NaF ratio. Lastly, PXRD and Raman spectroscopy studies demonstrated that the brookite formed at the expense of anatase phase crystallites and there was a critical TiO_2:NaF ratio between (1-2 equivalents) where the conversion of anatase to brookite started to occur.

By directly hydrothermally treating titanium isopropoxide in presence of 0.25 OX equivalents and 0.1 equivalents NH_4F, phase pure blue rutile could be produced. It was found that as with the blue anatase and brookite, the rutile was blue due to the bulk Ti^{3+} defects stabilised by F doping. It was found by PXRD that rutile only formed at low Ti:NH_4F ratios (0.1 or less), while at higher ratios anatase was formed. The rutile was very blue, absorbing more red light than the highly coloured blue brookite and anatase samples. It also had the greatest amount of bulk Ti^{3+} detectable *via* variable photon energy XPS. Interestingly, it was found by TEM that the F^- ion had modified the shape of the rutile crystallites resulting in a greater exposure of the {101} facet.

Finally, the photocatalytic activity of the blue TiO_2 was tested under broad spectrum, UV and visible light. It was found that most of the samples produced were photoactive and had good activity relative to P-25. In fact, a few samples had greater activity than P-25. Interestingly, the blue rutile showed the greatest photocatalytic activity when normalised for surface area. Also, despite many reports to the contrary, the blue brookite was photoactive and even more photoactive than P-25 for MB degradation. However, the most interesting result was that the blue anatase phase TiO_2 was 5 times more active than P-25 for RB-19 degradation under visible light (400 nm cut-off filter). Thus demonstrating that the blue TiO_2 may be useful as a visible light photocatalyst.

8.1 Future Work

8.1.0 The Hydrothermal Treatment of Oxalic Acid Sols

The following future work should be carried out to confirm findings or further explore:

1. The CO_2 reverse phase transformation should be further investigated by:
    a. By taking a rutile sample and autoclave it under hi-pressure CO_2.
    b. Hydrothermally treating amorphous TiO_2 under hi-pressure CO_2.

8.1.1 Defect Characterisation in Blue Anatase

The following future work should be carried out to confirm findings or further explore:

1. The work should be carried out to confirm Ti^{3+} and its location:
    a. EPR measurement at a lower temperature to confirm bulk *vs* surface Ti^{3+}
    b. SQUID measurements on sample synthesised at different concentrations NH_4F.
    c. Large-scale synthesis followed by digestion (H_2SO_4) of TiO_2 and titration of Ti^{3+}.
    d. Full analysis of depth profiling data on all samples to determine bulk Ti^{3+}.
2. The work should be carried out to confirm Ti vacancies:
    a. Thermal gravitational analysis, weight loss of OH^- groups.
    b. Measure the conductivity of the TiO_2.
3. The work should be carried out to confirm F doping:
    a. Large-scale synthesis followed by digestion of TiO_2 (NaOH + HCl) and the addition of CaCl, weigh precipitated CaF.
    b. XPS on NaOH washed blue TiO_2, determine bulk F^- doping.
    c. PIGE on samples synthesised with different ratios of NH_4F (washed and unwashed NaOH).
4. The work should be carried out to confirm colour and size:
    a. asure UV-VIS DRS on highly compressed samples (eliminates size effects).

8.1.2 Blue Rutile and Brookite phase TiO_2

The following future work should be carried out to confirm findings or further explore:

1. The exposed facets and aspect ratio of blue rutile should further explore:
    a. By synthesising a wider range of samples at lower NH_4F ratios.
    b. Look at alternative F^- sources.
2. Characterise the brookite:
    a. Identify Ti^{3+} location and quantity.
    b. Identify and quantify Ti Vacancies.

8.1.3 Photocatalysis

The following future work should be carried out to confirm findings or further explore:

1. The reproducibility and error in the photocatalytic activity measurements should be improved by:
    a. Reducing the light intensity.
    b. Do more repeats.
    c. Centrifuge sample three times rather than two.
    d. Ensure dissolved oxygen is the same for each measurement.
    e. Ensure pH is the same for each measurement.
    f. Confirm degradation rates with total carbon measurement.
    g. Ensure light intensity is reproducible.
2. The photocatalytic activity of the F^- modified rutile should be further explored by:
    a. Looking at the reactivity of the rutile under visible light only.
    b. Changing the relative aspect ratio and {101} facet exposure.
3. The photocatalytic activity of the F^- modified brookite should be further explored by:
    a. Looking at the reactivity of the brookite under visible light only.
    b. Changing the relative aspect ratio.
4. Explore visible light catalysis:
    a. Test more samples under Xe light with a cut-off filter.
    b. Test the photocatalytic activity using a colourless target such as phenol.
    c. Use LEDs with different wavelengths

Appendix

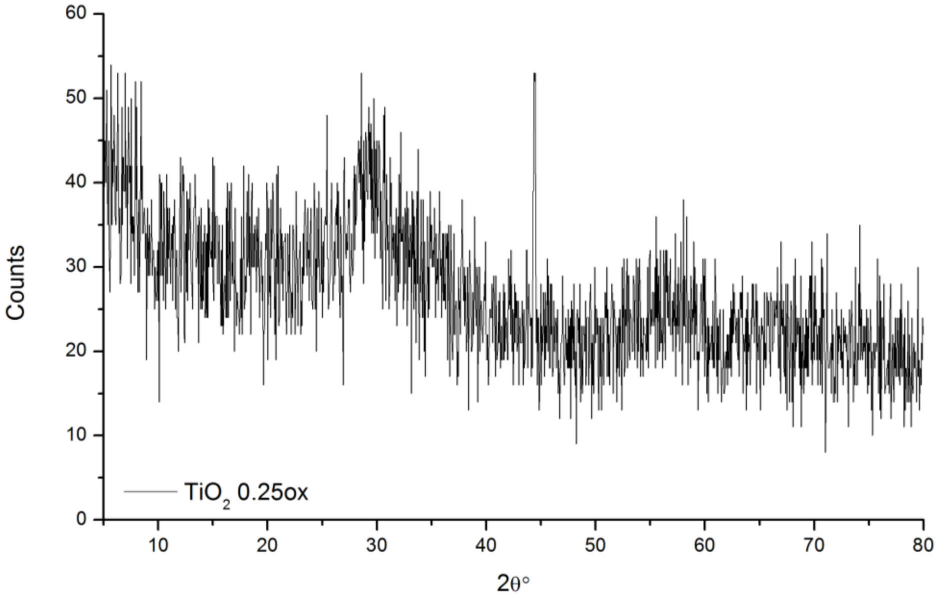

Figure S1 PXRD diffractogram of dried TiO_2 0.25ox sol

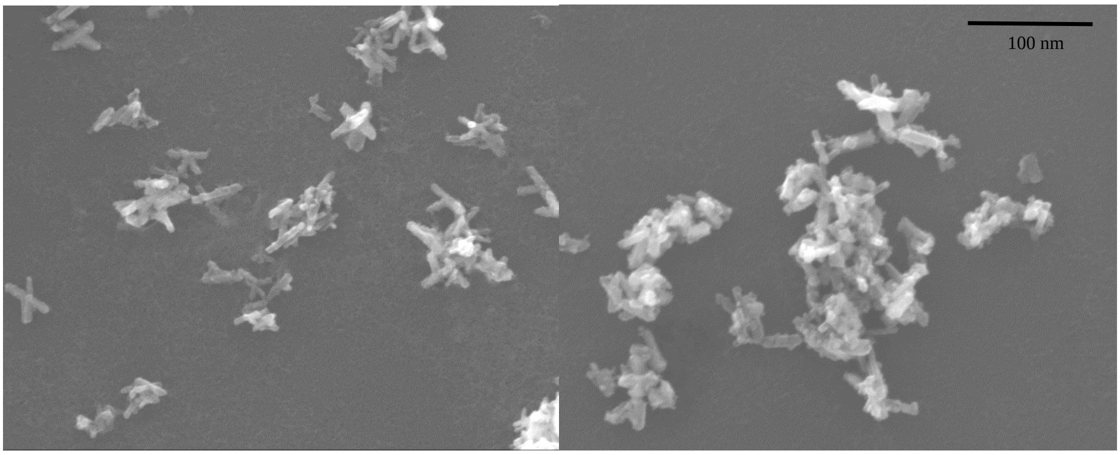

Figure S2 SEM images of rutile rods from the hydrothermal treatment of a TiO_2 0.25ox sol at 170 °C (left) and 220 (right).

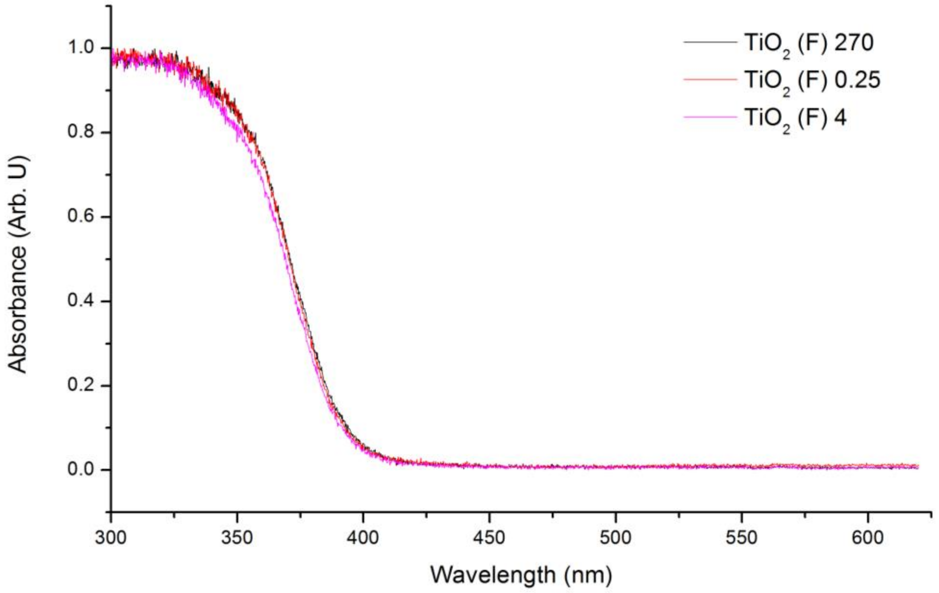

Figure S3. UV-VIS DRS spectra of series (F)

References

1. Yang, F., *et al.*, *National Science Review* (2015) **2** (2), 183
2. Halperin, W., *Rev. Mod. Phys.* (1986) **58** (3), 533
3. Volokitin, Y., *et al.*, *Nature* (1996) **384**, 621
4. Corma, A., and Garcia, H., *Chem. Soc. Rev.* (2008) **37** (9), 2096
5. Hashmi, A., and K., S., *Chem. Rev.* (2007) **107** (7), 3180
6. Linsebigler, A., *et al.*, *Chem. Rev.* (1995) **95** (3), 735
7. Kabra, K., *et al.*, *Ind. Eng. Chem. Res.* (2004) **43** (24), 7683
8. Bak, T., *et al.*, *J. Phys. Chem. Solids* (2003) **64** (7), 1043
9. Chan, S., *et al.*, *J. Chem. Technol. Biotechnol.* (2011) **86** (9), 1130
10. Chen, J., *et al.*, *Building and Environment* (2011) **46** (9), 1827
11. Fujishima, A., and Honda, K., *Nature* (1972) **238** (37-38), 37
12. Quagliarini, E., *et al.*, *J. Cult. Herit.* (2012) **13** (2), 204
13. MGázquez, M., *et al.*, *MSA* (2014) **5** (7), 441
14. Burdett, J., *Inorg. Chem.* (1985) **24** (14), 2244
15. Burdett, J., *et al.*, *J. Am. Chem. Soc.* (1987) **109** (12), 3639
16. Fahmi, A., *et al.*, *Phys. Rev. B* (1993) **47** (18), 11717
17. Hanaor, D., and Sorrell, C., *J. Mater. Sci.* (2011) **46** (4), 855
18. Finnegan, M., *et al.*, *J. Phys. Chem. C* (2007) **111** (5), 1962
19. Gribb, A., and Banfield, J., *Am. Mineral.* (1997) **82** (7), 717
20. Shojaee, E., *et al.*, *Phys. Rev. B: Condens. Matter Mater. Phys.* (2011) **83** (17), 174302/1
21. Paola, A., *et al.*, *Catalysts* (2013) **3** (1), 36
22. Chen, X., and Mao, S., *Chem. Rev.* (2007) **107** (7), 2891
23. Zhao, X., *et al.*, *J. Non-Cryst. Solids* (2008) **354** (12-13), 1424
24. Yoldas, B., *J. Mater. Sci.* (1986) **21** (3), 1087
25. Pulisova, P., *et al.*, *Catal. Today* (2011) **161** (1), 84
26. Liu, T., *et al.*, *J. Hazard. Mater.* (2008) **155** (1-2), 90
27. Yang, G., *et al.*, *Nature* (2008) **453** (7195), 638
28. Wen, Z., *et al.*, *J. Mater. Chem.* (2011) **21** (20), 7052
29. Wang, Y., *et al.*, *Chem. Commun.* (2011) **47** (10), 2829
30. Amano, F., *et al.*, *Chem. Commun.* (2009) **0** (17), 2311
31. Sonawane, R., and Ramakrishna, S., *Mater. Sci. Eng. B* (2012) **177** (9), 652
32. Yu, J., and Zhang, J., *Dalton Trans.* (2010) **39** (25), 5860
33. Xie, S., *et al.*, *Chem. Commun.* (2011) **47** (23), 6722
34. Wen, Z., *et al.*, *Chem. Commun.* (2011) **47** (15), 4400

35. Xiang, Q., *et al.*, *Chem. Commun.* (2011) **47** (15), 4532

36. Zhang, J., *et al.*, *Chin. J. Catal.* (2011) **32** (6-8), 983

37. Inada, M., *et al.*, *J. Ceram. Soc. Jpn.* (2011) **119** (6), 451

38. Ohno, T., *et al.*, *New J. Chem.* (2002) **26** (9), 1167

39. Luttrell, T., *et al.*, *Sci. Rep.* (2014) **4**, 4043

40. Pan, J., *et al.*, *Angew. Chem. Int. Ed.* (2011) **50** (9), 2133

41. Rehman, S., *et al.*, *J. Hazard. Mater.* (2009) **170** (2–3), 560

42. Zeltner, W., and Tompkins, D., *ASHRAE Trans.* (2005) **111**, 523

43. Nowotny, M., *et al.*, *J. Phys. Chem. C* (2008) **112** (14), 5275

44. Asahi, R., and Morikawa, T., *Chem. Phys.* (2007) **339** (1–3), 57

45. Nowotny, M., *et al.*, *Phys. Status Solidi B* (2005) **242** (11), R88

46. Su, J., *et al.*, *RSC Adv.* (2014) **4** (27), 13979

47. Czoska, A., *et al.*, *J. Phys. Chem. C* (2008) **112** (24), 8951

48. Zuo, F., *et al.*, *J. Am. Chem. Soc.* (2010) **132** (34), 11856

49. Naldoni, A., *et al.*, *J. Am. Chem. Soc.* (2012) **134** (18), 7600

50. Zou, X., *et al.*, *Chem. Eur. J.* (2013) **19** (8), 2866

51. Liu, X., *et al.*, *Nanoscale* (2013) **5** (5), 1870

52. Liu, G., *et al.*, *J. Phys. Chem. C* (2009) **113** (52), 21784

53. Xing, M., *et al.*, *J. Catal.* (2013) **297** (0), 236

54. Zuo, F., *et al.*, *Angew. Chem. Int. Ed.* (2012) **51** (25), 6223

55. Hamdy, M., *et al.*, *ACS Catal.* (2012) **2** (12), 2641

56. Grabstanowicz, L., *et al.*, *Inorg. Chem.* (2013) **52** (7), 3884

57. Xin, X., *et al.*, *Sci. Rep.* (2016) **6**, 23684

58. Wang, Y., *et al.*, *RSC Adv.* (2015) **5** (43), 34302

59. Mills, A., *Appl. Catal., B* (2012) **128** (30), 144

60. Schubert, U., Chemistry and Fundamentals of the Sol–Gel Process. In *The Sol-Gel Handbook*, Wiley-VCH Verlag GmbH & Co. KGaA(2015), pp 1

61. Kemmitt, T., *et al.*, *Curr. Appl. Phys.* (2013) **13** (1), 142

62. Macwan, D., *et al.*, *J. Mater. Sci.* (2011) **46** (11), 3669

63. Li, Y., *et al.*, *J. Solid State Chem.* (2004) **177** (4-5), 1372

64. Yang, W., *et al.*, *Chem. Commun.* (2011) **47** (6), 1809

65. Brock, W., and Lahoratory, H., Hydrogen Fluoride: How Toxic Is Toxic (A Hazard and Risk Analysis). In *Halon Options Technical Working Conference*, p 559

66. Ye, M., *et al.*, *Mater. Lett.* (2011) **65** (15-16), 2384

67. Ye, M., *et al.*, *Mater. Lett.* (2010) **65** (2), 363

68. Kawasaki, S., *et al.*, *Res. Chem. Intermed.* (2009) **35** (3), 299

69. Mori, K., *et al.*, *Chem. Eng. Sci.* (2008) **63** (20), 5066

70. Ye, X., *et al.*, *Nanostruct. Mater.* (1997) **8** (7), 919

71. Uekawa, N., *et al.*, *Chemistry Letters* (2000) **29** (4), 382

72. Young, A., and McQuillan, A. J., *Langmuir* (2009) **25** (6), 3538

73. Zhang, Q., *et al.*, *J. Phys. Chem. B.* (2004) **108** (39), 15077

74. Lapidus, G., *et al.*, *J. Phys. Chem.* (1964) **68** (7), 1863

75. Hinshelwood, C., and Topley, B., *J. Chem. Soc., Trans.* (1923) **123** (0), 1014

76. Bhosale, R., *et al.*, *Dalton Trans.* (2011) **40** (43), 11374

77. McNicoll, C., *et al.*, *INT J NANOTECHNOL* (2014) **11** (5-8), 493

78. Yu, J., *et al.*, *Chem. Mater.* (2002) **14** (9), 3808

79. Buslaev, Y., *et al.*, *Bull. Acad. Sci. USSR, Div. Chem. Sci.* (1962) **11** (3), 361

80. Wang, J., *et al.*, *Appl. Catal., B* (2013) **134–135**, 198

81. Wang, X., *et al.*, *Appl. Phys. A* (2016) **122** (10), 884

82. Kotsyubynsky, V., *et al.*, *MATER WERKS* (2016) **47** (2-3), 288

83. Yang, H., *et al.*, *Chem. Eng. J.* (2013) **214** (0), 229

84. Xu, J., *et al.*, *Appl. Surf. Sci.* (2008) **254** (10), 3033

85. Barbosa, M., *et al.*, *Materials Research* (2017) **20** (4), 920

86. Wu, H., *et al.*, *CrystEngComm* (2015) **17** (38), 7254

87. Yec, C., and Zeng, H. C., *J. Mater. Chem. A* (2014) **2** (14), 4843

88. Barnard, A., and Curtiss, L. A., *Nano Lett.* (2005) **5** (7), 1261

89. Barnard, A., *et al.*, *Surf. Sci.* (2005) **582** (1–3), 173

90. Li, W., *et al.*, *J. Cryst. Growth* (2000) **208** (1–4), 546

91. Grzmil, B., *et al.*, *Pol. J. Chem. Technol.* (2009) **11** (3), 15

92. Li, W., and Zeng, T., *PLoS One* (2011) **6** (6), e21082

93. Yang, X., *et al.*, *Chem. Mater.* (2011) **23** (15), 3486

94. Gock, E., and Heinz Jacob, K., *Direct Dissolution of Rutile with Sulfuric Acid*. (1980), pp. 308

95. Wei, W., *et al.*, *RSC Adv.* (2012) **2** (22), 8286

96. Gonchar, A., Package 2 Nuclei preparation and hydrolysis of titanyl sulphate.; RDTitan, (2015)

97. Wang, J., *et al.*, *Appl. Catal., B* (2013) **134–135** (0), 198

98. Gordon, T., *et al.*, *J. Am. Chem. Soc.* (2012) **134** (15), 6751

99. Chen, X., *et al.*, *Science* (2011) **331** (6018), 746

100. Xiong, L., *et al.*, *J Nanomater* (2012) **2012** (0), 13

101. Zhou, S., *et al.*, *Phys. Rev. B* (2009) **79** (11), 113201

102. Wang, S., *et al.*, *J. Am. Chem. Soc.* (2015) **137** (8), 2975

103. Nakamura, I., *et al.*, *J. Mol. Catal. A: Chem.* (2000) **161** (1–2), 205

104. Darby, M., *Brit. J. Appl. Phys.* (1967) **18** (10), 1415

105. Arrott, A., *J. Appl. Phys.* (2008) **103** (7), 07C715

106. Kittel, C., *Introduction to Solid State Physics (8th ed.)*. John Wiley and Sons Ltd:

107. Rostron, P., *et al.*, *laser* (2016) **21**, 24

108. Choi, H. C., *et al.*, *Vib. Spectrosc* (2005) **37** (1), 33

109. Zhang, J., *et al.*, *Appl. Surf. Sci.* (2014) **311** (0), 521

110. Warren, B., *X-ray Diffraction*. Dover Publications: New York, 1969, pp. 381

111. Wang, W., *et al.*, *Catal. Commun.* (2012) **22** (0), 19

112. Xu, Y., *et al.*, *RSC Adv.* (2017) **7** (52), 32461

113. Grey, I., and Wilson, N., *J. Solid State Chem.* (2007) **180** (2), 670

114. Fuentes, G., *et al.*, *Surf. Interface Anal.* (2002) **33** (3), 230

115. Ruzicka, J., *et al.*, *RSC Adv.* (2014) **4** (40), 20649

116. Chen, X., *et al.*, *Sci. Rep.* (2013) **3**, 1510

117. Pan, S., *et al.*, *J. Mater. Chem. A* (2015) **3** (21), 11437

118. Xiong, L.-B., *et al.*, *J. Nanomater.* (2012) **2012** (5-8), 0

119. Bakar, S., and Ribeiro, C., *Appl. Surf. Sci.* (2016) **377**, 121

120. McMullan, D., *Scanning* (1995) **17** (3), 175

121. McNicoll, C., *et al.*, *INT J NANOTECHNOL* (2017) **14** (1-6), 265

122. Chen, X., *et al.*, *Nature* (2013) **3**, 1510

123. Xia, T., and Chen, X., *J. Mater. Chem. A* (2013) **1** (9), 2983

124. Calatayud, D., *et al.*, *J. Phys. Chem. C* (2015) **119** (36), 21243

125. Li, F., *et al.*, *J. Mater. Res.* (2017) **32** (8), 1563

126. Zuoli, H., *et al.*, *J. Am. Ceram. Soc.* (2012) **95** (12), 3941

127. Guo, M.-L., *et al.*, *Chin. Phys. Lett* (2010) **27** (5), 057103

128. Sahoo, R., *et al.*, *Hydrometallurgy* (2001) **62** (3), 157

129. Kulkarni, D., and Wachs, I., *Appl. Catal., A* (2002) **237** (1), 121

130. Rivard, J., Kinetics of the Catalytic Dehydration of 2-Propanol in an Aqueous Medium. Thesis, University of Alberta. (2000)

131. Hoang, S., *et al.*, *J. Am. Chem. Soc.* (2012) **134** (8), 3659

132. Li, J., and Xu, D., *Chem. Commun.* (2010) **46** (13), 2301

133. Rhee, C. H., *et al.*, *J. Mater. Res.* (2011) **20** (11), 3011

134. Ding, S., *et al.*, *J. Mater. Chem.* (2011) **21** (6), 1677

135. Zhang, Y., *et al.*, *RSC Adv.* (2015) **5** (97), 79479

136. Rietveld, H., *J. Appl. Cryst.* (1969) **2** (2), 65

137. Ahmad, I., and Bhattacharya, S., *Appl. Phys. Lett.* (2009) **95** (19), 191906

138. Bokhimi, A., *et al.*, *J. Mater. Res.* (1995) **10**, 11

139. Morales, B., *et al.*, *J. Mater. Res.* (1995) **10** (11), 2788

140. Wang, S., *et al.*, *J. Am. Chem. Soc* (2015) **137** (8), 2975

141. Hebenstreit, E., *et al.*, *The adsorption of chlorine on TiO_2 (1 1 0) studied with scanning tunneling microscopy and photoemission spectroscopy*. (2002)

142. Wang, B., *et al.*, *PCCP.* (2013) **15** (24), 9891

143. De Groot, F., *et al.*, *Phys. Chem. Miner.* (1992) **19** (3), 140

144. Ruus, R., *et al.*, *Solid State Commun.* (1997) **104** (4), 199

145. Henderson, G., *et al.*, *Phys. Chem. Miner.* (2002) **29** (1), 32

146. Cox, A., *et al.*, *Am. J. Phys.* (2002) **70** (6), 620

147. Cabrera, M. I., *et al.*, *J. Phys. Chem.* (1996) **100** (51), 20043

148. Miao, G., *et al.*, *Eur. J. Inorg. Chem.* (2012) **2012** (35), 5864

149. Maisano, M., *et al.*, *J. Photochem. Photobiol. C* (2016) **28**, 29

150. Cukie"s, R., *et al.*, *J. Chem. Phys.* (1980) **73** (10), 5244

151. Macarthur, D., *Int. J. PIXE* (1991) **1** (4), 311

152. Liu, S., *et al.*, *J. Am. Chem. Soc.* (2010) **132** (34), 11914

153. Zhao, Z., *et al.*, *Chem. Commun.* (2014) **50** (21), 2755

154. Zhu, G., *et al.*, *J. Mater. Chem. A* (2013) **1** (34), 9650

155. Hu, W., *et al.*, *Cryst. Growth Des.* (2009) **9** (8), 3676

156. Lawrence, R., and Tanner, C., Production of rutile titanium dioxide. Wyeth Holdings Corp US, (1950), A2494492

157. Jiao, Y., *et al.*, *CrystEngComm* (2011) **13** (12), 4167

158. Takako, N., *et al.*, *Chemistry Letters* (1999) **28** (9), 911

159. Yang, H., *et al.*, *Chem. Eng. J.* (2013) **214**, 229

160. Merceille, A., *et al.*, *Adsorption* (2011) **17** (6), 967

161. Pan, J., and Jiang, S., *J. Colloid Interface Sci.* (2016) **469**, 25

162. Ohno, T., *et al.*, *J. Mol. Catal. A: Chem.* (2015) **396**, 261

163. Roel, K., *et al.*, *J. Mater. Chem.* (2008) **18** (20), 2311

164. Park, D.-R., *et al.*, *J. Catal.* (1999) **185** (1), 114

165. Zhang, T., *et al.*, *J. Photochem. Photobiol.* (2001) **140** (2), 163

166. Ruzicka, J., Synthesis of titanium dioxide nanoparticles: phase, morphology and size control. Thesis, University of Canterburry, Canterburry NZ, (2013)

167. Faridah, A., *et al.*, *Aust. J. Chem.* (2014) **68** (3), 471

168. Hanaor, D., *et al.*, *Surf. Coat. Technol.* (2011) **205** (12), 3658

169. Ismail, A., and Bahnemann, D, *J. Mater. Chem.* (2011) **21** (32), 11686

170. Ohno, T., *et al.*, *J. Catal.* (2001) **203** (1), 82

171. Scanlon, D., *et al.*, *Nat. Mater* (2013) **12** (9), 798

172. Murakami, N., *et al.*, *J. Phys. Chem. C* (2011) **115** (2), 419

173. García, P., *et al.*, *Revista Investigación & Desarrollo* (2017) **1** (17), 43

174. L, T., *et al.*, Thermal stability analysis of high brightness LED during high temperature and electrical aging. In *Optical Engineering + Applications*, SPIE(2007), Vol. 6669, p 10